Theoretical Limits to Tidal Stream Energy Extraction

Christopher Vogel
Magdalen College
University of Oxford

A thesis submitted for the degree of
Doctor of Philosophy
Trinity 2014

Acknowledgements

I would like to thank Prof. Guy Houlsby and Prof. Richard Willden for their advice, encouragement, and supervision throughout my DPhil. They provided excellent intellectual stimulation and gave me the freedom to develop my academic interests. Although Prof. Alistair Borthwick only supervised me during my first term in Oxford, I would also like to thank him for his support and encouragement as I first started to learn about tidal energy. I would also like to thank Alison May for the many ways she helped me during my DPhil. Discussions with my fellow doctoral students have been useful, and I would like to extend particular thanks to Clarissa Belloni, Conor Fleming, and Justine Schluntz for their comments and feedback on my work.

I am grateful to the Oxford Martin School for funding my DPhil, and to Magdalen College for providing financial support to attend a conference in Tokyo. I am also grateful for the many teaching opportunities I had during my time in Oxford.

I would finally like to thank the support of my family and friends while I have been studying here, and for making my time in Oxford so rewarding.

Abstract

Theoretical Limits to Tidal Stream Energy Extraction

A thesis submitted for the degree of Doctor of Philosophy

Christopher Vogel

Magdalen College, Oxford

Trinity Term 2014

Tidal stream energy has gained attention as a source of predictable and renewable energy. Devices resembling underwater wind turbines, placed in fast tidal streams, have been proposed to extract this energy. Arrays of many such devices will need to be deployed to deliver a significant amount of energy to the electricity grid. One consequence of energy extraction is that the array provides a resistance to the tidal stream, which may change the local and far field hydrodynamics, which in turn affects the power available to the array. Array-scale hydrodynamic changes affect the flow presented to the devices, which in turn affects the total resistance the array provides to the flow. This thesis is concerned with the interactions between device, array, and the tidal stream resource, to better understand the power potential of turbine arrays.

Linear momentum actuator disc theory is employed to describe the operation of an idealised turbine array partially spanning a wide channel. The model is comprised of two quasi-independent sub-models, an array-scale model, describing flow phenomena around the array, which provides the upstream boundary condition to the device-scale model, describing the flow around a device. The thrust applied by the array is the sum of the thrust applied by the devices, completing the sub-model coupling.

The numerical simulation of arrays in depth-averaged simulations is then investigated using the two-scale concept developed in the analytic partial-array model. It is shown that the device-scale flow must be modelled with a sub-grid scale model in order to correctly describe the unresolved device-scale flow and hence estimate the power available to an idealised array. Turbulence modelling in depth-averaged simulations of turbine arrays is also discussed.

Temporal variations in tidal amplitude and strength mean that generator capacity will need to be economically matched to the available resource. As device performance may consequently depart from the relationship derived in idealised models when power capping is employed, blade element momentum theory is modified to parameterise tidal turbine performance during power capping. The array-scale effect of power capping is studied in depth-averaged simulations, in which it is shown that a significant reduction in device thrust may occur during power capping, reducing the impact of energy extraction from the tidal stream.

Nomenclature

Common Variables

α	Non-dimensionalised turbine-scale core flow speed
β	Non-dimensionalised turbine-scale bypass flow speed
η	Basin efficiency
ν	Molecular viscosity
ρ	Density
A	Cross-sectional/swept area
B	Blockage ratio
b	Flow passage width, centre-to-centre device spacing
C_P	Power coefficient
C_T	Thrust coefficient
D	Turbine diameter
E	Total energy
Fr	Froude number
g	Gravitational acceleration
H	Total head
h	Flow depth
$\dot{m}$	Mass flow rate
P	Instantaneous power
p	Static pressure
Re	Reynolds number
T	Thrust applied to the fluid
t	Time
$\mathbf{u} = (u, v, w)$	Velocity vector

$\mathbf{x} = (x, y, z)$ Position vector

Common Subscripts

$_0$	Array-scale upstream flow boundary
$_1$	Immediately upstream of array/turbine-scale upstream flow boundary
$_2$	Immediately upstream of device
$_3$	Immediately downstream of device
$_4$	Turbine-scale hydrostatic pressure equalisation point
$_5$	Immediately downstream of array/turbine-scale downstream flow boundary
$_6$	Array-scale hydrostatic pressure equalisation point
$_7$	Array-scale downstream flow boundary
$_A$	Array-scale variables
$_c$	Channel
$_d$	Device, core flow streamtube
$_b$	Bypass streamtube
$_G$	Global-scale variables
$_L$	Local/device-scale variables
$_{mix}$	Mixing region
$_t$	Turbine
$_{tot}$	Total

Chapters 2, 3, and 6

ζ	Free surface elevation, non-dimensional array-scale static head
θ	Non-dimensional turbine-scale static head
λ_0, λ_1	Parameters related to bed friction and tidal devices, respectively
σ	Non-dimensionalised array-scale core flow speed
τ	Non-dimensionalised array-scale bypass flow speed
ω	Tidal frequency
A_C	Channel cross-sectional area

a Tidal amplitude

C_d Seabed drag coefficient

F Opposing force on flow in a channel, per unit mass

L Array width

n Number of turbines in array

Q Volume flow rate in channel

p_∞ Static pressure in the far field

p_t^+ Static pressure upstream of actuator disc

p_t^- Static pressure downstream of actuator disc

u_∞ Free stream velocity

u_t Through-disc velocity

u_w Far wake velocity

$\mathcal{V}, \mathcal{L}, I, R, \mathcal{C}$ Electrical voltage, inductance, current, resistance, and capacitance

W_C Channel width

X Force acting on surface of core flow streamtube

Chapters 4, 5, and 6

$\langle() \rangle$ Spatial average

$\bar{()}$ Time-averaged component

$()'$ Fluctuating component

$()^n$ Parameter value at the n^{th} time step

Γ Domain surface

γ Non-dimensional velocity scale

Δ Grid size

δ Kronecker delta

ϵ Energy dissipation rate

θ Numerical stability parameter

κ Non-dimensional length scale

λ	Ratio of eddy length scale to forcing eddy length scale
ν_T	Turbulent eddy viscosity
ξ	Free surface elevation
τ, τ_b	Shear stress, bed shear stress
τ	Non-dimensional time scale
ϕ	Finite element test function
ψ	Finite element basis function
χ	Non-dimensional length scale
Ω	Numerical domain
ω	Vorticity, turbulent eddy angular velocity
C	Kolmogorov constant
c_s	Smagorinsky constant
F	Acceleration due to body force
f	Coriolis parameter
K	Turbulent kinetic energy
K	Two-dimensional turbulent kinetic energy
k	Turbulent fluctuation wave number
L, L_f	Turbulent eddy length scale, turbulent eddy forcing length scale
l	Characteristic eddy length scale
T	Reynolds-averaging time period
Δt	Numerical time step
P_a	Atmospheric pressure
p	Pressure
S	Strain rate tensor
$\mathbf{U} = (U, V)$	Depth-averaged velocity
u	Characteristic eddy velocity scale
Z	Two-dimensional enstrophy

Chapters 7 and 8

$()_i$	Value of the i^{th} annulus
α	Angle of attack
β, β_s	Twist angle,pitch angle
γ	Relaxation factor, ratio of flow speed to rated flow speed
$\delta()$	Incremental value of variable on an annular ring
ε	Convergence parameter
λ	Tip-speed ratio
σ	Blade solidity
ϕ	Angle of incidence
Ω	Rotational speed of turbine
a, a_2	Turbine plane axial velocity induction factor
a_4	Volume-flux constrained turbine wake axial velocity induction factor
a'	Turbine plane tangential velocity induction factor
b	Turbine wake axial velocity induction factor
b_4	Bypass axial velocity induction factor
C_d	Drag coefficient
C_l	Lift coefficient
CF	Capacity Factor
c	Blade chord
D	Drag force
d	Rotor diameter
F	Prandtl tip-loss factor
L	Lift force
N_B	Number of blades
PF	Power factor
P_R	Rated power

p_∞	Static pressure in the far field
p_d^+	Static pressure upstream of rotor
p_d^-	Static pressure downstream of rotor
Q	Torque, volume flow rate
R	Rotor radius
r	Radial position
s	Inter-turbine spacing distance
U_a	Array flow speed
u_θ	Tangential flow speed through device
u_d	Axial flow speed through device
u_r	Rated flow speed
u_{rel}	Flow speed relative to blade

Contents

Chapter 1

Introduction

Quare patet quod si in aliis scientiis debemus venire in certitudinem sine dubitatione et ad veritatem sine errore, oportet ut fundamenta cognitionis in mathematica ponamus
If in other sciences we should arrive at certainty without doubt and truth without error, it behooves us to place the foundations of knowledge in mathematics
- Roger Bacon

The growing worldwide demand for energy, coupled with concerns about the environment and energy security, has led to an increased interest in harnessing renewable energy resources (MacKay, 2008). In light of public opinion, government policies, and environmental constraints, as well as the need to provide a reliable and consistent power supply, it is widely accepted that a diverse range of renewable generation sources must be developed (Lund and Mathiesen, 2009). A key challenge for electricity market operators will be that some renewable energy sources, such as wind and solar power, are intermittent and prone to rapid fluctuations in capacity. The ability of a network to cope with such intermittency is enhanced through dispersion of generation sites and having a diverse portfolio of generation sources, as intermittent sources tend to vary independently of each other (Grubb, 1991). Marine renewable energy therefore has the potential to form an important component of future renewable energy networks. The tides are considered to be a particularly promising marine energy resource as the tides, although intermittent, are predictable, which has benefits for electricity networks (Callaghan and Boud, 2006).

Ambitious government aims, such as the European Council's 'Energy 2020' targets, stating that 20% of the European Union's total energy supply should come from

renewable sources by 2020 (European Commission, 2010), have spurred research and development activities in renewable energy sources. A key challenge identified in the 'Energy 2020' plan was the need to diversify generation supplies in order to ensure energy security and reliability. The United Kingdom's Marine Energy Challenge, a programme designed to accelerate development of marine renewable energy technologies, identified that approximately 20% of the total electricity demand in the UK could be supplied by marine technologies (Callaghan and Boud, 2006). Studies commissioned by the Marine Energy Challenge suggest that 10% of electricity demand might be met by tidal energy. The potential contribution of various sites around the UK and the impacts of tidal energy extraction has been the subject of many subsequent studies. Similar energy targets have encouraged interest in North America, for example, where it is estimated that up to 7% of total US electricity demand could be supplied through tidal stream energy, and up to 10% of total electricity demand in both New Zealand and Australia (Sinclair Knight Merz, 2006; Geoscience Australia, 2010).

1.1 Origin of the Tides

The relationship between the tides and the moon and the spatial variation in tidal amplitude and phase has been known since antiquity (Deparis *et al.*, 2013). Tidal amplitudes of the order of one metre and low flow speeds mean that the energy flux in the deep ocean is generally too low for economic energy extraction. It is instead at the coasts, where the energy flux is concentrated, that tidal energy extraction may be economically feasible. It is important to understand the processes that govern the transmission of energy from the deep oceans to the coast, and the spatial and temporal variability in the strength of the tides at the coast, in order to appreciate the dynamics of tidal currents and the energy that may be harnessed from the tides.

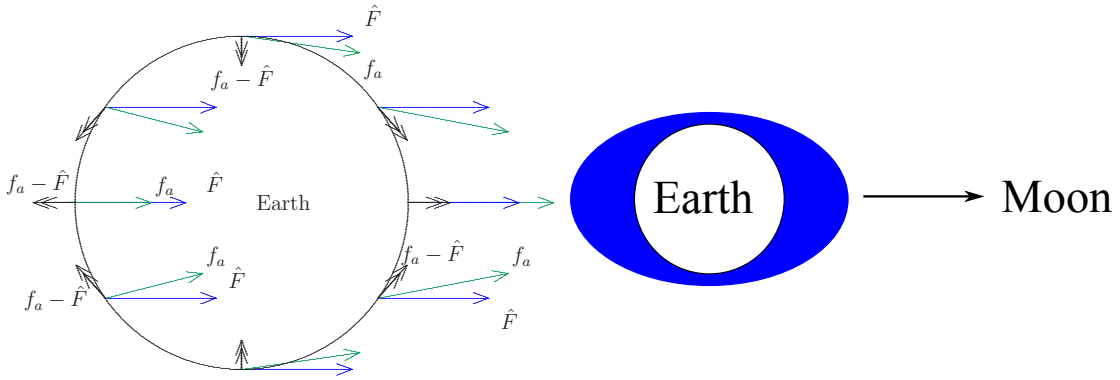

Figure 1.1: (a) Gravitational attraction between Earth and Moon (blue), gravitational attraction of Moon on the Earth's surface (green), and the net force on the Earth's surface (black) , and (b), resulting water distribution.

1.1.1 The Equilibrium Tide in the Deep Ocean

Newton considered a spherical body of mass m_1 covered in a uniform depth of water and its satellite of mass m_2 in the *Principia Mathematica*, finding the net attraction of the two bodies to be (Komar, 1976):

$$\hat{F} = G\frac{m_1 m_2}{r^2}, \tag{1.1}$$

where the gravitational constant $G = 6.6 \times 10^{-11}\text{Nm}^2\text{kg}^{-2}$, and r is the distance between the centres of mass of the two bodies. The attraction of the satellite on individual elements of the planet, f_a, varies according to their relative position to the satellite; water on the near side of the planet experiences a greater attraction towards the satellite than on the opposite side, as indicated in Figure 1.1, drawing the water on the body into an oblate spheroid with an amplitude of approximately 54cm. The gravitational interaction of the Earth and Sun also generates tides, approximately $\frac{27}{59}$ the strength of the lunar tides, with the much greater distance between the Sun and the Earth counteracting the larger mass of the Sun (Komar, 1976). The departures from the mean net attraction, $f_a - \hat{F}$, are responsible for raising the tides.

The rotation of the Earth means that the location of high tide moves across the surface of the planet, giving rise to the apparent propagation of high and low tide. Longer term variations in the tides, such as the monthly spring-neap tidal cycle, are due to the amplification from alignment of the major axes of the spheroids due to the Sun and the Moon and attenuation when the major axes are perpendicular. Although Newton's theory provided a basic theoretical model to understand the tide raising forces and the tides in the deep ocean, several phenomena were not explained by the theory, such as the time delays between the tide and transit of the perturbing body, the phase difference between transit and the maximum and minimum tides, and the variation in tidal amplitude over small spatial areas (Deparis *et al.*, 2013).

1.1.2 Periodicity of the Tides in the Deep Ocean

A long wave in the deep oceans (of depth approximately 4000m) has a wave speed of approximately 200ms^{-1}, whereas the sub-lunar point on the equator travels with an average speed of 450ms^{-1}. The speeds are almost equal at approximately 60°N/S. The oceans are thus too shallow for an equilibrium tide to propagate at the same speed as the Moon's position above the Earth, even in the absence of continents. The continents divide the oceans into different basins and restrict the propagation of waves around the Earth. Consequently, each ocean basin has individual modes of oscillation and therefore differing responses to tide generating forces. Wave propagation is also influenced by Coriolis accelerations due to the rotation of the Earth (Pugh, 1987).

Laplace (1782) developed a dynamic theory of the tides to address the shortcomings of equilibrium tide theory. Laplace noted that the depth of the oceans is very small relative to the radius of the Earth, and treated the problem as a quasi-two dimensional flow (Deparis *et al.*, 2013). Denoting the horizontal velocity of a water particle $\mathbf{u}$, the Earth's angular velocity ω, and ζ the radial deformation of the fluid

layer, Laplace formulated dynamical and continuity equations:

$$\frac{\partial \mathbf{u}}{\partial t} + 2\omega \wedge \mathbf{u} = -g\nabla\zeta + \nabla V + \nabla\Phi, \tag{1.2}$$

$$\frac{\partial \zeta}{\partial t} + \nabla \cdot h\mathbf{u} = 0, \tag{1.3}$$

where g is acceleration due to gravity, V the tidal potential, Φ the potential of the self-gravity of the fluid layer, and h is the depth of the fluid particle (Deparis *et al.*, 2013). Movement of the Sun and the Moon relative to the Earth's equator was modelled with a series of satellites, each contributing a component of the combined tide-raising forces acting on the oceans. Each satellite generated its own tide, with unique amplitude, period, and phase, called a tidal constituent. Although harmonic analysis of the tides reveals over one hundred tidal constituents, approximately 80% of tidal amplitude and phase can be accounted for with just seven constituents (Defant, 1961). A key innovation of Laplace's work was the introduction of the $2\omega \wedge \mathbf{u}$ term, accounting for acceleration in a rotating reference frame, later known as Coriolis acceleration. Tidal propagation was no longer assumed to occur in straight lines around the Earth, but instead followed curved paths due to the action of the Coriolis force.

1.1.3 Interaction Between Deep Ocean and Continental Shelf

Tidal propagation across the oceans is generally obstructed by the presence of continental landmasses, with the exception of the Southern Ocean. Tides progress around the oceanic basins, with the greatest tidal elevations achieved at the coasts and centred on regions of small tidal range, called amphidromic points, as illustrated in Figure 1.2. The tides are thus a result of the interaction between the tides generated in the deep ocean, deflection of tide propagation by the Coriolis force, and oceanic and continental shelf bathymetry (Plumb and Marshall, 2007).

Propagation of the tides on the continental shelves is slower than in the deep

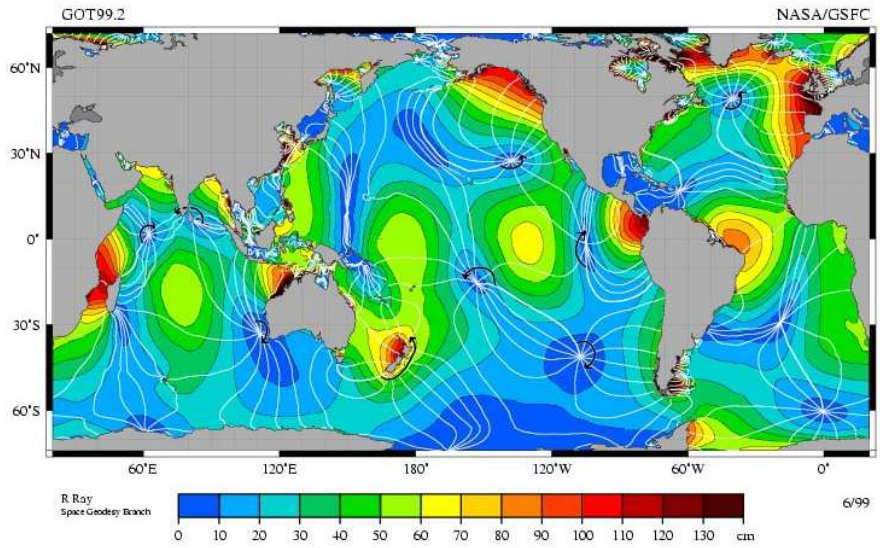

Figure 1.2: Map of M2 tidal elevation (in colour) and amphidromes (line intersections).

ocean, as the water is much shallower (Plumb and Marshall, 2007). The effects of direct tidal forcing in such small bodies of water are relatively small compared to the effects of forcing from the open ocean boundaries. Tides on the continental shelves are also influenced by the reflection of tidal waves along the coastline, allowing incident and reflected tidal waves to combine. The tides at the coast are thus primarily the result of tidal wave propagation across the continental shelves (Pugh, 1987).

The tidal amplitude may become large near the coast through two principal mechanisms; the first being the narrowing of a channel or estuary, concentrating the energy of the incoming tide, and the second being constructive interference between incoming and reflected components of the tide (Plumb and Marshall, 2007). Natural resonance is achieved if the continental shelf is close to one-quarter (for the largest tidal amplitudes) of a tidal constituent wavelength, allowing a standing wave to form. This occurs in a number of places around the world, such as in the Bay of Fundy, Canada, where quarter wavelength resonance is established with the M2/S2 tidal constituents, and the tidal range increases to over ten metres from approximately one metre in the Gulf of Maine. On the other hand, diurnal tides are established in the Gulf of Mexico

because the Gulf is resonant with the K1/O1 diurnal tidal constituents (Pugh, 1987).

Regions where tidal resonance occurs are of interest to tidal developers as the energy transmitted from the deep oceans to the continental shelves is concentrated in these locations, enhancing the economic and technical feasibility of extracting energy from the tides. Feasibility will be driven by the magnitude of the tidal resource at a particular location, its temporal variability through the interaction of the dominant tidal constituents and bathymetry, and the response of the system to energy extraction, in particular whether the system moves closer to or away from the natural resonant frequency with the deep ocean. These considerations will have an impact on the choice of technology used to extract energy from the tides.

1.2 Harnessing the Tidal Resource

Energy extraction from the tides can be broadly classified into two categories. The first requires the construction of a barrage or dam to enclose an area, such as an estuary or a bay, which allows the difference in potential energy of the water between high and low tides to be exploited. The second involves the deployment of devices to extract energy from tidal currents, much in the same way as wind turbines extract energy from the wind. The second of these methods is the focus of this thesis.

1.2.1 Tidal Barrages

Tidal barrages are formed by damming a body of water to separate it from the open ocean. Sluice gates are opened as the tide comes in, allowing water into the impoundment area. The gates are closed at high tide, trapping the water until a sufficient height difference has developed between the trapped water and the falling (ebb) tide. The water is then released through turbines in the barrage into the open sea, with energy extracted as the water flows from the area of higher potential energy

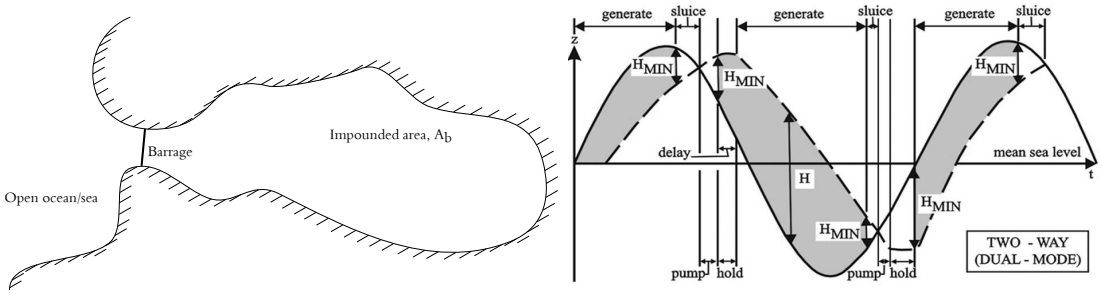

(a) (b)

Figure 1.3: (a) Plan view of a hypothetical tidal barrage spanning the entrance to a bay, and (b), a diagram of the water elevation in a tidal barrage operating in dual mode, from Burrows *et al.* (2009).

inside the barrage to lower potential energy outside the barrage. The process may be used during the flood tide, with the water entering the barrage through the turbines, allowing generation on both the flood and ebb tides.

Garrett and Cummins (2004) analysed the maximum power, averaged over a tidal cycle, that could be extracted by a tidal barrage operated on the flood and ebb tides, illustrated in Figure 1.3. A sinusoidal tidal elevation $\xi = a\cos(\omega t)$ was assumed at the entrance to the bay, where a was the tidal amplitude, ω the angular frequency of the tide, and t time. Assuming that the bay enclosed an area of uniform depth A_b, and that the water instantaneously filled and emptied from the barrage, the maximum averaged power was found to be $2\pi^{-1}\rho g A_n \omega a^2$, where ρ is the density of water and g is acceleration due to gravity. As the water does not instantaneously fill and empty the barrage, the potential energy difference across the barrage is reduced, resulting in the available power being some fraction of the maximum average power. This, in addition to the complexities of non-uniform bathymetry in bays and estuaries giving rise to a non-constant area A_b as the impounded area fills and empties, leads to challenging optimisation problems to determine the optimal filling and emptying schedule of the barrage to maximise the power (Ryrie, 1995). The power may also be improved by allowing water to be pumped in and out of the barrage to increase the height difference between the two bodies of water (Yates *et al.*, 2013).

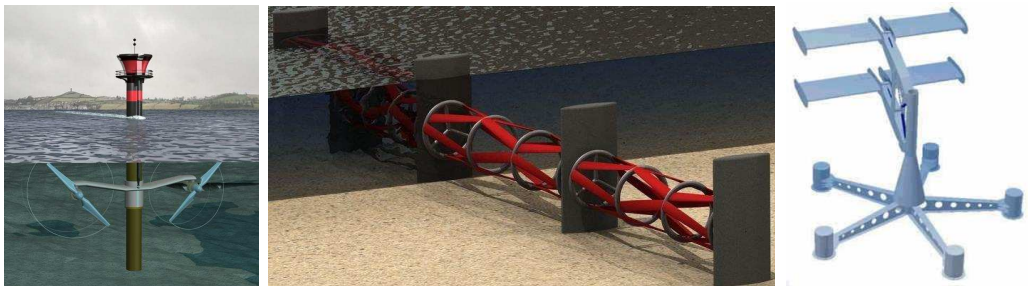

(a) (b) (c)

Figure 1.4: (a) Marine Current Turbines SeaGen horizontal axis turbine. Image from Fraenkel (2007). (b) THAWT Darrieus-type turbine. Image from McAdam *et al.* (2009). (c) Oscillating hydrofoil type device. Image from DTI (2005).

Tidal barrages currently in operation around the world include the 240MW La Rance tidal barrage in France, the Annapolis-Royal barrage in the Bay of Fundy, Canada, and one in Kislaya Bay, near Murmansk, Russia (Charlier and Finkl, 2009). Further barrages have also been proposed, in particular in the Bristol Channel, and Bay of Fundy, as well as a number around China, South Korea, and South America, although planning and construction is slow due to the high cost of construction and the significant impacts that barrages have on the environment (Baker, 1991).

1.2.2 Tidal Current Turbines

Tidal current (stream) devices are designed to extract energy from the bulk motion of water in tidal currents. The devices, examples of which are shown in Figure 1.4 may broadly be classified into three general types: horizontal axis turbines; Darrieus-type cross-flow turbines; and, oscillating hydrofoils. Development has largely converged on the horizontal axis turbine, with many devices currently under development and testing. The European Marine Energy Centre (EMEC) was established in the Orkney Islands to provide facilities for testing tidal current devices and offers support facilities for installation and maintenance, as well as grid connection (Charlier and Finkl, 2009).

The choice of turbine to harness best the tidal resource will depend on a number of different considerations, and may vary according to the site and turbine deployment

configuration. Despite the multiplicity of designs, a successful turbine will need to be economical to construct, install, and maintain, as well as having good hydrodynamic performance to maximise the power extraction. As tidal devices will be installed in strong tidal currents, installation will be expensive and challenging and therefore reducing installation complexity will be important. The supporting structure and foundations will also play an important role in the choice of turbine, as support structure drag has a significant effect on the power available to the turbine (Muchala and Willden, 2014). The motivation behind Darrieus type devices in particular, such as the THAWT device shown in Figure 1.4, is to maximise the cross-section of the flow occupied by the turbine whilst minimising the need for support structure, and hence the associated structural drag (McAdam *et al.*, 2009).

Despite the complexities of selecting the optimal device to maximise power extraction, tidal current turbines have attracted significant research and commercial interest. Tidal current turbines may have a lower environmental impact than a tidal barrage, as well as being cheaper and the possibility of developing turbine arrays incrementally. The reduced environmental impact and lower capital outlay required for tidal current devices means that there is lower investment and regulatory risk in comparison to a tidal barrage, making tidal current technology attractive.

It is expected that, regardless of the exact device choice, devices will need to be arranged in a fence or array-like configuration of many turbines to generate a significant amount of power (Garrett and Cummins, 2007), with the configuration depending on how constrained the flow is by channels, headlands, islands, or other geographic features. Furthermore, numerous studies by Garrett and Cummins and others indicate that inter-turbine spacing plays in determining the power available to turbines. The flow around a single device has received considerable attention, and the 'array-scale' flow, which concerns the power available to the turbine array, has been gathering more attention, and forms the central focus of this thesis.

1.3 Thesis Objectives

Significantly harnessing the tidal stream resource will require the deployment of large numbers of tidal turbines in array configurations. The importance of inter-turbine spacing and turbine-scale flow phenomena on the power available to turbines has become established in the literature, however the importance of array-scale flow phenomena on the power available from the flow is less well understood. This challenge is addressed through three primary objectives, the first two concerned with modelling array-scale flow around a finite width array of idealised turbines in a wide channel analytically and numerically, and the third to incorporate realistic turbine thrust and power characteristics to investigate the power extracted by an array and the effect on the flow in a tidal channel.

1.3.1 Objective 1: Array-scale Flow Phenomena

Linear Momentum Actuator Disc Theory (LMADT) has been successfully applied to wind and tidal turbines as an approximation to the flow around the rotor allowing the turbine's power to be assessed analytically. If an array is comprised of a sufficient number of turbines, three-dimensional turbine-scale flow phenomena occur over a much shorter distance and much faster than the larger, predominantly two-dimensional array-scale flow phenomena, allowing the two flow scales to be separated and analysed quasi-independently. LMADT has been extended to approximate the flow field around an array in a channel with a free surface, providing a semi-analytic tool for investigating the array-scale flow and power available to the turbines. This is coupled with LMADT analysis of a single turbine to determine the power available to the array and the far field impacts of energy extraction.

1.3.2 Objective 2: Simulating Tidal Turbine Arrays

One of the challenges in modelling tidal turbine arrays is that the highly turbulent flow field around a tidal turbine is three-dimensional and characterised by length scales which are much smaller than those characterising the array-scale flow, which is predominantly two-dimensional. However, it is computationally infeasible to resolve both length scales sufficiently to provide an accurate description of the effect of turbulent mixing on a tidal array, and instead the contribution of turbine-scale mixing must be approximated within the depth-averaged simulations. Turbulence is believed to play an important role in wake mixing, and an objective of this thesis is to investigate the modelling of turbulent mixing in depth-averaged flows.

A distinction is made between the power available to a turbine for conversion into mechanical energy, which is the inviscid limit of the shaft power of a turbine (Adcock *et al.*, 2014), and the power dissipated in the mixing processes in the turbine wake. The total power removed from the flow is the sum of the available power and the dissipated power. This distinction is important in depth-averaged simulations because the turbine-scale flow field cannot be simulated accurately, and therefore the available power cannot be correctly determined. This thesis also investigates the challenge of representing correctly the array thrust as well as correctly computing the power available to the turbines. Concepts from the analytic section of this thesis are utilised in order to model the turbine-scale flow within the array-scale simulation to account for the effect of the bypass flow on turbine-scale performance.

1.3.3 Objective 3: Turbine Power Capping

Analytic theory and much of the numerical analysis of large tidal turbine arrays has considered the flow around idealised turbines which extract axial momentum from the flow with perfect hydrodynamic efficiency, neglecting, for example, the angular momentum imparted on the flow and the shedding of tip-vortices. Realistic turbine

performance, and thus turbine array performance, will therefore be different to that of an idealised array as considered in the previous two sections. Furthermore, turbine power will be limited (capped) to some level by the choice of generator capacity which matches the revenue generated by the available power with the tidal resource and installation costs. Turbine performance may therefore change with respect to flow speed in a manner which diverges from that in actuator disc theory.

The third objective of this thesis has been to simulate arrays with realistic turbine performance characteristics. Firstly, blade element momentum theory, widely applied to wind turbine design, is modified to account for the volume-flux constrained flow within which tidal turbines operate to develop a semi-analytic tool to determine thrust and power characteristics for a specified turbine design. This allows turbine performance to be evaluated in a variety of blockage conditions and also allows the effect of blade feathering and similar control mechanisms to be investigated. The thrust and power characteristics are then implemented within depth-averaged simulations of turbine arrays, allowing the effect of turbine power capping to be investigated on the array-scale, addressing the second aspect of the objective to simulate arrays with realistic turbine performance characteristics.

1.4 Thesis Outline

This thesis includes an analysis of the flow around an idealised tidal turbine array, the depth-averaged simulation of an idealised array, and development of a novel blade element momentum theory model. The thesis has been broadly divided into three sections, beginning with analytic models of idealised arrays, progressing to numerical simulations of idealised arrays, and finally numerical simulations of arrays with more realistic turbines.

The first section investigates the use of analytic models in modelling the flow

around an idealised array of tidal turbines. Chapter 2 begins with a review of actuator disc theory and its application to wind turbines. Traditional actuator disc theory is not directly applicable to tidal turbines due to the confined flow field, and analytic models proposed to determine the available power in a uniform tidal flow by turbines are reviewed. Extension of actuator disc theory to the confined flow field around a tidal turbine is discussed, leading to an analytic expression for the power available to an actuator disc from such a flow under a range of conditions. Chapter 3 adopts actuator disc theory for a single turbine to model the flow around an actuator disc array partially spanning a wide channel to determine the power available to the array.

The second section investigates depth-averaged numerical simulations of turbine arrays. Chapter 4 presents the shallow water equations, which describe two-dimensional depth-averaged flow, and briefly discusses their implementation in the continuous Galerkin Finite Element code TELEMAC-2D. The role of turbulence modelling in depth-averaged simulations is discussed in Chapter 5, focussing in particular on the differences between two- and three-dimensional turbulence. Chapter 6 investigates the power available to an array partially spanning a wide channel of constant cross-section in depth-averaged numerical simulations.

The final section simulates of arrays with realistic turbines rather than actuator discs, as the power extracted by real turbines will not always follow the cubic relationship with flow speed derived in actuator disc theory. Blade element momentum theory, which has been applied successfully to the design of wind turbines, is adapted in Chapter 7 for the volume-flux constrained flow around a tidal turbine. Modified blade element momentum theory is used in Chapter 8 to determine turbine characteristics with respect to flow speed under a variety of conditions to parameterise depth-averaged simulations of realistic turbine arrays (including power capping).

Chapter 9 presents the main conclusions of the thesis and suggestions for further work.

Chapter 2

Flow Around a Single Turbine

There is nothing more practical than a good theory
- Ludwig E. Boltzmann

This chapter reviews analytic methods developed to analyse the power of an array of tidal devices spanning a channel. LMADT for wind turbines is reviewed, which yields the simple result that the maximum fraction of the upstream kinetic flux that may be extracted is 59.3%. Such a simple relationship cannot be derived for tidal turbines, as the confined flow around the turbines results in a dynamic balance between the resistance imposed by, and the diversion of the flow around, the turbine.

Analytic models for turbines are considered in two broad categories; those modelling the overall effect of energy extraction from a channel or basin, and those modelling the flow around a device. The tidal channel is examined analytically using the zero-dimensional Navier-Stokes equations and its electrical analogy, from which it is shown that the available power depends on the forces driving flow in the channel, the natural resistance to the flow due to bed friction and other dynamic effects, and the resistance imparted by the tidal turbines.

LMADT extensions have been proposed to account for the confined flow field around the device imposed by the free surface, modelled as both a rigid lid and then a pressure and volume constraint on the flow. It is shown that blockage, the ratio of device frontal area to the cross-section of the surrounding flow passage is an important factor in determining the power of a tidal turbine. There is also a dependence on the Froude number of the flow. The chapter concludes with a review of the limitations of the LMADT approach for a turbine array completely spanning a tidal channel.

2.1 Wind Turbines

Actuator disc theory was developed by Rankine (1865) and Froude (1889) to describe the flow field around a ship propeller. The complicated three-dimensional problem was simplified by replacing the complex shape of the propeller with a simple, uniformly porous disc, and applying incompressible fluid flow assumptions to determine the steady state flow around the propeller. It was later shown by Lanchester (1915) and Betz (1920) that the same idea could be applied to an inverse propeller in an infinite flow field, of which the wind turbine is one example. Their approach involved using a simple representation of the rotor as a porous actuator disc, which imparts an axial thrust on the flow. The complexity of the flow problem was reduced and allowed a control volume analysis to be used to determine the dynamics of the simplified flow around the turbine.

2.1.1 The Lanchester-Betz Limit

Lanchester and Betz's application of LMADT to wind turbines showed that it was not possible to extract all of the projected kinetic flux upstream of the turbine, as any attempt to do so would cause the flow to divert around the turbine as it presented an increasingly large resistance to the flow. A diagram of the simplified flow field around a turbine is shown in Figure 2.1, and demonstrates that the streamtube enclosing the turbine expands as the flow speed in the wake of the turbine reduces to conserve the mass flux through the streamtube. Streamtube expansion upstream and downstream of the turbine increases as the applied thrust increases, as does the expansion of the turbine wake.

Analysis of the simplified flow field allows a number of observations to be made about the physics of wind turbines. The wind turbine is characterised by an actuator disc with a frontal area A_d, which corresponds to the swept area of the turbine

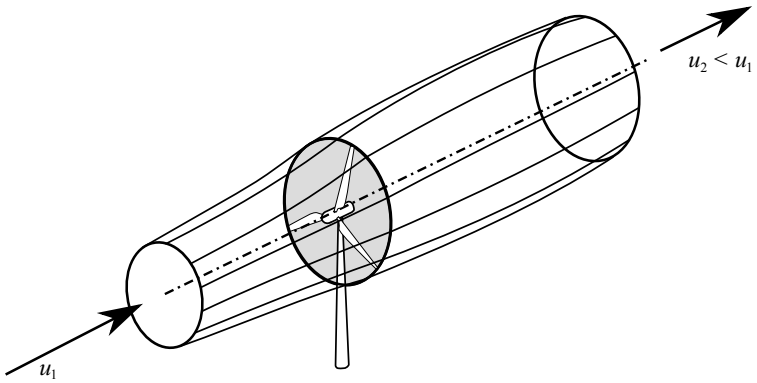

Figure 2.1: Diagram of a wind turbine and streamtube, with the idealised actuator disc shown in grey. Adapted from Burton *et al.* (2001).

rotor, and a thrust T_d, which corresponds to the thrust exerted by the turbine on the flow. Conservation of energy, described by the Bernoulli equation, upstream and downstream of the turbine yields:

$$p_\infty + \frac{1}{2}\rho u_\infty^2 = p_t^+ + \frac{1}{2}\rho u_t^2, \qquad p_t^- + \frac{1}{2}\rho u_t^2 = p_\infty + \frac{1}{2}\rho u_w^2, \tag{2.1}$$

where p_∞ is the static pressure in the far field, p_t^+ is the static pressure just in front of the actuator disc, p_t^- the static pressure just behind the actuator disc, u_∞ the free stream velocity, u_t the velocity through the actuator disc, and u_w the velocity in the far wake of the disc. It is assumed that no mixing occurs between the core flow through the disc and the bypass flow around the disc. Equilibrating forces across the actuator disc requires $p_t^+ - p_t^- = \frac{T_d}{A_d}$. Combining these equations yields:

$$T_d = \frac{1}{2}\rho u_\infty^2 A_d \left(1 - \frac{u_w^2}{u_\infty^2}\right). \tag{2.2}$$

Similarly, the conservation of momentum between the upstream and downstream boundaries of the flow (ignoring axial forces on the expanding streamtube) requires:

$$T_d = \rho u_\infty^2 A_d \frac{u_t}{u_\infty}\left(1 - \frac{u_w}{u_\infty}\right). \tag{2.3}$$

Equating (2.2) and (2.3) requires $\frac{u_t}{u_\infty} = \frac{1}{2}\left(1 + \frac{u_w}{u_\infty}\right)$, thus it is possible to express the solution as a function of $\frac{u_w}{u_\infty}$. Writing the power available to the actuator disc, $P_d = T_d u_t$, as a function of $\frac{u_w}{u_\infty}$ it is found that:

$$P_d = T_d u_t = \frac{1}{2}\rho u_\infty^3 A_d \frac{1}{2}\left(1 + \frac{u_w}{u_\infty}\right)^2 \left(1 - \frac{u_w}{u_\infty}\right) = \frac{1}{2}\rho u_\infty^3 A_d C_P, \tag{2.4}$$

where $C_P = \frac{1}{2}\left(1 + \frac{u_w}{u_\infty}\right)^2 \left(1 - \frac{u_w}{u_\infty}\right)$ is the power coefficient.

The variation of power with the thrust imposed by the actuator disc can be described by an inverted curve; no power is available when no thrust is applied, nor is power available when the thrust is so large that all the flow bypasses the disc. Between these limits lies a point at which the available power is maximised. At this point, a positive increment in thrust results in a reduction in the mass flux through the actuator disc, with more of the flow being forced into the bypass due to the additional thrust. The incremental reduction in velocity through the turbine is not offset by the incremental increase in thrust, resulting in an overall drop in the power. Lanchester and Betz showed that this optimal point, found by maximising Equation (2.4) with respect to $\frac{u_w}{u_\infty}$, corresponded to $\frac{16}{27}$ of the undisturbed kinetic flux passing through an equivalent cross-section projected into the flow upstream of the actuator disc. The $\frac{16}{27}$ fraction is known as the Lanchester-Betz limit, as it represents the maximum available power when the optimal retarding force is applied to a flow.

The momentum theory used to derive the Lanchester-Betz limit is a simplified representation of the aerodynamics of a turbine in an unbounded flow. The swirl or tangential velocity component introduced into the turbine wake is not considered by the one-dimensional streamwise analysis of actuator disc theory (Glauert, 1947). This rotational motion represents an additional loss of energy from the axial flow, reducing the power available to the turbine further below that of actuator disc theory (Burton *et al.*, 2001). Additional losses arise from the frictional drag between the fluid and the

turbine blades and support structure, which appear to the fluid as an additional axial resistance to the flow, but are not converted into useful power (Wilson and Lissaman, 1974).

2.1.2 Extensions to Betz Theory

The actuator disc theory of Lanchester and Betz has been extended in various ways to overcome some of the simplifications used to formulate the model. A rotating wake model was proposed by Glauert (1947) to modify the actuator disc so that it is possible to account for the rotational motion imparted on the flow by a rotating turbine. Multiple stream tube theory, double actuator disc theory and double multiple actuator disc theory were developed to account for differences in the wind speed seen by blades in vertical axis turbines (for example, Strickland (1975); Paraschivoiu (1988); Beri and Yao (2011)). Blade element theory incorporates the aerodynamic properties of turbine rotors to more realistically model the turbines, and has been successfully used to account for drag losses (Wilson and Lissaman, 1974). Despite the limitations of the simple LMADT model and the availability of more accurate models, the Lanchester-Betz limit has proved to be a useful benchmarking tool for wind turbine design and assessment, with modern turbine designs achieving approximately 90% of the Lanchester-Betz limit (Burton *et al.*, 2001).

2.2 Analytical Models for Tidal Turbines

Despite the multiplicity of designs for tidal stream turbines, the simplified physics of the flow around such devices may be analysed in a similar manner to wind turbines by using LMADT. Although differences exist in the designs of wind and tidal turbines, in principle, efficient tidal turbines should, like efficient wind turbines, extract energy from the streamwise flow with minimal wasteful rotational momentum imparted in

the wake. Actuator discs are therefore a convenient tool for analysing the dynamics of the flow around turbines and determining the power available to turbines in tidal flows.

Several differences exist between the physical regimes in which wind turbines and tidal turbines operate. LMADT, as derived for wind turbines, assumes the flow boundaries are far away from the actuator disc, and therefore the analysis developed by Lanchester and Betz only applies to tidal turbines in similar operating conditions (Fraenkel, 2002). When the flow boundaries are close to the turbine rotor the assumptions in standard actuator disc theory are not applicable.

In the far wake, LMADT indicates that there is a reduction in the kinetic energy due to energy extraction by the turbine, and therefore a decrease in the flow speed in the wake. On the other hand, open-channel flow theory predicts that energy extraction from a sub-critical flow results in a decrease in the free surface elevation and acceleration of the flow downstream of the turbine (White, 1994). The assumptions of LMADT work well for wind turbines, where the atmosphere is approximated as infinitely tall, but are not appropriate for tidal turbines operating in an environment where the free surface is within a few rotor diameters of the turbine. As a result, the Lanchester-Betz limit and LMADT derived for wind turbines are not directly applicable when assessing the flow around a tidal turbine.

Recognising that the analysis for wind turbines was not directly applicable to tidal turbines, early work by Black & Veatch (2005) introduced a 'Significant Impact Factor' (SIF), which was applied to the natural kinetic flux through the frontal area of the turbine (Equation (2.5)), to account for the limiting effect the flow diversion around the turbine has on the available power and other regulatory constraints.

$$P_d = \frac{1}{2}\rho u_\infty^3 A_d \text{ SIF}. \tag{2.5}$$

Although this simplistic approach recognised that the Lanchester-Betz limit was not appropriate for tidal turbines, it did not provide insight into the physics of energy extraction in tidal flows or distinguish between the physical and regulatory limitations to energy extraction.

A number of extensions to the LMADT developed for wind turbines have been proposed to provide an analysis more appropriate to turbines in tidal streams. These extensions can broadly be classified into three main categories: analysis of turbines completely spanning a tidal channel; a turbine in a volume constrained flow, also called the rigid lid model; and a turbine in an open channel. The first of these analyses, turbines completely spanning a tidal channel, was investigated by Garrett and Cummins (2005), examined the response of a channel between two large bodies of water to the introduction of an array of tidal turbines which completely spanned the channel cross-section. Recognising that it would not be possible to occupy the entire channel cross section with turbines, Garrett and Cummins (2007) considered a single tidal turbine in a volume constrained flow, where the free surface could not deform, but there was mixing in the wake between the core flow through the turbine and the bypass flow around the turbine. This was further extended by Houlsby *et al.* (2008) and Whelan *et al.* (2009) to consider a turbine in an open channel. Each extension is reviewed below.

2.3 Energy Extraction in a Tidal Channel

The limitations of the kinetic flux approach to determining the available power was investigated by Garrett and Cummins (2004), which showed that that there was no simple relationship between the average kinetic flux and the average maximum available power of a turbine. They also noted that the kinetic energy flux varies as A^{-2}, where A is the cross-sectional area of the channel, meaning that the resulting

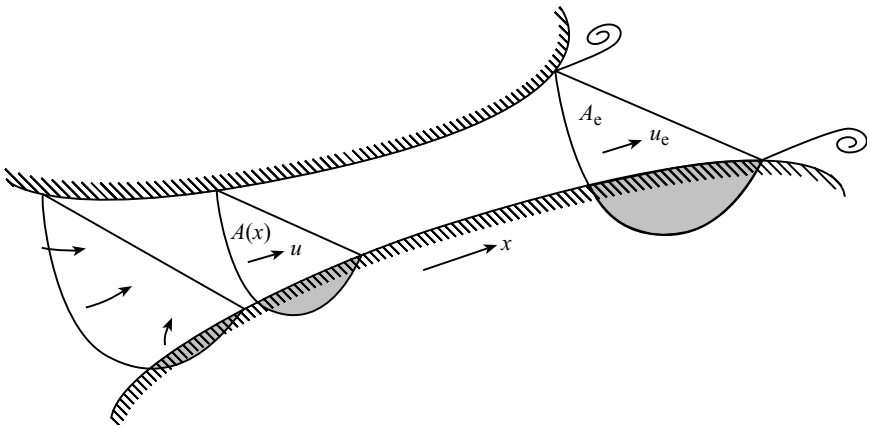

Figure 2.2: Diagram of a generic tidal channel between two large tidal basins, after Garrett and Cummins (2005).

power is sensitive to the location where it is evaluated (Garrett and Cummins, 2008). Garrett and Cummins (2005) proposed an analytical model using the zero-dimensional shallow water equations for an array of tidal turbines spanning a channel (Figure 2.2) between two large bodies of water:

$$\frac{\partial u}{\partial t} + u\frac{\partial u}{\partial x} + g\frac{\partial \zeta}{\partial x} = -F, \tag{2.6}$$

where ζ describes the free surface elevation and F is the opposing force on the flow, per unit mass, associated with natural friction in the channel as well as resistance to the flow by the presence of turbines. In order for the turbine force to be independent of streamwise position in the channel it is necessary for the turbines to completely span the cross-section of the channel. The current in the channel has a speed u, which is a function of $A(x)$, the cross sectional area of the channel, where x is the streamwise position along the channel.

Garrett and Cummins assumed that the channel was sufficiently short compared to the tidal wavelength that the volume flux was constant along the length of the channel and that the tidal elevations in the basins were unchanged by changes which occurred within the channel. Furthermore, it was assumed that the Froude number

was sufficiently small so that, as a first order approximation, the depth and velocity are functions of position only. Finally, Garrett and Cummins required that the channel length and cross-section did not change over time due to the tides. Using these assumptions, integrating Equation (2.6) gives:

$$c\frac{dQ}{dt} - g\zeta_0 = -\int_0^L F dx - \frac{1}{2}u_e|u_e|, \qquad c = \int_0^L A^{-1} dx, \tag{2.7}$$

where Q is the flow rate in the channel, $\zeta_0(t)$ is the difference in the water level in the two basins, assumed to be $\zeta_0(t) = a\cos(\omega t)$, where a is the amplitude of the head difference with frequency ω, and u_e is the exit velocity from the channel. The final term of Equation (2.7) arises from the non-linear advection term in Equation (2.6), and assumes that water is smoothly drawn into the channel at the inlet, but allows for the flow to exit as a jet into the downstream basin.

Introducing the drag coefficient of the seabed C_d, and assuming that the drag was quadratic in velocity, the last term of Equation (2.7) could be written as:

$$-\int_0^L F dx = -\int_0^L F_t dx - \alpha Q|Q|, \qquad \alpha = \int_0^L C_d(hA^2)^{-1} dx + \frac{1}{2}A_e^{-2}, \tag{2.8}$$

where A_e is the cross-sectional area of the channel exit and F_t is the force imposed by the turbines on the flow. It was further assumed that force imposed by the turbines on the flow was also quadratic in u, so that when the equation was non-dimensionalised, a parameter λ_1 could be used to describe the turbine thrust. Defining $Q_0 = ga(c\omega)^{-1}$, the non-dimensionalised equation became:

$$\frac{dQ'}{dt'} - \cos t' = -(\lambda_0 + \lambda_1)|Q'|Q', \tag{2.9}$$

where $Q' = Q_0^{-1}Q$, $t' = \omega t$, and $\lambda_0 = ga\alpha(c\omega)^{-2}$. The last term, λ_0, represents the ratio of drag losses and the velocity head at the channel exit to acceleration, and is

normalised by the amplitude of the driving current, therefore describing the balance between the different dynamic conditions in the channel. The driving head in the channel is balanced by the combination of the acceleration, the velocity head at the exit of the channel, and the natural drag of the sea floor and the imposed drag of the turbines.

One particularly interesting condition may be observed when the acceleration is negligible, leading to a quasi-steady flow through in the channel. The power available to the turbines is:

$$\rho Q \int_0^L F_t dx = \rho Q(g\zeta_0 - \alpha|Q|Q). \tag{2.10}$$

As Q is varied, this has a maximum $0.38\rho g Q_1 \zeta_0$, where the flux Q_1 has the magnitude $|Q_1| = \sqrt{g|\zeta_0|/\alpha}$ and the same sign as ζ_0. For $\zeta_0 = a\cos\omega t$, Q_1 can be written as $Q_{\max}|\cos\omega t|^{1/2}$, where $Q_{\max}$ is the maximum flux in the channel undisturbed by turbines. Averaging over a tidal cycle, noting that $\overline{|\cos\theta|^{3/2}} = 0.56$, the average power in Equation (2.10) becomes:

$$P_1 = 0.21\rho g a Q_{\max}. \tag{2.11}$$

Remarkably, the coefficient 0.21 changes to only 0.24 as the natural regime in the channel progresses from one with negligible background friction to one dominated by friction, as shown in Figure 2.3. This means that the average maximum power of a quasi-steady channel can be estimated to within 10% accuracy by selecting a coefficient $\gamma = 0.22$, without the need to understand the dynamical balance within the channel.

A key outcome was that the available power is not related to the kinetic flux in the channel in a simple way, and instead is determined by the work done by the tide. Indeed, Garrett and Cummins noted that the power only becomes a constant fraction of the kinetic flux in the limiting case where the separation effect at the channel outlet

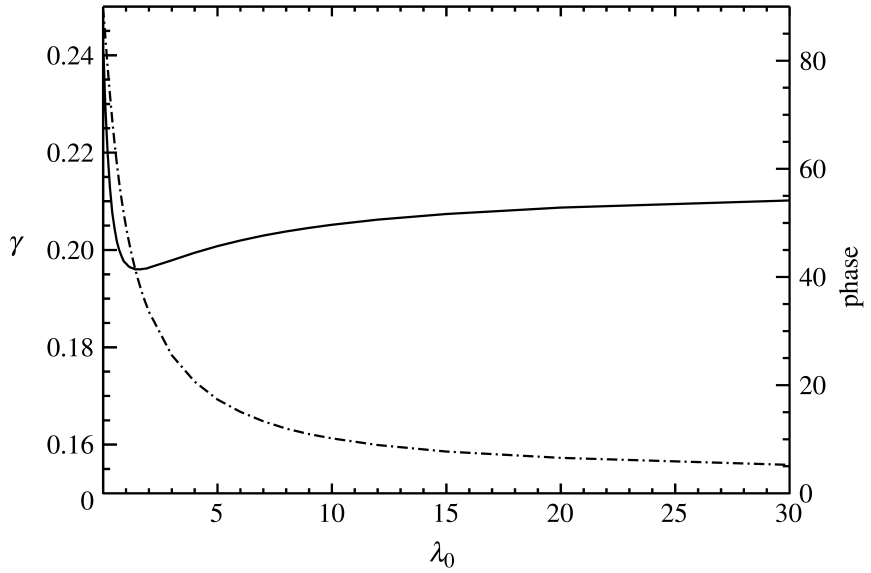

Figure 2.3: Variation of the multiplier γ giving the maximum average power as a function of the natural friction parameter λ_0 shown with the solid line and left axis. The phase lag (degrees) of the undisturbed state, of the volume flux behind the natural forcing, is shown with the dashed line and the right axis. From Garrett and Cummins (2005).

dominates the natural friction and acceleration within the channel:

$$P_1 = 0.38 \cdot \frac{1}{2}\rho A_e \overline{|u_{e0}|^3}, \tag{2.12}$$

where $u_{e0} = \sqrt{2g\zeta_0}$ is the instantaneous exit speed in the undisturbed channel.

Although the method proposed by Garrett and Cummins took the free surface of the channel into account and showed that there was no simple relationship between the kinetic flux through the turbine frontal area and the power available to the turbine, their analysis assumed that the channel cross-section was completely spanned by turbines. However, this will not be feasible in real turbine arrays, and the gaps between turbines will present flow passages with lower resistance to the oncoming flow, thus altering the flow and therefore the available power. As a result, although the analysis by Garrett and Cummins offered an important step towards understanding the dynamics of energy extraction by tidal turbines, further work was needed

to understand the effect of bypass regions between turbines due to turbine spacing requirements.

2.3.1 Electrical Analogy

An alternative method to study the flow in a tidal channel between two large basins is to consider an electrical circuit equivalent to the tidal channel. Application of equivalent circuit analysis to waves in harbours was pioneered by Miles (1971), and Lighthill (1978) discussed its application to shallow flows in channels, in which the alternating electric voltage is analogous to the time-varying hydrostatic pressure in the flow and the electric current represents the volume flow rate through the channel. The electrical analogy was applied by Rainey (2009) to determine the optimum position for a tidal barrage in the Severn Estuary to maximise its power, and then by Atwater and Lawrence (2010) to determine the idealised power potential of an array of tidal turbines completely spanning a sub-channel within a larger tidal channel. More recently, the electrical analogy has been applied to estimate the available power of the multiple channels of the Pentland Firth (Draper *et al.*, 2014). An advantage of the electrical analogy is that it allows sinusoidally varying flows to be analysed using established analytical methods for electric circuit problems.

The equivalent circuit for energy extraction from a sub-channel of a larger tidal channel between an open ocean and a bay is shown in Figure 2.4. The forcing of the open ocean is represented as an alternating voltage, and it is assumed that the open ocean is sufficiently large that the amplitude of the free surface oscillation is unaffected by changes in the tidal channel being examined. Although the head difference across the channel is assumed to remain constant, the flow through the channel may vary according to the impedance of the channel. Each sub-channel is described in terms of a resistance, representing the bed friction in the sub-channel, and an inductance, representing the phase delay in the sub-channel due to the acceleration of the water

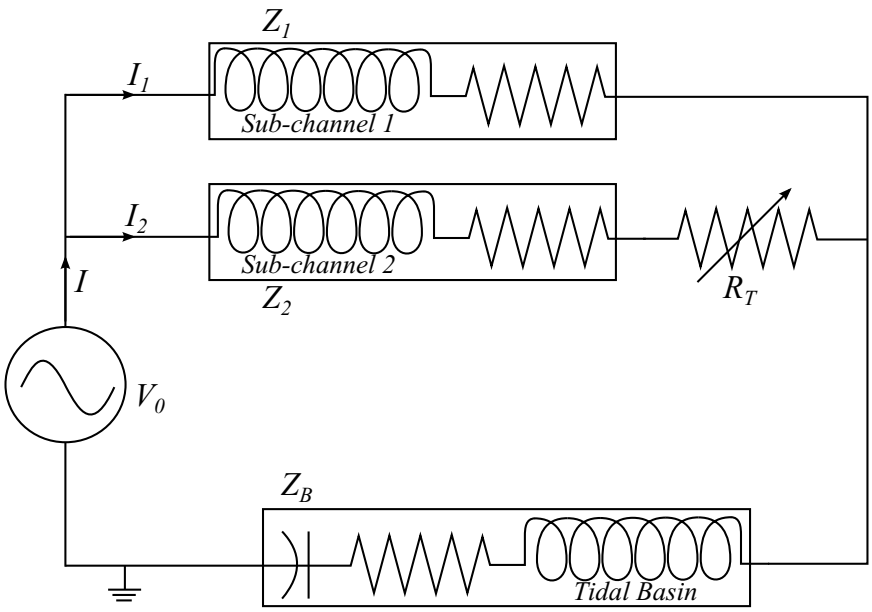

Figure 2.4: Equivalent electrical circuit diagram for energy extraction from one sub-channel in a tidal channel connecting a tidal basin with an open ocean. Adapted from Cummins (2013).

as the tidal wave propagates through it. A tidal bay also requires a capacitance to represent the storage and discharge of water that is $\frac{\pi}{2}$ out of phase with the driving frequency. The tidal turbines are modelled as a variable resistance R_T acting in a sub-channel.

The solution of the electrical analogy often utilises Thévenin's theorem for determining an equivalent circuit for the load resistance due to the turbines, R_T (Cummins, 2013). The resulting equation has the general form:

$$\mathcal{V} = \mathcal{L}\frac{dI}{dt} + RI + \mathcal{C}\int Idt, \tag{2.13}$$

where $\mathcal{L}$ is the circuit inductance, $\mathcal{C}$ is the circuit capacitance, and R comprises the resistance due to the seabed and the turbines (Draper, 2011). For a given voltage drop (head difference) across the turbines, a higher current (flow rate) results in greater power available to the turbines, which may be maximised. However, the greater the resistance imposed on the flow by the turbines, the lower the current will be in the

circuit, giving rise to the balance between turbine resistance and flow rate discussed earlier. It is also apparent that it is not possible to describe simply the available power solely in terms of either the head difference or the flow rate in the channel.

The use of Thévenin's theorem and other electrical methods to simplify and solve the equivalent circuit require a number of assumptions to be made about the flow through the channel. It is assumed that the current is constant throughout the channel, and therefore the flow must be non-divergent. This requires the length of the channel to be small compared to the tidal wavelength driving the flow through the channel. A linear relationship between the resistance imposed by, and the current passing through, the turbines is also assumed. This is a simplification of the real, quadratic relationship that drag has with flow speed, and hence limits the electrical analogy to first-order approximation of the resistance that the turbines impose on the flow. Despite these simplifying assumptions, equivalent circuit analysis offers insights into tidal flows in channels, and in particular multiply connected sub-channels, which are difficult to solve directly from the momentum equations.

2.4 Actuator Disc Theory for Tidal Turbines

The zero-dimensional model proposed by Garrett and Cummins (2005) for turbines in a tidal channel assumed that the turbine completely spanned the channel cross-section. This assumption did not take into account individual turbines nor did it allow passage of some of the flow around the turbines, commonly known as the bypass flow. The bypass flow limits the available power as it is possible for the water to pass around the turbine if the resistance to the flow is sufficiently large.

The flow around individual turbines has been analysed using extensions of Lanchester and Betz's actuator disc analysis of a wind turbine. These extensions may broadly be divided into two categories; a volume-flux constrained ('rigid lid') model,

due to Garrett and Cummins (2007), and an open channel model, due to Houlsby *et al.* (2008) and Whelan *et al.* (2009). It is assumed in both models that the channel walls are straight and parallel and that the channel seabed is flat.

The two classes of model have many similarities; it is assumed that there is a constant inflow and static head at the upstream boundary of the problem, and that the operation of the turbine, approximated as an actuator disc, does not affect the conditions at this boundary. The flow passage around the actuator disc is divided into two streamtubes, a core streamtube which encompasses the flow through the disc, and a bypass streamtube, containing the flow which passes around the disc. The core flow speed reduces and the static head increases as the upstream face of the actuator disc is approached. The flow speed is necessarily constant across the disc, but there is a static head discontinuity as a result of the thrust applied to the flow. In the wake of the disc, the core flow slows down and static head is recovered, resulting in expansion of the streamtube. Meanwhile, the bypass flow is accelerated, with an attendant drop in static head, as a consequence of the expanding core streamtube. At some point downstream of the actuator disc, the falling static head in the bypass and the rising static head in the core flow equalise. The core and bypass flows mix downstream of the hydrostatic pressure equalisation point to produce a uniform flow speed across the depth of the channel and new hydrostatic pressure which is necessarily lower than that at the inlet of the model.

The two classes of model differ principally in how they treat static head variation along the channel. Open channel flow theory predicts that energy extraction from a sub-critical flow results in a reduction in the water depth and acceleration of the flow downstream of the energy extraction. This is explicitly modelled in the open channel models of Houlsby *et al.* and Whelan *et al.*. However, if the change in flow passage cross-sectional area is negligible, then the static head variation along the channel may be considered simply as pressure variations along a channel with constant cross-

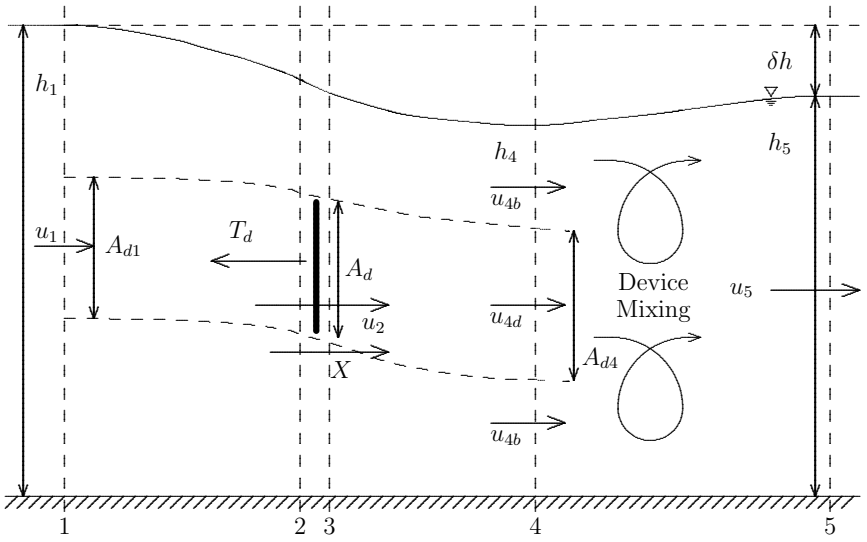

Figure 2.5: Side view of the one-dimensional model of flow around a single turbine in an open channel. After Houlsby *et al.* (2008).

section. This forms the basis of the volume-flux constrained, or rigid lid, model of Garrett and Cummins (2007). Thus, the rigid-lid model is an approximation to the open channel model which becomes exact as the change in water depth becomes negligible.

2.4.1 Open Channel Actuator Disc Theory

Whelan *et al.* (2007), and later Whelan *et al.* (2009), adapted Lanchester and Betz's analysis of a wind turbine by considering the consequence of a deformable free-surface on the flow through and around the turbine between the constant inflow boundary far upstream of the actuator disc and the downstream position where the hydrostatic pressure equalised in the core and bypass flows. However it was recognised by Garrett and Cummins (2007) that further energy would be removed from the flow due to the mixing of the core and bypass flows downstream of the hydrostatic pressure equalisation position, and Houlsby *et al.* (2008) extended the open channel actuator disc analysis to account for this downstream mixing on the power removed from the channel.

The static head variation along the channel in response to energy removal results in the variation of the cross-sectional area along the channel. A diagram of the inviscid, incompressible flow around a single actuator disc in a frictionless open channel of width b is shown in Figure 2.5. It is assumed that there is a constant flow speed u_1 and static head h_1 far upstream of the actuator disc, and that the flow speed and static head are not perturbed by the change in the flow in the channel due to the action of the actuator disc. The flow is separated into two streamtubes; the core flow, which encapsulates the flow through the disc, and the bypass flow, which contains the flow around the actuator disc. The disc exerts a thrust T_d on the flow, which results in a static head difference $h_2 - h_3$ across the actuator disc. The velocity in the core flow reduces to u_2 immediately upstream of the actuator disc. The core flow velocity is also u_2 immediately downstream of the actuator disc as it is assumed that the cross-sectional area of the core flow is constant immediately upstream and downstream of the disc. The velocity in the core flow reduces in the wake of actuator disc to u_{4d} as the core flow streamtube expands to a cross-sectional area A_{4d} and the static head is recovers h_4. Additionally, there may be a force X on the surface of the core flow streamtube acting to confine the core flow. The flow in the bypass is accelerated from u_1 to u_{4b} to conserve the mass flux in response to the expanding core streamtube and confinement of the flow due to the deformable free surface. The static head in the bypass reduces from h_1 to the hydrostatic equalisation head h_4 through conservation of the total head in the bypass. The core and bypass flows mix viscously between stations four and five downstream of hydrostatic pressure equalisation at station four to yield a new hydrostatic head h_5 and complementary uniform flow speed u_5. The static head reduces by δh between stations one and five as a result of energy extraction from a sub-critical open channel flow. The flow speed at the outlet of the channel is thus accelerated from u_1 to u_5 to maintain the mass flux through the channel.

Equations of conservation of mass, momentum, and energy are applied to the one-

dimensional model to formulate a system of equations that can be solved in order to determine the power available to the actuator disc. The power P_d is calculated as the product of the thrust of the disc on the flow, T_d, and the flow speed through the disc, u_2:

$$P_d = T_d u_2. \tag{2.14}$$

The thrust may be found by considering conservation of energy using the Bernoulli equation between stations one and two, and three and four in the core flow, and stations one and four in the bypass, noting that conservation of mass requires the flow speed at stations two and three of the core flow to be equal, yielding:

$$h_1 + \frac{1}{2g}u_1^2 = h_2 + \frac{1}{2g}u_2^2, \tag{2.15a}$$

$$h_3 + \frac{1}{2g}u_2^2 = h_4 + \frac{1}{2g}u_{4d}^2, \tag{2.15b}$$

$$h_1 + \frac{1}{2g}u_1^2 = h_4 + \frac{1}{2g}u_{4b}^2. \tag{2.15c}$$

The thrust applied by the actuator disc to the flow is equal to the static head difference across the disc integrated over the surface of the disc:

$$T_d = \frac{1}{2}\rho g A_d (h_2 - h_3), \tag{2.16}$$

where A_d is the frontal area of the disc. Rearranging Equations (2.15a) to (2.15c) for $h_2 - h_3$ and using the expression for the thrust on the disc in Equation (2.16) gives an expression for the thrust in terms of the difference in the squares of the bypass and core velocities at station four:

$$T_d = \frac{1}{2}\rho A_d \left(u_{4b}^2 - u_{4d}^2\right). \tag{2.17}$$

It is useful to be able to describe the importance of the turbine dimensions with

regards to power extraction. The concept of blockage, the ratio of the turbine frontal area to the cross-sectional area of the channel at the channel inlet, can be introduced as:

$$B = \frac{\text{Turbine frontal area}}{\text{Channel cross-sectional area}} = \frac{A_d}{bh_1}. \tag{2.18}$$

Conservation of mass in the core flow requires that:

$$A_{1d}u_1 = A_d u_2 = A_{4d}u_{4d}, \tag{2.19}$$

and across the entire water column at stations one and four that:

$$h_4 = Bh_1\frac{u_2}{u_{4d}} + h_1\frac{(u_1 - Bu_2)}{u_{4b}}. \tag{2.20}$$

Conservation of momentum between stations one and four requires the balance of the streamwise static head gradient, applied thrust, and change in momentum of the fluid between stations one and four:

$$\frac{1}{2}\rho g b\left(h_1^2 - h_4^2\right) - T_d = \rho A_d u_2\left(u_{4d} - u_1\right) + \rho\left(bh_1u_1 - A_d u_2\right)\left(u_{4b} - u_1\right). \tag{2.21}$$

The static head terms are eliminated from Equation (2.21) by rewriting Equation (2.15c) to yield an expression for $h_1 - h_4$, and eliminating h_4 by using the definition in Equation (2.20) and noting the definition for thrust in Equation(2.17), giving:

$$\begin{aligned}\left(u_{4b}^2 - u_1^2\right)&\left(\frac{u_{4b} + u_1}{u_{4b}} + Bu_2\frac{u_{4b} - u_{4d}}{u_{4b}u_{4d}}\right)\\ &= 4\left(\frac{1}{2}B\left(u_{4b}^2 - u_{4d}^2\right) + Bu_2\left(u_{4d} - u_1\right) + \left(u_1 - Bu_2\right)\left(u_{4b} - u_1\right)\right).\end{aligned} \tag{2.22}$$

The through-turbine velocity, u_2, may be found as:

$$u_2 = \frac{u_{4d}\left[2Bu_{4b}\left(u_{4b}^2 - u_{4d}^2\right) - \left(u_{4b} - u_1\right)^3\right]}{B\left(u_{4b} - u_{4d}\right)\left[\left(u_{4b}^2 - u_1^2\right) + 4u_{4b}u_{4d}\right]}. \tag{2.23}$$

The definition for h_4 in Equation (2.20) and the expression for u_2 may then be used to express Equation (2.15c) as:

$$\begin{aligned} &2Bu_{4b}\left(u_{4b}^2 - u_{4d}^2\right) - \left(u_{4b} - u_1\right)^3 \\ &\qquad = \left[\left(u_{4b} - u_1\right) - \frac{1}{2}u_{4b}Fr^2\left(\frac{u_{4b}^2}{u_1^2} - 1\right)\right]\left[\left(u_{4b}^2 - u_1^2\right) + 4u_{4b}u_{4d}\right], \end{aligned} \tag{2.24}$$

in which the Froude number is defined as $Fr^2 = \frac{u_1^2}{gh_1}$. It is useful to non-dimensionalise the velocities in this polynomial expression to eliminate u_1. Expressing velocity non-dimensionalisations as $\alpha_i = \frac{u_i}{u_1}$ in the core streamtube and $\beta_i = \frac{u_i}{u_1}$ in the bypass streamtube, the equation can be written as a quartic equation for β_4 as a function of α_4, B, and Fr^2:

$$\begin{aligned} Fr^2\beta_4^4 + 4\alpha_4 Fr^2\beta_4^3 + 2(2B_L - 2 - Fr^2)\beta_4^2 + 4(2 - 2\alpha_4 - Fr^2\alpha_4)\beta_4 \\ + (8\alpha_4 - 4 + Fr^2 - 4\alpha_4^2 B_L) = 0. \end{aligned} \tag{2.25}$$

The equation may be solved exactly if the flow is sub-critical, and the appropriate root is determined by noting that it is required that $0 \leq \alpha_4 \leq \alpha_2 \leq 1$ and $\beta_4 \geq 1$ for a physical solution of the system of equations.

It is assumed between stations one and four that the interface between the core and bypass streamtubes is frictionless and therefore there is no mixing between the two streamtubes. The difference in flow speed the develops drives the viscous mixing process between stations four and five. The two flows mix downstream of the hydrostatic pressure equalisation position at station four, removing further energy from the flow to produce a uniform flow speed u_5 and water depth h_5. The total energy removed from the flow is therefore the sum of the energy extracted by the actuator disc and the energy dissipated in the viscous mixing region.

The far field effects of the energy extracted by the actuator disc can be analysed by considering the conservation of momentum across the channel between stations

one and five:

$$\frac{1}{2}\rho g b\left(h_1^2 - h_5^2\right) - T_d = \rho b h_1 u_1 \left(u_5 - u_1\right). \tag{2.26}$$

Continuity between stations one and five requires that $h_1 u_1 = h_5 u_5$, which can be used to eliminate u_5 from the equation above. Defining $\delta h = h_1 - h_5$, Equation (2.26) is rearranged to give:

$$\frac{1}{2}\left(2\frac{\delta h}{h_1} - \left(\frac{\delta h}{h_1}\right)^2\right) - \frac{T_d}{\rho g b h_1^2} = Fr^2\left(\frac{{}^{\delta h}/_{h_1}}{1 - {}^{\delta h}/_{h_1}}\right). \tag{2.27}$$

The thrust coefficient C_T is defined as:

$$C_T = \frac{T_d}{\frac{1}{2}\rho A_d u_1^2}, \tag{2.28}$$

which allows Equation (2.27) to be expressed as a cubic for $\frac{\delta h}{h_1}$ in terms of the blockage ratio, Froude number, and thrust coefficient:

$$\frac{1}{2}\left(\frac{\delta h}{h_1}\right)^3 - \frac{3}{2}\left(\frac{\delta h}{h_1}\right)^2 + \left(1 - Fr^2\left(1 - \frac{1}{2}C_T B\right)\right)\frac{\delta h}{h_1} - \frac{1}{2}Fr^2 C_T B = 0. \tag{2.29}$$

The far-field change in free surface elevation, $\frac{\delta h}{h_1}$, characterises the far-field impact of energy extraction from the open channel and may be of interest with respect to assessing the performance of tidal turbines. It is informative to introduce an additional measure of efficiency, often called the 'basin efficiency' (see, for example Belloni and Willden (2011)), which has been proposed to supplement the traditional efficiency described by the power coefficient. The basin efficiency is the ratio of the available power relative to the total energy removed from the flow, P_{tot}, rather than relative to the flux across the disc as with the power coefficient:

$$\eta = \frac{\text{Power available to disc}}{\text{Power available to disc and dissipated in mixing}} = \frac{P_d}{P_{tot}}. \tag{2.30}$$

The total power removed between stations one and five is found from the difference in energy flux between the two stations. The change in energy flux between stations one and five can be expressed as the difference in total head $H_1 - H_5$ at the two stations:

$$P_{tot} = g\dot{m}\left(H_1 - H_5\right), \tag{2.31}$$

where $\dot{m} = \rho b h_1 u_1$ is the mass flow rate through the channel, $H_1 = h_1 + \frac{1}{2}\frac{u_1^2}{g}$, and $H_5 = h_5 + \frac{1}{2}\frac{u_5^2}{g}$. The total power removed from the channel can thus be expressed as:

$$P_{tot} = \rho g b h_1 u_1 \delta h \left(1 + \frac{1}{2} Fr^2 \frac{\frac{\delta h}{h_1} - 2}{\left(1 - \frac{\delta h}{h_1}\right)^2} \right). \tag{2.32}$$

The power coefficient is defined as the available power normalised against the upstream kinetic flux projected onto the disc's frontal area:

$$C_P = \frac{P_d}{\frac{1}{2}\rho u_1^3 A_d} = \frac{\alpha_2 u_1 T_d}{\frac{1}{2}\rho u_1^3 A_d} = \alpha_2 C_T, \tag{2.33}$$

which, in conjunction with Equation (2.32) allows the basin efficiency to be expressed as:

$$\eta = \frac{\alpha_2 Fr^2 B C_T (1 - \frac{\delta h}{h_1})^2}{\frac{\delta h}{h_1}\left(2(1 - \frac{\delta h}{h_1})^2 + Fr^2(\frac{\delta h}{h_1} - 2)\right)}. \tag{2.34}$$

The basin efficiency expression may be simplified by neglecting small terms. For many tidal channels it will be true that $Fr^2 \ll 1$, so that the total power removed from the channel, to the first order, may be approximated as $P_{tot} = \rho g b h_1 u_1 \delta h$. Defining the available power as $P_d = \alpha_2 u_1 T_d$, the basin efficiency may be expressed as:

$$\eta = \frac{\alpha_2 u_1 T_d}{\rho g b h_1 u_1 \delta h}. \tag{2.35}$$

Multiplying Equation (2.26) by u_1 yields a second expression for $u_1 T_d$:

$$u_1 T_d = \rho g b h_1 u_1 \left(\delta h - \frac{1}{2}\frac{\delta h^2}{h_1} - Fr^2 \frac{\delta h}{1 - \frac{\delta h}{h_1}} \right). \tag{2.36}$$

The basin efficiency may therefore be expressed as:

$$\eta = \alpha_2 \left(1 - \frac{\delta h}{h_1}\right) \frac{\left(1 - \frac{1}{2}\frac{\delta h}{h_1}\right)\left(1 - \frac{\delta h}{h_1}\right) - Fr^2}{2\left(1 - \frac{\delta h}{h_1}\right)^2 + Fr^2\left(\frac{\delta h}{h_1} - 2\right)}. \tag{2.37}$$

If Fr^2 is small but finite, the basin efficiency may be approximated as:

$$\eta = \alpha_2 \left(1 - \frac{1}{2}\frac{\delta h}{h_1}\right). \tag{2.38}$$

The basin efficiency may thus be expressed primarily in terms of α_2 with a small correction for the deformation of the free surface, which acts to reduce the basin efficiency for a given α_2. The consequences of this result shall be discussed further in relation to the rigid-lid model in Section 2.4.2.

Confining Force

A force, X, acts on the surface between the core and bypass streamtubes between stations one and four. Conservation of momentum requires:

$$X = \frac{1}{2}\rho g b h_1^2 \left((1 - B\alpha_2) - \frac{h_4}{h_1}\left(\frac{h_4}{h_1} - B\frac{\alpha_2}{\alpha_4}\right) - 2Fr^2 (1 - B\alpha_2)(\beta_4 - 1) \right). \tag{2.39}$$

The force on the upstream boundary due to the upstream water depth is equal to:

$$b\int_0^{h_1} \rho g z dz = \frac{1}{2}\rho g b h_1^2, \tag{2.40}$$

which has been factorised out of the expression for X in Equation (2.39) so that X can be considered in terms of the different magnitudes of the forces acting on the core and bypass flows. Rearranging Equation (2.15c) for $\frac{h_4}{h_1}$, Equation (2.39) yields an equation with the Froude number to three different powers:

$$\mathcal{O}(Fr^0) : \frac{X}{\frac{1}{2}\rho g b h_1^2} = B\frac{\alpha_2}{\alpha_4}\left(1-\alpha_4\right), \tag{2.41a}$$

$$\mathcal{O}(Fr^2) : \frac{X}{\frac{1}{2}\rho g b h_1^2} = Fr^2\left(1-\beta_4\right)\left(\frac{1}{2}\left(1+\beta_4\right)\left(B\frac{\alpha_2}{\alpha_4}-2\right)+2\left(1-B\alpha_2\right)\right), \tag{2.41b}$$

$$\mathcal{O}(Fr^4) : \frac{X}{\frac{1}{2}\rho g b h_1^2} = -\frac{1}{4}Fr^4\left(1-\beta_4^2\right)^2. \tag{2.41c}$$

The $\mathcal{O}(Fr^0)$ term represents the area over which the hydrostatic pressure head h_1 far upstream of the actuator disc acts. This is a strictly positively valued term for physical solutions of the open channel model, which requires $0 \leq \alpha_4 \leq \alpha_2 \leq 1, 0 \leq B \leq 1$, as can be seen from Equation (2.41a). It is also required that Equation (2.41c) be negative for all physical solutions, so that the $\mathcal{O}(Fr^4)$ term represents the adverse pressure gradient against which the core flow in the device wake must work to maintain the mass flux downstream of the disc. The contribution of Equation (2.41b) depends on the sign of:

$$\chi = \frac{1}{2}\left(1+\beta_4\right)\left(B\frac{\alpha_2}{\alpha_4}-2\right)+2\left(1-B\alpha_2\right). \tag{2.42}$$

For all physical solutions of the open channel model $\chi \leq 0$, with equality when $\alpha_2 = \alpha_4 = \beta_4 = 1$, as shown in Figure 2.6. This means that the $\mathcal{O}(Fr^2)$ expression for X in Equation (2.41b) is positive, and represents the additional force that acts on the surface of the core flow streamtube due to the change in free surface elevation in the channel. The $\mathcal{O}(Fr^2)$ term dominates the $\mathcal{O}(Fr^4)$ term for sub-critical flows, so that the net contribution of the free surface deformation is to provide a force which accelerates the flow in the core streamtube, increasing the flow speed through the

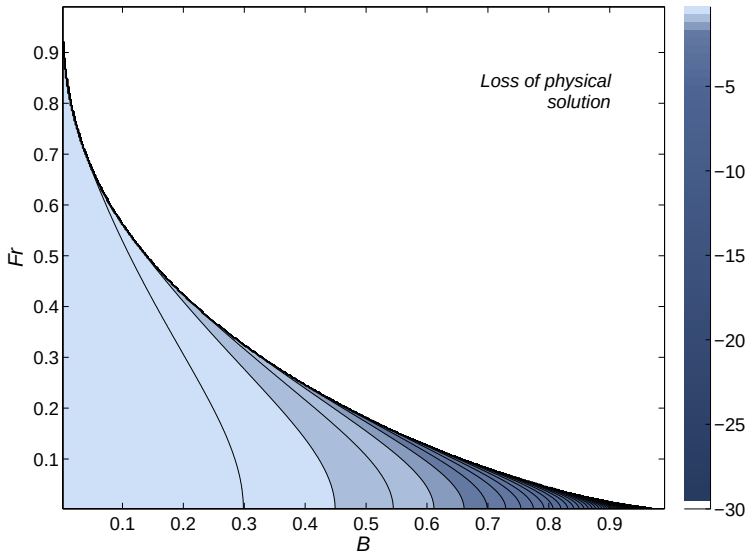

Figure 2.6: Maximum χ values across the space of possible blockage ratios and sub-critical Froude numbers in the open channel model.

tidal device and thereby increasing the available power more than one in which the free surface does not deform.

Constraints of the Open Channel Model

The open channel actuator disc model is limited by the flow conditions at station four. Equation (2.25) is not guaranteed to have a solution for general values of B and Fr (Houlsby *et al.*, 2008; Whelan *et al.*, 2009). The lack of a physical solution for an open channel flow often implies the onset of critical flow at some point in the flow field. This can be shown by considering energy conservation in the bypass streamtube:

$$E_4 = \frac{1}{2}\frac{u_1^2}{g} + h_1 = \frac{1}{2}\frac{\beta_4^2 u_1^2}{g} + h_4. \tag{2.43}$$

Criticality of the bypass flow corresponds to the condition where the derivative of the energy function with respect to h_4 is zero, $\frac{dE_4}{dh_4} = 0$, which defines the point where h_4 is so small that energy is only just conserved in the bypass. Any further reduction in h_4 results in the backup of flow and the possibility of a hydraulic jump developing.

Evaluating the derivative leads to:

$$\frac{d\left(\beta_4^2\right)}{d\left({}^{h_4}/_{h_1}\right)} = -\frac{2}{Fr^2}, \tag{2.44}$$

which corresponds to the point at which physically admissible solutions of Equation (2.25) cease to exist, thus the onset of critical flow in the bypass is a limiting factor to the existence of physical solutions.

2.4.2 Volume-flux Constrained Actuator Disc Theory

Actuator disc theory was applied to a volume-flux constrained flow by Garrett and Cummins (2007). The relationship between the volume-flux constrained and open channel actuator disc models can be examined through Equation (2.29). It is assumed in the volume-flux constrained model that $\frac{\delta h}{h_1}$ is small, so that the cross-sectional channel area is constant along the length of the channel. Neglecting high order $\frac{\delta h}{h_1}$ terms in Equation (2.29) yields an expression for $\frac{\delta h}{h_1}$:

$$\frac{\delta h}{h_1} = \frac{Fr^2 BC_T}{2 + Fr^2(BC_T - 2)}. \tag{2.45}$$

Taking $Fr^2 \to 0$, it can be seen that $\frac{\delta h}{h_1} \to 0$, and therefore the volume-flux constrained actuator disc model is the limit of the generalised open channel model when $Fr = 0$. The Froude number represents the relative balance between dynamic and static head in the flow, and thus $Fr^2 \to 0$ indicates that the dynamic energy in the flow is negligible relative to the static energy. Therefore the effect of the turbine thrust on the kinetic energy is negligible relative to the effect on static energy. Thus, in the limit $Fr^2 \to 0$, only the hydrostatic pressure changes far downstream of the actuator disc and there is no change in the flow speed between the channel inlet and outlet.

Neglecting the free surface deformation and attendant change in the channel's

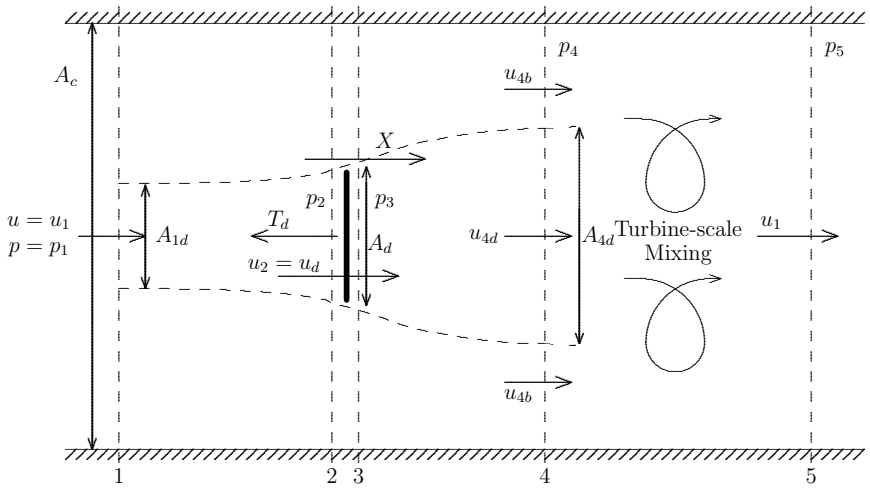

Figure 2.7: Plan view of the one-dimensional model of flow around a single turbine in a volume-flux constrained channel. After Houlsby *et al.* (2008)

cross-sectional area allows a number of simplifications to be made to the generalised model. If the channel's cross-sectional area does not change, then it is convenient to parameterise the inviscid and incompressible flow in the volume-flux constrained frictionless channel in terms of the flow speed, u, and the pressure p, at five stations along the channel length, as illustrated in Figure 2.7. The primary difference between the two models is that static head is now expressed as pressure, and the constant channel cross-sectional area means that the flow speed is u_1 at the downstream boundary of the model, with attendant hydrostatic pressure $p_5 \leq p_1$.

The definition of blockage changes slightly in the volume-flux constrained actuator disc model as the frontal area of the actuator disc is normalised against the constant channel cross-section A_c, rather than the channel cross-section at station one, bh_1, in the open channel model:

$$B = \frac{\text{Disc frontal area}}{\text{Channel cross-sectional area}} = \frac{A_d}{A_c}. \tag{2.46}$$

As in the open channel model, the system of equations describing the volume-flux constrained model are found by considering conservation of momentum, mass, and

energy to determine the available power. The volume-flux constrained actuator disc model is derived below to highlight the differences between it and the general model. Expressing Equations (2.15a) to (2.15c) in terms of pressure, the Bernoulli equations in the volume-flux constrained model are:

$$p_1 + \frac{1}{2}\rho u_1^2 = p_2 + \frac{1}{2}\rho u_2^2, \tag{2.47a}$$

$$p_3 + \frac{1}{2}\rho u_2^2 = p_4 + \frac{1}{2}\rho u_{4d}^2, \tag{2.47b}$$

$$p_1 + \frac{1}{2}\rho u_1^2 = p_4 + \frac{1}{2}\rho u_{4b}^2, \tag{2.47c}$$

The pressure difference across the actuator disc is equal to the thrust applied by the disc:

$$T_d = A_d(p_2 - p_3). \tag{2.48}$$

Combining Equations (2.47a) to (2.48), the thrust of the disc can be expressed as the difference in the squares of the bypass and core velocities at station four:

$$T_d = \frac{1}{2}\rho A_d \left(u_{4b}^2 - u_{4d}^2\right). \tag{2.49}$$

Conservation of mass for the core flow and the whole channel requires, respectively:

$$A_{1d}u_1 = A_d u_2 = A_{4d}u_{4d}, \tag{2.50}$$

$$A_c \left(u_{4b} - u_1\right) = A_{4d} \left(u_{4b} - u_{4d}\right). \tag{2.51}$$

Conservation of momentum between stations one and four is found by balancing the streamwise pressure gradient, thrust, and momentum flux of the core and bypass flows:

$$T_d = \left(p_1 - p_4\right) A_c + \rho A_c u_1^2 - \rho \left(A_c - A_{4d}\right) u_{4b}^2 - \rho A_{4d}^2 u_{4d}^2. \tag{2.52}$$

Noting that the pressure difference $p_1 - p_4$ may also be found by rearranging Equation (2.47c), and using the conservation of mass relationship given in Equation (2.51), the momentum balance may be rewritten as:

$$T_d = \frac{1}{2}\rho A_{4d}\left(u_{4b} - u_{4d}\right)\left(u_{4b} + 2u_{4d} - u_1\right). \tag{2.53}$$

Equating Equations (2.53) and (2.49), and noting the conservation of mass relationship Equation (2.50) for A_{4d}, yields an expression for the flow speed through the actuator disc:

$$u_2 = \frac{u_{4d}\left(u_{4d} + u_{4b}\right)}{u_{4b} + 2u_{4b} - u_1}. \tag{2.54}$$

Using the definition of blockage, Equations (2.50) and (2.51) combine to give:

$$u_{4b}\left(u_{4d} - u_1\right) = Bu_2\left(u_{4b} - u_{4d}\right), \tag{2.55}$$

which combined with Equation (2.54) gives:

$$\left(1 - B\right)u_{4b}^2 - 2\left(u_1 - u_{4d}\right)u_{4b} + u_1^2 - 2u_1u_{4d} + Bu_{4d}^2 = 0, \tag{2.56}$$

a quadratic equation for u_{4b}:

$$u_{4b} = \frac{u_1 - u_{4d} + \sqrt{B(u_1 - u_{4d})^2 + (1 - B)^2u_{4d}^2}}{1 - B}. \tag{2.57}$$

The positive root is required as it is expected that u_{4b} should tend to 1 as $B \to 0$. When the blockage tends to zero, the Lanchester-Betz case is recovered, with the optimal power calculated from Equation (2.14) being equal to $\frac{16}{27}$, or 0.59 times the energy flux $\frac{1}{2}\rho A_d u_1^3$ of the undisturbed flow through the turbine, when the velocity $u_{4d} = \frac{1}{3}u_1$.

The total power removed from the flow between stations one and five is found by

considering the difference in energy flux at the two stations:

$$P_{tot} = A_c u_1 \left(p_1 + \frac{1}{2}\rho u_1^2 \right) - A_c u_1 \left(p_5 + \frac{1}{2}\rho u_5^2 \right). \tag{2.58}$$

As continuity requires $u_1 = u_5$ in the volume-flux constrained model, this simplifies to:

$$P_{tot} = A_c u_1 \left(p_1 - p_5 \right). \tag{2.59}$$

Conservation of momentum between stations one and five requires:

$$T_d = A_c \left(p_1 - p_5 \right), \tag{2.60}$$

so that the total power removed from the flow may be simply expressed as:

$$P_{tot} = T_d u_1. \tag{2.61}$$

The basin efficiency of an actuator disc in a volume-flux constrained flow may thus be simply expressed as the ratio of the through-disc and upstream flow speeds:

$$\eta = \frac{P}{P_{tot}} = \frac{T_d u_2}{T_d u_1} = \frac{u_2}{u_1} = \alpha_2. \tag{2.62}$$

Garrett and Cummins (2007) showed for very low blockage ratios ($B \ll 1$), that available power is maximised if $u_{4d} = \frac{1}{3}u_1$, leading to a ratio $\eta = \frac{2}{3}$. When blockage is large however, such that $(1 - B) \ll 1$, then it was found that:

$$P_{\max} = \frac{16}{27} \left(1 - B \right)^{-2} \frac{1}{2}\rho u_1^3 A_d, \tag{2.63}$$

where the $(1 - B)^{-2}$ factor , as compared to the Lanchester-Betz limit, arises from the confining effect of the channel walls, increasing the pressure drop that can be

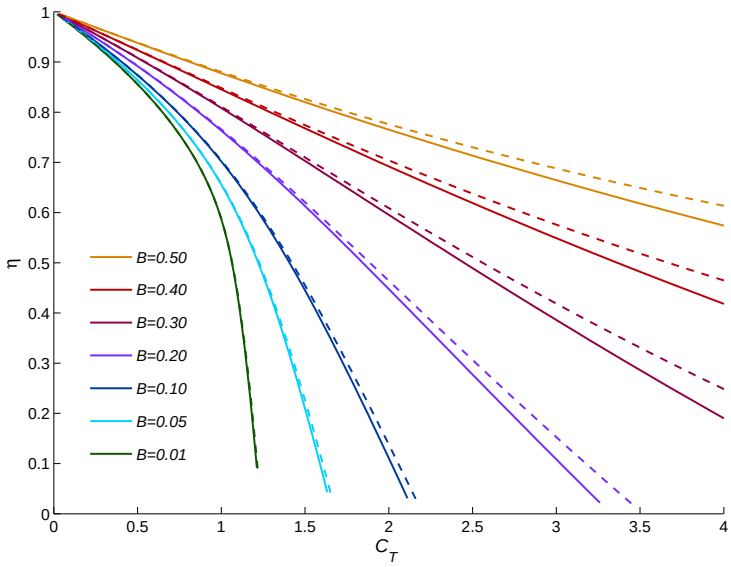

Figure 2.8: Basin efficiency variation with thrust coefficient for the volume-flux constrained (solid lines) and open channel (dashed lines) models for varying blockage ratios and $Fr = 0.20$ in the open channel model.

sustained across the turbine and thereby increasing the output power of the turbine. This relationship means that turbines occupying a fraction greater than $B = 0.23$ of the channel cross-section would result in the $\frac{16}{27}(1-B)^{-2}$ factor multiplying the kinetic flux exceeding 1, a consequence of the streamwise pressure drop that develops in the channel. It was found that, just as for the low blockage case, the optimal value for the velocity in the wake of the turbine was $u_{4d} = \frac{1}{3}u_1$.

In comparison to the open channel model, it can be seen that the approximation to the basin efficiency of a device in an open channel in Equation (2.38) is lower than that of the same device in a volume-flux constrained channel by a factor of $\left(1 - \frac{1}{2}\frac{\delta h}{h_1}\right)$ for the same non-dimensional flow speed through the disc plane, α_2. The decrease in basin efficiency is a consequence of the additional acceleration of the flow that occurs in the open channel in response to the deformation of the free surface, resulting in greater shear stresses between the core and bypass flows, thus introducing greater mixing losses and reducing the basin efficiency.

However, it is informative to compare the efficiency in the open channel and volume-flux constrained models for a given thrust coefficient, as shown in Figure 2.8. It can be seen that, for a given thrust level, a device in an open channel has a greater basin efficiency than one in a channel in which the free surface does not deform. The deformable free surface permits a higher velocity through the actuator disc to be sustained for a given thrust level as the deformation of the free surface results in the flow being less able to deflect around the disc, leading to a higher α_2 for the same thrust coefficient C_T. The basin efficiency is therefore higher for the disc in an open channel as the higher value of α_2 means that the reduction in flow speed in the core is lower, resulting in a lesser expansion of the core flow streamtube. This induces less acceleration of the bypass flow, and thus the difference in flow speed in the core and bypass flows at station four is smaller, hence reducing the shear stresses between the core and bypass flow as compared to the volume-flux constrained case, resulting in a lower level of mixing in the far wake, and thus a higher basin efficiency.

Confining Force

The confining force X that acts on the surface of the core streamtube was neglected in the traditional LMADT analysis due to Lanchester and Betz, and the volume-flux constrained analysis of Garrett and Cummins. The role of the confining force in the volume-flux constrained analysis was examined by Houlsby *et al.* (2008) by considering a momentum balance in the bypass flow between stations one and four:

$$A_c p_1 \left(1 - B\frac{u_2}{u_1}\right) - A_c p_4 \left(1 - B\frac{u_2}{u_{4d}}\right) - X = \rho u_1^2 A_c \left(1 - B\frac{u_2}{u_1}\right)\left(\frac{u_{4b}}{u_1} - 1\right). \quad (2.64)$$

Equation (2.47c) is rearranged for p_4, which can then be substituted into Equation (2.64) to give:

$$\begin{aligned} p_1 B A_c \frac{u_2}{u_{4d}} \left(1 - \frac{u_{4d}}{u_1}\right) &= X \\ &+ \frac{1}{2}\rho u_1^2 A_c \left(\frac{u_{4b}}{u_1} - 1\right) \left(2\left(1 - B\frac{u_2}{u_1}\right) - \left(1 - B\frac{u_2}{u_{4d}}\right)\left(\frac{u_{4d}}{u_1} + 1\right)\right). \end{aligned} \tag{2.65}$$

Houlsby *et al.* (2008) and Draper (2011) assume that p_1 is at atmospheric pressure and therefore neglect it. However, retaining this term for generality leads to an expression for X as:

$$X = A_c B \frac{u_2}{u_{4d}} \left(1 - \frac{u_{4d}}{u_1}\right) \left(p_1 - \frac{1}{2}\rho u_1^2 \left(\frac{u_{4b}}{u_1} - 1\right)\right). \tag{2.66}$$

Taking the pressure p_1 to be zero and noting that $\frac{u_{4b}}{u_1} \geq 1$ and $\frac{u_{4d}}{u_1} \leq 1$, with equality in the limit as $B \to 0$, X is in fact required to be less than zero, opposite in sign to that presented by Houlsby *et al.* and Draper. In those works, X was explained as a confining force which acted to force a greater proportion of the flow through the device, thereby enhancing power available to a device in a finite flow field as compared to one in an infinitely large flow field. The physical intuition of this explanation is correct, but relies on the condition:

$$p_1 - \frac{1}{2}\rho u_1^2 \left(\frac{u_{4b}}{u_1} - 1\right) > 0. \tag{2.67}$$

The positive relationship of X with p_1 arises from the positive pressure gradient in the x-direction that develops in the channel, as $p_4 < p_1$ when a device extracts energy from the channel. However, the pressure behind the device rotor is lower than this, i.e. $p_3 < p_4$, as the expansion of the core flow in the wake of the device occurs due to the reduction in streamwise velocity the accompanies the recover of pressure between sections three and four. The adverse pressure gradient in the core

flow between sections three and four causes a constriction of the bypass flow, acting on the surface between the core and bypass flows in the negative x-direction. This provides the force to accelerate the velocity in the bypass flow from u_1 to u_{4b} between stations one and four, the same result as in the open channel actuator disc model in Section 2.4.1.

In the limit as $B \to 0$ and the case examined by Lanchester and Betz of a turbine in an infinitely large flow field is recovered, the force $X \to 0$ as in that limit, the pressure at station four is assumed to be the same as the pressure far upstream of the device and hence there is no net pressure exerted on the streamtube of the core flow, which agrees with the traditional analysis.

Model Constraints

Garrett and Cummins (2007) note that one of the principal assumptions of the volume-flux constrained actuator disc model is that the cross-sectional area of the channel is unchanged as the flow passes through and downstream of the actuator disc. This requires that the change in height of the water in the channel is small in comparison to the water depth h_1, as discussed in the introduction to the section. The change in elevation is given by the pressure divided by ρg. The deformation of the free surface will be greatest at the section with the lowest pressure, p_4, along the channel, and this change will be small compared to the upstream h_1 if:

$$\frac{u_1^2}{gh_1} \ll \frac{9}{4}\frac{(1-B)^2}{B(3-B)}. \tag{2.68}$$

The requirement that the Froude number is small is generally sufficient to ensure that the channel cross-section is approximately constant along the channel, but this requirement becomes more strict as blockage increases because the increasing value of u_{4b} is associated with an increasing drop in water level at section four.

2.5 Turbine Fence Spanning a Tidal Channel

Garrett and Cummin's analysis of energy extraction in a tidal channel discussed in Section 2.3 showed that a dynamic balance exists between the energy extraction and the flow in the channel. As more resistance is applied to the channel, the flow rate through the channel reduces, limiting the maximum power that can be realised. However, this analysis assumed that the turbines spanned the entire channel cross-section, thus did not consider the bypass flow that would form around discrete turbines. The actuator disc models discussed in Section 2.4 considered the effect of such bypasses, showing that the available power was controlled by the dynamic balance between the resistance presented to the flow and acceleration of the flow in the bypass. The actuator disc models assumed that the upstream flow was unaffected by turbine operation, which is not consistent with the observation from the tidal channel analysis showing that the flow rate through the channel is dependent on the resistance to the flow in the channel.

Vennell (2010) combined the two problems by assuming that the wake recovery length scale in the actuator disc model was small compared to the length scale of the tidal channel, so that the actuator disc model could be considered within the tidal channel problem, allowing the feedback between the resistance presented by the turbines and the flow rate through the channel to be modelled. The non-dimensional farm drag coefficient, λ_T, was related to the thrust coefficient for a row of turbines, C_T:

$$\lambda_T = N_R^* C_T(B, \alpha_4), \tag{2.69}$$

where $N_R^* = \alpha N_R$ is the non-dimensional number of rows; the number of rows N_R non-dimensionalised by the parameter $\alpha = \frac{a}{\omega^2 L}$, with a being an acceleration term used by Vennell for conciseness. This allowed the two problems to be coupled and the system of equations solved numerically.

Vennell demonstrated that the maximum power available to a row of turbines completely spanning the channel cross-section was dependent on the bottom friction in the channel, which had the effect of reducing the channel's maximum extractable energy and shifting this point to higher applied farm thrust. It was shown that α_4 would increase from $\frac{1}{3}$ in the case where blockage $B = 0$, towards $\alpha_4 = 1$ as $B \to 1$, corresponding an infinite number of turbines each extract an infinitesimal amount of power from the flow. Although additional rows of turbines increased the maximum available power of the entire farm, the increment in farm power decreased with each additional row and α_4 increased, leading to a trade-off between the overall available power to the farm and the power available to each turbine, which would be an important economic factor in farm design.

Vennell (2010) assumed all the turbines in the farm operated at a single wake induction factor, α_4. As this does not necessarily take into account the interactions that exist between turbine rows and variations in channel cross-section, Vennell (2011) generalised the combined turbine-channel model to allow for a varying channel cross-section and varying wake induction factor $\alpha_{4,k}$ in different turbine rows. The parameter space of the model was expanded to allow for multiple wake induction factors in each row, yielding an optimisation problem to maximise the total farm power by solving for the optimal $\alpha_{2,k}$ for the k^{th} row of turbines:

$$\alpha_{2,k} - \left(\frac{-1}{C_{F,k}}\frac{\partial C_{F,k}}{\partial \alpha_{2,k}}\right)^{-1} = \left(\frac{-\alpha}{|U|^3}\frac{\partial |\bar{U}|^3}{\partial \lambda}\sum^{N_R}\frac{\alpha_{2,i}C_{R,i}}{A_i'^2}\right), \tag{2.70}$$

where $C_{F,k}$ is the farm drag coefficient based on the k^{th} row, $U = \frac{u(x,t)}{A(x)}$ is the transport along the channel, λ is the total drag in the channel, $C_{R,i}$ is the drag coefficient of the i^{th} row of turbines, and A_i' is the cross-sectional area of the channel at the i^{th} row. The right hand side of the equation is invariant across rows, so the variation of optimal $\alpha_{2,k}$ tuning (and then through the rigid lid model, $\alpha_{4,k}$) within a turbine

array is dependent on the bracketed term on the left hand side of the equation. At high blockage ratios, this term has very little variation, and thus all rows in high blockage arrays have quite similar $\alpha_{2,k}$ tunings, regardless of channel constrictions.

Vennell found that the optimal $\alpha_{4,k}$ was consistent for rows of similar blockage B where the channel cross-section had similar geometry, and almost completely independent of the channel's dynamic balance between driving head and seabed friction. The optimal value increased if there was a constriction, such as that due to a headland projecting into the channel, and power production was biased towards turbines placed within such a constriction. Farms with more turbines, and thus higher blockage, in each row captured a greater proportion of the power available in the channel than turbine farms with low blockage, which did not do much better than a farm of turbines operating at $\alpha_{4,k} = \frac{1}{3}$. The problem could also be formulated as a turbine placement problem; given a number of turbines, what is the most efficient way to deploy the turbines between rows in order to maximise the farm's power? Vennell showed that, as expected intuitively, it is most efficient to maximise the number of turbines in the row producing the most power, and then fill the second most efficient row, and so on, i.e., minimising the number of rows, and maximising the number of turbines in each row. This is to be expected, as energy is removed from the flow across each turbine row, and thus the energy flux incident on downstream rows is reduced, limiting the energy that is presented to downstream rows, thus limiting the power available for extraction.

2.6 Conclusions

Despite the outward similarities in the appearance of wind and tidal turbines, the dynamics of the flow around the turbines is significantly different due to the close proximity of the free surface to tidal turbines. The flow confinement due to the

free surface results in a feedback mechanism when evaluating the performance of tidal turbines between the flow and the resistance imparted by the turbines. Garrett and Cummins (2005) considered this mechanism in a tidal channel using the zero-dimensional Navier-Stokes equation and showed that the power available to the turbines depended on both how much the flow was reduced in the channel due to the additional resistance and the natural dynamical balance in the channel between the head difference driving the flow and energy losses on the seabed and channel exit. The tidal channel model may also be considered through an electrical analogy, where the circuit voltage represents the tidal amplitude across the channel and the circuit current represents the flow through the channel, which allows the modelling of multiple sub-channels where turbines are deployed only in a few of the sub-channels.

A second feedback mechanism that exists between the flow and the resistance imparted on the flow by the turbines is that of flow diversion around individual turbines. This is not captured in the tidal channel models, and requires a different analytical approach. Actuator disc theory was successfully applied to wind turbines by Betz and Lanchester to derive an upper bound on the fraction of the upstream kinetic energy, $C_{P,Betz} = 0.593$, that could extracted by a turbine in an unbounded flow field. The analysis was adapted by Garrett and Cummins for an actuator disc in a volume-flux constrained flow, and Houlsby *et al.* and Whelan *et al.* for an actuator disc in an open channel. It was shown that the volume-flux constrained model is recovered in the limit $Fr^2 \to 0$ from the more general open channel actuator disc model. A pressure gradient develops in the channel and the maximum available power increases as a result of energy extraction in a channel where the expansion of the core flow is constrained. The power available to the actuator disc also increases with Froude number, although to a lesser degree than with blockage.

Vennell (2010) combined the two approaches in order to examine the effect of the two feedback mechanisms in a single model, and showed that turbine operation

had to be optimised to balance the reduction in the flow through the channel with increasing turbine drag with the generally increasing available power as the drag of the turbines is increased. The available power also depended on the number of rows of turbines in the channel, where it was shown that the greatest power is achieved when rows of turbines are filled in order of decreasing efficiency, with a drop in the incremental benefit of each additional row.

The analytical approaches considered in this chapter have assumed that rows of turbines span the width of the channel cross-section, an assumption that will often not be possible to achieve due to variations in channel bathymetry, navigational requirements and competition with other marine commercial and defense activities. The importance of the bypass flow around turbines was examined in the turbine-scale models in Sections 2.4.1 and 2.4.2. These models assumed that there was a single scale to the wake mixing behind the turbines in the channel. However, if a row of a large number of turbines does not span the width of the channel, a bypass flow would develop around the row, or array, of turbines, forming an additional scale of wake mixing on the scale of the array rather than the scale of the constituent turbines. The two scale model required to capture this effect is considered in Chapter 3.

Chapter 3

Array Partially Spanning a Channel

Algebra is the intellectual instrument which has been created for rendering clear the quantitative aspect of the world
- Alfred N. Whitehead

A theoretical model is proposed to explore the power available to an array of tidal turbines partially spanning a wide open channel. It is assumed that the flow has two predominant scales; a turbine-scale flow, and an array-scale flow. The two scales are each analysed as quasi-inviscid open channel flow problems, in which conservation of mass, momentum and energy are considered. Kinematic and dynamic boundary conditions couple the two scale problems and provide a single multi-scale model. The available power is maximised by placing the turbines close together, which also enhances the efficiency of energy extraction. The importance of the Froude number is examined, and it is found that available power and efficiency are enhanced as the Froude number increases. In an infinitely wide channel, it is found that the maximum power coefficient depends on Froude number and local blockage only, with a clear peak when the local blockage is approximately 0.4. The power coefficient increases from the Lanchester-Betz limit of 0.593 to 0.798 at low Froude number, in accordance with the rigid lid findings of Nishino and Willden (2012b), and increases further as the Froude number is increased.

3.1 Introduction

The importance of the blockage ratio, B, the ratio of device frontal area to channel cross-sectional area, to the available power was discussed in Chapter 2. The simplified one-dimensional model of a turbine in a volume-flux constrained channel proposed by Garrett and Cummins (2007) showed that the maximum available power was proportional to $(1 - B)^{-2}$. Although such as simple relationship cannot be derived from models with free surface deformation, general agreement with this conclusion was found as maximising available power was strongly related to the fraction of the channel occupied by the actuator disc, amongst other factors (Whelan *et al.*, 2009; Draper, 2011). These models do not account for environmental, technical and regulatory factors that might restrict the permitted available power to some fraction of the maximum available power. They also do not account for the reduction in the flow that occurs as a consequence of the increased resistance to the flow due to the devices. Garrett and Cummins (2005) and Vennell (2010) proposed models to account for the change in the flow dynamics when energy is extracted by the tidal devices and showed that the flow could be significantly reduced when the hydrodynamic drag of the devices becomes significant relative to the resistance of the undisturbed channel, which then reduces the total energy that may be extracted from the channel.

It may not be possible to deploy devices across the entire channel width due to various economic and regulatory constraints, bathymetric variations, and the need to allow passage for shipping and marine life. If the turbine array does not span the entire channel, two principal scales exist: the first being flow phenomena that occur close to each tidal device; and the second the much larger flow features that occur on the scale of the array width. The acceleration of the array bypass flow due to the aggregate thrust and corresponding reduction in flow speed results in a different estimate of the available power, as compared to analyses in which the devices span the entire channel width. As such, analyses assuming the devices span the entire

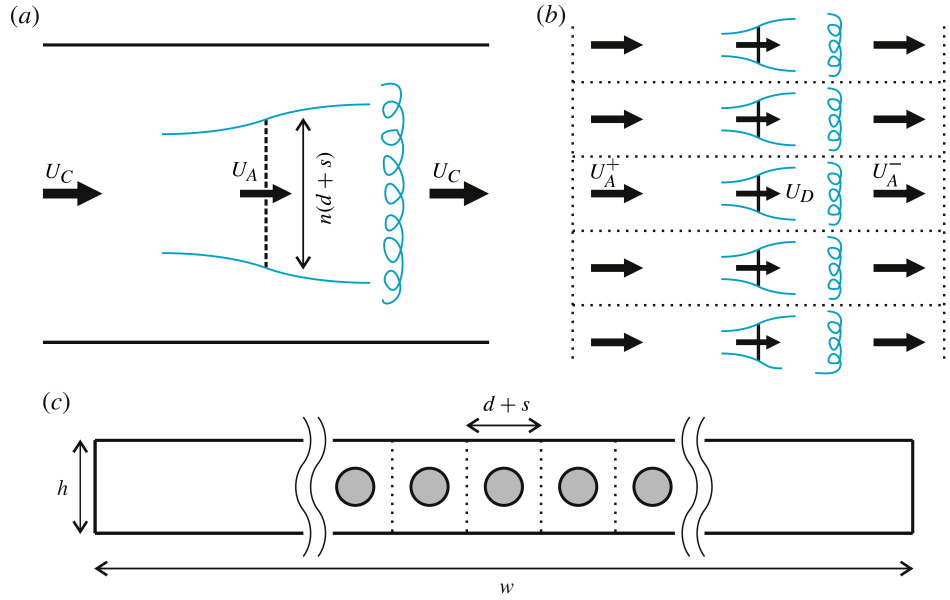

Figure 3.1: Diagram of the turbine array partially spanning a wide channel: a) array-scale flow expansion and mixing; b) device-scale flow expansion and mixing; and c) cross-sectional view of the channel. From Nishino and Willden (2012b).

channel cross-section, even if inter-device spacing is allowed for, do not capture the dynamics of flow diverting around the array.

Nishino and Willden (2012b) introduced the concept of a separation of scales, as shown in Figure 3.1, in which array-scale flow events occur more slowly and over longer distances than turbine-scale flow events, allowing the array-scale and turbine-scale flows to be treated as loosely coupled problems. This allowed the application of the volume-flux constrained model for an array of tidal turbines partially spanning a wide channel. The array-scale problem provided boundary conditions for the turbine-scale model, which was used in turn to determine the thrust applied to the flow, and thus dynamic coupling to the array scale problem, and the available power.

Tidal channels are free surface flows, and as such the water depth in the channel must change in order that energy be removed from the flow, increasing the Froude number and accelerating the flow. The volume-flux constrained model assumes that this effect is negligible, restricting its application to low Froude number channels and to conditions where the impact of the turbine array on the flow is small. As

discussed in Section 2.4.1, LMADT has been applied to turbines in constrained flow with a deformable free surface by Whelan *et al.* (2009) and extended to consider downstream mixing by Draper (2011) to allow analytic modelling of turbine arrays where free surface deformation may be important and the arrays completely span the width of the channel.

The model presented in this chapter incorporates a free surface into the scale separation framework to develop an analytic model of a tidal turbine array partially spanning a wide channel which allows the effects of free surface deformation on the power available to the array to be analysed. It is assumed there is a constant mass flux through the channel and therefore that turbine operation does not significantly affect the upstream boundary. In practical situations, flow conditions may be altered by power extraction, necessitating further extension of the analysis to consider variable mass flux. Note, however, that the assumption becomes exact in the case of turbines operating in an infinitely wide channel. It was further assumed that the flow is inviscid and that no mixing of flows occurs in the channel other than in the mixing zones of the two models.

3.2 Separation of Scales

The LMADT models in Chapter 2, in which the turbine array spanned the width of the channel, allowed a bypass flow to form around each actuator disc in response to the resistance imposed on the flow by the disc. After the static pressure in the bypass and core flows equalised at some distance downstream of the disc, the two flows were then assumed to mix and form a uniform flow far downstream of the device. As it was assumed that the devices presented a uniform resistance to the flow, there was only a single scale of wake mixing behind the turbines.

However, if the array of turbines does not completely span the channel there will be

an additional flow around the array of a large number of turbines partially spanning the channel. The flow in the streamtube encompassing the array slows down in response to the aggregate thrust applied by the devices, and there will consequently be an accelerated bypass flow which develops to ensure conservation of mass flux through the channel. In a similar manner to the flow around individual devices, the static pressure in the core and bypass flows will equilibrate some distance downstream of the array, after which the two flows will mix to produce a uniform velocity far downstream of the array.

There are therefore two scales of flow in the partial array problem; a turbine-scale flow, and an array-scale flow, as illustrated in Figure 3.2. The array of width L is composed of n turbines each of frontal area A_L and diameter D partially spanning a channel of width W_C and upstream depth h_0. There is a flow passage of width $b = d + s$ encompassing each actuator disc, such that $L = nb$. The incompressible flow in the channel is assumed to be inviscid, except in the far-wake region of the turbine-scale model between stations four and five (Figure 3.2a), and the array far-wake region between stations six and seven of the array-scale model (Figure 3.2b). The velocity u_0 at the upstream boundary of the channel is assumed to be spatially uniform and unaltered by turbine operation. The water depth is permitted to vary along the length of the channel. It is furthermore assumed that the static pressure is uniform across the channel cross-section at stations zero, six, and seven of the array-scale model, in addition to the static pressure equalisation assumption in the turbine-scale flow passages at stations one, four, and five.

Two principal length scales exist in the flow; the device diameter D, and the array length L. Turbine-scale energy extraction and mixing scales on the device diameter, whereas the flow around the array scales on the array width. If there are many turbines in the array, then $L \gg D$ and the three-dimensional turbine scale flow occurs over a much shorter spatial and temporal scale than flow around the array,

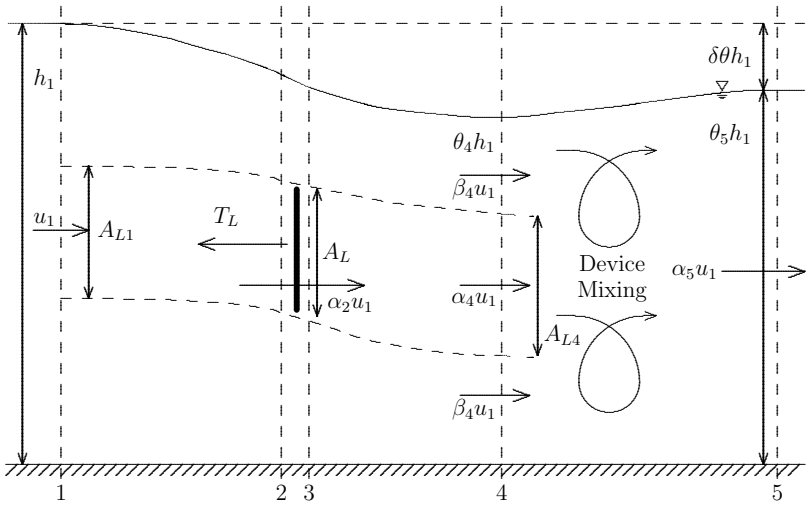

(a) Turbine-scale flow mixing and free surface change.

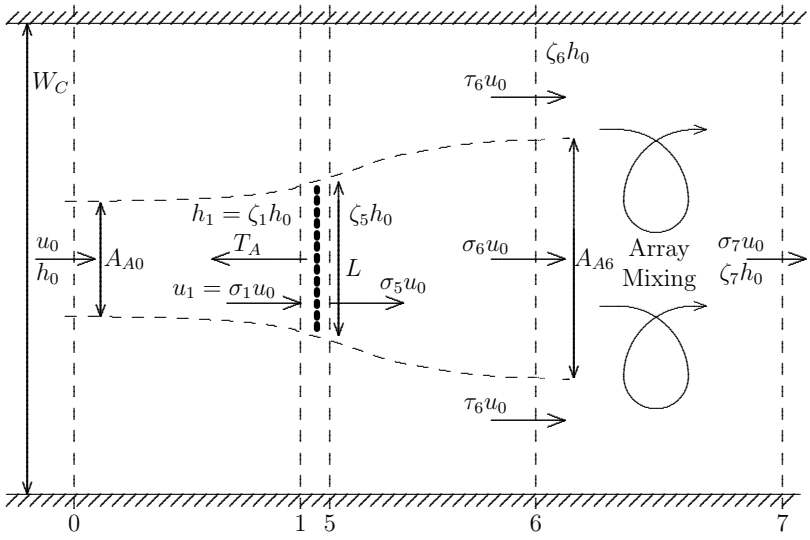

(b) Array-scale flow mixing and free surface change.

Figure 3.2: The scale-separated partial array model: (a) turbine-scale, and (b) plan view of the array-scale.

which will tend to being two-dimensional, as the array width is much greater than the channel depth. The difference in the turbine and the array length scales is assumed to be sufficiently large such that turbine-scale core and bypass wake mixing is completed upstream of the cross-stream depth equalisation (hydrostatic pressure recovery) in the array scale problem. The partial fence problem may thus be considered in terms of the two loosely coupled quasi-inviscid problems shown in Figure 3.2; a turbine-scale problem and an array-scale problem. Each problem is evaluated separately as an

open channel flow, adapting the open channel analysis presented in Section 2.4.1 to the two-scale partial fence problem. The array-scale problem thus provides upstream boundary-conditions to the turbine-scale model, which then provides the internal downstream boundary at station five required to close the pressure head and velocity discontinuity between stations one and five of the array-scale model.

In the volume-flux constrained partial array model derived by Nishino and Willden (2012b) these assumptions led to an array-scale model and a turbine-scale model defined mathematically by the same equations, albeit with different variables to account for different scales of the problem. The multi-scale open channel model, in contrast, has two different systems of model equations defining the turbine-scale and array-scale models. It is assumed in the open channel turbine-scale model that the velocity through the actuator disc is equal just upstream and downstream in order to ensure that the mass flux through the disc is conserved. Consequently a static discontinuity develops across the actuator disc in the turbine-scale model in response to the thrust applied to the flow by the turbine. However, in the array-scale problem, stations one and five, encapsulating the turbine-scale problem, are collocated, enabling complementary velocity and height discontinuities as well as a static head change. The additional equations required to close the array-scale problem lead to a model with a different, algebraically more complicated, system of equations than the turbine-scale model.

3.2.1 Parameterisation of the Two Scale Model

The turbine-scale and array-scale problems are non-dimensionalised by scaling the velocities and pressure heads in terms of the upstream height and velocity at station zero in the array-scale problem and station one in the turbine-scale problem. In the turbine-scale problem, non-dimensional heights are denoted with $\theta_i = h_i/h_1$, and non-dimensional speeds with $\alpha_i = u_i/u_1$ in the core and $\beta_i = u_i/u_1$ in the bypass

flow regions. In the array-scale problem, $\zeta_i = h_i/h_0$ denotes non-dimensional heights, and $\sigma_i = u_i/u_0$ and $\tau_i = u_i/u_0$ the core and bypass non-dimensional flow speeds respectively.

Additional blockage ratios and thrust and power coefficients are required to describe the combined model in light of the multiple reference areas and velocities that are present in the two models. At the device-scale, shown in Figure 3.2a, the local blockage ratio B_L is defined as the frontal area of the actuator disc A_L to the cross-sectional area of the surrounding flow passage of width b and upstream water depth h_1:

$$B_L = \frac{\text{Turbine frontal area}}{\text{Flow passage cross-sectional area}} = \frac{A_L}{bh_1}. \tag{3.1}$$

The device thrust coefficient C_{TL} is defined as the device thrust T_L normalised on the upstream dynamic pressure of the flow in the turbine-scale problem projected onto the device frontal area:

$$C_{TL} = \frac{T_L}{\frac{1}{2}\rho u_1^2 A_L}. \tag{3.2}$$

The power coefficient C_{PL} is the product of the device thrust and the flow speed through the actuator disc, and is normalised on the kinetic flux of the upstream flow in the turbine-scale problem projected onto the device frontal area:

$$C_{PL} = \frac{\alpha_2 u_1 T_L}{\frac{1}{2}\rho u_1^3 A_L} = \alpha_2 C_{TL}. \tag{3.3}$$

At the array scale, shown in Figure 3.2b, the array blockage, B_A, is defined as the fraction of the channel cross-section, $W_C h_0$, occupied by the frontal area of the array, A_A, which is the sum of the cross-sectional areas of the turbine-scale flow passages:

$$B_A = \frac{\text{Array frontal area}}{\text{Channel cross-sectional area}} = \frac{A_A}{W_C h_0}. \tag{3.4}$$

The thrust imposed by the array, T_A, is the sum of the thrust of the n devices in the

array, leading to the definition of the array thrust coefficient C_{TA}:

$$C_{TA} = \frac{T_A}{\frac{1}{2}\rho u_0^2 A_A} = \frac{nT_L}{\frac{1}{2}\rho u_0^2 nbh_1} = \sigma_1^2 B_L C_{TL}. \tag{3.5}$$

The power available to the array, P_A, is the sum of the power available, P_L, and dissipated, $P_{L,mix}$, in the wake of each actuator disc at the local scale. The array power coefficient, C_{PA}, is defined as the power available to the array normalised against the upstream kinetic flux at station zero projected onto the frontal area of the array:

$$C_{PA} = \frac{P_A}{\frac{1}{2}\rho u_0^3 A_A} = \frac{n(P_L + P_{L,mix})}{\frac{1}{2}\rho u_0^3 A_A}. \tag{3.6}$$

The array scale parameters are defined in terms of the cross-sectional area of the turbine-scale flow passages, which incorporates the frontal area of the actuator disc and the cross-sectional area of the bypass flow around the disc. It can be useful to define a 'global' scale, normalised with respect to the sum of the frontal area of the devices and which therefore more accurately reflects the proportion of the channel cross-section physically occupied by the devices. The global blockage B_G is therefore defined as:

$$B_G = \frac{\sum \text{Turbine frontal area}}{\text{Channel cross-sectional area}} = \frac{nA_L}{W_C h_0} = B_A B_L. \tag{3.7}$$

The global thrust coefficient, C_{TG}, is the sum of the thrust applied by each device normalised by the dynamic pressure of the array-scale problem projected onto the frontal area of each device:

$$C_{TG} = \frac{nT_L}{\frac{1}{2}\rho u_0^2 nA_L} = \sigma_1^2 C_{TL}. \tag{3.8}$$

The global power coefficient, C_{PG}, is the sum of the power available to each device normalised by the kinetic flux at station zero projected onto the frontal area of each

device:

$$C_{PG} = \frac{nP_L}{\frac{1}{2}\rho u_0^3 n A_L} = \sigma_1^3 C_{PL}. \tag{3.9}$$

Specifying the local thrust coefficient C_{TL} allows the non-dimensionalised array-scale and turbine-scale models to be directly decoupled and solved separately. The array-scale model determines the flow through the array which provides the upstream boundary to the turbine-scale model which is solved to determine the available power for the devices. Considering the two models individually is an efficient method of solving the overall problem as it eliminates the need to solve the turbine-scale model within the array-scale model, and allows the solution for the two scales to be easily matched.

3.3 Turbine-scale Model

The turbine-scale model utilises the open channel actuator disc model presented in Chapter 2 and illustrated in Figure 3.2a for a single actuator disc of frontal area A_L in a flow passage of centre-to-centre device spacing b. The flow is assumed to be incompressible and inviscid, although it is assumed that a mixing region exists in the far wake of the device. As the array scale model provides the upstream boundary to the turbine-scale model, the water depth and uniform velocity at station one are the same in the turbine-scale and the array-scale models. The flow speed reduces to $\alpha_2 u_1$ as it passes through the actuator disc, reducing further to $\alpha_4 u_1$ in the wake of the disc. Energy is conserved through the core flow passage except across the actuator disc. Meanwhile, the energy conserving flow bypassing the disc continuously accelerates to reach $\beta_4 u_1$ at station four, where hydrostatic pressure variation is recovered across core and bypass flows resulting in a static head $\theta_4 h_1$. Downstream of station four, the turbine-scale core and bypass flows remix, resulting in energy loss, leading to a new uniform velocity $\alpha_5 u_1$, and water depth $\theta_5 h_1$.

Although not considered in Whelan *et al.*'s paper, the mixing region between stations four and five is an important part of the model as it results in the uniform velocity (and corresponding water depth) at station five that is required to close the array-scale model. Energy extraction from the sub-critical open channel flow results in the free surface at the outlet of the turbine-scale model being lower than that at the inlet, with a corresponding increase in velocity to conserve mass flux. Thus the power available to the device is a function of both the upstream flow speed and the far field (from stations one to five) change in free surface elevation. The turbine-scale downstream flow is then imposed on the array-scale model at station five, completing the model coupling.

The turbine-scale model is used to determine the power available to the actuator disc and the effect that this has on the flow. The available power, P_L, is the product of the disc thrust, T_L, and the velocity through the disc, $\alpha_2 u_1$; i.e., $P_L = \alpha_2 u_1 T_L$, or can be expressed non-dimensionally as:

$$C_{PL} = \alpha_2 C_{TL} \tag{3.10}$$

Mathematically, it is convenient to non-dimensionalise the turbine-scale model as this yields two sub-problems: a 'near field' problem describing the flow between stations one and four, and a 'far field' problem, which describes the change in the flow between stations one and five. The two problems are related through the local thrust coefficient C_{TL}, which parameterises the thrust the actuator disc applies to the flow. The near field problem is solved to determine the available power and the far field problem is solved to determine the downstream height change $\delta\theta = \theta_1 - \theta_5$ (where it is noted that $\theta_1 \equiv 1$) which provides the necessary equations to close the array-scale model. The near field and the far field problems are described in terms of the turbine thrust coefficient, blockage, and local Froude number, $Fr_L = \frac{u_1}{\sqrt{gh_1}}$.

3.3.1 Near Field Turbine-scale Problem

The near field problem is derived by considering conservation of mass and momentum relationships and the Bernoulli equation between stations one and four in the core and bypass flows. Although it is physically meaningful to specify the thrust coefficient C_{TL} as the parameter describing the effect of the resistance of the turbine on the flow, it is simpler algebraically to use the wake induction factor α_4 as the specified turbine parameter instead, as shown in Section 2.4.1. In the context of the coupled array- and turbine-scale models, although the specification of C_{TL} as the turbine parameter does lead to the solution of an equation with radicals in C_{TL}, it also allows the decoupling of the near field and far field problems in addition to the quasi-independent turbine and array scale problems, which has advantages in solving the array-scale model.

The near-field turbine-scale model is defined by Equations (2.14) to (2.25) in Section 2.4.1. Taking α_4 as the mathematically convenient independent variable, a quartic polynomial for β_4 is found in terms of α_4, B_L, and Fr_L^2:

$$Fr^2\beta_4^4 + 4\alpha_4 Fr^2\beta_4^3 + 2(2B_L - 2 - Fr^2)\beta_4^2 + 4(2 - 2\alpha_4 - Fr^2\alpha_4)\beta_4 + (8\alpha_4 - 4 + Fr^2 - 4\alpha_4^2 B_L) = 0. \quad (2.25)$$

The device thrust is defined as:

$$C_{TL} = \beta_4^2 - \alpha_4^2, \quad (3.11)$$

and the non-dimensional through-turbine flow speed may be expressed as:

$$\alpha_2 = \frac{\alpha_4 \left[2B_L\beta_4\left(\beta_4^2 - \alpha_4^2\right) - \left(\beta_4 - 1\right)^3\right]}{B_L\left(\beta_4 - \alpha_4\right)\left[\left(\beta_4^2 - 1\right) + 4\beta_4\alpha_4\right]}. \quad (3.12)$$

The local power coefficient may be determined from Equation (3.3), completing the near-field turbine-scale model.

3.3.2 Far Field Turbine-scale Problem

The far field problem determines the downstream uniform flow speed and depth boundary of the turbine-scale problem which is used as the inner upstream boundary coupling to the array-scale mixing problem. The far field problem is found by considering conservation of mass and momentum relationships between stations one and five, which gave rise to the cubic in $\frac{\delta h}{h_1}$ expressed in Equation (2.27). Adopting the non-dimensionalisations of the turbine-scale model, this becomes a cubic in $\delta\theta$ given a specified local blockage ratio B_L, local Froude number Fr_L, and thrust coefficient C_{TL}:

$$\delta\theta^3 - 3\delta\theta^2 + \left(Fr_L^2\left(B_L C_{TL} - 2\right) + 2\right)\delta\theta - Fr_L^2 B_L C_{TL} = 0. \tag{3.13}$$

The head difference between stations one and five, $h_1 - h_5 = \delta\theta h_1 = \delta\zeta h_0$, is made to be consistent between the array- and turbine-scale problems, and the coupling between the two problems can be written by expressing Equation (3.13) in terms of variables at station zero. Noting that the array-scale Froude number can be written as $Fr_A = \frac{u_0}{\sqrt{g h_0}}$, this yields:

$$\delta\zeta^3 - 3\zeta_1\delta\zeta^2 + \left(\sigma_1^2 Fr_A^2\left(B_L C_{TL} - 2\right) + 2\zeta_1\right)\zeta_1\delta\zeta - \zeta_1^2\sigma_1^2 Fr_A^2 B_L C_{TL} = 0. \tag{3.14}$$

3.4 Array-scale Model

The flow in the array-scale problem is assumed to be a two-dimensional shallow water flow, as the cross-stream extent of the channel is much greater than the depth of the channel. The array, composed of n turbines, is a fence of width $L = nb$ which extends the entire depth of the flow, has a frontal area $A_A = Lh_1$. It is therefore required that n must be sufficiently large to satisfy the scale separation assumption. Furthermore, the flow across the face of the fence is assumed to be uniform, thus we neglect any array end effects. The flow in the array-scale problem is assumed to

be a two-dimensional shallow water flow, as the cross-stream extent of the channel is much greater than the depth of the channel. The requirement that this places on n has been investigated by Nishino and Willden (2013) through comparison to 3D computed fence flows with the result that errors in analytic model prediction fall below 6% for $n \geq 8$.

In the array-scale model, the thrust imposed by the turbine array causes the inviscid flow to decelerate to $\sigma_1 u_0$ in front of the array, providing the upstream boundary to the turbine-scale model. There is a change in height and velocity due to the energy extraction of the turbines, resulting in further acceleration and height reduction to station five at the exit of the turbine-scale problem, which provides the internal upstream boundary condition to the array mixing problem. The array-scale wake then expands further downstream until there is lateral hydrostatic pressure equalisation between the array core and bypass flows at station six. The two array flows remix and produce a uniform velocity $\sigma_7 u_0$, greater than the inlet velocity due to mass flux conservation in response to the decrease in water depth to $\zeta_7 h_0$ resulting from energy removal from the sub-critical flow.

As with the turbine-scale model, both a 'near field' and a 'far field' problem can be formulated for the array-scale model, where the near field model describes the flow between stations zero and six, and the far field model describes the change in the flow between stations zero and seven. The primary difference between the near and far field problems in the turbine- and array-scale models is that the closure of the array-scale near field problem requires the solution of the turbine-scale far field problem due to the velocity and head discontinuity across the array.

3.4.1 Near Field Array-scale Problem

The flow speed in the array core flow decreases from u_0 upstream of the array to $\sigma_1 u_0$ in front of the array, and then decreases further from $\sigma_5 u_0$ to $\sigma_6 u_0$ in the wake of the

array, as shown in Figure 3.2b. The static head increases from h_0 to $\zeta_1 h_0$ in front of the array, and then decreases from $\zeta_5 h_0$ to $\zeta_6 h_0$ in the array wake. As discussed in the far-field turbine-scale model, there is a static head discontinuity and a complementary velocity discontinuity between stations one and five due to energy extraction by the turbine array. Applying the Bernoulli equations to the array core flow gives:

$$h_0 + \frac{1}{2g}u_0^2 = \zeta_1 h_0 + \frac{1}{2g}\sigma_1^2 u_0^2; \qquad \zeta_5 h_0 + \frac{1}{2g}\sigma_5^2 u_0^2 = \zeta_6 h_0 + \frac{1}{2g}\sigma_6^2 u_0^2. \tag{3.15}$$

In the array bypass, the flow smoothly accelerates from u_0 to $\tau_6 u_0$, and the pressure head decreases from h_0 to $\zeta_6 h_0$, so the Bernoulli equation is therefore:

$$h_0 + \frac{1}{2g}u_0^2 = \zeta_6 h_0 + \frac{1}{2g}\tau_6^2 u_0^2. \tag{3.16}$$

Combining Equations (3.15) and (3.16) and recalling that $Fr_A = \frac{u_0}{\sqrt{g h_0}}$, yields:

$$\zeta_1 - \zeta_5 = \frac{1}{2}Fr_A^2\left(\left(\sigma_5^2 - \sigma_1^2\right) + \left(\tau_6^2 - \sigma_6^2\right)\right). \tag{3.17}$$

Conservation of mass at station six requires:

$$\zeta_6 = \frac{B_A \sigma_1 u_0}{\sigma_6 u_0} + \frac{u_0 - B_A \sigma_1 u_0}{\tau_6 u_0}, \tag{3.18}$$

and conservation of momentum in the core and bypass flows in the near field problem between stations one and six requires:

$$\left(1 - \zeta_6^2\right) - Fr_A^2 B_A C_{TA} = 2Fr_A^2\left(B_A \sigma_1\left(\sigma_6 - \tau_6\right) + \left(\tau_6 - 1\right)\right). \tag{3.19}$$

The effect of the turbine array in the array-scale problem may be specified in terms of one of a number of control parameters, such as C_{TA}, σ_6, or $\delta\zeta_A = 1 - \zeta_7$. As the array thrust is linked to the turbine thrust through Equation (3.5), it is convenient to specify

C_{TA} to solve the array-scale problem and then match the array thrust coefficient with the appropriate device thrust coefficient to determine the power available to the array. Substituting Equations (3.16) and (3.18) into Equation (3.19) yields an expression for σ_1 in terms of C_{TA}, B_A, σ_6, and τ_6:

$$\sigma_1 = \frac{\sigma_6 \left(2\tau_6 B_A C_{TA} - (\tau_6 - 1)^3\right)}{B_A(\tau_6 - \sigma_6)\left((\tau_6^2 - 1) + 4\tau_6\sigma_6\right)}. \tag{3.20}$$

An expression for σ_1 in terms of Fr_A, B_A, σ_6, and τ_6 is found by substituting Equation (3.18) into Equation (3.16):

$$\sigma_1 = \frac{\sigma_6 \left((\tau_6 - 1) - \frac{1}{2}Fr_A\tau_6(\tau_6^2 - 1)\right)}{B_A(\tau_6 - \sigma_6)}. \tag{3.21}$$

Equating Equation (3.20) with Equation (3.21) yields an expression for σ_6 as a function of Fr_A, B_A, C_{TA}, and τ_6:

$$\sigma_6 = \frac{2B_A C_{TA} + (\tau_6 - 1)^2\left(\frac{1}{2}Fr_A^2(\tau_6 + 1)^2 - 2\right)}{4\left((\tau_6 - 1) - \frac{1}{2}Fr_A^2\tau_6(\tau_6 + 1)\right)}. \tag{3.22}$$

Having developed a system of equations for σ_1 and σ_6 in terms of the array parameters C_{TA}, B_A, and Fr_A, and the bypass induction factor τ_6, it remains to express τ_6 in terms of the array parameters. The array thrust coefficient can be expressed as the difference in the static head upstream and downstream of the array:

$$C_{TA} = \frac{2}{Fr_A^2}\left(\zeta_1 - \zeta_5\right). \tag{3.23}$$

An expression for $\zeta_1 - \zeta_5$ is found by considering the Bernoulli equation in the array-scale core and bypass flow, Equations (3.15) and (3.16):

$$\zeta_1 - \zeta_5 = \frac{1}{2}Fr_A^2\left((\tau_6^2 - \sigma_6^2) + (\sigma_5^2 - \sigma_1^2)\right). \tag{3.24}$$

This equation is slightly different from the equivalent for the turbine-scale model, as the velocity discontinuity across the array introduced in the array-scale model results in the additional $\sigma_5^2 - \sigma_1^2$ term, whereas it is assumed that the velocity is continuous through the actuator disc in the turbine scale model, such that $\alpha_2 = \alpha_3$ (the equivalent of which would be $\sigma_1 = \sigma_5$ in the array-scale model). Continuity requires:

$$\zeta_1 h_0 \sigma_1 u_0 = \zeta_5 h_0 \sigma_5 u_0, \tag{3.25}$$

which allows σ_5 to be eliminated from Equation (3.24) to give:

$$\zeta_1 - \zeta_5 = \frac{1}{2} Fr_A^2 \left((\tau_6^2 - \sigma_6^2) + \sigma_1^2 (\frac{\zeta_1^2}{\zeta_5^2} - 1) \right), \tag{3.26}$$

and therefore the array thrust coefficient in Equation (3.23) may be expressed as:

$$C_{TA} = \left((\tau_6^2 - \sigma_6^2) + \sigma_1^2 (\frac{\zeta_1^2}{\zeta_5^2} - 1) \right). \tag{3.27}$$

Recalling the definition of $\delta\zeta = \zeta_1 - \zeta_5$ as the array-scale change in the static head between stations one and five, ζ_5 can therefore be expressed in terms of ζ_1 and the change in static head:

$$\zeta_5 = \zeta_1 - \delta\zeta. \tag{3.28}$$

The far-field turbine-scale problem, defined in Equation (3.14), is a cubic for $\delta\zeta$ in terms of σ_1, ζ_1, B_L, Fr_A^2, and C_{TL} (from which C_{TA} is defined). Equation (3.15) may be rearranged to express ζ_1 as:

$$\zeta_1 = 1 - \frac{1}{2} Fr_A^2 (\sigma_1^2 - 1). \tag{3.29}$$

These equations are combined to solve Equation (3.27) for τ_6:

$$\tau_6^2 = C_{TA} + \sigma_6^2 - \sigma_1^2 \left[\frac{\left(1 - \frac{1}{2} Fr_A^2 (\sigma_1^2 - 1)\right)^2}{\left(1 - \frac{1}{2} Fr_A^2 (\sigma_1^2 - 1) - \delta\zeta\right)^2} - 1 \right], \tag{3.30}$$

where it is noted that $\delta\zeta = f_1(\sigma_1, \zeta_1, B_L, C_{TL}, Fr_A)$, $\sigma_1 = f_2(\sigma_6, \tau_6, B_A, Fr_A)$, and $\sigma_6 = f_5(\tau_6, B_A, C_{TA}, Fr_A)$.

The system of equations is closed by substituting Equation (3.22) into Equation (3.30), the result of which is used to solve for τ_6 in terms of the model parameters, B_A, C_{TA}, and Fr_A^2. The system of equations defining the near field array-scale problem, cannot be solved analytically due to the static head and velocity discontinuity between stations one and five. The equations must instead be solved numerically. As the equations have a shallow gradient close to the physically admissible roots, a bounded root-finding algorithm is required to solve the system. The Brent-Dekker method, which combines the bisection, secant, and inverse quadratic interpolation methods (Brent, 1973), was employed in MatLab to provide guaranteed convergence to the roots of the system of equations.

3.4.2 Far Field Array-scale Problem

The far field effects of energy extraction are determined by considering the change in momentum and conservation of mass between stations zero and seven. Conservation of momentum requires:

$$\frac{1}{2}\rho g W_C \left(h_0^2 - (\zeta_7 h_0)^2\right) - T_A = \rho W_C h_0 u_0 \left(\sigma_7 u_0 - u_0\right). \tag{3.31}$$

As the free surface is permitted to deform between stations zero and seven, conservation of mass requires:

$$h_0 u_0 = \zeta_7 h_0 \sigma_7 u_0. \tag{3.32}$$

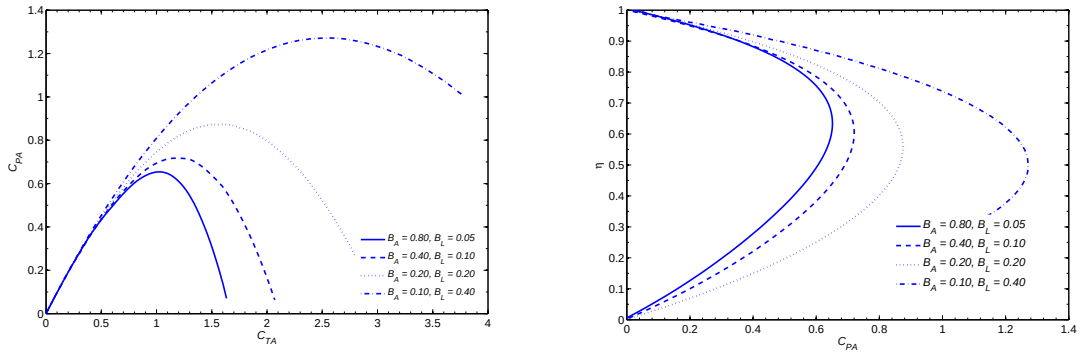

Figure 3.3: Effect of array and local blockage ratios on thrust and power coefficients (left) and basin efficiency (right) for $B_G = 0.04$ and $Fr_A = 0.10$.

Defining $\delta\zeta_A = 1 - \zeta_7$ as the overall change in free surface elevation in the channel between stations zero and seven, the far field problem yields a cubic equation for $\delta\zeta_A$ in terms of the array thrust coefficient C_{TA}, array blockage, B_A, and array-scale Froude number, Fr_A:

$$\delta\zeta_A^3 - 3\delta\zeta_A^2 + \left(Fr_A^2\left(B_A C_{TA} - 2\right) + 2\right)\delta\zeta_A - Fr_A^2 B_A C_{TA} = 0. \tag{3.33}$$

The far field effects of energy extraction can be determined from Equation (3.33) without any further analysis of the problem. However, in order to determine the available power, it is necessary to solve both scales of the problem in order to determine α_2 and thus the power available at the turbine-scale.

3.5 Available Power

The effect of varying turbine spacing is shown in Figure 3.3, where the array blockage may be interpreted as the fraction of the channel occupied by the turbine array, the local blockage as the proportion of the array occupied by the turbines, and the global blockage is the proportion of the entire channel area occupied by turbines (which is kept constant) at $B_G = 0.04$.

As the local blockage increases and the array blockage decreases the thrust on the turbines and the available power increases. When the turbines are placed very far apart, as in the $B_A = 0.80, B_L = 0.05$ case, the peak C_{PA} is relatively low, albeit slightly greater than Betz, due to the array thrust, C_{TA}, being relatively low. This is because the flow is relatively free to divert around each turbine, and therefore the thrust, a function of local through turbine plane flow speed squared, that can be applied to the flow is limited as the velocity through each turbine drops quickly. A greater power coefficient is achieved by increasing the local blockage ratio (which necessitates a reduction in the array blockage to maintain the global blockage ratio $B_G = 0.04$), resulting in the peak array power coefficient approximately doubling from $C_{PA,max} = 0.65$ for $B_A = 0.80, B_L = 0.05$ to $C_{PA,max} = 1.27$ when $B_A = 0.10, B_L = 0.40$. As the local blockage increases, there is greater resistance to flow diverting around each turbine due to proximity of neighbouring turbines, so that the velocity through the turbines is higher, thus the thrust and correspondingly the power remain higher too.

Basin efficiency was introduced in Section 2.4.1 to compliment the traditional efficiency used to parameterise turbines through the power coefficient. The basin efficiency represents the fraction of the total energy removed from the flow that is extracted by the actuator disc. Multiple definitions for basin efficiency are possible in a scale-separated flow, depending on which powers are used to define the ratio. The turbine-scale basin efficiency, η_L, is the ratio of the power available to a turbine, P_L to the power removed from the turbine-scale flow, $P_{L,tot}$, (c.f. Equation (2.37)):

$$\eta_L = \alpha_2 \frac{1 - \frac{1}{2}\delta\theta - Fr_L^2 \frac{1}{1-\delta\theta}}{1 + \frac{1}{2} Fr_L^2 \frac{\delta\theta - 2}{(1-\delta\theta)^2}}. \tag{3.34}$$

The array-scale basin efficiency, η_A, may similarly be calculated as the ratio of the

power available to the array, P_A, to the power removed from the channel, $P_{A,tot}$:

$$\eta_A = \alpha_2 \frac{1 - \frac{1}{2}\delta\zeta - Fr_A^2 \frac{1}{1-\delta\zeta}}{1 + \frac{1}{2}Fr_A^2 \frac{\delta\zeta - 2}{(1-\delta\zeta)^2}}. \tag{3.35}$$

The overall basin efficiency of the tidal array is the ratio of the aggregate available power to the total power removed from the flow through the channel. This is simply the product of the turbine-scale and array-scale basin efficiencies, and the following results shall be presented in terms of the overall basin efficiency, the ratio of energy extracted at the turbines to the energy removed from the flow:

$$\begin{aligned} \eta &= \frac{\text{Power available to turbines}}{\text{Power available to turbines and dissipated in mixing}} \\ &= \frac{C_{PA}}{(C_{PA} + C_{PA,mix})} = \eta_L \eta_A. \end{aligned} \tag{3.36}$$

Increasing B_L causes the basin efficiency to decrease at peak power coefficient, as the larger thrusts imposed at higher B_L cause greater shear between the turbine wake and bypass flow, which in turn increases the energy dissipation in the mixing region. The basin efficiency at the peak power coefficient $C_{PA} = 0.65$ in the $B_A = 0.80, B_L = 0.05$ case is $\eta = 0.64$, so that 1MW extracted by the turbine removes about 1.6MW from the flow. This contrasts with the case where $B_A = 0.10, B_L = 0.40$ for which $\eta = 0.50$ when $C_{PA} = 1.27$, so that 1MW extracted by the turbine removes 2MW from the flow. However, higher local blockage ratios are more efficient for a given array power coefficient, such that the basin efficiency for closely spaced turbines, $B_A = 0.10, B_L = 0.40$, is $\eta = 0.85$ at $C_{PA} = 0.65$ compared to $\eta = 0.64$ when widely spaced $B_A = 0.80, B_L = 0.05$. For a given level of power delivery, the velocity through the turbine is higher when the turbine blockage is higher due to the reduced deflection of the flow, and therefore there is reduced shear stress between the bypass flow and turbine wake, and thus less energy dissipation in the mixing region, improving the basin efficiency. Equivalently, the same power is achieved with less thrust at closer

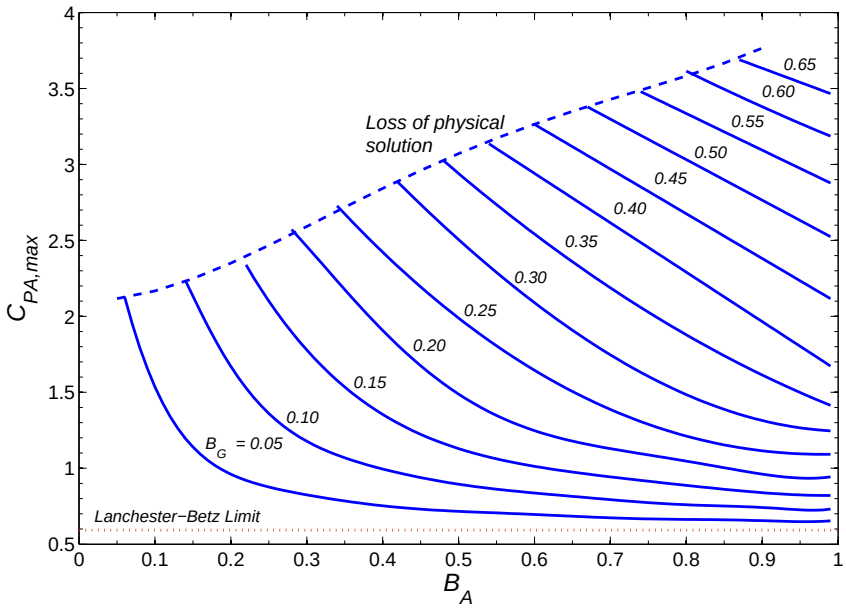

Figure 3.4: Effect of increasing the array blockage on the maximum power coefficient for a range of constant global blockage ratios at Froude number $Fr_A = 0.10$.

turbine spacings.

The general effect of the global blockage on the maximum power coefficient is shown in Figure 3.4. In all cases, even the case of turbines uniformly distributed over the channel width, i.e. $B_A = 1$, it is possible to improve upon the Lanchester-Betz limit due to the blockage of the channel. For a given global blockage, i.e. number of turbines, as B_A is reduced and the fence only partially occupies the channel width, local blockage B_L is increased and the flow is less able to deflect into the turbine bypasses. Thus the turbines can support a greater pressure drop across them, increasing the power and thrust at the peak operating point as local blockage increases. This maximum power occurs at reduced velocity through the turbine plane as B_L increases and the bypass becomes more constrained, albeit achieving a higher flow velocity. This leads to the decrease in η at maximum power with increasing blockage noted in the previous figure. However, if C_{PA} is specified, efficiency η is seen to increase with B_L, and for a fixed η, maximum C_{PA} is delivered at maximum B_L.

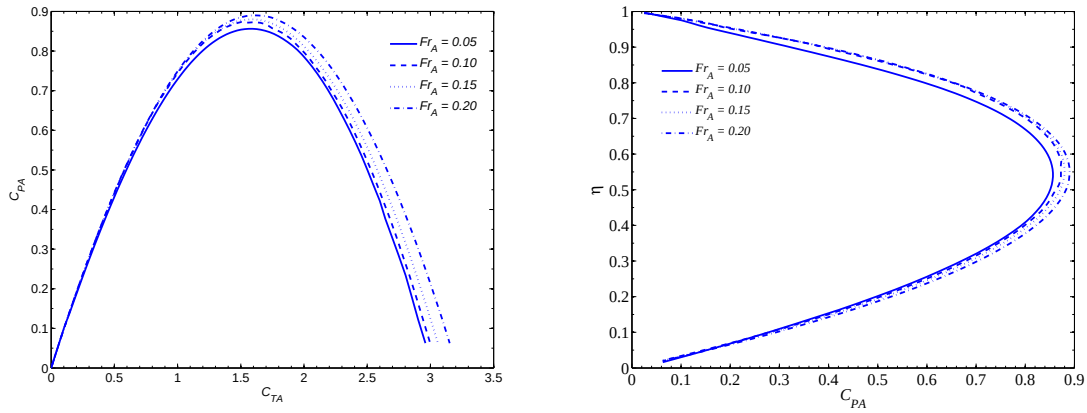

Figure 3.5: Effect of increasing the Froude number on the thrust and power coefficients (left) and basin efficiency (right) for $B_A = 0.20$ and $B_L = 0.20$.

The maximum blockage ratio that can be achieved is limited by how closely turbines can be packed and clearance requirements from the seabed, other turbines and the surface. A further constraint is imposed in the turbine-scale model to prevent the bypass flow from becoming supercritical, which may occur when the acceleration of the flow around the turbine causes the Froude number in the bypass to become greater than 1. Hence, particularly at large global blockages, there is a limited subspace of feasible solutions.

Figure 3.5 shows the effect of the Froude number on the thrust and power coefficients and the basin efficiency. Increasing the Froude number increases the maximum power and thrust coefficients; in the case of $B_A = 0.2, B_L = 0.2$, $C_{PA} = 0.86$ when $Fr_A = 0.05$ rises to $C_{PA} = 0.89$ for $Fr_A = 0.20$. The corresponding efficiency at peak power is $\eta = 0.536$ at $Fr_A = 0.05$ and increases to $\eta = 0.552$ when $Fr_A = 0.20$.

The Froude number always appears as Fr_A^2 in the model equations, and may be interpreted as the ratio of dynamic to static head in the flow. The operation of a turbine causes the relative balance of dynamic and static head to change, the extent of which is determined by the upstream Froude number and its effect on the operation of the turbine. At the turbine plane, there is a step change in static head, while the flow speed is continuous across the turbine. The wake expansion region between

stations three and four is characterised by the exchange of dynamic to static head, resulting in a recovery of the static head at the expense of reducing the flow speed. The volume constraint introduced by the free surface causes an acceleration of the flow in the bypass region, which reduces the static head in the bypass. Station four is defined as the point at which the falling static head in the bypass equalises with the rising static head in the wake region after which the two flows mix between stations four and five, resulting in a uniform outflow velocity at station five. The change in free surface height at the outlet relative to the inlet is due to the energy extraction by the turbine and the resulting transfer of static energy to dynamic energy as the flow accelerates to conserve mass flux in the channel.

The rate of change of free surface height to total head removal is related to the Froude number by $(1 - Fr_A^2)^{-1}$. Hence, as Fr_A is increased, downstream height reduces more quickly for fixed total head removal, and thus the turbine bypasses are further volume flux constrained leading to greater static head drop at station four. For a given head drop, and therefore thrust, higher power is available to the turbine because a higher flow speed is maintained through the turbine as less acceleration is required of the flow in the bypass as Froude number increases. Correspondingly, a given level of power is achieved with a lower thrust as Froude number increases and thus lower overall power removed from the flow. Thus efficiency increases with Froude number for a given C_{PA}.

3.6 Special Cases

Two special cases of the general two-scale model of an array partially spanning a wide channel are of particular interest for their consequences on energy extraction. The first is the case where the change in elevation, $\delta\zeta$, tends to zero, in which case the scale-separated volume-flux constrained model of Nishino and Willden (2012b)

is recovered, and the second is the case where the channel width W_C tends towards infinity while the array width remains finite, such that the array blockage tends to zero. These cases shall be investigated in further detail here.

3.6.1 Volume-flux Constrained Model

The analysis presented by Nishino and Willden (2012b) was for a volume-flux constrained flow, which is the limit of the present model when the Froude number tends to zero. It is assumed in the volume-flux constrained case that the change in water depth in the channel is negligible compared to the water depth, so that $\delta\theta, \delta\zeta_A \approx 0$, and thus that in the far field, energy extraction from the flow results solely in a change in the pressure field across the channel. The change in the pressure field however does not result in a change in the free surface elevation, and therefore there is no acceleration of the flow far downstream of the devices.

Neglecting high order terms in $\delta\theta$, Equation (3.13) may be rearranged for $\delta\theta$, yielding:

$$\delta\theta = \frac{Fr_L^2 B_L C_{TL}}{2 + Fr_L^2 \left(B_L C_{TL} - 2\right)}. \tag{3.37}$$

An equivalent expression is found for the array-scale model by neglecting higher order terms in $\delta\zeta_A$ in Equation (3.33), yielding:

$$\delta\zeta_A = \frac{Fr_A^2 B_A C_{TA}}{2 + Fr_A^2 (B_A C_{TA} - 2)}. \tag{3.38}$$

Equations (3.37) and (3.38) show that in taking $Fr_L^2 \to 0$ and $Fr_A^2 \to 0$, $\delta\theta \to 0$ and $\delta\zeta_A \to 0$, and the volume-flux constrained case is recovered in the turbine-scale and array-scale models. The volume-flux constrained models of the two scale-separated problems therefore correspond to ones in which the Froude number of the flow is zero and the effect of the free surface on the flow is neglected. This alters the calculation

of the static pressure head, which in the generalised two-scale model is:

$$\int_0^h \rho g b z dz = \frac{1}{2}\rho g b h^2, \tag{3.39}$$

but is simply the pressure $p = \rho g h$ multiplied by the cross-sectional area of the channel, i.e. pA_C, in the volume-flux constrained model. This reduces the order of the pressure term in the model equations, and therefore leads to a solution to the volume-flux constrained model of reduced algebraic complexity as compared to the open channel model. Garrett and Cummins (2007) state that the volume-flux constrained model is limited by the requirement that:

$$Fr^2 \ll \frac{9}{4}\frac{(1-B)^2}{B(3-B)}. \tag{3.40}$$

Given the Froude number, Equations (3.37) and (3.38) thus allow the magnitude of the change in free surface elevation to be evaluated and thereby determine the magnitude of the acceleration of the flow far downstream of the device. If the flow acceleration is small and the condition in Equation (3.40) holds, then the volume-flux constrained model may be sufficient as the additional higher-order physics modelled in the generalised model is negligible relative to the lower order physics captured with the volume-flux constrained model.

As discussed in the previous section, the Froude number always appears as Fr_L^2 or Fr_A^2 and represents the relative importance of dynamic to static head in the flow. When $Fr_L^2 \to 0$, the kinetic energy is negligible relative to the static energy, and therefore the effect of a device on the kinetic energy is negligible relative to the effect on the static head. Equivalently, when $Fr_A^2 \to 0$, the effect of the turbine array on the dynamic in the flow is negligible relative to its effect on the static head for the same reason. Thus, in the limits of $Fr_L^2 \to 0$ and $Fr_A^2 \to 0$, only the hydrostatic pressure changes far downstream of the device and the array, and there is no change

in the flow velocity at the channel outlet, as is assumed in, and therefore recovering, the models of Garrett and Cummins (2007) and Nishino and Willden (2012b).

3.6.2 Infinitely Wide Channel

When the channel width becomes large, $W_C \to \infty$, the array occupies a relative region of the flow that becomes infinitesimally small, and therefore only the small fraction of the flow close to the array is affected by the energy extraction of the devices. When $W_C \to \infty$, the array-scale blockage ratio $B_A \to 0$, and therefore the global blockage ratio $B_G \to 0$ also. The local blockage ratio, B_L, however remains finite, as two different length scales emerge in the conservation of mass and momentum equations, one scaling on the device flow passage, and the other scaling on the channel dimensions, as shown by the conservation of momentum equation between stations one and six:

$$\frac{1}{2}\rho g W_C h_0^2 \left(1-\zeta_6^2\right) - T_A = \rho h_0 u_0^2 \left(L\zeta_1\sigma_1\left(\sigma_6-1\right) + \left(W_C - L\zeta_1\sigma_1\right)\left(\tau_6-1\right)\right). \quad (3.41)$$

In the limit $\frac{L}{W_C} \to 0$, it can be shown from the conservation of mass equations that $\tau_6, \zeta_6 = 1$, and therefore the array does not affect the far field flow. The $\mathcal{O}(W_C)$ terms in the momentum equation scaling on the channel dimension are therefore:

$$\mathcal{O}(W_C): \quad \frac{1}{2}\rho g W_C h_0^2 \left(1-\zeta_6^2\right) - T_A = \rho h_0 u_0^2 W_C \left(\tau_6 - 1\right), \quad (3.42)$$

where it is currently unknown whether T_A remains finite in size as $\frac{L}{W_C} \to 0$. However, observing that conservation of mass requires $\tau_6, \zeta_6 = 1$ in the limit $W_C \to \infty$, it must therefore be required that $\mathcal{O}(W_C)\, T_A = 0$. Considering $\mathcal{O}(L)$ terms in the momentum equation yields, again noting $\tau_6 = 1$:

$$\mathcal{O}(L): \quad T_A = \rho L h_0 u_0^2 \zeta_1 \sigma_1 \left(1-\sigma_6\right). \quad (3.43)$$

The $\mathcal{O}(L)$ scaling of the array thrust indicates that, although the array is made up of many turbines, the aggregate effect of those devices is negligible on the far field flow and that the flow is only altered in the vicinity of the array. Non-dimensionalising Equation (3.43) gives a simple relationship for the array thrust coefficient:

$$C_{TA} = \frac{2\sigma_1(1-\sigma_6)}{B_L}. \tag{3.44}$$

These equations complete the array scale model, and are solved in conjunction with Equation (3.13) for the inner flow to determine the overall solution.

Figure 3.6 shows the effect of varying the Froude number on the maximum power coefficient, with the results of the rigid lid case of Nishino and Willden (2012b) included for comparison. Increasing the Froude number causes the maximum power coefficient to increase from the results of the rigid lid case, where $C_{PA,Max} = 0.798$ at $B_L \approx 0.4$ which increases by over 10% to $C_{PA,Max} = 0.888$ at $B_L \approx 0.45$ when the Froude number increases to $Fr_A = 0.30$. It should be noted that, even in the rigid lid case, this represents an increase in the maximum power coefficient of almost 35% from the Lanchester-Betz limit, $C_{PA,Max} = 0.593$. Although the channel is infinitely wide, the local blockage of the devices in the finite depth causes the Lanchester-Betz limit, derived for an infinite flow field in all directions, to be surpassed. The maxima in the $C_{PA,Max}$ curves indicate that, even when the array blockage is negligible, maximum available power occurs only when reasonably substantial local blockage ratios are achieved. For maximum power, $B_L \approx 0.4$ which corresponds to a device of diameter D operating in water of depth $2D$ with no inter-device spacing, i.e. a device flow passage of area $2D^2$.

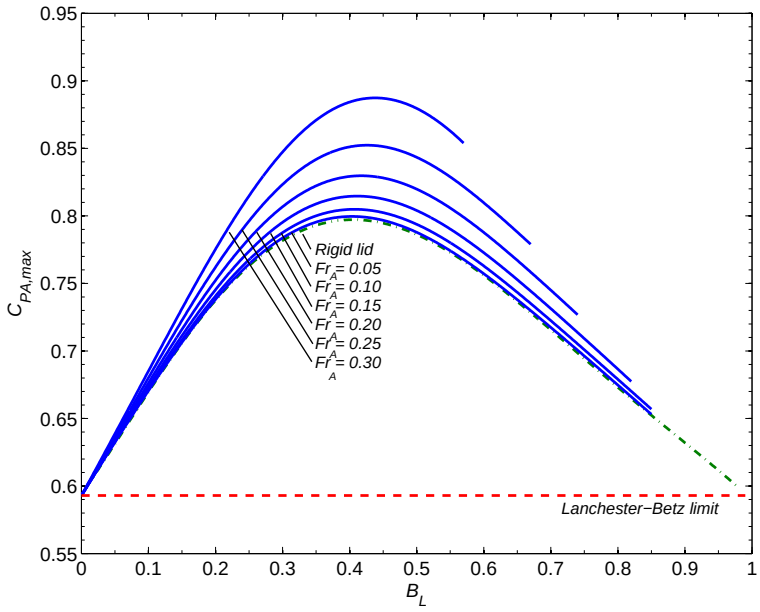

Figure 3.6: Effect of local blockage and Froude number on the maximum power coefficient, compared to the rigid lid case of Nishino and Willden (2012b) and the Lanchester-Betz limit.

3.7 Conclusions

A theoretical model has been proposed to examined the energy extraction of an array of tidal turbines partially spanning an open channel by assuming that the flow around each device and the flow around the array occur on different spatial and temporal scales. Flow mixing downstream of the device was assumed to occur much more quickly than flow mixing downstream of the array due to the relative scale of the dimensions of the device diameter and array width. The two scales were coupled wherein the flow through the array provided the upstream flow speed and hydrostatic pressure boundary conditions to the turbine-scale model. The aggregate thrust of the devices and resulting change in flow speed and hydrostatic pressure at the downstream boundary of the turbine-scale problem provided the internal boundary condition that led to the array-scale mixing problem. The two models were investigated as open channel flow problems following the open channel actuator disc model presented in

Section 2.4.1.

It was found that an array partially spanning a channel could increase available power above that achieved by the same number of devices placed homogeneously across the channel. The power available to an array increases as the local blockage increases as a result of increased resistance to flow diverting around each device due to the presence of neighbouring devices. As the devices cause a change in the balance of the dynamic and static head in the flow, it was also expected that the Froude number, which may be expressed as the ratio of these two quantities, should be important. Available power increases with Froude number as the deformation of the free surface increases with increasing Froude number, constraining the volume-flux in the device bypass and thus maintaining a higher flow speed through the turbines, resulting in a greater available power.

Two limiting cases of the model were also investigated; the limit of an infinitely wide channel, and the volume-flux constrained model. It was shown in the limit of an infinitely wide channel there exists an optimal blockage ratio of approximately $B_L = 0.4$ to maximise energy extraction and that the rigid lid limit of 79.8% kinetic energy extraction of Nishino and Willden (2012b) increases with increasing Froude number. In channels of finite width, it is generally possible, for fixed global blockage and thus number of devices, to increase the available power by increasing the local blockage, although there are geometrical constraints to this. The volume-flux constrained models of Garrett and Cummins (2007) and Nishino and Willden (2012b) are recovered in the limit $Fr_A^2 \to 0$ when the change in the downstream height of the flow becomes negligible and the operation of the device changes only the static head drop across the channel.

Chapter 4

Dynamics of Shallow Water Flows

So far as the theories of mathematics are about reality, they are not certain; so far as they are certain, they are not about reality
- Albert Einstein

The Shallow Water Equations (SWEs) describe viscous, incompressible flows where the vertical dimension is much smaller than the horizontal dimensions. Several approximations and assumptions are made in the derivation of the SWEs which may have implications for depth-averaged simulations of tidal turbine arrays. The chapter reviews the formulation of the Navier-Stokes equations, the three-dimensional governing equations for a viscous, incompressible fluid. The Reynolds-averaged Navier-Stokes (RANS) equations, a temporally-averaged form of the Navier-Stokes equations, are investigated further as they are most commonly implemented in fluid flow simulations. The Boussinesq approximation is discussed as an approach often invoked to simplify the turbulent terms to close the RANS equations.

The numerical solution of the shallow water equations is discussed in the second part of this chapter. An open-source finite element solver TELEMAC-2D was selected, and the implementation of the shallow water equations in a finite element framework is reviewed. The finite element method discretises unknown functions with simple interpolating basis functions and discretises equations with a series of test functions. TELEMAC-2D uses the Galerkin finite element method, where the same functions are used for the basis and test functions, allowing the shallow water equations to be implemented as a linear system of equations with an appropriate choice of turbulence model. The chapter concludes with a review of the turbulence model options in TELEMAC-2D.

4.1 The Navier-Stokes Equations

The Navier-Stokes equations describe three-dimensional viscous fluid motion, and were derived by a number of researchers in the 19^{th} century, representing a breakthrough in the understanding of fluids. The key advance was the realisation that intermolecular forces or internal stresses acted on fluid particles, giving rise to viscous fluid motion. The generality of the Navier-Stokes equations has been demonstrated through their application to many different fluids and flow regimes. However, they are difficult to solve without the use of simplifying assumptions due to the broad range of spatial and temporal scales that occur in real flows.

4.1.1 Origin of the Navier-Stokes Equations

The Navier-Stokes equations were independently derived by a number of researchers in the first half of the 19^{th} century, first by Navier (1823) and then Poisson (1831), based on theories of action of intermolecular forces. This introduced second derivatives of the velocity multiplied by some constant, a function of the spacing between molecules, to the equations describing non-viscous fluids of Euler (1757).

Saint-Venant (1843) derived the equations for a viscous flow, considering internal stresses rather than intermolecular forces (Anderson, 1997). Stokes (1845), unaware of the progress made in France, derived the equations of motion for a moving fluid with friction, obtaining the viscosity coefficient μ used today.

The equations derived by Navier and Poisson are equivalent to the equations of Saint-Venant and Stokes because the physical interpretation for the viscosity coefficient of the latter two formulations derives from kinetic theory of gases, from which it can be shown that the viscosity coefficient is directly proportional to the molecular mean free path - the mean distance between collisions between molecules (Anderson, 1997). The hypotheses underlying the equations have largely been demonstrated to

agree well with experimental evidence from fluid studies (Prandtl and Tietjens, 1934).

4.1.2 Formulation of the Navier-Stokes Equations

The Navier-Stokes equations can be derived from Newton's second law of motion, and are used to describe an incompressible Newtonian flow in three dimensions $\mathbf{x} = (x, y, z)^T$, where $\mathbf{u} = (u, v, w)^T$. The key equations are outlined here, and a full derivation may be found in texts such as Prandtl and Tietjens (1934) and Batchelor (1967). Einstein subscript notation is adopted, where repeated indices in a term denote summation over all the values of the index. Introducing $i, j = 1, 2, 3$, so that $x_1 = x, x_2 = y$, and $x_3 = z$, the continuity equation is given by:

$$\frac{\partial u_i}{\partial x_i} = 0. \tag{4.1}$$

The Navier-Stokes equations are:

$$\frac{\partial u_i}{\partial t} + u_j \frac{\partial u_i}{\partial x_j} = F_i - \frac{1}{\rho}\frac{\partial p}{\partial x_i} + \nu \frac{\partial^2 u_i}{\partial x_j \partial x_j}, \tag{4.2}$$

where t is time, F_i is the acceleration due to the body force in the i^{th} direction, ρ is the fluid density, p is the pressure, and ν is the molecular viscosity. The terms on the left hand side, the unsteady and advective accelerations, represent the inertia of the fluid. Terms on the right hand side are the forces acting on an elemental volume of fluid, namely body forces such as gravity, pressure and the dissipative viscous forces.

4.1.3 Reynolds Decomposition

Turbulent eddies in a flow have time scales that are much smaller than those of the mean flow. The computational cost of directly solving for all the scales of motion in a turbulent flow are prohibitively high in all but the smallest of domains, so it

is desirable to restrict the scale of motions being solved to those of interest only. Reynolds (1895) proposed a method for doing this in which a time-varying quantity such as velocity, u_i, is defined to be comprised of a time-averaged component, denoted with an overbar, $\bar{u}_i$, and a fluctuating component, denoted with a prime, u_i':

$$u_i = \bar{u}_i + u_i', \tag{4.3}$$

The separation of an instantaneous quantity into time-averaged and fluctuating components is known as Reynolds decomposition. The components are defined such that $\bar{u}_i$ is the time-average of u_i over some period T, which is large relative to the characteristic time scale of the turbulent fluctuations but short compared to the characteristic time scale of the mean flow, so that:

$$\bar{u}_i = \frac{1}{T}\int_{\tau}^{\tau+T} u_i dt, \tag{4.4}$$

and therefore:

$$u_i' = \frac{1}{T}\int_{\tau}^{\tau+T} \left(u_i - \bar{u}_i\right) dt = 0. \tag{4.5}$$

Substituting the Reynolds decomposition Equation (4.3) into the continuity equation, Equation (4.1), gives:

$$\frac{\partial u_i}{\partial x_i} = \frac{\partial \left(\bar{u}_i + u_i'\right)}{\partial x_i} = \frac{\partial \bar{u}_i}{\partial x_i} + \frac{\partial u_i'}{\partial x_i} = 0. \tag{4.6}$$

Assuming that $\bar{u}_i$ and u_i' are continuous and differentiable, then time averaging Equation (4.6) yields:

$$\frac{1}{T}\int_{\tau}^{\tau+T} \frac{\partial \bar{u}_i}{\partial x_i} dt + \frac{1}{T}\int_{\tau}^{\tau+T} \frac{\partial u_i'}{\partial x_i} dt = \frac{\partial \bar{u}_i}{\partial x_i} + 0 = \frac{\partial \bar{u}_i}{\partial x_i} = 0, \tag{4.7}$$

where the definitions for $\bar{u}_i$ and u'_i, have been applied. It follows that:

$$\frac{\partial u'_i}{\partial x_i} = 0. \tag{4.8}$$

A Reynolds decomposition for each instantaneous quantity may be substituted into the momentum equation, Equation (4.2), to give:

$$\begin{aligned} \frac{\partial \left(\bar{u}_i + u'_i\right)}{\partial t} + \left(\bar{u}_j + u'_j\right) \frac{\partial \left(\bar{u}_i + u'_i\right)}{\partial x_j} = \\ \left(\bar{F}_i + F'_i\right) - \frac{1}{\rho} \frac{\partial \left(\bar{p} + p'\right)}{\partial x_i} + \nu \frac{\partial^2 \left(\bar{u}_i + u'_i\right)}{\partial x_j \partial x_j}, \end{aligned} \tag{4.9}$$

which is then time-averaged to give, using the definitions in Equations (4.4) and (4.5):

$$\frac{\partial \bar{u}_i}{\partial t} + \overline{\left(\bar{u}_j + u'_j\right) \frac{\partial \left(\bar{u}_i + u'_i\right)}{\partial x_j}} = \bar{F}_i - \frac{1}{\rho} \frac{\partial \bar{p}}{\partial x_i} + \nu \frac{\partial^2 \bar{u}_i}{\partial x_j \partial x_j}. \tag{4.10}$$

The advection term requires further investigation, as it is the spatial derivative of the time-averaged product of two velocities, $\overline{u_i u_j}$. Expanding the velocity product gives:

$$\overline{u_i u_j} = \overline{\left(\bar{u}_i + u'_i\right)\left(\bar{u}_j + u'_j\right)} = \overline{\bar{u}_i \bar{u}_j + \bar{u}_i u'_j + \bar{u}_j u'_i + u'_i u'_j} = \bar{u}_i \bar{u}_j + \overline{u'_i u'_j}. \tag{4.11}$$

From Equation (4.4) the time-average of the product of time-averaged velocities, $\overline{\bar{u}_i \bar{u}_j}$, is simply the product of the time-averaged velocities. The time average of the product of a time-averaged velocity and a fluctuating velocity is zero, following from the definition given in Equation (4.5), that the time-average of a velocity fluctuation is zero. The $\overline{u'_i u'_j}$ term remains because the turbulent fluctuations in the three spatial directions may be correlated, in which case the time-average of the product of fluctuations may not be zero. It is this term which introduces the turbulent stresses into the RANS equations and is often simplified through the Boussinesq approximation,

discussed below. The momentum equation thus is:

$$\frac{\partial \bar{u}_i}{\partial t} + \bar{u}_j \frac{\partial \bar{u}_i}{\partial x_j} + \frac{\partial \overline{u_i' u_j'}}{\partial x_j} = \bar{F}_i - \frac{1}{\rho}\frac{\partial \bar{p}}{\partial x_i} + \nu \frac{\partial^2 \bar{u}_i}{\partial x_j \partial x_j}. \tag{4.12}$$

4.1.4 Boussinesq Approximation

The Boussinesq eddy viscosity concept draws an analogy between momentum transfer in a gas, described by the molecular viscosity, and the momentum transfer in a flow due to turbulent eddies, which is assumed to be described with an eddy viscosity $\nu_{_T}$. The eddy viscosity is not a property of the fluid like the molecular viscosity, but depends on the state of turbulence in the flow. Under this assumption, the Reynolds stress term, $\overline{u_i' u_j'}$ is approximated as:

$$-\overline{u_i' u_j'} = \nu_{_T} \left(\frac{\partial \bar{u}_i}{\partial x_j} + \frac{\partial \bar{u}_j}{\partial x_i} \right) - \frac{2}{3} K \delta_{ij}, \tag{4.13}$$

where K is the turbulent kinetic energy and δ_{ij} is the Kronecker delta. The first term is the shear stress of a Newtonian fluid; the product of the strain rate and the molecular viscosity. The second term ensures that the normal stresses sum to $2K$, which is required by the definition of K. As this acts as a normal stress, a modified pressure term is defined such that $p^* = \bar{p} + \frac{2}{3}\rho K$, thus it is not strictly necessary to determine K in the Boussinesq approximation. The momentum equation therefore becomes:

$$\frac{\partial \bar{u}_i}{\partial t} + \bar{u}_j \frac{\partial \bar{u}_i}{\partial x_j} = \bar{F}_i - \frac{1}{\rho}\frac{p^*}{\partial x_i} + \frac{\partial}{\partial x_j}\left(\nu \frac{\partial \bar{u}_i}{\partial x_j} + \nu_{_T} \left(\frac{\partial \bar{u}_i}{\partial x_j} + \frac{\partial \bar{u}_j}{\partial x_i} \right) \right). \tag{4.14}$$

It should be noted that p^* is usually written as $\bar{p}$ for convenience. Dispersive momentum transport by turbulent eddies is generally much larger than laminar diffusion,

therefore the eddy viscosity is generally much larger than the molecular viscosity:

$$\nu_T >> \nu, \tag{4.15}$$

so that the laminar diffusion term $\nu \frac{\partial^2 \bar{u}_i}{\partial x_j \partial x_j}$ may often be neglected, yielding:

$$\frac{\partial \bar{u}_i}{\partial t} + \bar{u}_j \frac{\partial \bar{u}_i}{\partial x_j} = \bar{F}_i - \frac{1}{\rho} \frac{\partial \bar{p}}{\partial x_i} + \nu_T \frac{\partial}{\partial x_j} \left(\frac{\partial \bar{u}_i}{\partial x_j} + \frac{\partial \bar{u}_j}{\partial x_i} \right). \tag{4.16}$$

The Boussinesq approximation does not provide a closure for the turbulence term itself; instead it provides a framework for constructing a turbulence model to determine ν_T (Rodi, 1980). The eddy viscosity analogy assumes that the mean free path of the turbulent eddies is small compared to the dimensions of the flow, but large compared to the eddy dimensions, as is the case for molecules in kinetic gas theory. Unlike molecules, turbulent eddies are not small compared to the flow dimensions, and the interactions between eddies, which act to distort and rip eddies apart, are not similar to discrete collisions between molecules. Bradshaw (1972) notes that most basic fluid flows used as test cases for the Reynolds stress are in states of local equilibrium or self-preservation, and the eddy viscosity and mixing length are simply-behaved for dimensional reasons, thus they give good agreement with experimental results. However, the analogy between turbulent and molecular viscosity is not correct, particularly for more complicated flows. Furthermore, additional inaccuracies arise from the assumption and parameters involved in the transport equations and linear constitutive equations used to determine ν_T (Schmitt, 2007), therefore the following derivation of the shallow water equations shall not use the Boussinesq approximation in order to reduce modelling biases in the turbulent stress terms of the Navier-Stokes equations.

4.2 The Shallow Water Equations

The high Reynolds number of many tidal flows and the large domains over which they occur means that there is a very broad range of spatial and temporal scales of fluid motion, and it is therefore computational expensive to solve the full complement of Navier-Stokes equations. Reynolds decomposition eliminates some small scale fluctuations, but the three-dimensional problem remains very large and expensive to solve. Furthermore, the large range of turbulent scales in the flow makes it difficult to select and parametrise an appropriate turbulence model which accurately captures both the smallest and largest scale turbulent eddies.

The RANS equations can often be simplified further in the case of tidal flows as the wavelength of a tidal wave is very large compared to the depth of the fluid. As a shallow water flow, average motions in the vertical dimension are small (and usually negligible) compared to those in the horizontal dimensions, and therefore the problem can be reduced to two dimensions. The shallow water equations are derived from the three-dimensional Reynolds Averaged Navier-Stokes equations in the following section to investigate the consequences for turbine modelling in depth-averaged simulations.

4.2.1 Deriving the Shallow Water Equations

The Reynolds-averaged continuity and Navier-Stokes equations derived in the previous section were:

$$\frac{\partial \bar{u}_i}{\partial x_i} = 0, \tag{4.17}$$

and

$$\frac{\partial \bar{u}_i}{\partial t} + \bar{u}_j \frac{\partial \bar{u}_i}{\partial x_j} + \frac{\partial \overline{u_i' u_j'}}{\partial x_j} = \bar{F}_i - \frac{1}{\rho}\frac{\partial \bar{p}}{\partial x_i}, \tag{4.18}$$

where the molecular viscosity term is negligible compared to the turbulent stress term and an approximation has not been hypothesised for the Reynolds stress term. If

the vertical velocities in these are typically small compared to those in the horizontal direction, as for tidal flows, they are negligible compared to horizontal flow motions. If the vertical pressure gradient is linear with gravity, the vertical momentum equation, for which $i = 3$, noting that $F_3 = -g$, reduces to:

$$\frac{1}{\rho}\frac{\partial \bar{p}}{\partial x_3} = -g. \tag{4.19}$$

If the pressure at the fluid surface, $x_3 = \xi$, is atmospheric, $\bar{p}(\xi) = P_a$, integrating Equation (4.19) over the depth yields the hydrostatic pressure distribution:

$$\bar{p} = \rho g\,(\xi - z) + P_a. \tag{4.20}$$

Depth integrating the continuity equation utilises Leibniz's rule:

$$\begin{aligned}\int_{-h_0}^{\xi} \frac{\partial \bar{u}_i}{\partial x_i} dx_3 = \frac{\partial}{\partial x_k}\int_{-h_0}^{\xi} \bar{u}_k dx_3 - \bar{u}_k|_{\xi}\frac{\partial \xi}{\partial x_k} - \bar{u}_k|_{-h_0}\frac{\partial h_0}{\partial x_k} \\ + \bar{u}_3|_{\xi} - \bar{u}_3|_{-h_0} = 0,\end{aligned} \tag{4.21}$$

where the index $k = 1, 2$, and $a|_b$ denotes the value of a at $x_3 = b$. There is a no-slip boundary condition at the bottom of the flow and a kinematic boundary condition at the free surface, which require:

$$u_i|_{-h_0} = 0, \qquad \text{and} \qquad \frac{\partial \xi}{\partial t} + \bar{u}_k|_{\xi}\frac{\partial \xi}{\partial x_k} = \bar{u}_3|_{\xi}, \tag{4.22}$$

respectively. Substituting the boundary conditions in Equation (4.22) into Equation (4.21) yields:

$$\frac{\partial}{\partial x_k}\int_{-h_0}^{\xi} \bar{u}_k dx_3 + \frac{\partial \xi}{\partial t} = 0. \tag{4.23}$$

Defining the depth- and time-averaged velocity $\bar{U}_k$ as:

$$\bar{U}_k = \frac{1}{h}\int_{-h_0}^{\xi} \bar{u}_k dx_3, \tag{4.24}$$

where $h = \xi + h_0$, this simplifies to give the depth-averaged continuity equation:

$$\frac{\partial \xi}{\partial t} + \frac{\partial \bar{U}_k h}{\partial x_k} = 0. \tag{4.25}$$

The procedure for depth averaging the RANS momentum equation is similar to that for the continuity equation. The vertical ($i = 3$) momentum equation has already been solved in Equation (4.20), allowing the index $l = 1, 2$ to be introduced to replace the index j. Considering each term individually:

$$\frac{\partial \bar{u}_k}{\partial t} + \bar{u}_l \frac{\partial \bar{u}_k}{\partial x_l} + \frac{\partial \overline{u_k' u_l'}}{\partial x_l} = \bar{F}_k - \frac{1}{\rho}\frac{\partial \bar{p}}{\partial x_k}. \tag{4.26}$$

Expanding the first term with the Leibniz rule gives:

$$\int_{-h_0}^{\xi} \frac{\partial \bar{u}_k}{\partial t} dx_3 = \frac{\partial}{\partial t}\int_{-h_0}^{\xi} \bar{u}_k dx_3 - \bar{u}_k|_{\xi}\frac{\partial \xi}{\partial t} - \bar{u}_k|_{-h_0}\frac{\partial h_0}{\partial t}, \tag{4.27}$$

the last term of which may be eliminated with the no-slip boundary condition at $x_3 = -h_0$ to give:

$$\int_{-h_0}^{\xi} \frac{\partial \bar{u}_k}{\partial t} dx_3 = \frac{\partial \bar{U}_k h}{\partial t} - \bar{u}_k|_{\xi}\frac{\partial \xi}{\partial t}. \tag{4.28}$$

The Leibniz rule expansion of the second term in Equation (4.26) gives:

$$\begin{aligned}\int_{-h_0}^{\xi} \frac{\partial \bar{u}_k \bar{u}_l}{\partial x_l} dx_3 = \frac{\partial}{\partial x_l}\int_{-h_0}^{\xi} \bar{u}_k \bar{u}_l dx_3 - \bar{u}_k|_{\xi}\bar{u}_l|_{\xi}\frac{\partial \xi}{\partial x_l} - \bar{u}_k|_{-h_0}\bar{u}_l|_{-h_0}\frac{\partial h_0}{\partial x_l} \\ + \bar{u}_k|_{\xi}\bar{u}_3|_{\xi} - \bar{u}_k|_{-h_0}\bar{u}_3|_{-h_0},\end{aligned} \tag{4.29}$$

which simplifies with the no-slip boundary condition and the definition of the depth-

and time-averaged velocity to:

$$\int_{-h_0}^{\xi} \frac{\partial \bar{u}_k \bar{u}_l}{\partial x_l} dx_3 = \frac{\partial h \bar{U}_k \bar{U}_l}{\partial x_l} - \bar{u}_k|_\xi \bar{u}_l|_\xi \frac{\partial \xi}{\partial x_l} + \bar{u}_k|_\xi \bar{u}_3|_\xi. \tag{4.30}$$

The kinematic boundary condition, multiplied by $\bar{u}_k|_\xi$, is:

$$\bar{u}_k|_\xi \frac{\partial \xi}{\partial t} + \bar{u}_k|_\xi \bar{u}_l|_\xi \frac{\partial \xi}{\partial x_l} = \bar{u}_k|_\xi \bar{u}_3|_\xi. \tag{4.31}$$

Summation of Equations (4.28), (4.30) and (4.31) yields the first two terms of the depth-averaged equations:

$$\frac{\partial \bar{U}_k h}{\partial t} + \frac{\partial \bar{U}_k \bar{U}_l h}{\partial x_l}. \tag{4.32}$$

Leibniz's rule expands the third term of Equation (4.26) as:

$$\begin{aligned} \int_{-h_0}^{\xi} \frac{\partial \overline{u'_k u'_l}}{\partial x_l} dx_3 = \frac{\partial}{\partial x_l} \int_{-h_0}^{\xi} \overline{u'_k u'_l} dx_3 - \overline{u'_k|_\xi u'_l|_\xi} \frac{\partial \xi}{\partial x_l} - \overline{u'_k|_{-h_0} u'_l|_{-h_0}} \frac{\partial h_0}{\partial x_l} \\ + \overline{u'_k|_\xi u'_3|_\xi} - \overline{u'_k|_{-h_0} u'_3|_{-h_0}}. \end{aligned} \tag{4.33}$$

The terms in Equation (4.33) at the bottom of the flow can be parametrised in terms of a bed shear stress $\tau_{b,k}$, defined as:

$$-\frac{\tau_{b,k}}{\rho} = \overline{u'_k|_{-h_0} u'_l|_{-h_0}} \frac{\partial h_0}{\partial x_l} + \overline{u'_k|_{-h_0} u'_3|_{-h_0}}. \tag{4.34}$$

The terms at the fluid surface can be treated in a similar manner to derive a wind shear stress τ_w, but will be neglected for the sake of brevity. A depth- and time-averaged velocity fluctuation product can be defined as:

$$\overline{U'_k U'_l} = \frac{1}{h} \int_{-h_0}^{\xi} \overline{u'_k u'_l} dx_3, \tag{4.35}$$

so that the third term of Equation (4.26) becomes:

$$\int_{-h_0}^{\xi} \frac{\partial \overline{u_k' u_l'}}{\partial x_l} dx_3 = \frac{\partial \overline{U_k' U_l'} h}{\partial x_l} + \frac{\tau_{b,k}}{\rho}. \tag{4.36}$$

The treatment of the force term depends on the relevant body forces. On a rotating body, the Coriolis force would result in a force vector:

$$\bar{\mathbf{F}} = \begin{bmatrix} 2f\bar{u}_2 \\ -2f\bar{u}_1 \end{bmatrix}, \tag{4.37}$$

where f is the Coriolis parameter. Depth-integration of the fourth term in Equation (4.26) then results in:

$$\mathbf{F}_{da} = \int_{-h_0}^{\xi} \begin{bmatrix} 2f\bar{u}_2 \\ -2f\bar{u}_1 \end{bmatrix} dx_3 = 2f \int_{-h_0}^{\xi} \begin{bmatrix} \bar{u}_1 \\ -\bar{u}_2 \end{bmatrix} = 2f \begin{bmatrix} \bar{U}_1 h \\ -\bar{U}_2 h \end{bmatrix}. \tag{4.38}$$

The depth-averaged form of the fifth term is determined using the pressure relationship derived from the vertical momentum equation, Equation (4.20), which, recalling $h = \xi + h_0$, leads to:

$$\frac{1}{\rho} \int_{-h_0}^{\xi} \frac{\partial \bar{P}_k}{\partial x_k} dx_3 = g \int_{-h_0}^{\xi} \frac{\partial \bar{\xi}}{\partial x_k} dx_3 = gh \frac{\partial \xi}{\partial x_k}. \tag{4.39}$$

Combining Equations (4.32), (4.36), (4.38), and (4.39) yields the depth-averaged momentum equation:

$$\frac{\partial \bar{U}_k h}{\partial t} + \frac{\partial \bar{U}_k \bar{U}_l h}{\partial x_l} + \frac{\partial \overline{U_k' U_l'} h}{\partial x_l} = F_{da,k} - gh \frac{\partial \xi}{\partial x_k} - \frac{\tau_{b,k}}{\rho}. \tag{4.40}$$

4.2.2 Limitations of the Shallow Water Equations

Two scales of turbulent motion exist in shallow water flows; relatively small three dimensional eddies, which have the scale of the water depth, and two dimensional eddies which have a scale larger than the water depth. The velocity $\bar{U}_k$ is averaged spatially over the depth of the flow and temporally over a period T, which must be large enough to encompass the three dimensional fluctuations, but not so large as to obscure variations in the two-dimensional mean flow. The time step Δt required to achieve stable numerical solution of the equations may be smaller than T, leading to a solution with misleading temporal accuracy. The capability of a depth-averaged simulation to model rapid transient features in the flow is therefore limited.

The product $\overline{U'_k U'_l}$ is the depth integral of the velocity fluctuations $\overline{u'_k u'_l}$, representing the stress on the flow due to the transfer of momentum by velocity fluctuations. This stress does not vary in a linear manner as the magnitude will vary across the water column according to the shear profile, and may also vary within the domain of interest if there are features (such as changes in bathymetry) which alter its shape. Consequently, the depth-averaged velocity does not necessarily represent the velocity of elemental volumes of fluid in the water column. Velocity fluctuations near the seabed were combined to give the bed shear stress term $\tau_{b,k}$, as shown in Equation (4.34). Similarly, shear stresses at the fluid surface, such as those due to wind, depend on the product of velocity fluctuations at the surface of the fluid. However, the depth-averaging process means that it is not possible to determine the magnitude of these shear stresses in terms of the velocity fluctuations at their respective locations - the depth-averaged velocity must be used instead.

Empirical models are used to relate the depth- and time-averaged velocity to the friction coefficients needed to determine the shear stresses. These models attempt to construct a relationship between the depth-averaged velocity and the shear stresses induced by the velocity fluctuations, but as fluctuations are a flow phenomenon rather

than a fundamental fluid property, the empirical models may not be accurate in flow conditions dissimilar to those used to derive the model. This makes determination of the appropriate shear stresses difficult for problems where the velocity shear profile may be significantly altered from natural flow conditions, such as near tidal turbine arrays. The effect of tidal turbines on the shear stress profile and turbulent mixing needs to be better understood in order to parametrise better the shear stresses in the shallow water equations.

The vertical pressure variation was approximated as hydrostatic, an assumption which is satisfied provided accelerations in the vertical direction are negligible. Furthermore, it was assumed that all the points on the free-surface, defined in Equation (4.22), could be uniquely defined as a function of x, y, and t. This does not allow breaking waves, and also assumes that the turbine rotor does not pierce the surface of the flow. Numerical stability limitations may also impose a limitation on the turbine thrust, as hydraulic jumps may be induced in an open channel flow if the thrust is large (Draper, 2011).

A further assumption in the derivation of the shallow water equations is that there is no mean current over the vertical direction during the depth integration. The consequence of this assumption can be re-examined by considering the advection term of the RANS equations:

$$\int_{-h_0}^{\xi} \frac{\partial \bar{u}_k \bar{u}_l}{\partial x_l} dx_3 = \frac{\partial}{\partial x_l} \int_{-h_0}^{\xi} \bar{u}_k \bar{u}_l dx_3 - u_k|_{\xi} u_l|_{\xi} \frac{\partial \xi}{\partial x_l} - \bar{u}_k|_{-h_0} \bar{u}_l|_{-h_0} \frac{\partial h_0}{\partial x_l}. \tag{4.41}$$

Considering just the first term on the right hand side and introducing the appropriate depth-averaged variables to $\bar{u}_1$ and $\bar{u}_2$:

$$\frac{\partial}{\partial x_l} \int_{-h_0}^{\xi} \bar{u}_k \bar{u}_l dx_3 = \frac{\partial}{\partial x_l} \int_{-h_0}^{\xi} (\bar{U}_k + \bar{u}_k - \bar{U}_k)(\bar{U}_l + \bar{u}_l - \bar{U}_l) dx_3, \tag{4.42}$$

which, using the definition for the depth- and time-averaged velocities, simplifies to:

$$\frac{\partial \bar{U}_k \bar{U}_l h}{\partial x_l} + \frac{\partial}{\partial x_l} \int_{-h_0}^{\xi} (\bar{u}_k - \bar{U}_k)(\bar{u}_l - \bar{U}_l) dx_3. \tag{4.43}$$

The second term in the final statement is zero if the vertical velocity is homogeneous over the depth (Draper, 2011). This term is dispersive, and is sometimes modelled as an additional turbulent term, taking into account the fluctuations around the spatial mean vertical velocity arising from currents in the flow, and are not due to a current averaged over the vertical direction. Dispersive stresses in the flow near a turbine may be increased by vertical motions imparted by the turbine, and will affect the length of the wake behind the turbine. Such stresses need to be modelled in turbine-scale simulations so they can be parametrised as an extra stress term in a similar manner to the turbulence model.

4.3 Numerical Implementation

The shallow water equations are often solved numerically because of the complexity of the bathymetry and coastlines in the regions of interest. Many software packages have been developed to solve the equations, such as Gerris and TELEMAC-2D (Popinet, 2003; Hervouet, 2007). Numerical simulations in this thesis were performed in TELEMAC-2D, an open-source program for solving the shallow water equations using the finite element method (Hervouet, 2007). TELEMAC-2D was selected because custom functions, such as turbine thrust, are easily integrated into the code, and it is well support by a consortium of institutions; BfW, EDF R&D, and HR Wallingford.

The shallow water equations are discretised for implementation in a two-dimensional mesh. Three main techniques exist for discretising equations; the finite difference (FD), the finite element (FE), and the finite volume (FV) methods. The governing

equations are discretised in such a way that derivatives in the function variables are eliminated (usually) to yield a linear system of equations which can be solved computationally. Each method has strengths and weaknesses, as summarised by Durbin and Medic (2007), with FE and FV methods most commonly used in fluid simulations due to their flexibility in dealing with complex meshes and regions of varying mesh density. TELEMAC-2D discretises the shallow water equations using the FE method, which are summarised below, and a more comprehensive account of the derivation for the TELEMAC system may be found in Hervouet (2007).

4.3.1 Finite Element Method

Equations are implemented in the finite element method with an interpolation method to discretise the unknown quantities, and a variational method (often 'weighted residuals' is used) to discretise the equations. Under the interpolation method a function u in infinite dimensional space is replaced with an approximate function u_h constructed from a finite number of dimensions n by introducing a basis function ψ:

$$u_h = \sum_{i=1}^{n} u_i \psi_i. \tag{4.44}$$

The basis function, which is usually a simple low-order interpolating function, is defined such that ψ_i has a value of one at i and is zero on all other degrees of freedom:

$$\psi_j = \begin{cases} 1 & j = i \\ 0 & j \neq i \end{cases}. \tag{4.45}$$

The basis function is often a piecewise constant, linear or quadratic function, and exact representation of u is only possible if the basis function is of the same order as u. If an exact representation of the function u, defined by the equation $f(u) = g$, the true function value on a continuous domain Ω, is not possible, then $f(u_h) = g$ cannot

be ensured, so it is necessary to minimise the difference between the interpolant and the true function value $f(u_h) - g$. This is done by determining the test functions ϕ:

$$\int_{\Omega} \left(f(u_h) - g \right) \phi_i d\Omega = 0. \tag{4.46}$$

The basis functions ψ and test functions ϕ may in principle be two different functions. However, it is often convenient to define $\psi_i = \phi_i$ to simplify the discretisation of the equations. The FE method in which the weighting functions are defined such that $\psi_i = \phi_i$ is called the (continuous) Galerkin finite element method.

4.3.2 Discretising the Shallow Water Equations

The shallow water equations are a set of partial differential equations which vary in both time and space. Temporal discretisation in TELEMAC-2D is achieved using a first-order forward differencing finite difference scheme where:

$$\frac{\partial f}{\partial t} = \frac{f^{n+1} - f^n}{\Delta t}, \tag{4.47}$$

where Δt is the time step, f^n is the function value at the current (n^{th}) time step, and f^{n+1} is the function value at the $n + 1^{\text{st}}$ time step. The accuracy of the finite differencing approach can be improved by using the method of fractional steps, in which the function $\tilde{f}$ is assessed at intermediate positions between n and $n + 1$ to develop an improved approximation to the function gradient. The fractional step method requires discretisation of the other terms of the equation at the same moment in time as the fractional step, which is not always possible with the advection terms. Temporal discretisation becomes the process of solving:

$$\frac{\tilde{f} - f^n}{\Delta t} + \text{advection terms} = 0, \tag{4.48}$$

$$\frac{f^{n+1} - \tilde{f}}{\Delta t} + \text{other terms} = 0. \tag{4.49}$$

Such a discretisation scheme is described as semi-implicit, and for numerical stability the function f is expressed as:

$$f = \theta f^{n+1} + (1-\theta) f^{n}, \tag{4.50}$$

where θ is a parameter, usually $\theta = 0.5$, chosen to ensure stability of the numerical solution in TELEMAC (Hervouet, 2007). Temporal discretisation of Equation (4.25) leads to:

$$\frac{\xi^{n+1} - \xi^{n}}{\Delta t} + \frac{\partial \left(\theta \bar{U_k}^{n+1} + (1-\theta)\bar{U}_k^{n}\right)\left(\theta h^{n+1} + (1-\theta)\, h^{n}\right)}{\partial x_k} = 0. \tag{4.51}$$

In the momentum equations it is necessary to introduce f'^{n+1} as an estimate of f^{n+1} for quantities in which the value f^{n+1} is required during a fractional step sub-iteration. Within a fractional step f'^{n+1} is equal to f^{n} before the sub-iterations are carried out, and then f^{n+1} as determined in the previous sub-iterations. Denoting $f^{*} = (\theta f^{n+1} + (1-\theta)\, f^{n})$ and $f^{\dagger} = (\theta f'^{n+1} + (1-\theta)\, f^{n})$, the momentum equations are temporally discretised as:

$$\frac{\bar{U}_k^{n+1} - \bar{U}_k^{n}}{\Delta t} + \frac{\partial \bar{U}_k^{*} \bar{U}_l^{*} h^{*}}{\partial x_l} + \frac{\partial \overline{U_k'^{*} U_l'^{*} h^{*}}}{\partial x_l} = F_{da,k} - g h^{\dagger} \frac{\partial \xi^{*}}{\partial x_k} - \frac{\tau_{b,k}}{\rho} \tag{4.52}$$

Spatial discretisation is achieved using the Galerkin finite element method, in which a function f is discretised as:

$$f = \sum_{i=1}^{m} f_i \phi_i, \tag{4.53}$$

where m is the number of discretisation points, f_i is the function value at point i, and ϕ_i is the Galerkin weighting function associated with that point. The equations are

multiplied by the test function and integrated over the domain. For the continuity equation this yields:

$$\int_\Omega \left(\frac{\xi^{n+1} - \xi^n}{\Delta t} \right) \phi_i^n d\Omega + \int_\Omega \left(\frac{\partial \bar{U}_k^* h^*}{\partial x_k} \right) \phi_i^n d\Omega = 0. \tag{4.54}$$

The impermeability boundary conditions are found by using the chain rule on the second term and integrating the velocity derivative component by parts:

$$\int_\Omega \left(h^\dagger \frac{\partial \bar{U}_k^*}{\partial x_k} \right) \phi_i^n d\Omega = \int_\Gamma h^\dagger \bar{U}_k^* \phi_i^n d\Gamma - \int_\Omega \bar{U}_k^* \frac{\partial h^\dagger \phi_i^n}{\partial x_k} d\Omega. \tag{4.55}$$

The flux across the boundary Γ must be zero if the boundary is solid, otherwise the flux across the boundary must be calculated as a boundary condition.

The number of degrees of freedom in the vertical and horizontal directions may vary, so that the decompositions of h and $\bar{U}_k$ may be expressed as:

$$h = \sum_{i=1}^{N_h} h_i \phi_i^h \quad \text{and} \quad \bar{U}_k = \sum_{i=1}^{N_U} \bar{U}_{k,i} \phi_i^U. \tag{4.56}$$

After this decomposition, the continuity equation becomes:

$$\begin{aligned} \sum_{j=1}^{N_h} \frac{(\xi^{n+1} - \xi^n)}{\Delta t} \int_\Omega \phi_i^h \phi_j^h d\Omega + \sum_{j=1}^{N_h} h_j \int_\Omega \bar{U}_k^\dagger \frac{\partial \phi_j^h}{\partial x_k} \phi_i^h d\Omega \\ + \int_\Gamma h^\dagger \bar{U}_k^* \phi_i^h d\Gamma - \sum_{j=1}^{N_U} \bar{U}_k^* \int_\Omega \phi_j^U \frac{\partial h^\dagger \phi_i^h}{\partial x_k} d\Omega = 0. \end{aligned} \tag{4.57}$$

The momentum equations are similarly multiplied by ϕ_i and integrated over the

domain. After decomposition of the depth and velocity variables, this becomes:

$$\sum_{j=1}^{N_U} \frac{\bar{U}_{k,j}^{n+1} - \bar{U}_{k,j}^{n}}{\Delta t} \int_\Omega \phi_j^U \phi_i^U d\Omega + \sum_{j=1}^{N_U} \bar{U}_{k,j}^* \bar{U}_{l,j}^* \int_\Omega h^\dagger \frac{\partial \phi_j^U}{\partial x_l} \phi_i^U d\Omega$$
$$+ \sum_{j=1}^{N_U} \overline{{U'_{k,j}}^* {U'_{l,j}}^*} \int_\Omega h^\dagger \frac{\partial \phi_j^U}{\partial x_l} \phi_i^U d\Omega = \int_\Omega F_{da,k} \phi_i^U d\Omega \qquad (4.58)$$
$$- \sum_{j=1}^{N_h} g h^\dagger \xi_j \int_\Omega \frac{\partial \phi_j^h}{\partial x_k} \phi_i^U d\Omega - \int_\Omega \frac{\tau_{b,k}}{\rho} \phi_i^U d\Omega.$$

As the weighting functions are known, allowing the integrals to be evaluated as coefficients of a mass matrix:

$$M_{i,j} = \int_\Omega \phi_i \phi_j d\Omega \text{ etc}, \qquad (4.59)$$

which enables the continuity and momentum equations to be expressed in the form of $AX = B$, where the matrix A is made of combinations of the mass matrices M and X is a vector comprised of ξ and $\bar{U}_k$. The final form of the linear system of equations depends on the turbulence closure model used to eliminate the $\overline{U'_k U'_l}$ term which remains unknown in the equations presented above, and the treatment of the semi-implicit time discretisation parameter θ. Further details can be found in Hervouet (2007). A number of options for resolving the turbulent stress term exist in the TELEMAC system, and are briefly summarised in the following section.

4.4 Turbulence Closure Models

Elimination of the turbulent stress term, $\overline{U'_k U'_l}$, is achieved usually with the Boussinesq approximation, discussed in Section 4.1.4, in which the turbulent stress is written in terms of the shear in the mean velocities, multiplied by a turbulent viscosity parameter. The turbulent viscosity parameter is modelled on the hypothesis of isotropic

turbulence in the flow, and a range of models exist to close the problem. The most common turbulence closure models for the RANS equations may be classified as zero, one, or two equations models, which seek to determine the magnitude of the turbulence eddy viscosity. Several alternative models exist, such as Smagorinksy's large eddy models (Hervouet, 2007), and Reynolds stress models. Both provide an alternative formulation of the Navier-Stokes equations which avoids the use of the Boussinesq hypothesis, but required increased computational effort. Turbulence closures to the RANS equations are less accurate, but with correctly calibrated parameters, it is possible to get reasonably accurate approximations to a turbulent flow.

4.4.1 Zero Equation Models

Zero-equation models are the simplest form of eddy viscosity model and assume that the viscosity is constant or directly dependent on known or easily calculable parameters. A common approach in large domains is to assume a constant turbulent viscosity parameter, although the magnitude of this parameter varies significantly between sites, with documented values ranging from 0.12ms^{-1} in the Mackenzie River, to 1500ms^{-1} in the Missouri River (Fischer, 1979).

The first zero-equation model was proposed by Prandtl (1925), which proposed an algebraic relationship between the turbulent viscosity and the mixing length, and has since been widely applied to parameterise turbulence. TELEMAC-2D implements the Elder model, in which longitudinal and transverse diffusion coefficients are proposed, and related to the eddy viscosity simply through the mean shear velocity in the flow (Hervouet, 2007). Zero-equation models are popular, but do not explain the relationship between turbulent energy production, convection, or dissipation, giving rise to more complicated models. Zero equation models are easy to implement and quick to compute, but are inadequate for describing flows in which the turbulent length scales vary.

4.4.2 One Equation Models

Prandtl (1945) recognised the need to include previous flow history in the turbulent viscosity by introducing a transport equation for the turbulent kinetic energy, modelling its production, convection, diffusion, and dissipation. The one-equation model more accurately reflects the spatially varying nature of turbulence rather than simply assuming that the eddy viscosity is constant throughout the flow (Rodi, 1980). However, one equation models do not perform well in free shear flows or cases of decaying turbulence.

4.4.3 Two Equation Models

Many two equation turbulence models have been proposed for the RANS equations, comprised of two transport equations, one for the turbulent kinetic energy and another for the turbulent length scale or an equivalent parameter. Local production and dissipation of the turbulent kinetic energy are assumed to be approximately equal, implying that turbulent and mean flow quantities are locally proportional at any point in the flow (Celik, 1999). A key advantage of the two-equation models over the zero- and one-equation models is that it is not necessary to know the turbulent structure of a flow *a priori*. A large number of two-equation turbulence models have been proposed, including the $k - \epsilon$ model, in which ϵ represents the dissipation and destruction of turbulent kinetic energy, and the $k - \omega$ model, in which ω describes only the dissipation of turbulent kinetic energy (Cebeci, 2004). However, the $k - \epsilon$ model is the only two-equation turbulence model implemented in TELEMAC-2D. Although the turbulence closures to the RANS equations are less accurate than DNS or LES, there are significant computational savings achieved by solving the RANS equations, and, with correctly calibrated parameters, it is possible to get reasonably accurate approximations to a turbulent flow.

4.5 Conclusions

The formulation of the Navier-Stokes equations and the derivation of the shallow water equations has been outlined. The shallow water equations are an important tool for determining the power potential of turbine arrays, as they offer a computationally feasible method of simulating a large number of turbines and the surrounding environment. However, the assumptions made during the derivation of the equations means that depth-averaged simulations of tidal turbines are more restrictive than three dimensional Navier-Stokes simulations. In particular, there are limitations on the flow regimes which can be simulated, as hydraulic jumps, for example, cannot be accurately represented in the shallow water equations. Furthermore, the empirical relationships used to close the shallow water equations, by providing approximations to the shear and turbulent stresses in the flow, may not be appropriate when tidal turbines are operating and significantly affecting the shear profile in the flow.

The challenges that face tidal turbine modelling arising from the derivation of the shallow water equations can be broadly categorised into two main areas: the first being the role of turbulent mixing in the flow, in particular in the vicinity of the turbines, and the second being the representation of three dimensional turbines in a two dimensional simulation. The first of these challenges shall be addressed in Chapter 5, and the second in Chapter 6.

Chapter 5

Turbulence in the Shallow Water Equations

Big whorls have little whorls
That feed on their velocity,
And little whorls have littler whorls
And so on to viscosity.
- Lewis F. Richardson

Turbulence is an important dissipative and diffusive phenomenon in many flows which is responsible for the transfer of energy from the mean flow to the turbulent cascade, where energy is eventually degraded to heat. Although turbulence is a fundamentally three-dimensional process, in some flows with much greater horizontal extent than vertical depth the turbulent dynamics may be approximated as being two-dimensional. Turbulence behaves differently in two- and three-dimensional flows, and this chapter begins by comparing the two types of turbulence and their physics. The dynamics of two-dimensional turbulence have not been widely considered in the context of simulating tidal arrays. A two-dimensional turbulence model for steady turbulence in which the production, convection, and destruction of turbulence are in equilibrium, is proposed based on the coherent structures, or turbulent eddies, that are observed in turbulent flows. The chapter concludes with a discussion of the modelling implications of a depth-averaged eddy turbulence model.

5.1 Introduction

Turbulence is a largely chaotic state that describes many fluid flows and results in interactions and the transfer of energy between a wide range of scales in the flow. It is characterised by the Reynolds number, the ratio between non-linear inertial forces, responsible for flow instability, and linear viscous forces, responsible for dissipative damping and stabilisation of the flow. Fully developed turbulent flow occurs at high Reynolds numbers, $Re = \mathcal{O}(10^7)$ in aeronautics, and $Re = \mathcal{O}(10^{10})$ in oceanographic flows. Flows which are highly turbulent are typically characterised by large velocities, which give rise to strong advection, large turbulent length scales due to the domain size, or low viscosity, corresponding to weak dissipation of energy in the fluid (Farge *et al.*, 1999). Although the transport processes which drive turbulence are understood - the Navier-Stokes equations are an exact set of equations that apply to turbulent fluids - the nature of turbulence is so strongly dependent on boundary and initial conditions that it makes all but the simplest problems intractable (Rodi, 1980). Matters are further complicated by the lack of certainty about the existence and uniqueness of solutions of the Navier-Stokes equations when non-linear advection becomes dominant, as it does in highly turbulent flows (Farge *et al.*, 1999).

5.1.1 Characteristics of Turbulence

The particular features of a flow that makes it turbulent are hard to define, although such flows can be broadly described as including diffusive, dissipative, irregular continuum flows which have higher Reynolds numbers (Tennekes and Lumley, 1972). The irregularity of turbulent flows makes deterministic approaches for their understanding difficult, and leads instead to the use of statistical methods for spatially- or temporally-averaged representations of the flows. Turbulent flows are strongly diffusive and tend to promote rapid transfer of momentum, heat and mass. Turbulent

flows are also dissipative, and the viscous shear stresses that are generated increase the dissipation of turbulent kinetic energy. Another key feature of turbulent flows is that turbulence is a continuum phenomenon, dependent on the flow, rather than a property of a particular class of fluids, and thus turbulence is strongly affected by boundary and initial conditions. Analytic understanding of turbulence is made difficult as the time dependence of an averaged quantity in the Navier-Stokes equations cannot be described by a finite number of differential equations as a result of the non-linearity of the convective term (Batchelor, 1969).

Turbulence is often described in terms of eddies, or vortical structures, which correspond to the swirling structures often seen in turbulent flows. The eddies can be parameterised in terms of their length scale, l, velocity scale, u, and time scale, $\frac{l}{u}$. The eddies possess kinetic energy, and one feature of turbulent flows is that the turbulent kinetic energy exists over a wide range of spatial scales. Kolmogorov (1941a) proposed an energy spectrum scaling in the dissipation range of $k^{\frac{-5}{3}}$ where k is the wave number of a turbulent fluctuation:

$$E(k) = C\epsilon^{\frac{2}{3}}k^{\frac{-5}{3}}, \tag{5.1}$$

where C is the Kolmogorov constant. Conceptualising turbulent flows as consisting of eddies or vortex filaments led to the description of the energy cascade as the result of the vortex filaments being stretched, carrying turbulent kinetic energy to smaller scales. Kolmogorov (1941b) hypothesised that the average energy dissipation rate, $\langle\epsilon\rangle$, is independent of the fluid viscosity ν when the viscosity is small, and that small scale fluctuations at high Reynolds numbers are statistically independent of the large scales, and are locally homogeneous, isotropic and steady. These assumptions have been shown to be reasonably satisfactory within the limits given by the theory (Sreenivasan and Antonia, 1997).

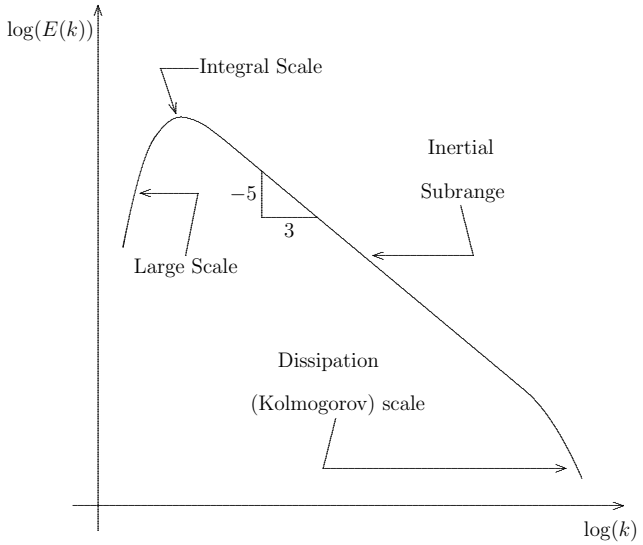

Figure 5.1: Diagram showing the turbulent energy cascade and turbulent length scales

Figure 5.1 shows how the energy spectrum results in a transfer of energy from the largest scales, through Kolmogorov's $\frac{-5}{3}$ power law cascade, to the dissipation scales where the turbulent kinetic energy is finally dissipated as heat. The largest scale of turbulent flows, based on the scale of the flow domain, contains most of the turbulent energy and therefore dominates momentum, mass and heat transfer. The integral scale is defined to be $\mathcal{O}(10^{-1})$ (often taken to be ≈ 0.2) of the largest scale, and is an important region in the turbulent energy cascade due to its relationship with the scale at which the turbulence is forced. The energy at the integral scale cascades through the inertial scale with a $\frac{-5}{3}$ power law to the dissipation scale, where the turbulent kinetic energy is finally dissipated as heat. In the limit $Re \to \infty$ ($\nu \to 0$), three-dimensional turbulence becomes independent of the viscosity and the initial conditions of the flow, and is driven entirely by the rate at which energy is transferred from the slower large eddies to the smallest eddies in the flow.

A strain rate field is required to sustain a turbulent flow. Eddies in a strain rate field undergo stretching, destroying the eddies and forming smaller ones, which eventually leads to viscous dissipation at the smallest scales. The energy cascade is driven by the vortex stretching process and results in large eddies, which are strongly

dependent on flow domain properties, being turned into progressively smaller eddies which become increasingly homogeneous and domain-independent. The difference between the smallest and largest scales increases as the flow becomes more turbulent, making it very computationally expensive to resolve all the turbulent fluctuations in a high Reynolds number flow. This necessitates the use of turbulence models to reduce the complexity of the problem and make it more tractable.

5.1.2 Two-dimensional Turbulence

Under certain conditions some aspects of a flow may be regarded as almost two-dimensional, such as those flows which are described by the shallow water equations. In such flows, the horizontal dimensions are usually much larger than the vertical dimension, and large-scale turbulence may therefore be described to a good approximation as behaving as if it were two-dimensional. Turbulent processes are fundamentally three-dimensional, and thus the small-scale turbulence within these flows is still three-dimensional. Two-dimensional turbulence is therefore necessarily locally anisotropic (but may still be homogeneous), in contrast to the common assumption in three-dimensional turbulence modelling of homogeneous isotropic turbulence. Furthermore, the nature of turbulent processes ensures that the small and large scales of the flow interact. Thus, although influenced by the dynamics of the small-scale, turbulence in two dimensions is dominated by large-scale eddies in the flow (Davidson, 2004).

The two basic properties of turbulence, randomness and non-linearity, are present in both two- and three-dimensional turbulence. However, two-dimensional turbulence contrasts with the behaviour of three-dimensional turbulence described above in a number of ways, the key differences being an *inverse* cascade of energy from the smaller scales to the larger scales (Fjørtoft, 1953), the near conservation of energy in a two-dimensional turbulent flow (Batchelor, 1969), and the persistence of coherent

structures in the flow (Oetzel and Vallis, 1997; Davidson, 2004).

Two-dimensional turbulence may be described in terms of two quadratic invariants, the kinetic energy, K, and the enstrophy, Z (Iwayama *et al.*, 2002). Denoting the flow velocity $\mathbf{u}(x)$ and angle brackets to define a spatial average, the kinetic energy may be defined as:

$$\mathsf{K} = \frac{1}{2}\langle \mathbf{u}(x) \cdot \mathbf{u}(x) \rangle, \tag{5.2}$$

and, denoting the vorticity as ω, the enstrophy is defined as:

$$\mathsf{Z} = \frac{1}{2}\langle \omega(x)^2 \rangle. \tag{5.3}$$

Assuming that the kinetic energy is the unique invariant describing a two-dimensional flow and that the turbulent eddies were self-similar, Batchelor (1969) found that two-dimensional turbulence exhibited a dual cascade phenomenon, in which there was an *inverse* cascade of kinetic energy and a direct cascade of the enstrophy. Batchelor determined a k^{-3} scaling for the enstrophy decay, which does not agree very well to that observed in three-dimensional flows, where the scaling k^{-n} where n is slightly greater than 3 (Davidson, 2004). In the limit $Re \to \infty$, it was found that the dissipation of $\mathsf{K} \approx 0$, and the dissipation of Z remains finite. The conservation of kinetic energy in two-dimensional turbulence is in stark contrast to that observed in three-dimensional where the dissipation of K is finite and of order $\frac{u^3}{l}$ for $Re \to \infty$ (Davidson, 2004). In conventional three-dimensional turbulence, the vortex filamentation process intensifies the small scale vorticity, increasing viscous dissipation at the Kolmogorov scales. The dissipation of energy in three dimensions is therefore driven by the rate at which the large scale eddies break up (Davidson, 2004). In two-dimensional turbulence, on the other hand, the invariance of the vorticity means that the vortex filamentation process does not lead to an increase in overall vorticity and is instead fixed by the initial conditions of the flow (Batchelor, 1969).

One feature of two-dimensional flows that Batchelor did not fully appreciate was the role of persistent coherent structures (vortices) which formed in two-dimensional turbulent flows (Kraichnan and Montgomery, 1980). Coherent vortices are distinct from turbulent eddies as the eddy turnover time for a coherent structure is much larger than $\frac{l}{u}$. Rather than being stretched through the filamentation process described for turbulent vortex filaments, coherent vortices interact with each other as a collection of point vortices (Davidson, 2004). The coherent structures emerge in the flow from the randomness in the flow field in the initial conditions and grow through the merging of like-signed vortices. Thus, over a long period of time the number of coherent vortices reduces, they grow large in size, and may come to dominate the flow after a long period of time if they are of sufficient strength relative to the background straining field that develops in the flow (Oetzel and Vallis, 1997). The coherent vortices thus represent the largest spatial scales of the system, and are driven through the inverse cascade of energy from the intermediate scales in the flow, giving rise to the description of two-dimensional turbulence as a self-organising system (Kraichnan and Montgomery, 1980).

The dual cascade of turbulent energy in two-dimensions means that the standard diagram of the distribution of turbulent energy with respect to wave number in three-dimensions in Figure 5.1 does not fully represent the distribution of energy in a two-dimensional flow. Instead, both a $-\frac{5}{3}$ range and a -3 range exist in two-dimensional turbulence, although the exact coefficients for energy and enstrophy transfer in these ranges are less well established than for three-dimensional turbulence (Kraichnan, 1971). The dual cascade of two-dimensional turbulence is shown in Figure 5.2. If energy and enstrophy enter the dual cascade over the wave number range $(k_2^{\mathsf{K}}, k_1^{\mathsf{Z}})$, where $k_2^{\mathsf{K}} \approx k_1^{\mathsf{Z}}$, the energy and enstrophy inertial ranges can be defined as $[k_1^{\mathsf{K}}, k_2^{\mathsf{K}}]$ and $[k_1^{\mathsf{Z}}, k_2^{\mathsf{Z}}]$ respectively. The smallest wave number in the domain, $k_{\min}$, is $k_{\min} = 1$, or $k_{\min} = 0$ if the domain is unbounded and hence large scale dissipation is not necessary.

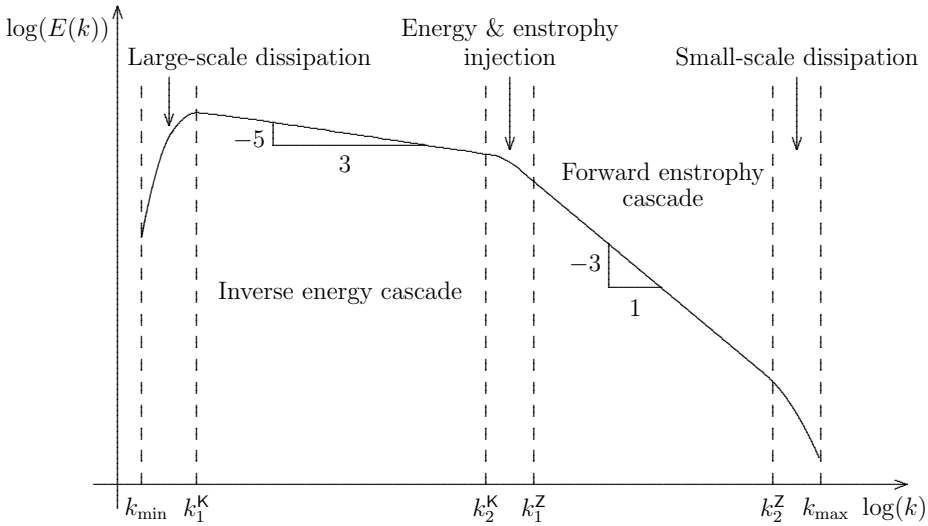

Figure 5.2: Diagram showing the dual energy and enstrophy cascade and wave number for two-dimensional turbulence. Energy and enstrophy are injected in the range $(k_2^{\mathsf{K}}, k_1^{\mathsf{Z}})$. Adapted from Farazmand *et al.* (2011).

The largest wave number in the domain, $k_{\max}$, corresponds to the Kolmogorov scale and depends on the resolution of the model and the Reynolds number of the flow.

A further difference between two- and three-dimensional flows is that molecular viscosity does not exist in a strictly two-dimensional flow (Dorfman and Cohen, 1970), which leads to a breakdown in the eddy-viscosity representation of turbulence presented in Section 4.4 (Kraichnan, 1976). This breakdown, in addition to the dual energy and enstrophy cascade, means that turbulence modelling in shallow water flows, in particular where energy and enstrophy are injected into the turbulent cascade at some intermediate wave number, requires particular attention.

5.2 Turbulence Modelling in Numerical Simulations

It is computationally challenging to solve completely all motions within a turbulent flow, as the interaction of the vortex filaments in the flow generates rapid velocity variations at unpredictable regions in the fluid, requiring fine numerical resolution to

represent fully the entire range of length scales in the flow (Batchelor, 1969). This has led to the development of a range of approaches for simulating turbulent flows. These approaches broadly fall into three categories; RANS turbulence models, direct numerical simulations, and large eddy simulations. The zero-, one-, and two-equation models for the RANS equations presented in Section 4.4 have been widely used in both three-dimensional and two-dimensional simulations. However, as discussed above, the eddy viscosity approximation is not always an appropriate approach for modelling turbulence, so some alternative approaches, firstly for three-dimensional, and then two-dimensional simulations, are summarised below.

The most computationally intensive method of simulating three-dimensional flows are Direct Numerical Simulations (DNS) of the Navier-Stokes equations, where all the turbulent motions are explicitly resolved in the simulation. The success of DNS depends on knowledge of the smallest length scales to be simulated, which may be obtained through Kolmogorov's theories presented in Section 5.1.1. DNS studies require very fine grid resolution, which is a limiting factor in the use of DNS in large, highly turbulent three-dimensional flows. Nieuwstadt (1990) demonstrate that a further challenge with DNS is that the number of grid points N required to capture all the motions in a flow scales as:

$$N \approx Re^{\frac{9}{4}}, \tag{5.4}$$

where doubling the Reynolds number requires the grid resolution to be increased by a factor of 4.76. The substantial computational requirements of DNS has limited the technique's use in fully turbulent flows and large domains, with the limit of recent computational facilities having allowed resolutions of 4096^3 at Reynolds numbers of 10^5 (Ecke, 2005). These limits are generally too restrictive for coastal modelling, and therefore sub-grid turbulence models are required.

One approach to reduce the computational demand of simulating a turbulent flow is to filter the turbulent motions so that the finest turbulent motions, which are responsible for the expensive resolution requirements of DNS at high Reynolds numbers, are not directly simulated and the effect that they have on the simulated flow is modelled in a sub-grid turbulence model instead. This class of simulations is known as Large Eddy Simulations (LES), first proposed by Smagorinsky (1963). Smagorinsky related sub-grid scale turbulent eddies to the strain rate through:

$$\tau_{ij} = \frac{1}{3}\tau_{kk}\delta_{ij} - 2\nu_T \bar{S}_{ij}, \tag{5.5}$$

where the isotropic part of the equation, τ_{kk} is usually incorporated with the pressure term, ν_T is the eddy viscosity, and $\bar{S}_{ij}$ is the strain rate tensor of the filtered velocity field. The eddy viscosity is expressed as:

$$\nu_T = (c_s\Delta)^2|\bar{S}|, \tag{5.6}$$

where c_s is the Smagorinsky constant, Δ is the grid size and $\bar{S} = \sqrt{\bar{S}_{ij}\bar{S}_{ij}}$. Large eddies are affected by the boundary and initial conditions, whereas the small scale turbulent fluctuations are believed to be homogeneous and isotropic, and therefore independent of the anisotropy and heterogeneity of the large eddies. The Smagorinsky constant is hypothesised to reflect this universality of the sub-grid scale eddies. However, different researchers have determined a number of different values for the constant, suggesting that there may be some additional physics in small scale turbulence (Zhai *et al.*, 2007).

Large eddy simulations may also be undertaken for depth-averaged flows, although the sub-grid scale model is different to that for three-dimensional flows on account of the differences between two- and three-dimensional turbulence. One consequence of depth-integration is that the smallest physically meaningful length-scale in the model

is the depth h, and horizontal resolution $\Delta x \leq h$ has little physical meaning (although may be required for numerical stability). Madsen *et al.* (1988) identified that this gives rise to four different scales of filtering in depth-averaged LES. The smallest of these scales was the filtering of random molecular motion, which gives rise to molecular diffusion and is parametrised with the molecular viscosity. The second smallest scale, common to both two- and three-dimensional simulations, was the filtering of turbulent motion below a given, unresolved, scale related to the numerical mesh, which gives rise to the turbulent diffusion modelled with an eddy viscosity parameter. The second-largest scale was the depth-average filter, which filters the vertical velocity profile, and leads to the introduction of dispersion, bed shear stresses, and horizontal shear stresses. The final, and largest scale was the horizontal averaging over a cell of size Δx, which introduces additional dispersion and eddies into the simulation.

The largest scales are unique to depth-averaged models and are generally accepted to be the most significant of the scales (Hinterberger *et al.*, 2007). Modelling depth-averaged turbulence is challenging because the sub-grid turbulence is no longer isotropic nor in equilibrium, as is often assumed in three dimensional LES (Nadaoka and Yagi, 1998). Computing the sub-grid scale turbulence requires the parametrisation of the characteristic length scale of the sub-grid turbulence, l_D, defined by Nadaoka and Yagi (1998) as:

$$l_D = \alpha h \quad (\alpha < 1), \tag{5.7}$$

where α is a parameter relating the characteristic sub-grid turbulence length scale to the depth. The relationship between l_D and the water depth is one of the key features of two-dimensional turbulence, as the size of the largest sub-grid eddies is constrained by the depth of the flow. The value of α is influenced by factors such as the velocity shear profile and requires detailed knowledge about the state of the

turbulence in the flow. Nadaoka and Yagi suggest that $\alpha = 0.067$ may often be appropriate, although they note that general approaches to estimate α have yet to be developed. The characteristic turbulent length scale is used to parameterise the eddy viscosity and energy dissipation rate in the model in a similar approach to that for three-dimensional LES.

5.2.1 Turbulence Models in Tidal Simulations

Two scales of flow may be identified in relation to tidal turbine arrays, as introduced in Chapter 3. The turbine-scale flow events and mixing occur close to the tidal devices and are characterised by a length scale on the order of the diameter of the tidal device. Array-scale flow events and mixing occur over much larger spatial and temporal scales, and are characterised by a length scale on the order of the array width. As the array width is typically much larger than the depth of the flow, array-scale flow events are predominantly two-dimensional, whereas turbine-scale flow events, characterised by the device diameter which is less than the water depth, are three-dimensional. As discussed in the previous section, the turbulence models used in two- and three-dimensional simulations of tidal arrays should be different in order to reflect the different turbulent phenomena in the different flows.

A common simplifying assumption made in numerical simulations of turbine arrays is that the array spans the width of the channel, allowing the array-scale bypass to be neglected and thereby allowing the simulation to be simplified to a single turbine or small group of turbines. It is then feasible to analyse a single tidal device using a high resolution three-dimensional simulation to study the evolution of the turbine-scale wake. Three-dimensional RANS simulations with a $k - \epsilon$ turbulence model closure have been widely used to simulate individual or small groups of turbines. A staggered array of seven turbines was studied by Bai *et al.* (2009), which required 500,000 elements in a domain with a central symmetry boundary condition, such that

it was only necessary to simulate half the domain. Turnock *et al.* (2011) studied a single turbine in a range of inter-turbine spacing configurations, and comment that satisfactory convergence of the solution for the flow requires at least six million cells, with at least 40% of those within the turbine wake. Bai *et al.* (2013) followed the work of Turnock et al. to study staggered pairs of turbines in a domain with symmetry boundary conditions in order to simulate the array spanning the channel width. Large eddy simulations have also been used in three-dimensional studies of pairs of turbines. Churchfield *et al.* (2013) simulated staggered and non-staggered turbine arrangements in a domain with periodic boundary conditions. Approximately twelve million cells were required with a filter resolution of 0.5 metres, limiting the application of LES to small numbers of turbines and domains.

The computational expense of simulating a large number of turbines and the associated array-scale bypass flow necessitates the use of two-dimensional simulations. In contrast to three-dimensional simulations, grid resolution requirements in two-dimensional simulations are driven predominantly by the need to resolve bathymetric variations and the coastline rather than resolving fine turbulent fluctuations. Turbulence modelling is less well established in depth-averaged simulations, with a number of studies relying solely on dissipation within the numerical simulation to suppress turbulent fluctuations (see McCombes *et al.* (2009), Divett *et al.* (2011), Funke *et al.* (2014), for examples). The damping achieved in this manner is entirely dependent on the discretisation technique used on the governing equations, and conflicts with the general aim of using a discretisation scheme which introduces as little artificial dissipation to the system as possible. Two-dimensional simulations which explicitly include turbulence closure models tend to utilise simpler constant or zero-equation turbulence closure models, such as those employed by Ahmadian *et al.* (2012), Adcock *et al.* (2013), and Plew and Stevens (2013). An eddy-viscosity closure offers an inexpensive way of introducing a turbulence parameter which may be tuned to get the

desired eddy recirculation length in the wake of objects. A constant eddy viscosity, such as that used by Garrett and Greenberg (1977), A_H, is used to parameterise the horizontal mixing processes only, and therefore neglecting the contribution of vertical turbulent motions. Zu *et al.* (2007) use a value of $A_H = 100\text{m}^2\text{s}^{-1}$ to generate smooth solutions when simulating tidal dynamics in the South China Sea, whereas Hench and Luettich (2003) use $A_H = 7\text{m}^2\text{s}^{-1}$ for a shallow inlet, demonstrating the specificity of a single viscosity parameter to a given problem and its inability to yield further information about the turbulence.

Two-equation eddy viscosity models for two-dimensional flows have been formulated by analogy to the two-equation models for three-dimensional flows (Mellor and Yamada, 1982). The attractions of two-equation turbulence models are two-fold; firstly, they offer, with suitable constants, a reasonably accurate model of the effect of depth-averaged turbulence in a flow, and secondly, the two-equation models tend to model correctly the dissipation of small-scale turbulent energy if the large-scale turbulent eddies are correctly specified at the initial conditions. The second condition arises from the fact that small-scale eddies are independent of the boundary conditions that generate the anisotropic large-scale eddies, and therefore the small-scale eddies over time tend to become more accurately modelled. Two-equation RANS turbulence models show reasonable, but not completely satisfactory agreement with experiments (Jirka, 2001). Although experimental agreement is improved through the use of two-dimensional LES turbulence closures, the scheme has not been used as a turbulence closure model in the context of tidal turbine modelling.

Tidal flows are often highly turbulent. Tidal turbines, with a length scale that is a substantial fraction of the water depth but small compared to the horizontal extent of a large turbine array, will have an important effect on the turbulent dynamics of a tidal flow. Existing turbulence closure models can be, and have been, employed in three-dimensional simulations of small numbers of tidal turbines to incorporate the

effects of turbulence on the turbine-scale flow around the turbines. Two-dimensional turbulence is less well understood, and the two-dimensional turbulence closure models that have been employed in simulations of tidal turbine arrays have not fully reflected the dynamics of two-dimensional turbulence in the context of tidal turbines, borrowing instead from oceanographic models. In the remainder of this chapter, a two-dimensional turbulence closure model is proposed for depth-averaged tidal turbine simulations.

5.3 Turbulent Eddy Model

Turbulent phenomena are characterised by four key stages; generation, advection, cascade, and the final dissipation of turbulent kinetic energy. Simulation of the complete spectrum of turbulent processes in a flow requires computationally expensive direct numerical simulations, and these are limited to Reynolds numbers that are often lower than those of interest in tidal flows. Turbulence models are required to characterise some of the effects that the different stages of turbulence have on the mean flow below the spatial (LES) or temporal (RANS) scales that are resolved within the numerical model. In this section a turbulence model is proposed based on two-dimensional turbulence theory to parameterise the effect of the unresolved turbulence on the mean flow simulated in depth-averaged simulations.

5.3.1 Derivation of the Turbulent Eddy Model

A large part of the turbulent kinetic energy in turbulent flows is contained in discernible, self-sustaining structures, or eddies (Albukrek *et al.*, 2002). These eddies remove energy and enstrophy from the mean flow and transfer it, through the dual turbulent cascade, to the scales where it is finally dissipated, as was illustrated in Figure 5.2. It is assumed for the majority of this process, the eddies are self-similar, and

that the energy in the system approximately follows the $\frac{-5}{3}$ and -3 power law scaling ratios with wavelength that has been analytically established for two-dimensional turbulence. For the purposes of simplicity, it is further assumed that the transfer of energy through the turbulent cascade is steady and therefore that the mechanism by which momentum and energy are transferred across different turbulent scales does not need to be explicitly modelled.

The shallow water equations were derived in Chapter 4 through the Reynolds averaging and subsequent depth-averaging of the Navier-Stokes equations. The resulting two-dimensional flow field is described in terms of a velocity time averaged over a sufficiently long period T to allow turbulent fluctuations to be neglected over the depth of the flow and further averaged over the depth of the flow. The depth- and time-averaged Reynolds stress term is:

$$\frac{\partial \overline{U_k' U_l'} h}{\partial x_l}, \tag{5.8}$$

an expression for which must be found in order to close the system of equations. As the Reynolds averaging process yields a mean velocity field devoid of turbulent fluctuations, the turbulent fluctuations in the Reynolds stress term are assumed in this model to produce a fluctuating velocity field that is superimposed on the mean velocity field. At any point in the flow domain the fluctuation field has a time average of zero over the period T.

A hypothetical eddy with diameter L and velocity components U' and V' is shown in Figure 5.3. The velocity components are normalised against $|U'|_{max}$ and $|V'|_{max}$ respectively in order to highlight the contribution each component of the eddy makes to the velocity fluctuations. The eddies tessellate with neighbouring eddies to produce, in the absence of flow boundaries, an infinite field of eddies of different sizes. The eddy is hypothesised to have a constant angular velocity, so that the rotational

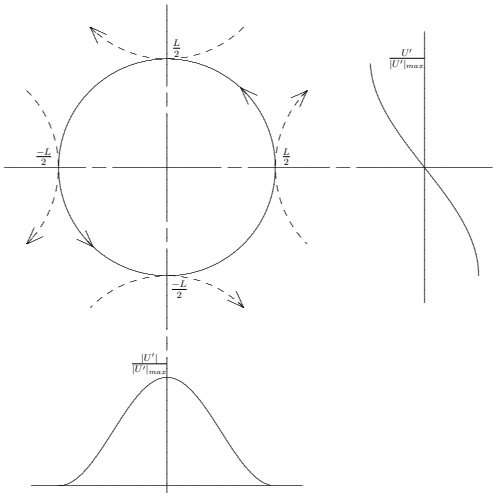

(a) Diagram of normalised velocity $\frac{U'}{|U'|_{max}}$ and normalised magnitude $\frac{|U'|}{|U'|_{max}}$ for a turbulent eddy.

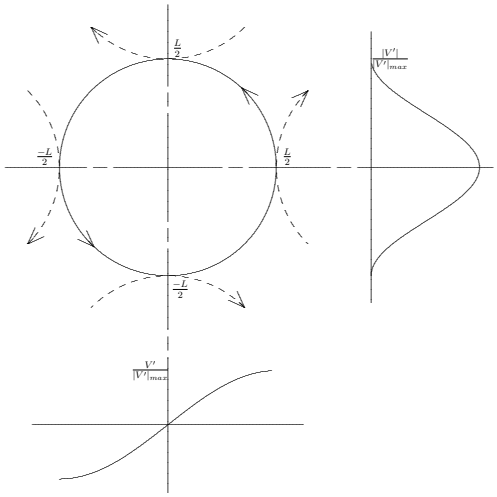

(b) Diagram of normalised velocity $\frac{V'}{|V'|_{max}}$ and normalised magnitude $\frac{|V'|}{|V'|_{max}}$ for a turbulent eddy.

Figure 5.3: Normalised velocity and magnitude components of a turbulent eddy with diameter L. The dashed arrows represent the rotation of neighbouring eddies.

velocity of the eddies is greatest at the perimeter and reduces towards the centre of the eddy. The angular velocity is an increasing function of turbulence intensity, such that stronger eddies are associated with higher levels of turbulence. This means that U' and V' are related through the rotation of the eddy, and therefore the correlation between the two fluctuations means that the time-average of the fluctuation product $\overline{U'_k U'_l}$ is not zero, satisfying the requirement originally introduced by Reynolds decomposition in Chapter 4. Turbulence is strongly affected by the boundary conditions of the domain, but these effects shall be neglected in the present study in order to preserve the generality of the analysis.

In the x-direction, the magnitude of velocity U' is maximum when $x = 0$ and zero when $x = \pm\frac{L}{2}$. This can be described as one cosine wavelength:

$$\frac{|U'|}{|U'|_{max}} = \frac{1}{2}\left(1 + \cos\left(\frac{2\pi x}{L}\right)\right). \tag{5.9}$$

The sign of the U' velocity of an anti-clockwise eddy is negative for positive y, the top

half of the eddy, and positive for negative y, the bottom half of the eddy, and reverses for a clockwise eddy. The sinusoidal variation of the sign of U' between $y = \frac{L}{2}$ and $y = \frac{-L}{2}$ occurs over half a wavelength, and the eddy sign has a period of two eddies in the x-direction:

$$\mathrm{sgn}(U') = \frac{-\sin\left(\frac{\pi y}{L}\right)\cos\left(\frac{\pi x}{L}\right)}{|\sin\left(\frac{\pi y}{L}\right)\cos\left(\frac{\pi x}{L}\right)|}. \tag{5.10}$$

The magnitude of the velocity V' is maximum at $y = 0$ and zero when $y = \pm\frac{L}{2}$ and can be described as one cosine wave:

$$\frac{|V'|}{|V'|_{max}} = \frac{1}{2}\left(1 + \cos\left(\frac{2\pi y}{L}\right)\right). \tag{5.11}$$

The sign of velocity of V' is positive for positive x and negative for negative x, and is a half sine wave between $x = \frac{-L}{2}$ and $x = \frac{L}{2}$ and has a period of two eddies in the y-direction:

$$\mathrm{sgn}(V') = \frac{\sin\left(\frac{\pi x}{L}\right)\cos\left(\frac{\pi y}{L}\right)}{|\sin\left(\frac{\pi x}{L}\right)\cos\left(\frac{\pi y}{L}\right)|}. \tag{5.12}$$

The turbulent eddies are convected downstream by the mean flow at speed $\bar{U}_\infty$. Averaged over a time T which is much longer than the turbulent time scale, the convection of turbulent eddies means that the time-average of the velocity fluctuations at any point in the flow is zero. The time dependence of U' and V' is the same, as they are both convected by the mean flow, therefore:

$$U'(t) = V'(t) = \cos\left(\frac{\bar{U}_\infty \pi t}{L}\right). \tag{5.13}$$

The magnitude of the eddy's tangential velocity is the root of the product of the magnitude of the velocities in the x- and y- directions:

$$\sqrt{U'^2 + V'^2} = \frac{1}{2}\sqrt{\left(1 + \cos\left(\frac{2\pi x}{L}\right)\right)^2 + \left(1 + \cos\left(\frac{2\pi y}{L}\right)\right)^2}. \tag{5.14}$$

Consistent with the constant angular velocity assumption of the turbulent eddies, the velocity is greatest at the edge of each eddy and decreases towards the centre of the eddies. Adjacent eddies therefore are contra-rotating, with the signs determined by the functions defined in Equations (5.10) and (5.12). It remains to find the amplitude of the eddies.

Assuming a single forcing at an intermediate scale, denoted L_f, at which energy and enstrophy enter the turbulent energy spectrum, enstrophy cascades from the forcing scale to higher wave numbers where it is eventually dissipated by molecular viscosity, and energy cascades from the forcing scale to lower wave numbers where it is eventually dissipated by large scale structures in the flow. Eddy size is bounded by the dimensions of the flow domain, and driven by the wave number at which forcing occurs. The angular velocity ω of an eddy shall be defined as a function of the free stream velocity U_∞ and the forcing length scale:

$$\omega = f\left(\frac{\bar{U}_\infty}{L_f}\right). \tag{5.15}$$

It is assumed that the angular velocity represents the turbulence intensity in the flow, and that the eddies are self-similar across the different length scales. Vigorous mixing occurs in more turbulent flows due to the turbulent eddies rotating more quickly. The tangential velocity of the eddies may be described as

$$U_i' = f\left(L\frac{\bar{U}_\infty}{L_f}\right), \tag{5.16}$$

where L is the length scale of the eddy. If, to the first order, the function f is linear in the free-stream velocity, then by introducing a coefficient $\lambda = f\left(\frac{L}{L_f}\right)$ the magnitude of the tangential velocity of the turbulent eddies is:

$$U_i' = \lambda\bar{U}_\infty. \tag{5.17}$$

The forward enstrophy cascade and the inverse energy cascades are considered separately, noting that the energy flux from the forcing is split roughly evenly between the two cascades (Chertkov *et al.*, 2007). Beginning with the forward enstrophy cascade, non-dimensionalising the turbulent kinetic energy and the wave number on those of the intermediate-scale forcing, the energy - wave number relationship in the inertial range of the forward cascade becomes:

$$\log\left(\frac{E(k)}{E(k_f)}\right) = -3\log\left(\frac{k}{k_f}\right), \tag{5.18}$$

where $_f$ denotes the wave number of the forcing. $E(k)$ is the average fluctuating kinetic energy per unit mass:

$$E(k) = \frac{1}{2}U_i'U_i'. \tag{5.19}$$

Substituting the turbulent kinetic energy and the eddy length scales into (5.18), it can be shown that:

$$\frac{U_i'U_i'}{U_{f,i}'U_{f,i}'} = \left(\frac{k}{k_f}\right)^{-3}. \tag{5.20}$$

The tangential velocity of the large eddy, $U_{f,i}'$ was given in (5.17), therefore the amplitude of the fluctuation velocity is calculated to be:

$$U_i'^{\mathsf{Z}} = U_{f,i}'\left(\frac{k}{k_f}\right)^{\frac{-3}{2}} = \lambda_f\bar{U}_\infty\left(\frac{k}{k_f}\right)^{\frac{-3}{2}}, \tag{5.21}$$

where the superscript Z is used to denote that the amplitude corresponds to the forward enstrophy cascade. The relationship is subject to the condition that $k > k_f$ in the forward enstrophy cascade.

Following the procedure for the forward enstrophy cascade, the energy - wave number relationship in the inertial range of the non-dimensionalised inverse cascade is given by:

$$\log\left(\frac{E(k)}{E(k_f)}\right) = \frac{-5}{3}\log\left(\frac{k}{k_f}\right). \tag{5.22}$$

Substituting for the definition of the turbulent kinetic energy per unit mass therefore gives:

$$\frac{U_i' U_i'}{U_{f,i}' U_{f,i}'} = \left(\frac{k}{k_f}\right)^{\frac{-5}{3}}, \tag{5.23}$$

and therefore the amplitude of the velocity fluctuations in the inverse energy cascade are given by:

$$U_i'^{\mathsf{K}} = U_{f,i}' \left(\frac{k}{k_f}\right)^{\frac{-5}{6}} = \lambda_f \bar{U}_\infty \left(\frac{k}{k_f}\right)^{\frac{-5}{6}}, \tag{5.24}$$

in which the superscript K denotes the inverse energy cascade. $k < k_f$ in the inverse energy cascade.

With expressions for the fluctuation amplitudes specified in Equations (5.21) and (5.24), Equations (5.10), (5.13), and (5.14) are combined to give expressions for the U' fluctuations due to turbulent eddies:

$$\begin{aligned} U' = &-\frac{1}{2} U_{\text{amp}}' \frac{\sin\left(\frac{\pi y}{L}\right)\cos\left(\frac{\pi x}{L}\right)}{|\sin\left(\frac{\pi y}{L}\right)\cos\left(\frac{\pi x}{L}\right)|} \\ &\frac{1}{2}\sqrt{\left(1+\cos\left(\frac{2\pi x}{L}\right)\right)^2 + \left(1+\cos\left(\frac{2\pi y}{L}\right)\right)^2}\cos\left(\frac{U_\infty \pi t}{L}\right). \end{aligned} \tag{5.25}$$

Similarly, the V' fluctuating velocity is found by combining Equations (5.12), (5.13), and (5.14):

$$\begin{aligned} V' = &\frac{1}{2} V_{\text{amp}}' \frac{\sin\left(\frac{\pi x}{L}\right)\cos\left(\frac{\pi y}{L}\right)}{|\sin\left(\frac{\pi x}{L}\right)\cos\left(\frac{\pi y}{L}\right)|} \\ &\frac{1}{2}\sqrt{\left(1+\cos\left(\frac{2\pi x}{L}\right)\right)^2 + \left(1+\cos\left(\frac{2\pi y}{L}\right)\right)^2}\cos\left(\frac{U_\infty \pi t}{L}\right). \end{aligned} \tag{5.26}$$

U_{amp}' and V_{amp}' are determined according to:

$$U_{\text{amp}}' = V_{\text{amp}}' = \begin{cases} \lambda_f \bar{U}_\infty \left(\frac{k}{k_f}\right)^{\frac{-5}{6}} & k < k_f \\ \lambda_f \bar{U}_\infty \left(\frac{k}{k_f}\right)^{-3} & k > k_f \end{cases} \tag{5.27}$$

The contribution that the Reynolds stress term $\overline{U_k' U_l'}$ makes to the steady shallow water equations requires some knowledge about the boundary conditions and forcing that the flow experiences. The steady shallow water equations are:

$$\frac{\partial \bar{U}_k \bar{U}_l h}{\partial x_l} + \frac{\partial \overline{U_k' U_l'} h}{\partial x_l} = F_{da,k} - gh\frac{\partial \xi}{\partial x_k} - \frac{\tau_{b,k}}{\rho}. \tag{5.28}$$

If they are to be significant in the shallow water equations, the turbulent stress terms must be of a similar magnitude to the advection terms. The relative magnitudes of the terms can be tested by substituting approximate scales into the equations to make scaling arguments. Introducing the spatial scales $\kappa = \frac{x}{h}$ and $\chi = \frac{h}{L}$, the velocity scale $U_k = \gamma \bar{U}_\infty$, and the temporal scale $\tau = \frac{\bar{U}_\infty t}{L}$, the first two terms can be written as:

$$\frac{\partial \bar{U}_k \bar{U}_l}{\partial x_l} \approx \frac{\gamma^2 \bar{U}_\infty^2}{\kappa}, \tag{5.29}$$

$$\frac{\partial \overline{U_k' U_l'} h}{\partial x_l} \approx -\frac{1}{16}\frac{{U'_{\text{amp}}}^2}{\kappa}\left(1+\cos\left(2\kappa\chi\pi\right)\right)^4 \cos\left(\tau\pi\right), \tag{5.30}$$

where

$$U'_{\text{amp}} = \begin{cases} \lambda_f \bar{U}_\infty \left(\frac{\chi}{\chi_f}\right)^{\frac{-5}{6}} & k < k_f \\ \lambda_f \bar{U}_\infty \left(\frac{\chi}{\chi_f}\right)^{-3} & k > k_f \end{cases} \tag{5.31}$$

The cosine terms remain bounded between zero and one for all χ and τ, so the relative size of the turbulence terms is determined by the first terms in (5.30). Dividing equation (5.30) by (5.29):

$$\frac{\frac{\partial \overline{U_k' U_l'} h}{\partial x_l}}{\frac{\partial \bar{U}_k \bar{U}_l}{\partial x_l}} \approx -\frac{1}{16}\frac{\lambda_f^2}{\gamma^2}\frac{\chi}{\chi_f}^{-2n}, \tag{5.32}$$

where:

$$n = \begin{cases} \frac{3}{2} & k < k_f \\ \frac{5}{6} & k > k_f \end{cases}. \tag{5.33}$$

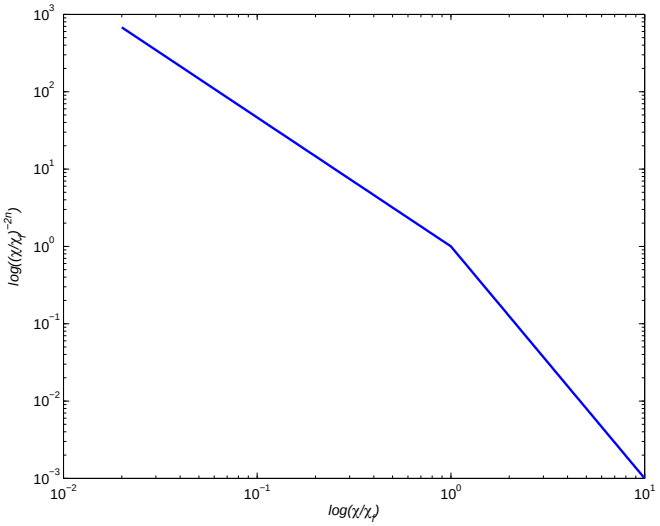

Figure 5.4: Variation of the function $\frac{\chi}{\chi_f}^{-2n}$ as $\frac{\chi}{\chi_f}$ increases which corresponds to eddies becoming smaller.

The Taylor Series expansion of Equation (5.32) of $\delta\chi = \frac{\chi}{\chi_f} - 1$ about $\frac{\chi}{\chi_f} = 1$ is given by:

$$\frac{\frac{\partial \overline{U_k' U_l'} h}{\partial x_l}}{\frac{\partial \bar{U}_k \bar{U}_l}{\partial x_l}} \approx -\frac{1}{16}\frac{\lambda_f^2}{\gamma^2}\left(1 + \sum_{m=1}^{\infty}(1+m)(-1)^m \delta\chi^m n\right). \tag{5.34}$$

This is a decreasing function in $\frac{\chi}{\chi_f}$, as shown in Figure 5.4. This shows that the turbulent kinetic energy, and therefore the contribution that the turbulent fluctuations make to the shallow water equations, relative to the advection term, reduces as the length scale of the fluctuations becomes smaller.

The dual cascade is forced at $\frac{\chi}{\chi_f} = 1$, and the length scale corresponding to χ_f is likely to be less than the flow depth, particularly in the context of tidal turbines where the characteristic length scale is some fraction of the flow depth. The energy of the turbulent eddies with a length scale half that of the turbine diameter represent just over 10% of the turbulent energy of the forcing eddies, and therefore it is assumed for simplicity that eddies of length scales less than that of the turbine diameter are, to a first approximation, negligible. Turbulent fluctuations on the scale of the forcing wave length reduce to 10% of the energy contained in fluctuations with a length

scale of $4D$. The size of the largest eddies is controlled by the extent of the flow domain, and therefore the magnitude of the energy contained in the largest eddies is constrained by the horizontal dimensions of the flow. This suggests that, even for moderately-sized channels, the contribution of the Reynolds stress terms to the shallow water equations is driven by the largest eddies in the flow rather than the sub-grid scale forcing. This is in agreement with the general understanding that the inverse energy cascade is responsible for transporting momentum to the largest eddies in a two-dimensional flow, which dominate shallow water turbulent processes (Davidson, 2004). It is therefore proposed that the largest eddies provide a good approximation to the magnitude of turbulent stresses in a shallow water flow, and shall be the focus of turbulence modelling.

The exact magnitude of the contribution made by the turbulent fluctuations relies on knowledge of λ, the ratio of the turbulent fluctuation velocity to the mean flow speed, a term which cannot be determined without experimental data. It may be assumed that it is not negligible for all turbulent fluctuations as it is known that at least some turbulent fluctuations are an important mechanism of momentum transfer in the shallow water equations from experimental evidence. In lieu of experimental data, a sensitivity study of the magnitude of λ_f has been conducted in TELEMAC-2D. An array of eight 20m diameter turbines each applying 1.25 MW to the flow was simulated. The inter-turbine spacing was 1 diameter, giving a total array width of 320 metres. Four different levels of λ_f were tested.

The results are presented in terms of the equivalent effective (molecular + turbulent) viscosity of the levels of λ_f to aid comparison with established turbulence models. Levels of λ_f were chosen to provide equivalent effective viscosities of 10^{-6} at level one, 10^{-4} at level two, 10^{-2} at level three, and 1 at level four. The spatial average of the axial flow speed through the array, $\langle u \rangle$, where the angled brackets denote the spatial average, and the available power, P, were assessed at the array

	Level 2	Level 3	Level 4	Level 1
$\langle \Delta u \rangle$	$6.7 \times 10^{-4}\%$	$2.4 \times 10^{-2}\%$	1.3%	$1.5061 \mathrm{ms}^{-1}$
ΔP	$< \epsilon$	0.8%	3.98%	10MW

Table 5.1: Comparison of spatially averaged flow speed through array and power for the four turbulence levels. $\langle \Delta u \rangle = \langle u|_i \rangle - \langle u|_1 \rangle$, $\Delta P = P|_i - P|_1$.

plane for each level of λ_f, and are reported normalised against the baseline level one case in Table 5.1. The baseline $\langle u \rangle$ and P are reported in the right-hand column of the table. The intermediate levels showed very little difference in flow speed to the baseline, with relative differences in flow speed below 0.1%, and the relative difference in flow speed was just over 1% for level four. The relative difference in power was less than round off error for level two, less than 1% for level three, and less than 4% for level four.

The results, which correspond to a range in effective viscosity of six orders of magnitude, demonstrate that the flow speed through the array and the available power are largely unchanged across a broad range of turbulence levels. The primary difference between the different turbulence levels is the array wake length, which is dependent on the thrust applied to the flow and the strength of the turbulent mixing that occurs in the wake of the array. Numerical studies suggest that the length of the wake is affected by the ambient level of turbulence, which is largely controlled by site-specific processes (Nishino and Willden, 2012a). This indicates that further work will be required to allow the application of the model to a specific tidal site. However, the flow speed through, and the power available to an array are relatively insensitive to the turbulence level, and therefore the work in the remaining chapters considering generic tidal flows shall use an intermediate level of turbulence, corresponding to level two here.

Two-dimensional turbulence is less well understood than three-dimensional turbulence, and there is less certainty about the dynamics of the k^{-3} enstrophy cascade than there is for the three-dimensional $k^{\frac{-5}{3}}$ energy cascade. Numerical experiments

have suggested that the enstrophy cascade may indeed have an exponent that varies between -3 and -6 (Tabeling, 2002). A number of factors contribute to this variation, chiefly the domain boundary conditions, the initial conditions of the flow, and the time the flow evolves over. This variation indicates that further investigation is required to understand fully the role of two-dimensional turbulence in the context of depth-averaged simulations of tidal turbines. However, theoretical models suggest that an exponent of -3 is appropriate, and experimental results suggest that this is higher than occurs in practice. The decay of enstrophy will increase for more negative exponents, reducing further the contribution of smaller turbulent scales to the turbulent energy spectrum, supporting the hypothesis that only large scale turbulence needs to be modelled as a first approximation.

5.4 Conclusions

Flows are fundamentally three-dimensional, and the interest in two-dimensional turbulence has arisen as an artefact of the desire to approximate some flows as two-dimensional, the key differences arising due to the invariance of both the energy and vorticity in two-dimensional turbulence. If the production, convection, and destruction of turbulence is in equilibrium, turbulent energy is concentrated in large, coherent structures, and the analysis of the energy contained within turbulent eddies suggests that the effects of the Reynolds stress term on the flow may be modelled to a first approximation by just considering the largest eddies. When spatial variation of the turbulence intensity is reasonably low, then it may be possible to use a constant similar to the eddy viscosity-type approximation, where the constant is calculated from experimental data or assessed through a parametric study.

Although a flow may be relatively homogeneous on the large scale, turbulence in the vicinity of tidal turbines may be non-homogeneous and have significant spatial

structure. The assumption that production, convection, and destruction of turbulence is in equilibrium probably is not valid in the near vicinity of turbines, necessitating a more advanced turbulence model. However, the scale analysis suggests that local turbulence production would soon be dominated by the larger eddies in the flow. Indeed, given the uncertainties in sub-grid and sub-depth modelling of turbulent flows, it may be preferable to employ a simpler turbulence model in the shallow water equations, particularly in light of the approximations made in the depth-averaging process.

Turbulence modelling in the SWEs is challenging because turbulence is a non-homogeneous and transient flow phenomenon, depending on local flow conditions which vary significantly in time and through the water column. The time- and depth-averaged flow variables used to describe the SWEs are approximations to the real conditions responsible for generating, diffusing and dissipating turbulent energy in a flow, and it may be argued that it is most important to capture accurately the transfer of energy from the mean flow, which can be simulated, into the turbulent energy cascade, which must be modelled. It has been shown that the largest eddies, in which much of the turbulent energy is concentrated, are the dominant form of eddies and therefore a fairly good approximation may be made through capturing these eddies accurately. However, this allows only a limited insight into the physical mechanisms responsible for turbulence in shallow water flows. Resolving the turbine-scale flow to develop a better understanding of the relationship between the depth-averaged flow variables and the available power is discussed in the next chapter.

Chapter 6

Scale Separation in a Depth-Averaged Simulation

The art of doing mathematics consists in finding that special case which contains all the germs of generality.
- David Hilbert

This chapter will first illustrate the differences between two- and three-dimensional simulations and explain how an array's power potential is erroneously calculated in two dimensional simulations. A correction is proposed by deriving an analytical model to more reflect accurately the power available to an array which can then be used to correct the estimates of two-dimensional simulations. The basic model is extended to include the deformation of the free surface due to energy extraction. The drag arising from the support structure will be neglected, although this correction can be added into the model with relative ease as an additional resistance to the flow.

6.1 Introduction

As discussed in Chapter 3, recent analytic models and numerical simulations of tidal turbine arrays partially spanning wide channels have demonstrated that there are two scales of flow to be considered: the device-scale flow, which consists of the flow around an individual turbine and the wake of the turbine; and the array-scale flow, which consists of the flow around the array and the array wake (Nishino and Willden, 2012b, 2013). One consequence of the diversion of flow around the array is the reduction

of the mass flux through the array, and it is this reduced mass flux that provides the upstream boundary condition to the device-scale flow problem. Two powers may be defined for a partial array; the device power, which is the power available to a single device; and the array power, the power removed from the flow, composed of the power available to each tidal device as well as the power dissipated in the mixing of the device-scale wakes. The array power is therefore necessarily greater than the sum of the power available to the devices in the array.

At the turbine-scale, the flow through the disc experiences a resistive thrust force, F_D, which removes momentum from the flow and causes a static head difference to form across the disc. Actuator disc theory suggests that two distinct streamtubes can be identified in the flow: one containing the flow through the turbine, which has reduced velocity relative to the upstream flow; and a bypass streamtube with increased velocity relative to the upstream flow. The static pressure in these streamtubes equilibrates at some distance downstream of the device, after which the flow in the streamtubes mixes viscously as a result of the shear stress generated by the mismatched flow speeds. The viscous mixing results in a further decrease in the overall energy of the flow.

The energy removed from the flow by the actuator disc requires a force to be applied to the flow, but no such force must be applied to extract energy lost in mixing from the flow. The 'mixing energy' is removed by the viscous stresses that arise from velocity gradients, and, ignoring bed friction, there can be no streamwise forces acting in the mixing zone as there is no surface on which a force may act. This is an important distinction to make, as it is significant in ensuring that the correct energy and momentum are removed from the flow.

Estimation of the power available to an array of turbines thus requires both the device-scale and the array-scale flows to be resolved. Three-dimensional simulations have been used to study small groups of tidal devices, where the grid resolution en-

sures that both the devices and the wake are resolved, thereby allowing the available power to be estimated (see, for example Nishino and Willden (2012a)). However, the computational expense of simulating many tidal devices in three-dimensions necessitates the use of two-dimensional simulations for large tidal arrays. The two-dimensional simulations typically solve the shallow water equations, which describe the flow in terms of depth-averaged quantities (for examples, see Walkington and Burrows (2009); Draper *et al.* (2010)). Representing the flow around individual devices can be challenging in depth-averaged simulations as the grid cells may be larger than the size of a turbine and/or turbine farm (Plew and Stevens, 2013). It becomes necessary in two-dimensional simulations to parameterise the relationship between the array power removed from the simulated flow and the available device power.

One of the challenges of depth-averaged simulations is relating the total power removed from the flow in the numerical simulation to the available power, the maximum power that can be extracted at the turbine plane by the tidal devices, as a straightforward relationship does not exist between the available power of a turbine array and the total power removed from the flow (Draper *et al.*, 2010). The relationship between array power, thrust, and the flow speed through the array may be determined through a variety of methods. If a particular turbine design is being considered and turbine data are available, the relationship between the flow speed through the array and device thrust and power can be determined through experiments, numerical simulation, and/or analytic models. Alternatively, it is often of interest to establish the available power through the use of idealised actuator discs, which act as perfectly efficient momentum extractors (examples include Elghali *et al.* (2007), Nishino and Willden (2012b) and Plew and Stevens (2013)). The relationship between the through-array flow speed and device thrust and power may be determined analytically or through numerical simulations.

Analytic corrections to continuous Galerkin depth-averaged array simulations

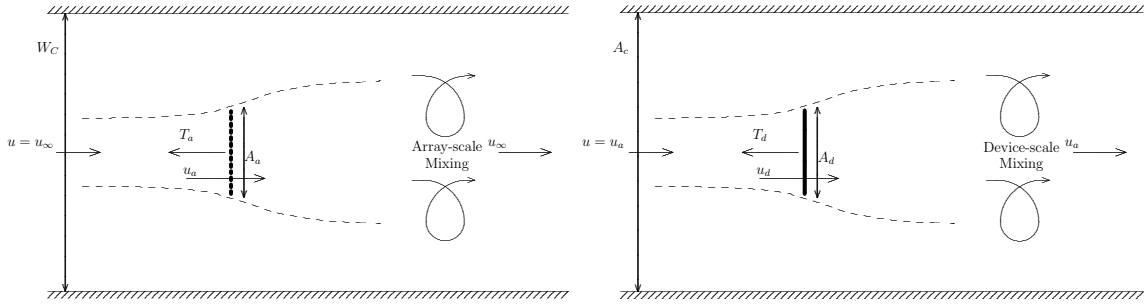

(a) (b)

Figure 6.1: Sketches of the multi-scale flow of a tidal array: a) an array of tidal turbines partially spanning a wide channel, and b) a single turbine and surrounding flow passage inside the array. The array velocity u_a provides the upstream boundary condition to the device-scale model.

based on actuator disc theory are developed in this chapter to determine the maximum power available to an array of actuator discs. The chapter begins with a review of the device- and array-scale flows and energy extraction and challenges in modelling sub-grid device flow. Analytic corrections are developed, the first based on the volume-flux constrained actuator disc analysis of Garrett and Cummins (2007), which is then extended to include the open channel analyses of Whelan *et al.* (2009) and Draper *et al.* (2010). Drag arising from the support structure is neglected, although this can be added into the model as an additional resistance to the flow.

6.2 Scale Separation in Tidal Energy Extraction

The separation of array and device scales is shown in Figure 6.1. The overall energy extraction by a tidal turbine array in a channel with an inlet velocity u_∞ can be separated into a number of key stages according to the spatial scale over which they occur. The total power removed from the tidal channel, P_{Tot}, is the sum of the available array, P_a, and the power dissipated in the array wake, $P_{a,Mix}$. The power removed in a turbine-scale flow passage is the sum of the available device power, P_d, and the power dissipated in device-scale mixing $P_{d,Mix}$. Each turbine exerts a thrust

T_d on the flow, and the thrust exerted by the array, T_a, is the product of the number of turbines in the array, n, and their respective thrusts. The velocity through the array is u_a, and the velocity through each device is u_d.

$$P_{Tot} = T_a u_\infty = P_a + P_{a,Mix}, \qquad P_a = T_a u_a = nP_d + nP_{d,Mix}, \quad \text{and} \quad P_d = T_d u_d. \tag{6.1}$$

As discussed in Chapters 2 and 3, the mixing losses represent the transfer of energy from the mean flow to viscous mixing processes that arise due to development of shear stresses between the core and bypass flows as a result of differing flow speeds. Although these losses cannot be converted into useful power, accurate prediction of the available array power requires that these losses are accounted for, as they effect the dynamics of the overall tidal resource. These effects were parameterised in previous chapters with the basin efficiency, which in the multiple scale framework of a partial array of tidal turbines may be defined as three ratios: the local efficiency of the device, η_L; array efficiency, η_A; and global efficiency, η, where the global efficiency is equal to the basin efficiency defined in the literature:

$$\eta_L = \frac{P_d}{P_a}, \qquad \eta_A = \frac{P_a}{P_{Tot}}, \quad \text{and} \quad \eta = \eta_L \eta_A = \frac{P_d}{P_{Tot}}. \tag{6.2}$$

The latter case is achieved when the cross section of a channel is completely blocked by tidal devices, forcing all the flow through the turbines and not inducing any downstream mixing, so that there is no bypass flow and therefore no downstream mixing. The efficiencies will generally lie somewhere between these two extremes as the acceleration of the bypass flow and deceleration of the core flow causes shearing between the two velocities, resulting in dissipation through wake mixing.

6.2.1 Matching the Array and Turbine Scales

Although the array-scale problem and the device-scale sub-problem may be analysed separately, the thrust applied by the array, T_a, is the sum of the thrust, T_d, applied by each of the n turbines in the turbine array, i.e., $T_a = nT_d$. However, the same relationship does not hold between the power of the array and the devices as the array power also includes the power dissipated in the wake of the devices, so that $P_a \neq nP_d$. Figure 6.2 compares depth-averaged analyses in which array thrust or array power are specified with a 3D RANS simulation of eight 20m diameter, d, actuator discs by Nishino and Willden (2013) in a channel with a uniform upstream flow speed of 2ms^{-1} and depth of $2d$. The total available power of the 3D array is 8.8MW resulting from the application of a total thrust of 7.3 MN.

A depth-averaged array with an available power of 8.8 MW, shown in Figure 6.2b, requires a total thrust of only 5.5 MN. Underestimation of the thrust comes from the erroneous assumption that the flow speed through the array is the same as the flow speed through the actuator discs and therefore that the total energy flux through the array is the same as that available to the discs. This fails to account for the bypass flow around the discs which limits the available power, thus underestimating the thrust required to achieve the desired power level. Figure 6.2c shows the case in which the same total thrust is applied as in the 3D simulation, with a total available power of 11 MW predicted. The overestimation again arises from the assumption that the flow speed through the array is the same as that through the turbines, which does not account for the device-scale bypass and corresponding reduction in mass flow through the discs that limits the available power.

The mismatch between the power and thrust in the two- and three-dimensional simulations arises because the unresolved flow in the turbine region is not correctly modelled in the two-dimensional simulations. Strategies for the implementation of actuator disc arrays in two-dimensional simulations may be summarised in three

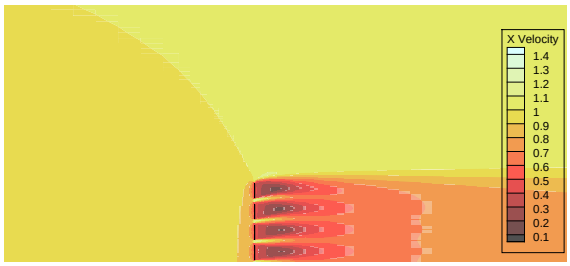

(a) Hub-height streamwise velocity contours from three-dimensional RANS actuator disc simulation of an eight rotor array, from Nishino and Willden (2013).

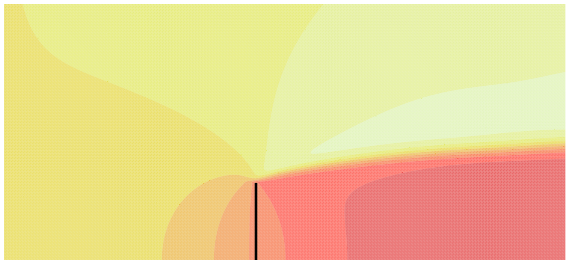

(b) Depth-average streamwise velocity contours from a depth-averaged simulation matching total available array power to the total available device power.

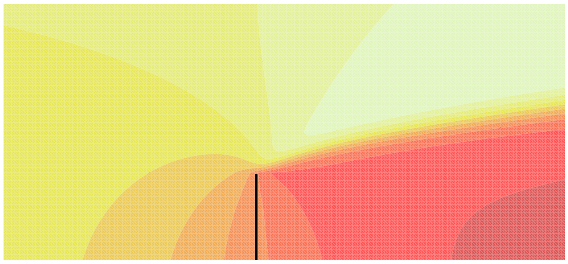

(c) Depth-average streamwise velocity contours from a depth-averaged simulation matching the thrust applied by array.

Figure 6.2: A comparison between the streamwise velocity contours at the hub-height in a three dimensional actuator disc simulation and two depth-averaged simulations matching the power and thrust coefficients of the turbine array.

categories:

1. Matching the thrust of the depth-averaged actuator discs to the thrust applied by the array, which over-predicts the available power, as $u_a > u_d$, but does simulate momentum removal from the flow correctly,

2. Matching the desired available power of the depth-averaged actuator discs to the power of the array, which under-predicts the thrust which must be applied in the SWE model thus incorrectly predicting the momentum removal from the flow and consequent far-field changes,

3. Matching the thrust as in (1) such that the momentum removal is correctly simulated, and modelling the device-scale flow field to determine the correct total available power for a given thrust applied by the array.

The only fully correct approach is (3). A correction is required so that the correct available power is calculated from the applied thrust, which requires modelling of the device-scale flow field. The array power, P_a is often known in a depth-averaged simulation as it can be calculated from the thrust imposed on the flow by the array. Therefore the array efficiency, η_A, defined in Equation (6.2) is known. The available device power, P_d, must be determined in order to find the maximum available power in order implement method (3).

Individual devices cannot be resolved within a depth-averaged simulation in a way that is both numerically stable and preserves the blockage ratios of the three-dimensional flow field around the device. One method to determine the available device power is to use the definitions in Equation (6.2) to determine P_d through the local efficiency, η_L, of the tidal devices, where η_L is determined analytically. The correction, multiplying the local efficiency η_L by the array power, P_a, shall be derived to obtain an expression for η_L for a given device thrust based on the analytical solution of the flow around a turbine in a passage in Chapter 2.

6.3 Modelling Sub-grid Turbine-scale Flow

As discussed in Chapter 2, analytical solutions for the power available to an array of turbines completely spanning a volume-flux constrained tidal channel by Garrett and Cummins (2007), and an array spanning an open channel by Houlsby *et al.* (2008). It is desirable to determine the correcting factor as a function of the thrust applied to the flow, as this then allows the correction to be applied as a post-processing step of the simulation. An analytical solution for η_L will thus be derived in the volume-flux constrained framework for a specified turbine thrust. In the open channel framework the basin efficiency is derived in terms of the change in free surface elevation so that the correction factor may be applied to cases, such as an enhanced bed friction

coefficient, where the thrust may not be directly specified.

6.3.1 Volume-flux Constrained Turbine-scale Flow

Three features are particularly important when assessing the power available to a tidal device: the mass flux through the turbine, known as the core flow; the mass flux around the turbine, known as the bypass flow; and the mixing region between stations four and five. Hydrostatic pressure in the core and bypass flows equilibrate at station four, although the flow speeds in the two streamtubes are not equal, developing a shear stress between the two flows, resulting in viscous mixing downstream of the hydrostatic pressure equalisation point. The total power removed from the tidal flow at the turbine-scale is therefore the sum of the available power, P_d, and the power dissipated in the mixing zone, $P_{d,Mix}$, as defined in Equation (6.1). The available power of an actuator disc is the product of the thrust and the through-disc velocity u_2. The volume-flux constrained actuator disc model is used to determine u_2, and therefore the available power P_d, for a specified thrust.

The force on the actuator disc is equal to the pressure difference across the disc, $T_d = (p_2 - p_3)A_d$. The pressure difference may also be expressed as a function of the difference in the flow speeds in the core and bypass flows by combining Bernoulli's equations in the core flow upstream and downstream of the turbine and the bypass flow, which yields, following the derivation of Equation (2.49):

$$T_d = \frac{1}{2}\rho A_d \left(u_{4b}^2 - u_{4d}^2\right). \tag{6.3}$$

The non-dimensionalised form of Equation (6.3) is rearranged for the bypass induction factor β_4 in terms of the core wake induction factor α_4 and the thrust coefficient C_{TL} to give:

$$\beta_4 = \sqrt{\alpha^2 + C_{TL}}. \tag{6.4}$$

Continuity between stations one and four in Equations (2.50) and (2.51), and conservation of energy in the bypass flow (Equation (2.47c)), requires:

$$\frac{\alpha_4}{\alpha_2} C_{TL} = (\beta_4 - \alpha_4)(\beta_4 + 2\alpha_4 - 1), \tag{6.5}$$

Equations (6.4) and (6.5) may be combined to give an expression for α_2 in terms of α_4 and C_{TL}:

$$\alpha_2 = \frac{\alpha_4 \left(\sqrt{C_{TL} + \alpha_4^2} + \alpha_4 \right)}{\sqrt{C_{TL} + \alpha_4^2} + 2\alpha_4 - 1}, \tag{6.6}$$

where $0 \leq \alpha_4 \leq 1$ is found from the solution of:

$$C_{TL}(1 - B) + (\alpha_4 - 1)^2 + 2\sqrt{C_{TL} + \alpha_4^2}(\alpha_4 - 1) = 0. \tag{6.7}$$

The available power of an actuator disc in a volume-flux constrained channel $C_{PL} = \alpha_2 C_{TL}$, is determined by solving Equation (6.7) for α_4 and thus determining α_2 from Equation (6.6). The total power removed from the flow is the sum of the available power and the power dissipated in turbine-scale mixing. The total power removed from the flow is found by considering the change in energy between stations one and five (Equation (2.58)), from which it was shown in Section 2.4.2 that the basin efficiency is simply the core flow induction factor through the actuator disc in the volume-flux constrained model:

$$\eta_L = \frac{C_{PL}}{C_{PL,Tot}} = \frac{\alpha_2 C_{TL}}{C_{TL}} = \alpha_2. \tag{6.8}$$

The effect of the local blockage ratio, B_L, on the variation of local efficiency η_L against local thrust coefficient C_{TL} is shown in Figure 6.3. The local efficiency decreases much more quickly at relatively low blockage ratios than at higher blockage ratios. When $C_{TL} = 1.00$, the local basin efficiency $\eta_L = 0.96$ when the blockage

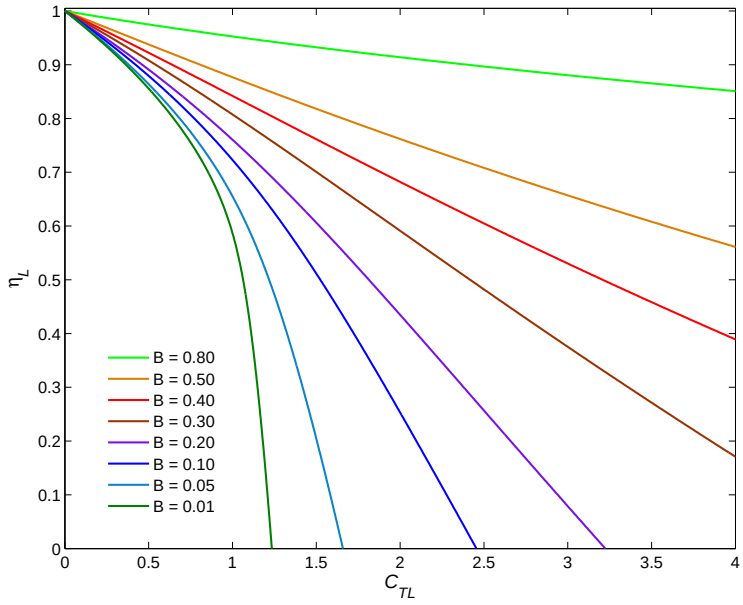

Figure 6.3: Plot of local efficiency, η_L, against local thrust coefficient, C_{TL}, for eight local blockage ratios, B_L.

ratio is $B = 0.80$, representing the case where the flow passage around the turbines is one diameter tall and one diameter wide. This contrasts sharply with a local basin efficiency $\eta_L = 0.65$ at the same thrust coefficient when the blockage ratio is $B = 0.05$, which is much more representative of current turbine array designs. Recalling that the relationship between available device power and the array power is $P_d = \eta_L P_a$, it is clear that applying a correction to the available device power is particularly important for low local blockage arrays.

The local efficiency is negatively correlated with the local thrust coefficient because an increment in thrust coefficient reduces the flux u_d through the device, which necessitates an acceleration of the bypass flow u_b to conserve mass flux. The increased velocity difference between the core and bypass flow speeds causes stronger shearing between the two flows in the device wake, and hence more energy dissipated in the wake mixing process. Local basin efficiency is particularly heavily penalised in low local blockage arrays as the thrust coefficient increases because the flow around the

turbine is relatively unconstrained and therefore there is little resistance to acceleration of the bypass flow. Turbines operate in a relatively constrained flow field in high blockage arrays and there is a much greater resistance to acceleration of the bypass flow due to a unit increase in thrust. As a result, high blockage arrays operate with higher local efficiency than low blockage arrays as the turbine thrust increases.

6.3.2 Open Channel Model for Turbine-Scale Flow

Section 2.4 discussed the differences in the modelling assumptions between the volume-flux constrained and open channel actuator disc models. It was assumed in the volume-flux constrained model that the pressure gradient established in the channel as a result of the energy extraction from the flow does not significantly change the channel's cross-sectional area, and therefore that the flow speed recovered to the free stream velocity far downstream of the actuator disc. Energy extraction from an open channel, however, results in a deformation of the free surface and consequently an acceleration of the flow in order to conserve mass flux through the flow passage. The open channel actuator disc model may therefore be employed to determine the basin efficiency from the observed free surface deformation in addition to a formulation in terms of the device thrust. This has advantages for application of the correction factor to simulations in which enhanced bed roughness or some other factor that cannot be directly linked to the device thrust.

The device thrust can be determined from a momentum balance between stations one and five:

$$T_d = \frac{1}{2}\rho g b \left({h_1}^2 - {h_5}^2\right) + \rho b h_1^f u_1^f \left(u_1 - u_5\right). \tag{6.9}$$

Recalling the definition of the change in free surface elevation $\delta h = h_1 - h_5$ and that conservation of mass requires $h_1 u_1 = h_5 u_5$, Equation (6.9) yields cubic in $\frac{\delta h}{h_1}$ that can be non-dimensionalised using the definitions in Section 2.4.1 and solved for the local

thrust coefficient:

$$C_{TL}^{f} = \frac{\frac{\delta h}{h_1}}{Fr_L^2 B_L \left(1 - \frac{\delta h}{h_1}\right)} \left(\left(\frac{\delta h}{h_1} - 2 \right) \left(\frac{\delta h}{h_1} - 1 \right) - 2Fr_L^2 \right). \tag{6.10}$$

The total power removed from the flow between stations one and five is the sum of the power available to the turbine, P_d and the power dissipated in the turbine-scale wake, $P_{d,Mix}$:

$$P_d + P_{d,Mix} = \frac{1}{2}\rho {u_1}^3 b h_1 - \frac{1}{2}\rho {u_1}^3 b h_1 \left(\frac{h_1}{h_1 - \delta h} \right)^2 + \rho g b h_1 u_1 \left(h_1 - h_5 \right). \tag{6.11}$$

Defining the power coefficient for the total power removed at the turbine scale in a flow passage with a free surface as $C_{PL,Tot} = \frac{P_d + P_{d,Mix}}{\frac{1}{2}\rho {u_1}^2 A_d}$, this can be rearranged to give:

$$C_{PL,Tot} = \frac{1}{B_L} \left(1 - \left(\frac{1}{1 - \frac{\delta h}{h_1}} \right)^2 + \frac{2}{Fr_L^2} \frac{\delta h}{h_1} \right). \tag{6.12}$$

The local basin efficiency η_L for the free surface model is the ratio of the available power of the turbine to the total power removed at the turbine scale:

$$\eta_L = \frac{P_d}{P_d + P_{d,Mix}} = \frac{C_{PL}}{C_{PL,Tot}} = \frac{\alpha_2 C_{TL}}{C_{PL,Tot}}. \tag{6.13}$$

Substituting the thrust coefficient calculated from the change in free surface elevation in Equation (6.10) and the coefficient for the total power removed from the flow $C_{PL,Tot}$ from Equation (6.12) into the local basin efficiency definition yields:

$$\eta_L = \frac{\alpha_2 \frac{\delta h}{h_1} \left(1 - \frac{\delta h}{h_1}\right)}{Fr_L^2} \frac{\left(\frac{\delta h}{h_1} - 2 \right) \left(\frac{\delta h}{h_1} - 1 \right) - 2Fr_L^2}{\left(1 - \frac{\delta h}{h_1}\right)^2 \left(1 + \frac{2}{Fr_L^2} \frac{\delta h}{h_1}\right) - 1}. \tag{6.14}$$

The Froude number, Fr_L, and the relative change in free surface elevation, $\frac{\delta h}{h_1}$, are

inputs from the depth-averaged simulation, leaving α_2 as an unknown quantity. The actuator disc induction factor can be found by solving the open channel actuator disc model presented in Section 2.4.1 for a given $\frac{\delta h}{h_1}$ ratio. Mathematically, it is simplest to follow the approach of solving for α_2 and $\frac{\delta h}{h_1}$ for a given α_4 and matching the solution with $\frac{\delta h}{h_1}$ determined from the simulation. The induction factor α_2 is expressed as a function of α_4 and β_4 (c.f. Equation (2.23)):

$$\alpha_2 = \frac{\alpha_4 \beta_4}{B_L(\beta_4 - \alpha_4)} \left(1 - \frac{1}{2} Fr_L^2 \left(\beta_4 - 1\right) - \frac{1}{\beta_4}\right). \tag{6.15}$$

The bypass velocity is found by solving the quartic in Equation (2.25). Noting the definition of the thrust coefficient $C_{TL} = \beta_4^2 - \alpha_4^2$, the cubic for $\frac{\delta h}{h_1}$ derived from the momentum balance across the turbine-scale flow between stations one and five is solved in terms of α_4 using the solution of the quartic in Equation (2.25) and Equation (2.29).

The equations for α_2 and $\frac{\delta h}{h_1}$ can be solved for a range of α_4 values so that the correct turbine induction factor α_2, and therefore local basin efficiency in Equation (6.14) can be selected given the measured change in free surface elevation ratio $\frac{\delta h}{h_1}$ from the simulation. Although this method represents more accurately the physics of the device scale flow, it is very sensitive to the location of the upstream and downstream boundaries of the region in which the array is simulated, as the change in free surface elevation is calculated at these points. It must be assumed that energy removal due to the turbine dominates energy losses due to bed friction and ambient turbulence, as these will also contribute to a change in free surface elevation.

6.4 Numerical Implementation of the Turbine-scale Correction Factor

Grid resolution constraints, particularly in coastal and continental shelf scale simulations mean that the size of cells in a numerical simulation is often much larger than the size of the tidal turbines being simulated. Furthermore, it is often necessary to smear the turbine region over multiple adjacent cells in the streamwise direction in order to achieve a numerically stable solution further abstracting the flow field in the numerical simulation from the turbine-scale flow field.

The total power removed from the flow at the turbine-scale is the sum of the available device power and the power dissipated by device-scale mixing for the n turbines in the array. This was termed the array power, P_a, in Equation (6.1). The thrust applied by the turbine array in the depth-averaged simulation is the sum of the thrust applied by the turbines in the array, nT_d if the turbines apply a uniform thrust. If the turbine thrust is known the array thrust can thus then be specified as a simulation parameter.

The array power, P_a, is the product of the streamwise velocity through the array, u_a, and the array thrust, T_a. The velocity u_a is extracted as an output of the depth-averaged simulation used to calculate the power removed from the flow by the array. The analytical corrections derived in this chapter may be used to determine the fraction of the array power that is available to the turbines by multiplying the array power by the local basin efficiency, η_L, corresponding to the thrust applied by the array.

A number of techniques exist to discretise the SWE solved in depth-averaged simulations. The Discontinuous-Galerkin Finite Element Method (DG-FEM) permits step discontinuities in the fluid depth and velocity across the boundary of adjacent elements, such as those that might arise by applying the device scale model with a

free surface along the edge of two elements (see, for example Draper *et al.* (2010)). The flow depth and velocity in the upstream cell provide the upstream boundary conditions to the device-scale model and are used to calculate the depth and velocity in the element downstream of the turbine array.

The Continuous-Galerkin Finite Element Method (CG-FEM) is more widely used to discretise the SWE in depth-averaged simulations, but does not allow step discontinuities in the depth and velocity of the flow between adjacent elements. It is therefore necessary for the region over which the thrust is applied to be 'smeared' in the streamwise direction of the flow to avoid numerical instabilities arising from the application of the array thrust. The total available array power in a CG-FEM scheme is:

$$P_a = \sum_{i=1}^{k} \sum_{j=1}^{l} T_{i,j} u_{i,j}, \tag{6.16}$$

where k and l are the number of nodes that the turbines are smeared across in the streamwise and cross-stream directions respectively, $T_{i,j}$ is the thrust applied at the $(i,j)^{\text{th}}$ position, and $u_{i,j}$ is the streamwise velocity at the $(i,j)^{\text{th}}$ position. The local basin efficiency multiplies the array power P_a to determine the total available power of the turbine array.

The local thrust coefficient, C_{TL}, is defined in terms of the array velocity u_a. It is often convenient to define the array thrust coefficient, C_{TA}, in terms of the channel velocity, u_∞, in a tidal channel where u_∞ is clearly defined at the channel inlet. Defining the global thrust coefficient, C_{TG}, as the thrust of n devices normalised by the dynamic pressure defined by the channel velocity and the frontal area of the n turbines, the relationship between the local thrust coefficient and the global thrust coefficient is:

$$C_{TG} = \frac{nT_d}{\frac{1}{2}\rho A_c u_\infty^2} = \alpha_1^2 B_G C_{TL}, \tag{6.17}$$

where $\alpha_1 = \frac{u_a}{u_\infty}$, and $B_G = \frac{nA_d}{A_c}$. This will shift the operating point on the local

efficiency curves, such as those in Figure 6.3 to the right, worsening basin efficiency, for a specified level of thrust.

6.5 Comparison to 3D RANS Simulation

The rigid lid analytic correction derived in Section 6.3.1 is applied to a depth-averaged simulation of an eight turbine array of 20m diameter actuator discs with an inter-turbine spacing of one diameter. The channel has an undisturbed flow speed of 2ms^{-1} and depth of two diameters. The channel is 80 diameters wide. The array is modelled in TELEMAC-2D as a single area of increased resistance (due to the thrust applied to the flow by the array) with a cross-sectional width of 16 diameters. The set up of the simulation is designed to be the depth-averaged equivalent of the three-dimensional rigid-lid RANS simulation of eight actuator discs by Nishino and Willden (2013). The three-dimensional thrust-power curve is known and provides the benchmark against which the depth-averaged modelling shall be compared.

The thrust-power curve of the three-dimensional RANS simulation is shown in Figure 6.4, and compared to two analytic models and two numerical simulations of the same channel. The array is modelled using open channel LMADT presented in Chapter 2, corresponding to the assumption that the limit to available power is governed only by the fraction of the channel cross section occupied by the array. The theoretical power curve, with a peak power coefficient of $C_{PG,max} = 0.93$, over predicts the simulated power curve for the same assumptions (only array blockage is important for available power), which has a peak power coefficient of $C_{PG,max} = 0.85$. The over-prediction arises because the analytic model does not consider the viscous mixing effects which act to remove additional energy from the flow, and nor does it allow for the cross-stream flux across the streamwise boundaries of the region in which the array is simulated numerically. The second factor arises from the need to distribute

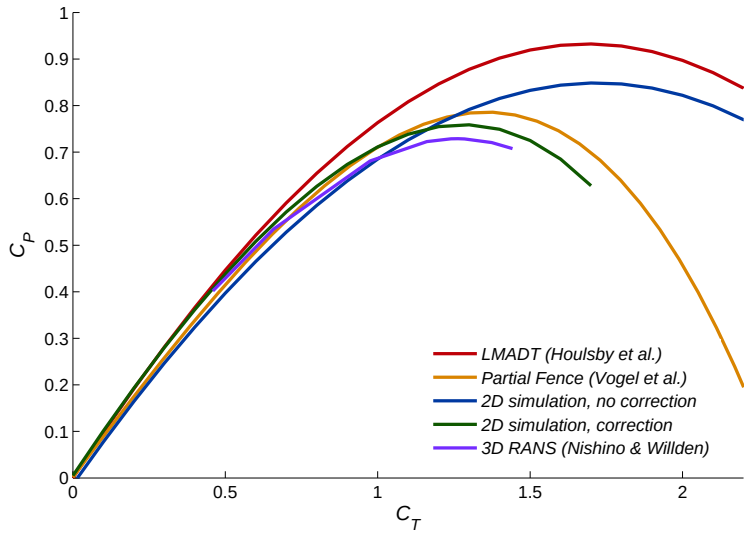

Figure 6.4: Comparison of analytic and numerical solutions for array power with and without device scale correction to three-dimensional numerical simulation of Nishino and Willden (2013).

the energy extraction of the array over a small distance in the streamwise direction to avoid numerical instabilities within the continuous Galerkin Finite Element code. The analytic and numerical results indicate that it is insufficient to consider solely the array blockage as the area ratio which constrains the available turbine power.

The local blockage is considered in addition to the array-scale blockage analytically, as presented in the two-scale analytic model in Chapter 3. The peak of the thrust-power curve decreases in magnitude to $C_{PG,Max} = 0.79$ because some of the device scale flow bypasses the turbine, reducing the power available to the turbines. The available device power is therefore necessarily less than the total power dissipated by the array

The peak power of the simulated array with local blockage correction, $C_{PG,max} = 0.76$, occurs at a lower thrust when the device-scale flow is included than the uncorrected simulation because the reduction in flow speed through the turbine plane due to the thrust at the device scale is compounded by the reduction in the velocity through the array due to the array thrust. The two-scale analytic model predicts a

slightly higher peak in the power curve than the corrected depth averaged simulation because the analytical model assumes that the flow is inviscid. The corrected simulation compares well to the three-dimensional RANS power curve, which has a peak power coefficient of $C_{PG,max} = 0.73$, a difference of 4% between the two simulations. This indicates that the two-scale blockage model captures the dominant physics that governs the power available to an array of turbines that partially spans a wide channel.

It is often of interest to specify a desired available power, and then determine the necessary thrust to achieve the specified power. It has been demonstrated that the available power is less than the power removed from the flow in depth averaged simulations as implied by the product of the array thrust and flux through the array. Indeed, a higher device thrust is required to achieve the specified total available power once the analytical correction has been applied in order to account for the device-scale bypass flow. The required device thrust can be found by solving for the analytical correction, given the local blockage ratio, and then finding the thrust required for the desired available power. This thrust may then be applied to the flow. It may not necessarily be possible for an array of turbines to achieve the desired available power, particularly at low blockages, where the flow may bypass the device as the thrust is increased in order to achieve the desired power.

The relationship between the available device power and the array power is characterised by the local efficiency, η_L. The reduction in the local efficiency of low local blockage scenarios in comparison to those with higher blockage ratios arises from the effect that changing the spacing between devices has on the bypass flow around the turbines. In low blockage configurations, the large distance between devices permits the formation of a large, relatively unconstrained bypass around each device. The flow is accelerated in the bypass around the device to maintain the total mass flux through the channel, and by considering the mass flux balance across the turbine

plane, it can be shown that the change in the non-dimensionalised velocity in the bypass, β_2, relative to the non-dimensional through-turbine velocity, α_2, is given by:

$$\frac{d\beta_2}{d\alpha_2} = \frac{B_L}{B_L - 1}. \tag{6.18}$$

For small blockage ratios ($B_L \ll 1$), β_4 scales roughly as $-B_L$ with the non-dimensional through-turbine velocity α_2, so that a small decrease in α_2 corresponds to a small increase in β_2. However, at higher blockage ratios, the $(B_L - 1)$ denominator means that small increases in the non-dimensional velocity α_2 are associated with large increases in β_2. As the acceleration required in the bypass of higher blockage configurations is much greater than that in low blockages, there is a greater resistance to flow in the bypass, allowing greater pressure gradients to be sustained across the devices, and consequently greater power is available for a given non-dimensional through-turbine velocity. It was shown that the local efficiency is equivalent to α_2 in the rigid lid case, and therefore arrays with higher local blockage maintain a high local efficiency over a greater range of thrust coefficient than do lower blockage arrays.

Over the range of global thrust coefficients that arrays are likely to operate at, high blockage arrays have a local efficiency close to $\eta_L = 1$, and therefore depth averaged simulations predict an available power which is, within the limits of modelling uncertainties, a relatively accurate representation of the power potential of the array. However, depth-averaged simulations of low blockage arrays may over predict the available power by almost 40%, which significantly misrepresents the power potential of the arrays, and therefore the analytic correction should be applied.

6.6 Comparison to Analytic Model

The correction method was compared to the partial array analytic model developed in Chapter 3 for arrays in a rectangular channel 1600m wide and 40m deep with a

N_{turbs}	B_G \ B_L	$\frac{\pi}{10}$	$\frac{\pi}{16}$	$\frac{\pi}{32}$
4	0.0196	0.0624	0.0998	0.1996
8	0.0393	0.1251	0.2002	0.4003
16	0.0785	0.2499	0.3998	0.7669
32	0.1575	0.5013	0.8021	1.0000

Table 6.1: Table of array blockage ratio corresponding to the global, and local blockage configurations for comparison of numerical results to analytic simulation.

uniform inflow speed of 2ms^{-1}, neglecting bed friction. A total of twelve scenarios were considered; three local blockage ratios, and four global blockage ratios. The local blockage ratios were $B_L = \frac{\pi}{10} \approx 0.32$, $B_L = \frac{\pi}{16} \approx 0.2$, and $B_L = \frac{\pi}{32} \approx 0.1$. The global blockages corresponded to arrays composed of four, eight, sixteen and thirty-two turbines, and the blockage data for the simulations are summarised in Table 6.1. Depth-averaged simulations with the rigid lid correction factor developed in Section 6.3.1 applied are compared to analytic solutions for the same local and array (and hence global) blockage ratios.

The effect of the number of turbines on the C_{TG} vs. C_{PG} relationship for a fixed local blockage ratio of $B_L = \frac{\pi}{16}$ is shown for corrected depth-averaged and analytic results in Figure 6.5. As the number of turbines increases, the peak C_{PG} increases, due to the effect longer arrays have on the array-scale flow phenomena. This can be understood by considering the differences in flow past turbines near the ends of the array (outboard turbines), and those in the centre of the array (inboard turbines). Outboard turbines experience a cross-stream component of flow in the direction of the array bypass, due to the reduced resistance to the flow of the array bypass as compared to the inboard direction. If the turbine thrust is uniform across the array, this asymmetric flow past the outer turbines results in a reduced axial flow through the turbines, reducing their power, as compared to inboard turbines. Turbines close to the centre of the array, in which the resistance to flow bypass around the turbines is approximately uniform either side of the turbines do not suffer the same reduction

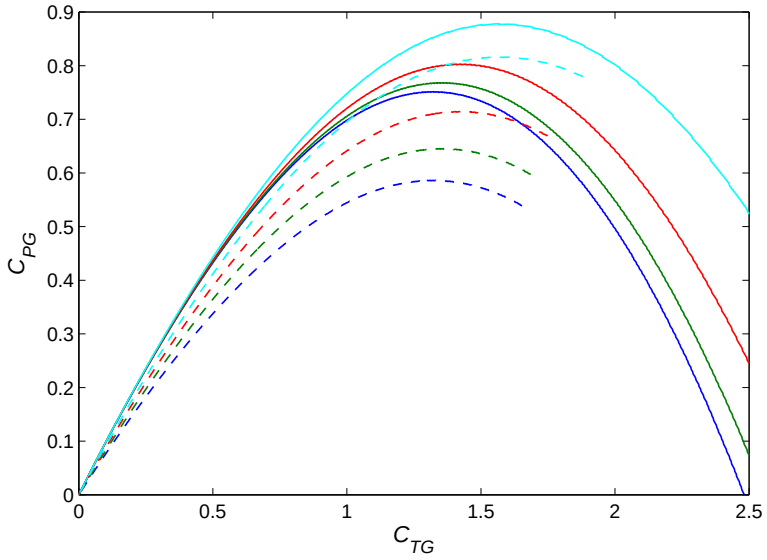

Figure 6.5: Comparison between simulated (dashed lines) and analytically predicted (solid lines) power coefficient C_{PG} vs. thrust coefficient C_{TG} for constant local blockage $B_L = 0.2$ for arrays of four (blue), eight (green), sixteen (red), and thirty-two (cyan) turbines.

in power as outboard turbines.

The array-scale effect of flow diversion around the outboard turbines is more significant for shorter arrays where a greater proportion of the turbines are affected by the array-end flow diversion. The partial array analytic model does not account for cross-stream variations in the flow, assuming that the flow is uniform across the array. Agreement between the corrected depth-averaged simulations and the analytic solutions for the thrust-power coefficient relationship improves as the number of turbines in the array increases because the assumption of uniform flow, which is valid for the inboard turbines, becomes a better approximation to what is simulated as array length increases. The relative difference between the analytic and simulated results decreases from approximately 20% for an array of four turbines to approximately 5% for 32 turbines, where the remaining differences can be attributed to viscous losses and other modelling differences between the idealised analytic solution and the depth-averaged simulation.

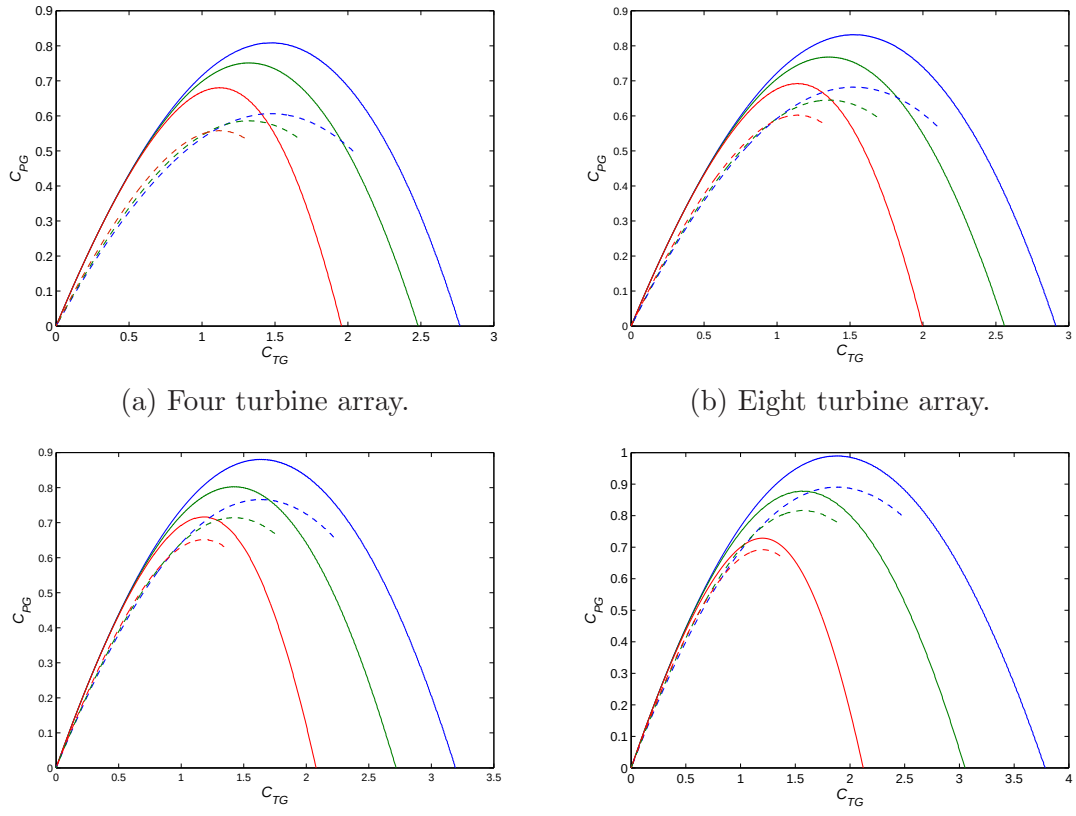

(a) Four turbine array.

(b) Eight turbine array.

(c) Sixteen turbine array.

(d) Thirty-two turbine array.

Figure 6.6: Comparison between simulated and analytically predicted power coefficient C_{PG} vs. thrust coefficient C_{TG} for arrays of different length and three local blockage ratios; $B_L = \frac{\pi}{32}$ (red), $B_L = \frac{\pi}{16}$ (green), and $B_L = \frac{\pi}{10}$ (blue).

The effect of local blockage ratio on the thrust vs. power coefficient relationship is investigated in Figure 6.6 for each of the different length arrays of turbines. The peak power coefficients increase as the number of turbines in the array increases, and agreement between the corrected depth-averaged simulations and the analytic solutions is improved for all local blockage ratios as the number of turbines in the array increases, for the reasons explained previously. For any given number of turbines, the peak power coefficient is achieved at the closest local blockage ratio, $B_L = \frac{\pi}{10}$, because at the device scale the turbines are able to apply a greater thrust to the flow due to the greater pressure difference that can be established across the turbines as a result of the reduced cross-sectional area of the turbine-scale bypass and greater confinement

of the flow. This improves the local efficiency for a given thrust coefficient, improving the performance of the array.

Figure 6.6 shows that the relative difference between the corrected depth-averaged simulations and the analytic solutions is greater at higher local blockage ratios and reduced at lower local blockage ratios for arrays of any length. Turbines at higher local blockage ratios apply a greater thrust to the flow and are thus more significantly affected by the cross-stream variation in flow that arises due to the finite length effect of flow diversion past the simulated arrays. Turbines in lower local blockage arrays do not benefit to the same extent from the mutual interactions which increase turbine power in higher local blockage arrays, as the greater inter-turbine spacing provides less resistance to the turbine-scale bypass of flow around the turbines. The lower blockage turbines must therefore apply a smaller thrust to the flow. Lower local blockage turbines are therefore less subject to the decrease in power experienced by the outboard turbines of the array, and therefore relative agreement with the analytic solution is improved, albeit for a lower peak power coefficient.

Agreement between the corrected depth-averaged simulations and analytic theory improves substantially as an array is increased from four to eight turbines, and then from eight to sixteen turbines, but is subject to diminishing returns as the array length increases and the remaining differences are due to differences in modelling the arrays and flow. The results are largely in agreement with those of Nishino and Willden (2013), and indicate that analytic theory and numerical simulation give fairly good agreement for arrays of at least eight turbines. The agreement is affected by the local turbine blockage, and higher blockage arrays generally need to be longer in order to reduce the impact of the outboard turbines on the overall array power to improve agreement with analytic models. However, the reduction in power of the outboard turbines is a necessary consequence of finite length arrays, and merits further attention to minimise the impact it has on the total power of the array.

6.7 Conclusions

Analytic correction factors for depth averaged simulations of turbine arrays have been developed using the local basin efficiency, which is determined as a function of the device thrust coefficient. The power available to an array of turbines is significantly over predicted when the turbine-scale flow is not included, with $C_{PG,max} = 0.85$, compared to the 3D RANS prediction of $C_{PG,max} = 0.73$, an over prediction of 27%. By comparison, applying the volume-flux constrained correction factor reduced the peak power coefficient to $C_{PG,max} = 0.76$, an error of 4%. The analytic correction factor may be applied during the post-processing of the simulation.

Variation in local basin efficiency with thrust coefficient depends on the local blockage ratio, and is negatively correlated with thrust coefficient, declining more steeply for lower than higher blockage ratios. Within the bounds of the thrust coefficients that arrays are likely to be operated at, the analytic correction factor plays a much more important role in correctly predicting the available power of low blockage arrays rather than high blockage arrays, where the error is less than 10%.

Agreement between corrected depth-averaged simulations and the analytic theory is affected by the number of turbines in the array and the local blockage ratio. The assumption of uniform upstream flow works well for the inboard turbines, but does agree well with the flow observed around the outboard turbines. Hence, as the array length increases, and the ratio of inboard to outboard increases, agreement with analytic theory improves. Diversion around the outboard turbines is increased at higher thrust coefficients, which occur at higher local blockage ratios, worsening agreement with the analytic theory. Conversely, low local blockage arrays apply a lower level of thrust to the flow, reducing the outboard turbine effect, thus improving agreement with analytic theory, albeit at a lower overall peak power coefficient than a higher local blockage array.

Chapter 7

Volume-flux Constrained Blade Element Momentum Theory

The essence of mathematics is not to make simple things complicated, but to make complicated things simple.
- Georg Cantor

Blade element momentum theory has been successfully used in the wind turbine industry. The theory relates turbine blade characteristics to the change in momentum in the flow, allowing the performance of specific turbine designs to be assessed. The theory has also been applied to the design of tidal turbines, embedded within numerical simulations to account for the effect of blockage on the momentum equations. A modified blade element momentum theory is proposed in which the momentum equations are adapted for the volume-flux constrained flow around a tidal turbine.

This chapter begins by reviewing the motivation and current techniques used for modelling tidal turbine rotors, outlining the potential contribution of a volume-flux constrained blade element momentum theory. The modelling assumptions and theory used to develop a blade element momentum model of a wind turbine are then reviewed in order to highlight the differences between the analysis of wind and tidal turbines. A volume-flux constrained blade element momentum model is then developed to account for these differences. The semi-analytic model is compared to results from numerical simulations of tidal turbines in unblocked and finite blockage conditions.

7.1 Introduction

Many tidal turbines will be required to harness a significant fraction of the global tidal resource; one estimate for extracting 1.9 GW from the Pentland Firth in the United Kingdom requires thousands of turbines (Adcock *et al.*, 2013). The scale separation in such analyses has been discussed in Chapters 3 and 6, highlighting the importance of blockage in predicting the power available to turbines. Analytic models provide a useful basis to understand the dynamics of the flow around an array of turbines, but they are restricted to idealized parameters to represent the turbines.

Numerical techniques, such as depth-averaged simulations, may be used to capture more complex flow features; multi-scale flow, shear, etc. Depth-averaged simulations provide a tractable means to determine the available power of an array of actuator discs, as discussed in Chapter 6. Such studies are used to establish performance limits and investigate flow dynamics around idealised turbines, but are not applicable to specific turbine designs. Blade Element Momentum (BEM) theory has been developed in the wind industry to relate rotor design characteristics, such as the lift and drag properties of the rotor blades, to the change in momentum in the flow, allowing the power available to wind turbines to be modelled semi-analytically (Hau and von Renouard, 2006). BEM models provide a means by which the power and thrust characteristics, and the parameters required in depth-averaged simulations to characterise turbine performance may be determined.

BEM theory has been utilised as a design tool for tidal turbines by embedding the standard wind turbine analysis within three-dimensional computational models to account for the flow expansion confinement due to blockage (see, for example Masters *et al.* (2011) and Schluntz (2014)). Although this accounts for the effects of blockage on turbine performance through the feedback established in the numerical simulations between the thrust applied by the rotor to the flow and the flow speed through the rotor, this is computationally expensive in comparison to the semi-analytical BEM

analysis that may be conducted for wind turbine.

Volume-flux constrained BEM model is developed to account for the effects of blockage on the flow through the turbine, allowing a relationship between thrust, power, and flow speed to be established semi-analytically for a turbine operating in non-zero blockage conditions. The results are compared to numerical simulations for a rotor designed for unblocked flow tested in a number of blockage conditions, demonstrating the capability of the modified BEM model to provide the necessary power and thrust characteristics to parameterise a tidal turbine in depth-averaged simulations.

7.2 BEM Theory in an Infinitely Large Domain

Glauert (1935) developed blade element momentum theory as a combination of blade element theory and momentum theory out of the efforts of a number of aerodynamicists in the 1920s to understand better the behaviour and performance of wings and propellers (Hau and von Renouard, 2006). BEM theory is an improvement over the simple actuator disc analysis of Lanchester and Betz because it allows the lift and drag generated by a particular rotor to be related to the change in momentum in the flow. BEM theory also accounts for the effect of the rotation imparted on the flow in its wake, which is important as the rotating flow increases the cost of extracting energy, reducing the turbine's power coefficient. As the turbine power coefficient depends on the rotational and translation motion of the flow through the turbine, the power coefficient is related to the tip speed ratio, the ratio of the tangential velocity of the rotor tip to the free stream flow speed. Turbine design consequently becomes a function of optimising both the power coefficient and the tip speed ratio. BEM theory for wind turbines is briefly summarised below, and a full discussion and derivation may be found in Burton *et al.* (2001) and Leishman (2006).

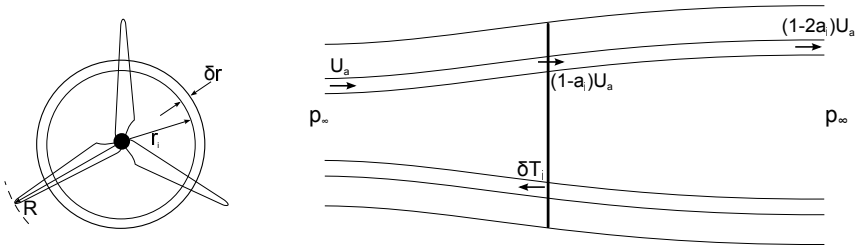

Figure 7.1: Diagram of the flow past a rotor in the i^{th} streamtube of width δr in the standard BEM model.

7.2.1 Model Assumptions

A rotor is modelled as a series of concentric annuli of radial width δr in BEM theory, as illustrated in Figure 7.1. It is assumed that there is no momentum transfer between adjacent annuli and hence there is no radial flow, thus allowing radial velocity components to be neglected and each annulus to be treated separately. It is also assumed that the rotor has infinitely many blades, so that every air particle passing through the rotor at a given radial position experiences the same change in momentum. This assumption allows the three-dimensional flow around individual blades to be neglected.

Blade element momentum theory represents a combination of blade element theory and momentum theory. The aerodynamic forces on a blade section in an annulus are determined through blade element theory, and the resulting change in axial and tangential flow speed is derived from momentum theory. The two theories, when combined, lead to two equations, an axial momentum balance and an angular momentum balance, which are solved iteratively to determine the flow speeds at the rotor plane and the lift and drag forces on the rotor blades.

7.2.2 Momentum Theory

Momentum theory is applied to each of the annular streamtubes passing through the rotor plane. The derivation of the axial momentum balance is similar to the

derivation of actuator disc theory. However an additional angular momentum balance is required in BEM theory to account for the rotation imparted on the flow by the rotor. Denoting the free stream flow speed to be U_a, the axial flow speed $u_{d,i}$ through the i^{th} streamtube at the rotor plane may be defined as:

$$u_{d,i} = (1 - a_i)U_a. \tag{7.1}$$

Further defining the flow speed in the turbine wake to be $u_{w,i} = (1 - b_i)U_a$, conservation of mass along each streamtube requires:

$$\rho A_{1,i} U_a = \rho A_{d,i}(1 - a_i)U_a = \rho A_{w,i}(1 - b_i)U_a, \tag{7.2}$$

where $A_{1,i}$ is the cross-sectional area of the streamtube far upstream of the rotor, $A_{d,i}$ is the cross-sectional area of the streamtube at the rotor plane, and $A_{w,i}$ is the cross-sectional area of the streamtube far downstream of the rotor when the wake is no longer expanding. The rate of change in momentum far upstream and downstream of the streamtube is due entirely to the force applied to the streamtube by the actuator disc. Denoting the pressure immediately upstream of the rotor $p^+_{d,i}$ and the pressure immediately downstream of the rotor $p^-_{d,i}$, the rate momentum change may be expressed as:

$$A_{d,i}\left(p^+_{d,i} - p^-_{d,i}\right) = (U_a - (1 - b_i)U_a)\rho A_{d,i} U_a(1 - a_i). \tag{7.3}$$

The pressure difference may also be found by applying the Bernoulli equation to the upstream and downstream sections of the streamtube, yielding:

$$\left(p^+_{d,i} - p^-_{d,i}\right) = \frac{1}{2}\rho\left(U_a^2 - (1 - b_i)^2 U_a^2\right), \tag{7.4}$$

so that:

$$u_{w,i} = (1 - 2a_i)U_a. \tag{7.5}$$

Half the reduction in axial speed therefore occurs upstream of the rotor plane, and half occurs in the wake of the rotor.

The cross-sectional area of the turbine streamtube at the rotor plane is, to the first order, given by $A_{d,i} = 2\pi r_i \delta r$. The incremental thrust of an annular section may be found from a force balance across an annular streamtube as:

$$\delta T_i = A_{d,i}\left(p^+_{d,i} - p^-_{d,i}\right) = 4\pi\rho r_i U_a^2 a_i(1 - a_i)\delta r. \tag{7.6}$$

As the force is applied at the actuator disc, the rate of work done by the disc is $\delta T_i u_{d,i}$, giving the available power in the i^{th} annulus:

$$\delta P_i = \delta T_i u_{d,i} = 4\pi\rho r_i U_a^3 a_i(1 - a_i)^2\delta r. \tag{7.7}$$

The rotating blades impart a torque on the flow, causing the air to rotate in the opposite direction to that of the rotor. The acquisition of tangential motion from the rotor occurs at the rotor plane and it is assumed that it does not change in the rotor wake. The tangential flow induction factor, a', is introduced to describe the change in tangential motion of the flow. The tangential flow speed in the i^{th} radial annulus is thus given by:

$$u_{\theta,i} = (1 + a'_i)\Omega r_i, \tag{7.8}$$

where Ω is the rotational speed of the rotor. The rate of change of angular momentum in the i^{th} streamtube is equal to the incremental rotor torque, δQ_i:

$$\delta Q_i = 4\pi\rho r_i^3 U_a(1 - a_i)\Omega a'_i\delta r. \tag{7.9}$$

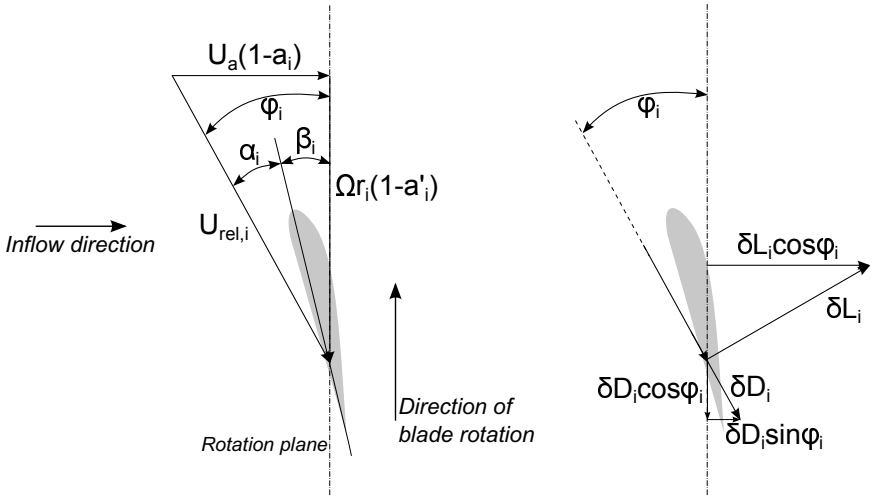

Figure 7.2: Diagram of the velocities (left) and forces (right) acting on a the i^{th} blade element.

7.2.3 Blade Element Theory

Blade element theory assumes that the flow around the blade elements in each annulus is two-dimensional. This allows the forces on each blade to be determined using two-dimensional aerofoil lift and drag characteristics, where it is assumed that the lift and drag coefficients, C_l and C_d respectively, are determined computationally or experimentally for the aerofoil being studied. Given the number of blades, N_B, section blade chord, c_i, section blade pitch angle β_i, and the rotor speed Ω, the forces and velocities on the blade may be resolved, as illustrated in Figure 7.2. The relative velocity, $u_{rel,i}$ is incident on the blade section at an angle ϕ_i to the direction of rotation of the turbine, such that:

$$\sin\phi_i = \frac{U_a(1-a_i)}{u_{rel,i}}, \quad \text{and} \quad \cos\phi_i = \frac{r_i\Omega(1+a'_i)}{u_{rel,i}}. \tag{7.10}$$

The angle of attack is given by:

$$\alpha_i = \phi_i - \beta_i. \tag{7.11}$$

Noting that the angle of attack, and therefore the lift coefficient, may vary across annuli, the lift force on an annular section of blade is defined as:

$$\delta L_i = \frac{1}{2}\rho u_{rel,i}^2 c_i C_{l,i} \delta r_i, \tag{7.12}$$

and the drag force as:

$$\delta D_i = \frac{1}{2}\rho u_{rel,i}^2 c_i C_{d,i} \delta r_i, \tag{7.13}$$

The axial thrust on the i^{th} annulus of the actuator disc is the sum of the lift and drag components acting in the axial direction:

$$\delta T_i = \delta L_i \cos\phi_i + \delta D_i \sin\phi_i = \frac{1}{2}\rho u_{rel,i}^2 N_B c_i \left(C_{l,i}\cos\phi_i + C_{d,i}\sin\phi_i\right)\delta r. \tag{7.14}$$

The torque on an annulus is the sum of the lift and drag components acting in the direction of rotation:

$$\delta Q_i = \delta L_i \sin\phi_i - \delta D_i \cos\phi_i = \frac{1}{2}\rho u_{rel,i}^2 N_B c_i \left(C_{l,i}\sin\phi_i - C_{d,i}\cos\phi_i\right)\delta r. \tag{7.15}$$

7.2.4 Blade Element Momentum Theory

The combination of blade element theory and momentum theory provide sufficient equations to describe completely the forces and velocities incident on the rotor. Combining Equations (7.6) and (7.14) yields:

$$4\pi\rho r_i U_a^2 a_i(1-a_i)\delta r = \frac{1}{2}\rho u_{rel,i}^2 N_B c_i \left(C_{l,i}\cos\phi_i + C_{d,i}\sin\phi_i\right)\delta r. \tag{7.16}$$

Similarly, combining the expressions for blade torque yields:

$$4\pi\rho r_i^3 U_a(1-a_i)\Omega a_i'\delta r = \frac{1}{2}\rho u_{rel,i}^2 N_B c_i \left(C_{l,i}\sin\phi_i - C_{d,i}\cos\phi_i\right)\delta r. \tag{7.17}$$

Defining the blade solidity σ_i as:

$$\sigma_i = \frac{N_B c_i}{2\pi r_i}, \tag{7.18}$$

these equations may be expressed in forms convenient for solving the axial and angular induction factors:

$$\frac{a_i}{1-a_i} = \frac{\sigma_i \left(C_{l,i}\cos\phi_i + C_{d,i}\sin\phi_i\right)}{4\sin^2\phi_i}, \tag{7.19}$$

$$\frac{a'_i}{1+a'_i} = \frac{\sigma_i \left(C_{l,i}\sin\phi_i - C_{d,i}\cos\phi_i\right)}{4\sin\phi_i\cos\phi_i}. \tag{7.20}$$

Equations (7.19) and (7.20) are solved iteratively for given β and σ along the blade and initial guesses for a and a'. The power extracted from the flow by the rotor may be determined once the solution has converged as the product of torque and angular velocity across the n annular streamtubes passing through the rotor:

$$P = \sum_{i=1}^{n} \delta Q_i \Omega. \tag{7.21}$$

7.2.5 Empirical Corrections

Many empirical corrections have been proposed to improve the agreement of BEM modelling with experiments, and a detailed study of corrections may be found in Burton *et al.* (2001). Some corrections are related to the assumption of equilibrium in the rotor flow field, where it is assumed that the flow instantaneously adjusts to updated flow conditions. The response to such changes occurs over a finite time period, requiring modification of the governing equations to better represent rotor performance.

A further limitation is the assumption that the flow is two-dimensional across a blade section and that any radial flow is negligible, implying that there is minimal pressure variation in the radial direction. This is inaccurate for heavily loaded rotors

where the radial pressure variation is significant and the outboard sections of blades where tip-vortices are generated. Generation of tip-vortices impacts the induced velocity at the blade tips, which affects the power extracted by the rotor. The accuracy of BEM theory is also reduced at blade roots, where the impact of structures such as the nacelle is significant. Empirical corrections are used to adjust the velocities and forces acting on the blade to improve agreement with experimental data. The Prandtl tip-loss model, is discussed in further detail in Section 7.3.3.

7.3 Volume-flux Constrained BEM Model

In an infinitely large flow field (where the turbine's blockage ratio is zero) it is assume that full recovery of the static pressure to the far upstream value occurs in the far wake of a turbine, and that the change in momentum due to the thrust applied to the flow is due entirely to the velocity deficit in the core flow far downstream of the turbine. However, a pressure gradient forms between the far upstream and far downstream positions of a volume-flux constrained turbine, allowing a larger thrust to be applied by the turbine to the flow, leading to the improved turbine performance. The pressure gradient that develops in the volume-flux constrained flow results in an acceleration of the flow bypassing the turbine which must be considered in addition to the flow through the turbine in order to close the system of equations that define the BEM model.

Following standard BEM analysis, the swept area of the turbine is partitioned into n concentric annular rings centred on the turbine's axis of rotation with radial width δr and cross-section δA, and conservation of momentum is considered along the n streamtubes passing through these rings. The usual assumption is made that there is no momentum transfer between adjacent streamtubes, so that the change in momentum in each streamtube is a function only of the thrust applied to the

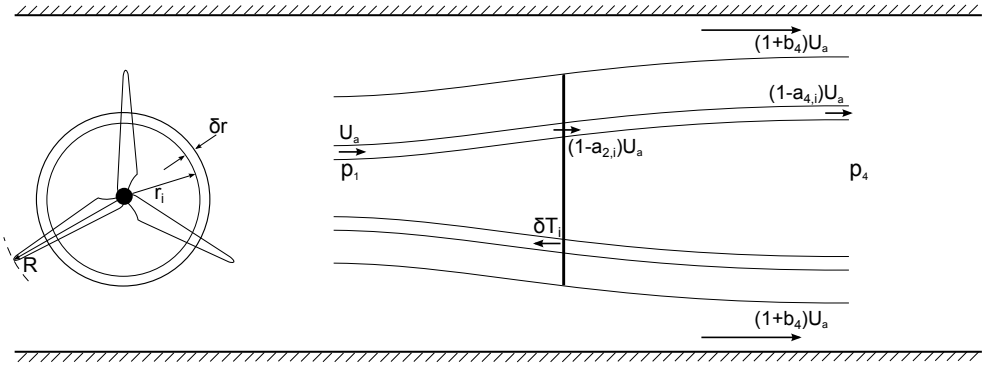

Figure 7.3: Diagram of the flow past a rotor in the i^{th} streamtube of width δr in the volume-flux constrained BEM model.

streamtube. The flow far upstream of the turbine has a uniform speed u_a, and the downstream boundary of the model is defined as the position at which the static pressure in the annular streamtubes passing through the turbine has equalised with the static pressure in the bypass flow around the turbine, as shown in Figure 7.3. Denoting quantities that vary with radius by the subscript i, the induction factor through turbine, $a_{2,i}$, and the induction factor in the turbine wake, $a_{4,i}$, are:

$$u_{2d,i} = (1 - a_{2,i})u_a, \tag{7.22a}$$

$$u_{4d,i} = (1 - a_{4,i})u_a. \tag{7.22b}$$

The bypass flow speed depends on the aggregate thrust applied by the annular streamtubes to the flow and thus is independent of annular position. The bypass induction factor, b_4 is therefore defined as:

$$u_{4b} = (1 + b_4)u_a. \tag{7.23}$$

In unblocked BEM theory, a fixed relationship $a_{4,i} = 2a_{2,i}$ may be used from momentum theory between the two induction factors in the turbine core flow because there is no acceleration of the flow bypassing the turbine. However, this assumption

must be relaxed in the volume-flux constrained model, and hence it is necessary to employ the volume-flux constrained model developed in Section 2.4.2 to provide a general relationship between u_{2d}, u_{4d}, and u_{4b} derived in Equation (2.54), which gives a relationship for $a_{2,i}$ in terms of $a_{4,i}$ and b_4:

$$a_{2,i} = \frac{b_4 + (1 - a_{4,i})(a_{4,i} - b_4)}{2(1 - a_{4,i}) + b_4}. \tag{7.24}$$

7.3.1 Determining the Bypass Flow Speed

An expression for b_4 is required to close the relationship between $a_{2,i}$ and $a_{4,i}$. Although the momentum change in each annular stream tube, and therefore the relationship between $a_{2,i}$ and $a_{4,i}$, is determined by the incremental thrust δT_i applied to the streamtube, the flow speed in the bypass depends on the total thrust applied by the turbine, and therefore b_4 is found by considering the aggregate thrust applied by the turbine to the annular streamtubes. Defining the total thrust to be:

$$T = \sum_{i=1}^{n} \delta T_i = \frac{1}{2} \rho A_d u_a^2 C_T, \tag{7.25}$$

where A_d is the total frontal swept area of the turbine and C_T is the overall thrust coefficient of the turbine. For clarity of the derivation, the definitions for the velocities at stations one and four in Equations (7.22) and (7.23) shall be substituted into the following expressions at the end. The change in momentum between stations one and four is found by considering the pressure difference across the turbine plane and the Bernoulli equation in the core and bypass flows to be (c.f. Section 2.4.2):

$$T = \frac{1}{2} \rho \left(u_{4b}^2 - u_{4d}^2 \right) A_d, \tag{7.26}$$

where it is noted that u_{4d} is an averaged value of the annular wake velocities at station four. The volume-flux constrained actuator disc model provides a quadratic

relationship between u_{4d} and u_{4b}:

$$(1-B)u_{4b}^2 - 2(u_a - u_{4d})u_{4b} + u_a^2 - 2u_a u_{4d} + Bu_{4d}^2 = 0. \tag{7.27}$$

Numerical stability of the solution as $B \to 0$ is ensured by writing u_{4b} in terms of u_{4d}, as this gives a $(1-B)$ term in the denominator. However, the quadratic may also be rearranged to give an expression for u_{4d} in terms of u_{4b}, as is convenient in the volume-flux constrained BEM model:

$$u_{4d} = \frac{u_a - u_{4b} \pm \sqrt{(1-B)(u_a - u_{4b})^2 + B^2 u_{4b}^2}}{B}, \tag{7.28}$$

in which the positive root is required to ensure $u_{4d} \geq 0$. Using the definitions for the induction factors $a_{4,i}$ and b_4, this may be equivalently written as:

$$a_{4,i} = 1 + \frac{b_4\sqrt{(1-B)b_4^2 + B^2(1+b_4)^2}}{B} \quad \forall i = 1, \cdots, n. \tag{7.29}$$

The latter expression is used to determine an initial guess for $a_{4,i}$ that is consistent with the initial guess for b_4 when iterating through the volume-flux constrained BEM model.

Eliminating u_{4d} between Equations (7.26) and (7.28) gives:

$$\frac{TB^2}{\frac{1}{2}\rho A_D} = B^2 u_{4b}^2 - \left((u_a - u_{4b}) + \sqrt{(1-B)(u_a - u_{4b})^2 + B^2 u_{4b}^2}\right)^2, \tag{7.30}$$

which, by expanding and simplifying the terms on the right hand side, noting the definition for C_T, eventually yields a quartic for $\beta_4 = (1+b_4)$ in terms of the blockage ratio B and the total thrust coefficient C_T:

$$3\beta_4^4 - 4\beta_4^3 + 2\beta_4^2(C_T(B-2)-1) + 4\beta_4(1+C_T(2-B)) - (1-BC_t)^2 - 4C_T = 0. \tag{7.31}$$

For appropriate values of C_T and B, this equation has a single root for which $\beta_4 \geq 1$, corresponding to $b_4 \geq 0$, which therefore allows the bypass induction factor to be calculated at each iteration of the model.

7.3.2 Finite Blockage BEM Model

The finite-blockage BEM model considers the incremental thrust and torque of an annular ring swept out by a blade element. The analysis follows the standard derivation of blade element momentum theory for wind turbines, such as that described in Burton *et al.* (2001), noting that the relationship between $a_{4,i}$ and $a_{2,i}$ is no longer constrained to $a_{4,i} = 2a_{2,i}$ and instead can be found using Equation (7.24).

It is assumed that the static pressure at stations one and four is uniform across all the annular streamtubes, so that conservation of axial momentum along the i^{th} annular stream tube requires:

$$(p_1 - p_4)\delta A_i - \delta T_i = -\rho \delta A_i u_a^2 (1 - a_{2,i}) a_{4,i}. \tag{7.32}$$

The difference in the upstream and downstream static pressure, $p_1 - p_4$, is eliminated using the Bernoulli equation in the bypass flow:

$$p_1 - p_4 = \frac{1}{2}\rho \left(u_{4b}^2 - u_1^2\right) = \frac{1}{2}\rho u_1^2 \left((1 + b_4)^2 - 1\right), \tag{7.33}$$

where again it should be noted that the bypass induction factor b_4 does not vary with radius. This arises from the assumption that the static pressure is uniform across all annuli and in the bypass flow at station four.

Equations (7.32) and (7.33) are combined to give an expression for the incremental thrust in terms of the annulus core induction factors, the bypass induction factor, and

the annulus cross-section, where it is noted that $\delta A_i = 2\pi r_i \delta r_i$:

$$\delta T_i = \rho \pi r_i u_a^2 \left(b_4^2 + 2b_4 + 2(1 - a_{2,i}) a_{4,i} \right) \delta r_i. \tag{7.34}$$

The incremental thrust on an annulus may also be expressed in terms of the lift and drag forces on the blade element in the annulus. The angle of incidence between the velocity relative to the blade and the direction of rotation is defined in Equation (7.11). Thus, given aerofoil properties such as the lift and drag coefficients, C_l and C_d respectively, which depend on the angle of attack, the number of rotor blades N_B, and the blade chord c_i on the i^{th} annulus, the incremental thrust can be found as:

$$\begin{aligned} \delta T_i &= \left(\delta L_i \cos \phi_i + \delta D_i \sin \phi_i \right) N_B \\ &= \frac{1}{2} \rho u_{\text{rel,i}}^2 N_B c \left(C_{l,i} \cos \phi_i + C_{d,i} \sin \phi_i \right) \delta r. \end{aligned} \tag{7.35}$$

Using the definition of annular solidity in Equation (7.18), the incremental thrusts in Equations (7.34) and (7.35) are equated to give:

$$b_4^2 + 2b_4 + 2(1 - a_{2,i}) a_{4,i} = \sigma_i \frac{u_{rel,i}^2}{u_a^2} \left(C_{l,i} \cos \phi_i + C_{d,i} \sin \phi_i \right). \tag{7.36}$$

Considering the components of velocity incident on the i^{th} blade and their relative angles, it is possible to show that:

$$(1 - a_{2,i}) u_a = u_{rel,i} \sin \phi_i, \tag{7.37}$$

which is used in Equation (7.36) to eliminate $u_{rel,i}$ and give an expression for $a_{4,i}$ in terms of the induction factors b_4 and $a_{2,i}$, the angle of incidence ϕ_i, and blade parameters σ_i, $C_{l,i}$, and $C_{d,i}$:

$$a_{4,i} = \frac{\sigma_i \left(1 - a_{2,i}\right)^2 \left(C_{l,i} \cos \phi_i + C_{d,i} \sin \phi_i \right) - b_4 \left(2 + b_4\right) \sin^2 \phi_i}{2(1 - a_{2,i}) \sin^2 \phi_i}. \tag{7.38}$$

The turbine is assumed to have a constant rotational speed Ω. Introducing a_i' as the rotational induction factor, the tangential velocity of the flow around the aerofoil section is given by $\Omega a_i' r_i$. The incremental torque on an annular ring, δQ_i, is then found by conserving angular momentum on the ring:

$$\begin{aligned}\delta Q_i &= \text{rate of change of momentum} \\ &= \text{mass flow rate} \cdot \text{change of tangential velocity} \cdot \text{radius}\end{aligned}$$

$$\delta Q_i = \rho \delta A_i u_a (1 - a_{2,i}) 2\Omega a_i' r_i^2. \tag{7.39}$$

The torque may equivalently be found by resolving blades forces on the turbine in the direction of rotation at distance r_i from the centre of rotation:

$$\begin{aligned}\delta Q_i &= r_i \left(\delta L_i \sin\phi_i - \delta D_i \cos\phi_i\right) N_B \\ &= \frac{1}{2}\rho u_{\text{rel,i}}^2 N_B c r_i \left(C_{l,i}\sin\phi_i - C_{d,i}\cos\phi_i\right)\delta r.\end{aligned} \tag{7.40}$$

Eliminating the incremental torque in Equations (7.39) and (7.40), it is found that:

$$2u_a(1 - a_{2,i})\Omega a_i' r_i = \frac{1}{2}u_{\text{rel,i}}^2 \frac{N_B c_i}{2\pi r_i}\left(C_{l,i}\sin\phi_i - C_{d,i}\cos\phi_i\right). \tag{7.41}$$

Noting that, by resolving velocity components on the i^{th} blade element:

$$u_{rel,i} = \frac{u_a(1 - a_{2,i})}{\sin\phi_i} = \frac{r_i\Omega(1 + a_i')}{\cos\phi_i}, \tag{7.42}$$

Equation (7.41) is used to give an expression for the tangential induction factor a_i':

$$a_i' = \frac{\sigma_i\left(C_{l,i}\sin\phi_i - C_{d,i}\cos\phi_i\right)}{4\sin\phi_i\cos\phi_i - \sigma_i\left(C_{l,i}\sin\phi_i - C_{d,i}\cos\phi_i\right)}. \tag{7.43}$$

The angle of incidence ϕ_i of the relative flow velocity $u_{rel,i}$ is found from the axial

velocity through the rotor and the tangential velocity of the rotor blades:

$$\tan \phi_i = \frac{(1 - a_{2,i})u_a}{r_i \Omega (1 + a'_i)}, \tag{7.44}$$

which then allows the improved estimate for the angle of attack α_i to be found, as the blade twist angle β_i is known from the rotor design:

$$\alpha_i = \phi_i - \beta_i. \tag{7.45}$$

7.3.3 Tip-loss Model

The analysis presented thus far assumes that all the fluid particles passing through the swept area of the rotor blades undergo the same loss of momentum. This assumes that there are sufficiently many blades in the rotor to ensure that all fluid particles interact with a blade as they pass through the rotor plane. However, this is often not the case, and a number of corrections have been proposed to address the effect that this has on the change in axial momentum in the flow.

One such method, Prandtl's tip loss model, has been widely applied to wind turbines to correct this problem (Leishman, 2006). The effect of the tip loss model is to reduce the axial induction factor $a_{2,i}$ to zero as the radial position approaches the tip of the rotor blade so that the velocity (and corresponding momentum) deficit reduces to zero towards the blade tips. This results in a proportional reduction in the incremental thrust and power as a result of the reduction in the momentum deficit at the tips. The Prandtl tip loss factor, F, is calculated as:

$$f_i = \frac{N_B}{2} \frac{R - r_i}{r_i \sin \phi_i} \tag{7.46}$$

$$F_i = \frac{2}{\pi} \arccos e^{-f_i}, \tag{7.47}$$

where R is the radius of the blade. In contrast to the standard BEM model, where the tip-loss model is applied to the turbine induction factor a and thus explicitly reduces both the turbine and wake velocity induction factors at the blade tips, the Prandtl tip-loss model is explicitly applied here only to $a_{4,i}$, as it is used to calculate $a_{2,i}$ (thus implicitly reducing the $a_{2,i}$ induction factor near the blade tips) and improves the agreement of the thrust and power calculations along the blade span with experimental tests of wind turbines.

7.3.4 Iterative Solution Procedure

Specifying blade and turbine parameters such as blade twist angle β, solidity σ, tip speed ratio λ, turbine local blockage B, and lift and drag curves, Equations (7.29) to (7.47) are sufficient to close the volume-flux constrained BEM model. An initial guess is required for b_4, with the choice of $b_4 = \delta$ where δ is some small perturbation from zero, and $a' = 0$ sufficient to provide good convergence to the final solution. The model is solved iteratively until convergence to ϵ is achieved, and it was found that $\epsilon = 10^{-6}$ provided quick convergence to an accurate solution. The convergence criterion was:

$$\epsilon = \max\left(|a_i'^{new} - a_i'^{old}|, |a_{4,i}^{new} - a_{4,i}^{old}|\right), i = 1, \cdots, n \tag{7.48}$$

where $a_i'^{new}$ and $a_{4,i}^{new}$ are updated each iteration with a relaxation factor γ:

$$\begin{aligned} a_i'^{new} =& \gamma \frac{\sigma_i \left(C_{l,i} \sin\phi_i - C_{d,i} \cos\phi_i\right)}{4 \sin\phi_i \cos\phi_i - \sigma_i \left(C_{l,i} \sin\phi_i - C_{d,i} \cos\phi_i\right)} \\ &+ (1-\gamma) a_i'^{old} \end{aligned} \tag{7.49}$$

$$\begin{aligned} a_{4,i}^{new} =& \gamma \frac{\sigma (1-a_{2,i})^2 \left(C_{l,i} \cos\phi_i + C_{d,i} \sin\phi_i\right) - b_4(2+b_4) \sin^2\phi_i}{2(1-a_{2,i}) \sin^2\phi_i} \\ &+ (1-\gamma) a_{4,i}^{old} \end{aligned} \tag{7.50}$$

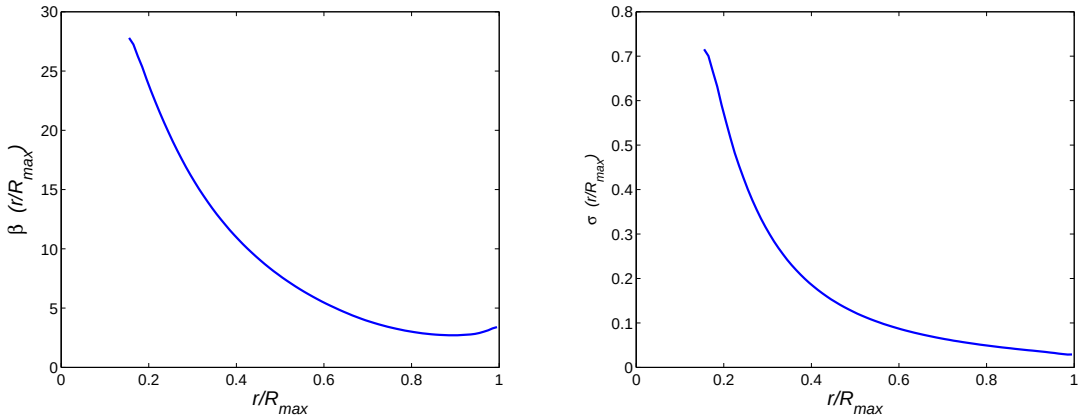

(a) Design blade twist angle for the unblocked turbine.

(b) Design solidity ratio for the unblocked turbine.

Figure 7.4: Design blade twist angle and solidity ratio vs. radius for the unblocked turbine designed by Schluntz (2014).

This improves convergence and stability. Typical values for γ are 0.2 initially, reducing by a factor of two after 100 iterations.

7.3.5 Comparison to Numerical Simulation

The volume-flux constrained BEM model developed in this chapter is compared to the results of numerical simulations of a turbine in different blockage configurations by Schluntz (2014). The two bladed, five metre diameter turbine, using the Risø-A1-24 aerofoil, was designed using a computational BEM design tool for operation in unblocked conditions. The design achieves a peak power coefficient $C_P = 0.57$ at a tip-speed ratio $\lambda = 5.1$. The design blade twist angle and solidity are shown in Figure 7.4.

Figure 7.5 compares the power coefficient vs. tip speed ratio curves of the unblocked design and the same turbine with a blockage ratio of $B = 0.20$. The peak power coefficient is increased from the unblocked maximum of $C_{P,max} = 0.57$ to a new maximum of $C_{P,max} = 0.73$ when the blockage ratio is $B = 0.20$. The tip-speed ratio for peak power coefficient increases from $\lambda = 5.1$ to $\lambda = 6.6$. The tip-speed ratio is

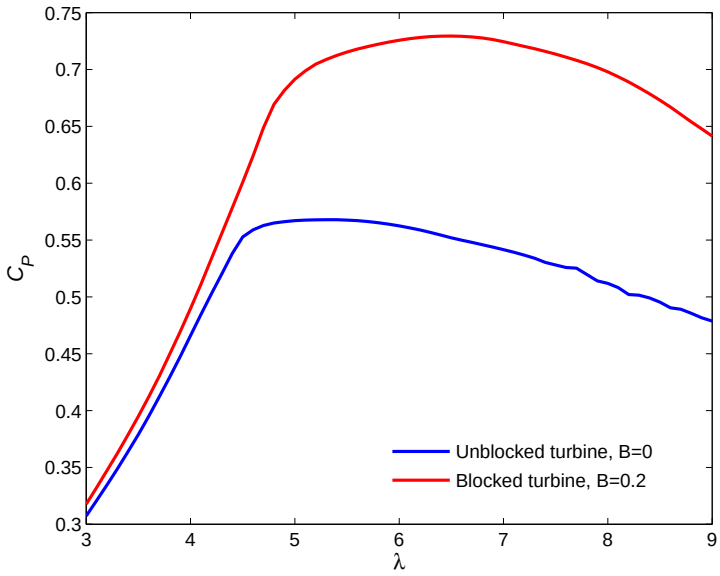

Figure 7.5: Comparison of the C_P vs. λ performance of the turbine in its design blockage ratio, $B = 0$, and in an off-design blockage ratio $B = 0.20$.

related to the thrust applied by the turbine and Figure 7.5 shows that deploying the turbine, designed for unblocked conditions, into a flow with a blockage ratio $B = 0.20$ allows a greater thrust to be applied to the flow and consequently a higher power to be removed from the flow. Deploying the turbine in higher blockage conditions, does not achieve the full increase in peak power coefficient predicted by an actuator disc model, which predicts a peak power coefficient of $C_{P,max} = 0.89$ for a blockage ratio $B = 0.20$, because it is not optimised for that blockage and therefore is unable to generate sufficient torque to achieve the theoretical power limit. Furthermore, viscous losses and vortex shedding mean that the power achieved by an optimally designed rotor will be below the theoretical power limit for an actuator disc.

The volume-flux constrained BEM model is compared to Reynolds-Averaged Navier-Stokes numerical simulations conducted by Schluntz (2014) for the same turbine design in Figure 7.6 for a range of spacing ratios (where $\frac{s}{d}$ is the spacing ratio normalised by the rotor diameter). Overall, the volume-flux constrained model agrees well with the RANS simulations, capturing both the trend of the numerical simulations and

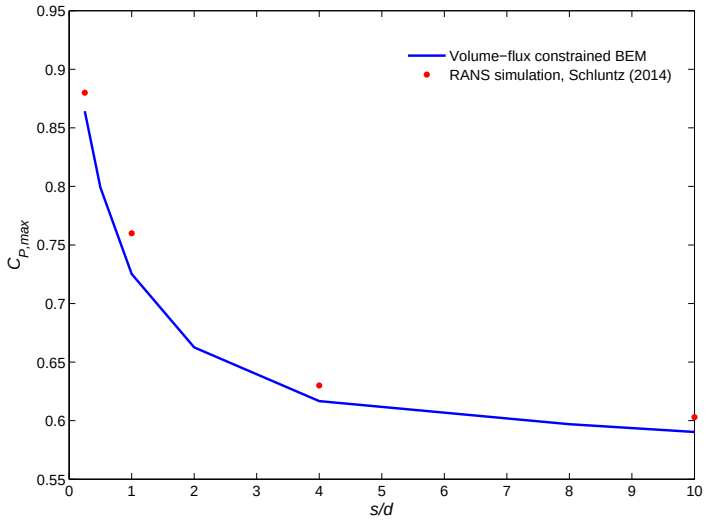

Figure 7.6: Comparison of the peak power coefficient vs. spacing ratio of the turbine using the volume-flux constrained BEM model (blue) and the RANS numerical simulations of Schluntz (2014) (red).

providing a very good approximation to the numerically determined peak power coefficient. It slightly underestimates the maximum power coefficient determined from the RANS simulations as the simulations incorporated a nacelle at the centre of the rotor, reducing the rotor swept area for a given blockage ratio (where blockage ratio is calculated using the sum of the rotor swept area and nacelle cross-section). The reduction in rotor swept area in the denominator of the power coefficient results in a higher power coefficient for the same power removed from the flow. Furthermore, the expansion of the wake in numerical simulations enhances the blockage effect in the flow, thus slightly increasing the flow speed through the turbine and therefore the peak power available to the turbine. Despite the small disagreement, the results indicate that the volume-flux constrained BEM model provides a very good approximation to the results seen in numerical simulations.

7.4 Conclusions

Blade element momentum theory has proved to be a very useful design and analysis tool for wind turbines. It has also proved to be useful in the design of tidal current turbines, although it has been necessary to embed the blade element model within a three-dimensional simulation of the flow around the turbine in order to model the effect the constrained expansion of the turbine wake has on the overall performance of the turbine. The key difference between the flows around a wind turbine and a tidal turbine is that a pressure gradient develops across the tidal turbine as a result of the volume-flux constraint imposed by the free surface and adjacent turbines. A volume-flux constrained blade element momentum theory has been developed to account for this dynamic, and the semi-analytic model has proved to agree very well with much more computationally expensive numerical simulations.

The uses of the volume-flux constrained BEM model are twofold; it is possible to utilise the theory to develop a design routine for volume-flux constrained turbines, and, once a turbine design has been established, it allows the thrust and power characteristics of the turbine to be determined in a variety of flow conditions. The volume-flux constrained BEM model shall be used in Chapters 8 to determine turbine characteristics when the turbine reaches rated power and the turbine performance has to be altered in order to maintain a specified rated power. The turbine thrust and power characteristics relative to upstream flow speed provide the necessary parameterisation of the turbine to conduct depth-averaged simulations of arrays of turbines and investigate the effects of power capping on array performance.

Chapter 8

Power Capping in a Tidal Array

Computers are useless. They can only give you answers.
- Pablo Picasso

The temporal variation in the strength of the tides that occurs due to the interaction of tidal constituents means that it may be economically advantageous to deliberately design a turbine array which does not maximise the peak power extracted from the tides. The most common methods used to limit the power of wind turbines are discussed, and the volume-flux constrained BEM model is used to determine the performance of the unblocked tidal turbine design of Schluntz (2014) as the blades are feathered during rated power operation.

The resultant thrust and power curves with respect to array flow speed are employed in depth-averaged simulations to investigate the performance of arrays with turbine power capping. Firstly, arrays with increasing local blockage are investigated in a channel with a fixed inflow speed, which shows that rated power is achieved at lower flow speeds as local blockage increases. Arrays with and without power capping are then simulated in tidal channels between two large basins to investigate the effect that power capping has on the flow through tidal channels. Two channels are considered, the first forced by the M2 semi-diurnal tidal constituent only, and the second by the M2 and S2 tidal constituents. The chapter concludes with a discussion of the factors that contribute to the selection of the rated power.

8.1 Introduction

Turbine operators wish to maximise the electrical power delivered to the grid over a given time period of, which may be one month if only the primary M2 (lunar semi-diurnal) and S2 (solar semi-diurnal) tidal constituents are considered. While at low flow speeds it may be reasonable to assume that turbines operate at their optimal power coefficient and tip speed ratio, this may not be the case at higher flow speeds. An electric generator which allows the peak monthly flow speed to be fully exploited would spend much of its lifetime operating significantly below its rated capacity, and would also not be able to exploit some of the lower flow speeds, due to, for example, the large inertia of the device. It would therefore be advantageous to install a smaller generator which, although it would not be capable of harnessing the full hydrodynamical power in peak flow conditions, would be able to harness more of the power in the flow over a tidal cycle, as well as potentially costing less. A consequence of using turbines with a rated power less than the peak power available in the tidal flow is that the power extracted from the flow is no longer related in a simple way to the cube of the flow speed, which requires the modelling of the turbines to be reviewed.

The power available to tidal turbines both individually and in large arrays has been estimated using a range of analytic and numerical methods. Analytic models, such as those presented in Chapters 2 and 3 provide a convenient first approximation to the power available to turbines. Such analytic models are based on actuator disc theory, and necessarily simplify both the turbine characteristics and surrounding flow field to provide a tractable model, and even more detail about the flow field can be included in numerical simulations, and high resolution three-dimensional simulations such as actuator line and blade resolved models. Detailed numerical simulations are limited to relatively small numbers of turbines, with the result that simulations of large arrays of turbines sacrifice some of the specificity of more detailed models of

smaller groups of turbines.

One simplifying assumption commonly made in analytic models and numerical simulations of large arrays of turbines approximated as actuator discs is that the turbine performance characteristics such as thrust coefficient do not change in response to varying flow conditions. Consequently the power output of the turbine is assumed to be proportional to the cube of the flow velocity. This simplification is unlikely to be feasible for many turbine designs, as it will be necessary to limit the power capture of the turbine to avoid the design strength being exceeded. Furthermore, the power capture of the turbine is likely to be limited by the generator capacity as a result of the variation in the tidal resource due to the variation in strength of the tides, as discussed in Section 1.1. The control of the turbine thrust and power results in significant departures from the momentum theory assumption of quadratic thrust and cubic power relationships with flow speed. It is therefore of interest to develop techniques which allow changes in turbine performance characteristics to be incorporated into large depth-averaged simulations.

Power capping will have a significant impact on how turbine arrays interact with tidal flows and the power that is extracted from them. The impact of an array on a tidal flow depends on the thrust it presents, which in turn depends on the rated power of the turbines and the means by which that rated power is maintained. These properties can be explored by considering the behaviour of the turbine during power capping given the hydrodynamic properties of the turbine blades. The impact of the turbine array will also depend on the inter-turbine spacing within the array, and therefore the volume-flux constrained BEM model developed in Chapter 7 will be used to determine the relationship between thrust, power, and flow speed when the turbine blockage is non-zero. If the rated power and power control mechanism during power capping of a turbine are known, then the volume-flux constrained BEM model can subsequently be used to determine the relationship between turbine thrust and flow

speed, which can then be used in numerical simulations of arrays of tidal turbines.

8.2 Turbine Power Capping

Two primary motivations for power capping exist: strength limitations in the turbine structure, and optimisation of the economics of the turbine and generator subject to the available tidal resource. The first motivation defines the flow speed at which the turbine must be shut down to prevent excessive damage to the rotor and turbine structure, whereas the second defines the maximum power that may be extracted from the flow by the turbine and the flow speed at which rated power is first achieved. The turbine must therefore have a hydrodynamically effective method for controlling its rotational speed and power.

The hydrodynamic forces on the rotor can be reduced by changing one of, or some combination of: the angle of attack of the blades, the swept area of the rotor, or the effective velocity at the rotor blades (achieved by changing the rotational speed of the rotor). The most effective of these methods for controlling the power of large turbines is to change the angle of attack (Hau and von Renouard, 2006). The power is reduced by decreasing the angle of attack (feathering) by rotating the blade around its longitudinal axis, and turbine cut-out is achieved by aligning the blade chord with the direction of the oncoming flow. Turbine power may also be controlled by increasing the angle of attack, which can lead to separation of the flow over the blade and the onset of stall. The increase in angle required to induce stall is generally smaller than limiting the power by decreasing the angle of attack. Pitching the blades toward stall tends to maintain a roughly constant load on the rotor blades, whereas the loads reduce if the blades pitch to feather, which may have structural benefits. However, limiting power through stall in wind turbines has not been found to be provide as smooth control as in pitching the blades to feather, which has favoured

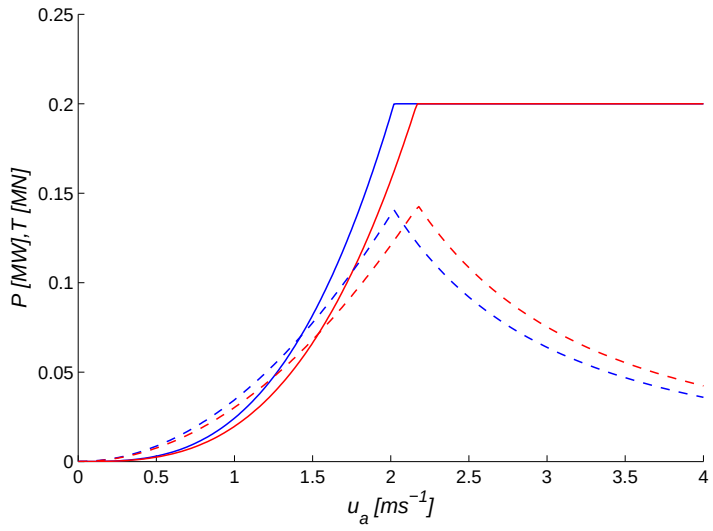

Figure 8.1: Comparison of power (solid) and thrust (dashed) of a 200 kW turbine in blocked (blue) and unblocked (red) conditions. The vertical dashed lines indicate the respective rated flow speeds.

the development of feather-controlled wind turbines (Hau and von Renouard, 2006). Smooth and continuous blade control also allows the output power to be controlled effectively.

8.2.1 Application to Turbine

The volume-flux constrained BEM model developed in Chapter 7 is applied to the turbine designed by Schluntz (2014) introduced in Section 7.3.5 to determine its performance characteristics during rated power operation. The turbine is compared in blocked ($B = 0.20$) and unblocked conditions in Figure 8.1, and it can be seen that a rated power of 200 kW is achieved at a rated flow speed $u_r = 1.99\text{ms}^{-1}$ in the blocked case, as compared to $u_r = 2.16\text{ms}^{-1}$ for the unblocked turbine. The rotor has a cut-out flow speed of 4ms^{-1}, above which the turbine shuts down. It can be seen that the peak thrust in the unblocked case is slightly higher than the peak thrust in the blocked case, although the exact relationship between thrust and flow speed will depend on the method adopted for maintaining rated power. The minimum flow

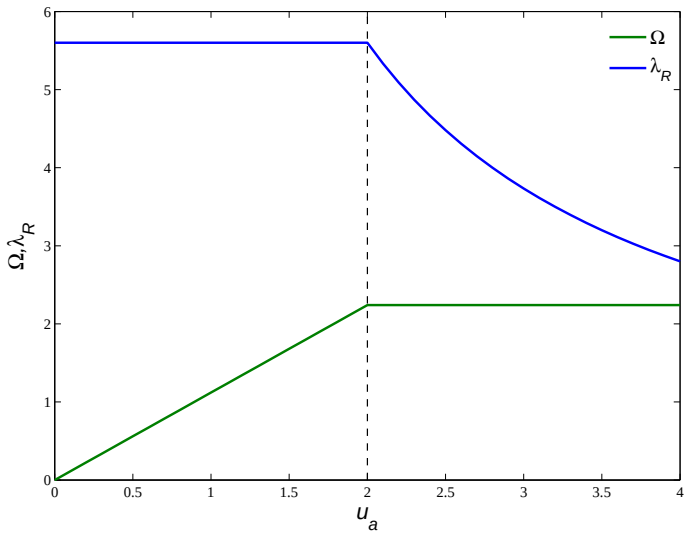

Figure 8.2: Variation of tip speed ratio λ and rotational speed Ω with flow speed u_a.

speed that must be achieved in order for the blades to start rotating (also known as the 'cut-in' speed) is neglected for simplicity.

It shall be assumed in the remainder of the chapter that rated power is maintained by pitching the blades to feather for the reasons discussed earlier. It shall further be assumed that the control strategy holds the rotational speed of the turbine constant while operating at rated power, consistent with the generator having an optimal rotational speed. As the peak power coefficient is maintained until rated power is achieved, the tip-speed ratio λ is also assumed to be constant until rated power is achieved. Therefore the rotational speed Ω increases linearly from stationary until rated power is achieved, beyond which Ω is constant with increasing flow speed and λ reduces, as show in Figure 8.2.

The turbine power coefficient, proportional to velocity cubed, reduces during power capping in order to maintain a constant overall rated power P_R:

$$C_{P,R} = \frac{P_R}{\frac{1}{2}\rho u_r^3 A_D}\frac{1}{\gamma^3} = C_{P,peak}\frac{1}{\gamma^3}, \tag{8.1}$$

where $\gamma = \frac{u_a}{u_r} \geq 1$ is the ratio of the flow speed to the rated speed. $C_{P,R}$ thus reduces

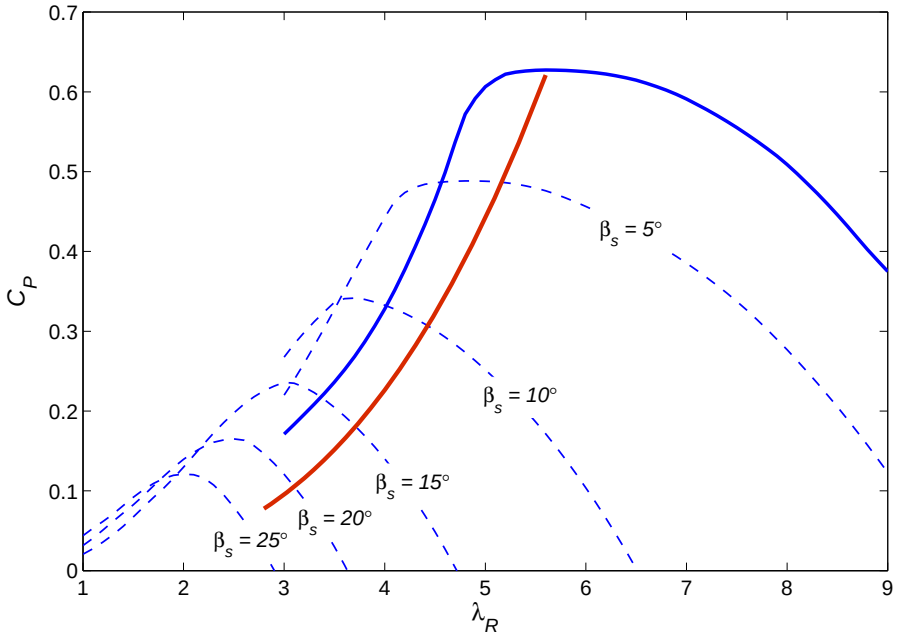

Figure 8.3: $C_P - \lambda$ trajectory (red) followed by turbine control algorithm during power capping. The solid blue curve is the $C_P - \lambda$ curve with $\beta_S = 0°$ blade pitch, and the dashed blue lines show the power curve for increasing blade pitch angles. The blockage ratio is $B = 0.20$.

from the turbine's peak power coefficient as γ^{-3}. Utilising the assumption that the rotational speed is fixed during the power capping regime, the tip speed ratio, which depends linearly on rotational speed and free stream velocity, must also reduce as the flow speed increases, as was illustrated in Figure 8.2:

$$\lambda = \frac{R\Omega_R}{u_a} = \lambda_R \frac{1}{\gamma}, \tag{8.2}$$

where R is the radius of the rotor and λ_R is the tip speed ratio at the rated flow speed.

Equations (8.1) and (8.2) describe the $C_P - \lambda$ trajectory that the turbine control algorithm follows during power capping, shown in red in Figure 8.3. The solid blue line in the figure is the design $C_P - \lambda$ curve in a blockage ratio $B = 0.20$. The dashed blue lines give the power coefficient vs. tip speed ratio curves for increasing blade

pitch-to-feather angles as labelled on the figure. It can be seen that pitching the blade to feather, which reduces the angle of attack, reduces the turbine power coefficient as blade pitch is increased. Peak power coefficient also shifts to lower tip speed ratios as blade pitch is increased. The turbine operates at the peak power coefficient $C_P = 0.63$ and corresponding tip speed ratio $\lambda = 5.5$ until rated power is achieved. The turbine control algorithm then tracks towards the bottom left of the red curve, increasing the blade pitch to approximately 25° before the cut-out flow speed is reached.

The thrust applied by the turbines to the flow can be specified in terms of two separate phases, in a similar manner to that of the turbine power. Below the rated flow speed, the turbine is assumed to operate constantly at the peak power coefficient and corresponding thrust coefficient, which is related to the power coefficient by a factor of the mean value $1 - a_2$ as determined from the volume-flux constrained BEM model. During the power capping phase, the thrust coefficient is the resultant axial force vector determined from the blade lift and drag forces at a given blade pitch angle. The thrust coefficient can be determined by matching the power coefficient vs. tip speed ratio control curve (red) to the power curves (dashed blue) at different feathering angles and determining the resultant thrust coefficient at those angles.

Matching the power coefficient vs. tip speed ratio relationship in power capping operation to the performance of the turbine with feathered blades yields a curve of thrust coefficient vs. flow speed, as shown in Figure 8.4. The thrust coefficient is constant at $C_T = 0.97$ until the new rated flow speed $u_r = 1.99\text{ms}^{-1}$ is achieved, after which the thrust coefficient rapidly reduces as the blades are pitched towards feather, ultimately reducing to $C_T = 0.11$ at $u_a = 4\text{ms}^{-1}$.

The relationship between thrust coefficient and velocity is dependent on the lift-drag ratio of the turbine blades at different angles of attack, and will therefore vary for different turbine designs. If a pitch-to-stall power capping mechanism is employed instead of the pitch-to-feather method proposed here, the thrust coefficient may not

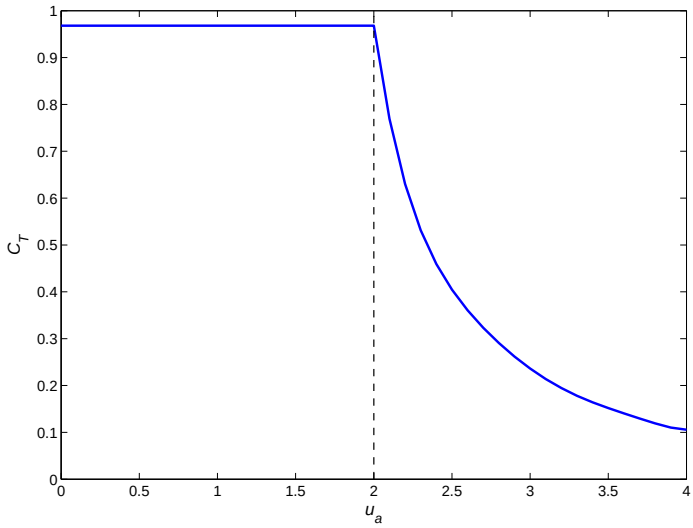

Figure 8.4: Thrust coefficient C_T vs. array flow speed u_a for the turbine in blockage ratio $B = 0.2$.

reduce as significantly as demonstrated here, and indeed may even increase. The higher thrust of pitch-to-stall devices may present sufficient impedance to the flow in the channel so as to reduce the flow rate through the turbine array. The merits and drawbacks of different control mechanisms are related closely to the specific turbine hydrofoil, the ambient flow conditions, and the generator and turbine structure, and should be carefully considered during the turbine design process, both for their effect on an individual turbine and on a turbine array.

The thrust vs. power curves for the present rotor in blocked ($B_L = 0.2$) and unblocked conditions are presented in Figure 8.5 in both dimensional and non-dimensional form. C_P vs. C_T is presented in non-dimensional form in Figure 8.5a. The turbine operates at top-right end of the blocked and unblocked curves from start-up until rated power is achieved, at $C_P = 0.63$, $C_T = 0.87$ for the blocked rotor and $C_P = 0.5$, $C_T = 0.75$ for the unblocked rotor. The rotors follow their respective trajectories toward the bottom-left of the curves to a final power coefficient $C_P = 0.08$ in both cases when the cut-out flow speed of 4ms^{-1} is reached. The thrust coefficient at the cut-out flow speed is different in the two cases, where the thrust coefficient of the blocked

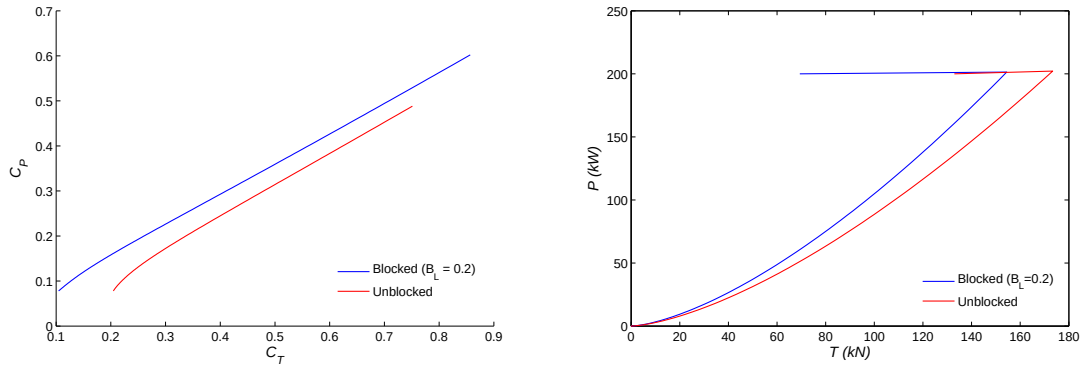

(a) C_P vs. C_T (b) P vs. T

Figure 8.5: Comparison of turbine C_P vs. C_T (left) and P vs. T (right) for turbine in blocked $B_L = 0.2$ (blue) and unblocked (red) flows.

rotor, $C_T = 0.10$, is approximately half that of the unblocked rotor, $C_T = 0.21$. This is a consequence of the thrust of the unblocked rotor at the cut-out velocity being approximately double that of the blocked rotor for the specified power capping characteristics. As expected, the gradient of the two curves is similar because the rotors maintain rated power through the same control mechanism.

It is informative to investigate the differences in the dimensional thrust vs. power curves of the rotor in blocked and unblocked conditions, as presented in Figure 8.5b. The thrust and power both increase from zero to the rated power, 200kW, after which the thrust is reduced whilst maintaining the power at 200kW. A number of key differences are observed between the blocked and unblocked cases: firstly, the gradient of the blocked curve is greater than that of the unblocked curve; secondly, rated power is achieved at a lower thrust for the blocked rotor than the unblocked rotor; and finally the thrust at cut-out is significantly lower for the blocked turbine than the unblocked turbine. The higher gradient of the blocked thrust vs. power curve is due to the greater power coefficient of the blocked turbine than that of the unblocked turbine. Thus, for a given thrust level, the blocked turbine will achieve a higher power than the unblocked turbine, hence the blocked turbine attains rated power at a lower thrust than the unblocked turbine. Once the blocked turbine reaches

rated power, its thrust begins reducing in order to maintain rated power, whereas the thrust on the unblocked turbine must continue to increase until rated power is achieved. As a result, the thrust of the blocked turbine is ultimately lower than that of the unblocked turbine when the cut-out flow speed is reached as the thrust on the blocked turbine has been reducing for a longer time.

The flow dynamics responsible for the differences between the thrust and power curves of the blocked and unblocked turbines arise as a result of the effect the volume-flux constraint has on the flow around the turbine. The wake expansion is increasingly constrained as the local blockage ratio increases, resulting in higher streamwise flow speeds in the wake and rotor plane. The higher streamwise rotor plane velocity means that the relative flow speed incident on the blades increases, resulting in higher thrust and torque along the blade span, and therefore increased thrust and power of the rotor. Thus, for a given upstream flow speed, rotors in more highly locally blocked flows are able to apply a greater thrust and extract a greater power from the flow than the same rotor in a lower local blockage. The higher streamwise flow speed that is developed in higher local blockages means that extracting a given power level may be achieved with a lower thrust, the reduction in thrust coefficient being a function of the lift and drag along the blade. The improvement in rotor performance in higher blockage ratios may be optimised by choosing the angle of attack, blade twist, and solidity in order to maximise power that is extracted from the flow in a specified blockage condition.

8.3 Effect of Power Capping in a Channel with Constant Flow Speed

The effect of turbine power capping on the power extraction of an array of sixteen 20m diameter turbines partially spanning a rectangular channel with a constant upstream

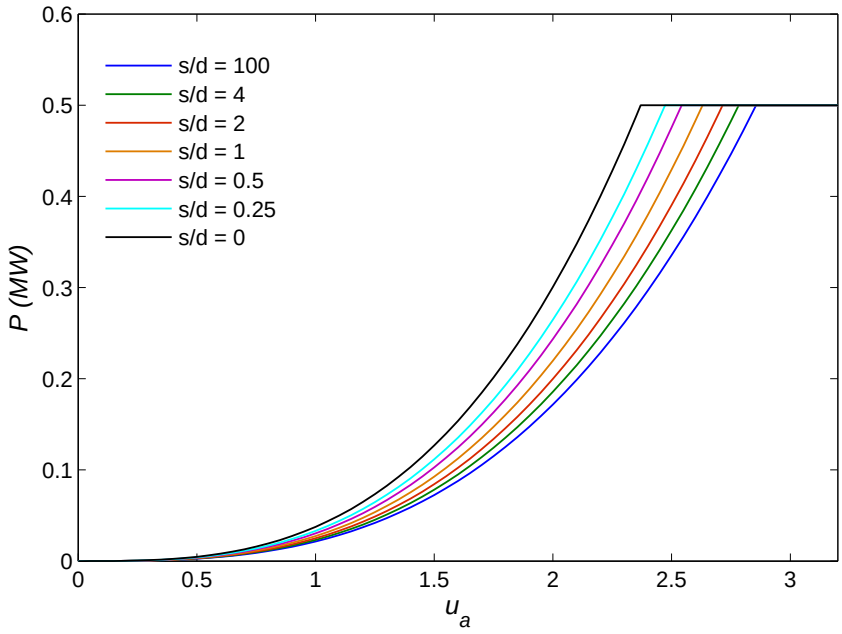

Figure 8.6: Turbine power P vs. array flow speed u_a for six inter-turbine spacing ratios.

flow speed is investigated for six different local blockage ratios. The channel has a constant depth of two diameters and the width of the channel is varied to maintain a constant array blockage of $B_A = 0.2$ for each of the different local blockage ratios. The upstream flow speed of the channel, u_a, is varied between 0 and 3.2ms^{-1}.

The turbines in the array are designed for operation in an unblocked flow with a rated turbine power of 0.5 MW, and are tested in a range of inter-turbine spacing ratios (corresponding to local blockage ratios between 0 and 0.4), parameterised by the inter-turbine spacing s, and the device diameter d. The 0.5 MW turbines have a rated flow speed of 2.86ms^{-1}. Figure 8.6 compares the turbine power vs. flow speed curves for a turbine near the centre of the array. The array flow speed at which the rated power of 0.5 MW is achieved reduces as the inter-turbine spacing reduces (local blockage increases), reducing to 2.37ms^{-1} when the inter-turbine spacing is reduced to $s = 0d$, so that the turbine blades touch, which corresponds to a local blockage of approximately $B_L = 0.40$.

Rated power is achieved at lower flow speeds when inter-turbine spacing is reduced due to an increase in the flow speed through the turbine for a given level of thrust. The increase in flow speed is achieved through the increased constraint on the expansion of the turbine wake when inter-turbine spacing is reduced. Greater thrust may be applied by turbines in more closely spaced arrays for a given flow speed, leading to the steeper power curves in Figure 8.6 before rated power is achieved. The higher thrust applied by the denser arrays allows rated power to be achieved at lower flow speeds than for sparse arrays. The dynamics may also be considered in reverse; for a given thrust, the through-turbine flow speed is higher for the more closely spaced turbines, allowing a greater power to be removed from the flow than for turbines spaced further apart.

It is consequently advantageous to minimise the inter-turbine spacing where possible in order to achieve the turbine rated power at lower flow speeds. Performance may be further improved through optimisation of the turbine design for the intended operational blockage ratio. The blade pitch and solidity can be prescribed to fully exploit the greater impedance of the constrained bypass flow that is achieved in closely spaced turbine arrays. Further benefits of dense turbine arrays may include minimisation of electrical cabling and more efficient use of support structures.

8.4 Effect of Power Capping in a Dynamic Tidal Channel

As discussed in Section 1.1, the magnitude of the tides at the coast varies over time due to the interaction of different tidal constituents. The strength of the tides at a particular coastal site, and the dominant constituents, depends on the resonances that develop from the interaction with the deep ocean, the continental shelf, and the bathymetry and geometry of the coastal site. One consequence of the temporal

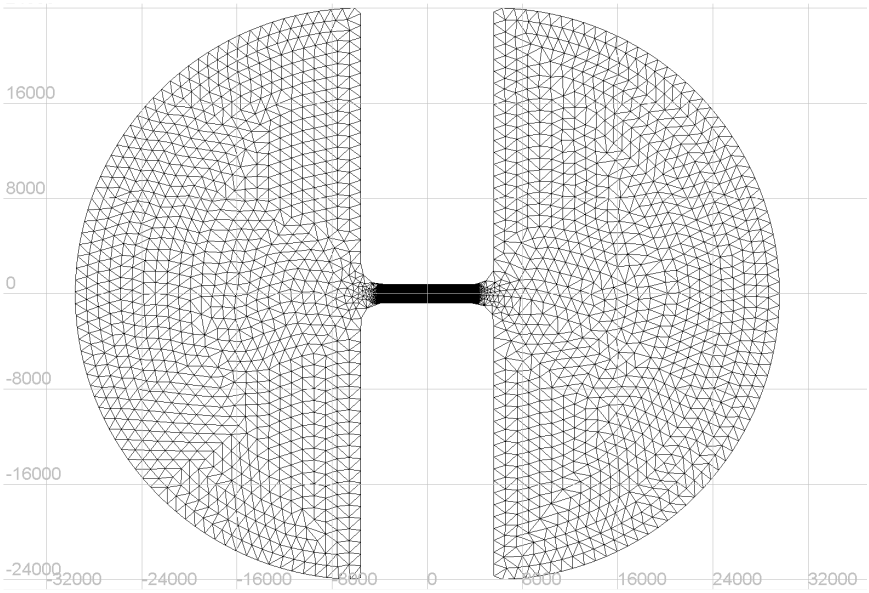

Figure 8.7: Flow domain for the dynamic tidal channel simulations. Dimensions are given in metres.

variability of the tides, as opposed to a flow in which there is a constant upstream flow speed, is that it becomes important for the economics of an array of tidal turbines to select an appropriate generator size for the available tidal resource. This section investigates the power extracted from an idealised tidal channel between two large bodies of water by an array of tidal turbine with turbine power capping, simulated in TELEMAC-2D. The geometry of the idealised tidal channel, which is 8000m long and 1600m wide in the inner portion, is shown in Figure 8.7. The depth of the channel and surrounding basins is constant at 40m. The channel expands smoothly into the large basins at either end with rounded inlets and outlets with a radius of 2000m. The flow in the channel is driven by a head difference that is applied to the east and west boundaries of the model, corresponding to the open oceans. Two cases are considered; forcing by the M2 tidal constituent only, to provide a simple comparison case; and forcing by the M2 and S2 tidal constituents, which is more reflective of real-world sites.

An eight turbine array is modelled in the centre of the inner portion the channel,

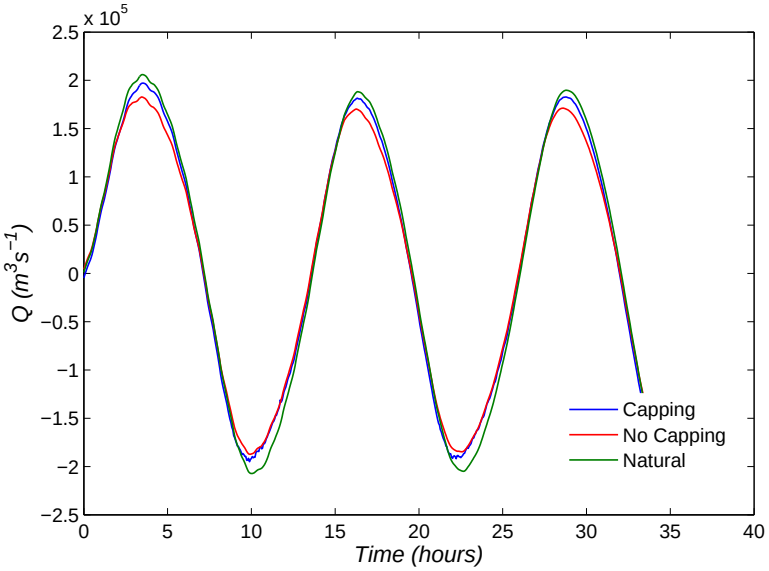

Figure 8.8: Volume flow rate in a tidal channel driven by the M2 tide with no turbine array (green), a turbine array without power capping (red), and a turbine array with power capping (blue).

using the thrust vs. velocity and power vs. velocity characteristics determined for the rotor considered previously in a blockage $B_L = 0.2$. As the thrust and power characteristics account for the effect of the unresolved flow around the turbine and the local blockage, it is not necessary to apply the correction factor for depth-averaged array simulations developed in Chapter 6 to these simulations. The rated power of each turbine is 1.25 MW, for an array rated power of 10 MW.

8.4.1 M2 Tidal Constituent

The channel is forced with the M2 tidal constituent with a period of 12.42 hours and a tidal range amplitude of 50 cm. Figure 8.8 shows the volume flux through the channel over three tidal cycles for the natural case where there is no energy extraction from the flow (shown in green), the array with turbine power capping (shown in blue), and the array without turbine power capping (shown in red). The peak volume flux through the channel in the natural case is $206600\text{m}^3\text{s}^{-1}$, which reduces to $196000\text{m}^3\text{s}^{-1}$ when the array with power capping is simulated, reducing further to $184900\text{m}^3\text{s}^{-1}$ when the

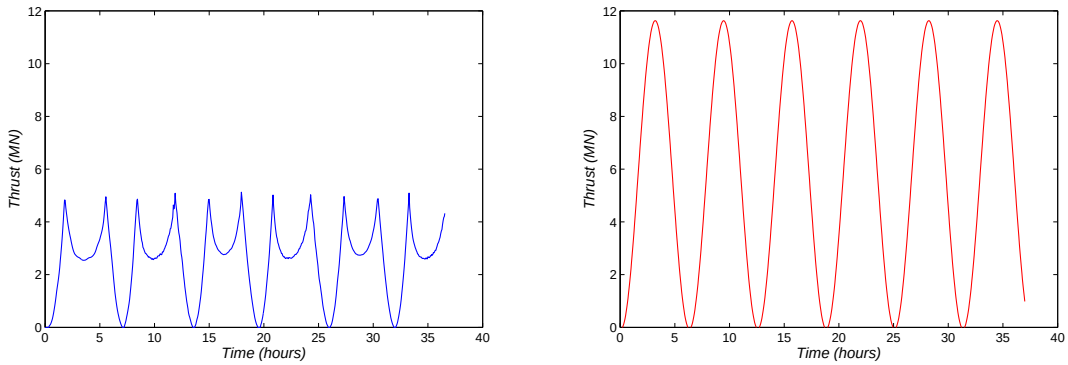

(a) Thrust vs. time for the power capping array.

(b) Thrust vs. time for the array without power capping

Figure 8.9: Comparison of thrust vs. time curves for the turbine array with (blue) and without (red) power capping implemented in a channel forced by the M2 tide.

array without power capping is simulated. The reduction in flow through the array arises as a result of the thrust applied to the flow in the channel by the turbine array.

The total thrust applied by the turbine array with and without power capping is shown in Figure 8.9. Turbine thrust in both cases increases at the same rate until rated power is achieved by the power capping array. The array thrust for the non-power capping array varies sinusoidally over time in constant proportion (through the constant thrust coefficient) to the flow speed through the array. The thrust of power capping array, by contrast, varies in a complicated manner over time as a result of power capping. Before the rated flow speed is achieved through the turbine array, the turbines in both arrays operate at the same thrust coefficient and thus the thrust of both arrays increases at the same rate. Once rated power is achieved the thrust of the non-power capping array continues to increase, whereas the thrust on the power capping array reduces in order to maintain a constant level of power extraction from the flow. The thrust reduces more quickly while the flow speed is increasing in the channel than it is decreasing because the reduction in thrust creates a positive feedback with the increasing flow speed in the channel. The higher flow speed through the turbine results in a lower array thrust, which in turn increases

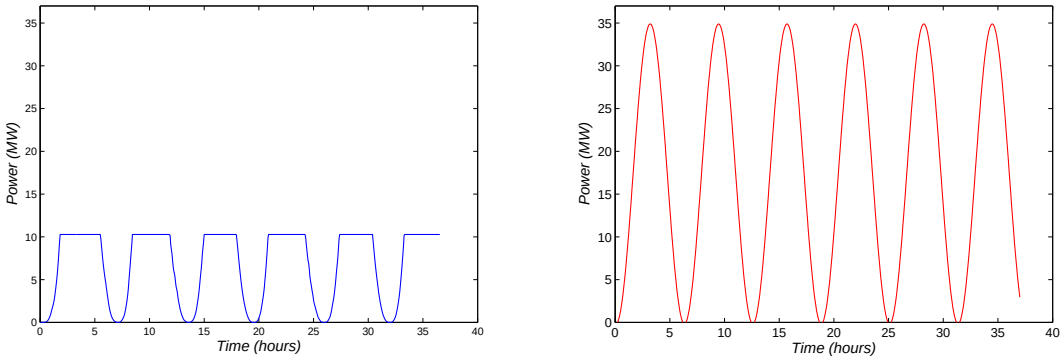

(a) Power vs. time for the power capping array.

(b) Power vs. time for the array without power capping

Figure 8.10: Comparison of power vs. time curves for the turbine array with (blue) and without (red) power capping implemented in a channel driven by the M2 tidal constituent.

the flow speed through the array. As the flow speed in the channel decreases, the array thrust increases to maintain rated power. The thrust coefficient and the rate of change of the thrust coefficient are both relatively small at the peak flow speed through the channel, thus small changes in the flow speed through the array yield only small changes in the thrust applied to the flow in order to maintain rated power. As the flow speed decreases and approaches the rated flow speed, the rate of change of thrust with flow speed increases, resulting in a negative feedback. The opposite feedbacks between the flow speed and array thrust during the power capping regime give rise to the asymmetric thrust-time curve.

The power extracted from the flow by the two arrays is shown in Figure 8.10. The rated power of the array, 10 MW, is relatively small compared to the power that might be extracted from the channel if it is assumed that the array power is proportional to the cube of the flow speed through the array, as in the non-power capping array. As the power capping array spends much of its time at rated power, the array applies a relatively low thrust to the flow, and hence there is only a small impact on the flow through the channel as compared to the natural case, as was shown in Figure 8.8.

The non-power capping array, which at peak extracts almost four times more

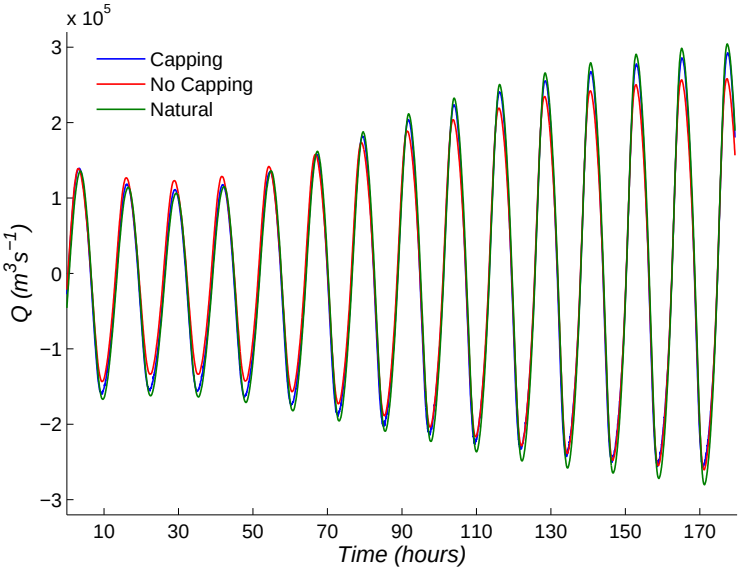

Figure 8.11: Volume flow rate in a tidal channel forced by the M2 and S2 tidal constituents with no turbine array (green), a turbine array without power capping (red), and a turbine array with power capping (blue).

power from the flow than the power capping array, causes a significant change in the flow through the array as compared to the undisturbed channel, and also significantly reduces the flow speed through the array as compared to the rest of the channel, which increases the mixing losses in the array wake. Stronger mixing in the array wake in turn results in more dissipation of energy from the flow than the power capping case, and hence the far field impact of power extraction is much greater when power capping is not employed within the array.

8.4.2 M2 and S2 Tidal Constituents

The channel is now forced with the M2 and S2 tidal constituents. The M2 tidal constituent is retained as in the previous channel, and the S2 tidal constituent, which has half the tidal amplitude of the M2 tide and a period of 12 hours, is added. The volume flux through the channels simulated with no power extraction, and then simulated with turbine arrays with and without power capping are shown in Figure 8.11. The peak undisturbed volume flow rate at the spring tide is approximately

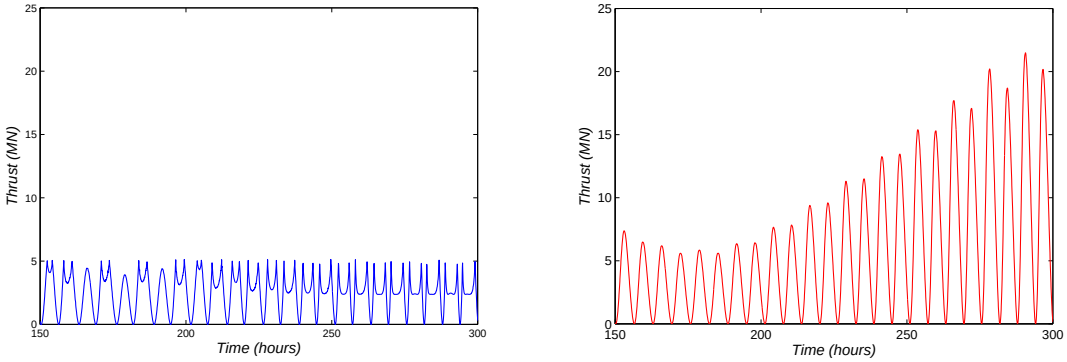

(a) Thrust vs. time for the power capping array.

(b) Thrust vs. time for the array without power capping

Figure 8.12: Comparison of thrust vs. time curves for the turbine array with (blue) and without (red) power capping implemented in a channel forced by the M2 and S2 tidal constituents.

twice that at the neap tide in the idealised channel. The volume flux through the channel is reduced in response to power extraction, by a relatively small amount for the channel with the power capping array, and more significantly in the case of the non-power capping array, where the volume flux is reduced by approximately 15% of the natural flux.

The thrust applied to the flow by the capping and non-capping arrays is shown in Figure 8.12. The thrust of the non-power capping array varies quadratically with the flow speed in the channel, and the flow speed through the array is reduced to approximately 75% of that at the upstream boundary of the channel at the spring tide. At the neap tides where the undisturbed flow rate through the channel is relatively small there is little reduction in the thrust applied by the power capping array during the power capping phases. Rated power is achieved relatively quickly, even for the majority of the neap tides due to the low level of power removed from the flow relative to the total energy in the channel.

The power capping regime becomes more established as the flow approaches the spring tide and the volume-flux through the channel increases. There are two main effects on the thrust during the power capping regime. Firstly, the thrust reduces to

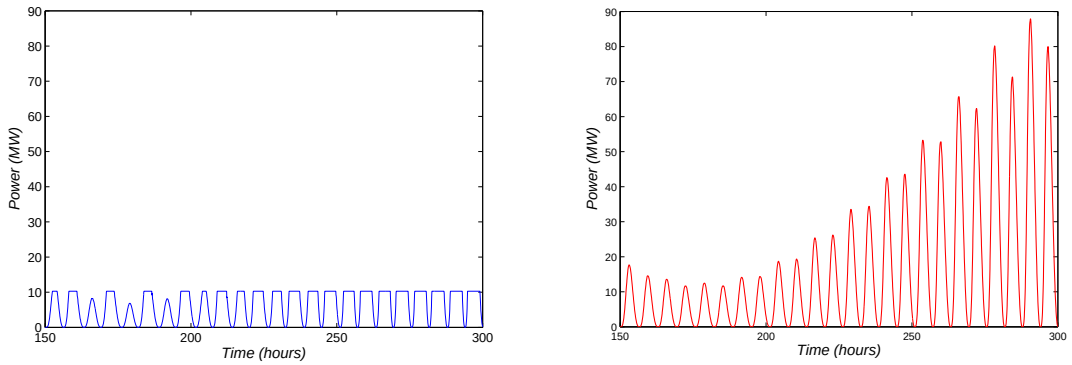

(a) Power vs. time for the power capping array.

(b) Power vs. time for the array without power capping

Figure 8.13: Comparison of power vs. time curves for the turbine array with (blue) and without (red) power capping implemented in a channel forced by the M2 and S2 tidal constituents.

lower levels until it plateaus at approximately 2.5 MN. Secondly, the rate of decrease in thrust described in Section 8.4.1 becomes greater as the volume-flux through the channel increases. The first of these phenomena is the result of the reduction in the incremental change in the thrust coefficient in Figure 8.4 at high flow speeds, and a state of equilibrium is reached with the increasing flow speed and the reducing thrust coefficient. The second dynamic is a result of the more rapid change in flow speed in the channel as the tidal range and flow speed increase as the spring tide is approached.

The power extracted from the flow by the capping and non-capping arrays is shown in Figure 8.13. The power extracted by the non-power capping array is cubically proportional to the flow speed. Although the turbine array is relatively small, a peak power extraction of approximately 90 MW is predicted in the channel, considerably higher than the rated power of the 10 MW turbine array. The greater power extraction can be sustained in the present channel as the energy in the flow is relatively high, and suggests that it may be appropriate to install more than eight power capping turbines. However, the impact of the non-power capping array on the flow is considerably greater, as evidenced by the significant reduction in volume flux through the channel, and there is stronger wake mixing downstream of the array.

8.4.3 Discussion

It is informative to define a number of statistics about the arrays. The capacity factor (CF) is the ratio of the power extracted by the array to the rated power over some period of time; a capacity factor of one indicates that the rated power is extracted at all times, and the capacity factor reduces as more time is spent below rated power. The capacity factor, CF_{M2}, of the power capping array in the channel forced with the M2 constituent is $CF_{M2} = 53.1\%$. In the case of the channel driven by the M2 and S2 tidal constituents the capacity factor is slightly higher, at $CF_{M2+S2} = 55.2\%$. The relatively high capacity factors of the arrays indicate that they operate at the rated power for a significant fraction of the tidal cycle, which is beneficial for the economic operation of the arrays.

The capacity factor does not directly reflect the power available in a time-varying flow, so the power factor is introduced as the ratio of the power extracted by the power capping array to the power extracted by the non-power capping array to reflect the maximum power that would be extracted from the flow at the optimal thrust coefficient. The power factor of the array in the first channel was $PF_{M2} = 47.4\%$, indicating that the power capping array was extracting a substantial proportion of the total power that might be extracted from the channel. In the second channel the power factor was $PF_{M2+S2} = 28.4\%$, indicating that less of the power available in the second channel was extracted relative to that in the first. This occurs because the flow speed in the channel is higher at the spring tide due to the superposition of the M2 and S2 tides. The peak power, proportional to the cube of the flow speed, thus increases in the M2 + S2 simulation. The relatively low power factor in the M2 + S2 channel indicates that it may be appropriate to deploy more turbines to extract more of the power available in the flow.

The power available to turbines in dynamically forced channels is a function of the flow conditions in the channel and the thrust applied by the turbines on the

flow. The minimal natural dissipation of the idealised channel presented in this chapter meant that the volume flux through the channel was primarily influenced by the array thrust in each simulation. However, Garrett and Cummins (2005) and Vennell (2010) have analytically considered the dynamic balances in channels between the tidal amplitude, bed friction and natural dissipation in the channel, and power available to the turbines, and found different behaviour depending on the relative magnitude of the different contributors. These factors, in conjunction with constraints such as limitations on the far field reduction in flow speed and mixing in the array wake, will play an important role in the optimal choice of the array's rated power.

8.5 Conclusions

The volume-flux constrained blade element momentum theory model developed in Chapter 7 has been applied to a rotor design where it was assumed that the pitch of the blades was feathered to reduce the thrust on the flow and hence limit the turbine power. It was further assumed that the tip speed ratio of the turbine reduced as the flow speed increased beyond the rated flow speed in order to maintain a constant rotational speed of the turbine. These conditions yield a control curve in $C_P - \lambda$ space which are sufficient to define the turbine performance during power capping and allow the device thrust to be determined. The parameterisation of the turbine in terms of P vs. u_a and T vs. u_a curves provides the necessary input to depth-averaged simulations to allow the effect of power capping on array performance to be studied. Rated power is achieved at a lower flow speed and lower thrust as the local blockage ratio increases. Equivalently, for a given thrust level, the flow speed through the turbine, and hence the power, is higher as the local blockage ratio increases. The thrust on a highly blocked turbine then reduces rapidly once rated power is achieved as the thrust required to maintain rated power reduces.

The thrust applied by the turbine to the flow reduces more quickly as the flow speed in the channel increases than the thrust increases as the flow speed decreases in the channel, as a positive feedback is established between the increasing flow speed and decreasing thrust applied to the flow. Power capping may be implemented for a number of reasons, such as limiting the impact of power extraction and economically sizing turbine generators to the energy available in the flow. The optimal choice of turbine which maximises the power extracted from the flow subject to constraints on the impact on the flow and economic and financial considerations will require many simulations of a wide range of parameters.

Removal of momentum from the flow results in a change in the volume flow rate through the channel, as seen in the differences between the capping and non-capping arrays. Analytic models have shown that the total power available in a channel is dependent on the dynamical balance in the channel between the driving head and the resistance to the flow through the channel of the bed friction, as well as other features such as the flow at the exit of the channel (Garrett and Cummins, 2005; Vennell, 2010). The impact of power extraction on the flow in a channel with a substantial background friction will be considerably different to that in a channel with little or no background friction, and this will alter the optimal rated power of an array in the channel. Further work should be done to investigate the effect of bed friction on array performance.

Chapter 9

Conclusions

How awful is a river without water!
- Ancient Egyptian proverb

This thesis has investigated the power that may be extracted from a flow by an turbine array partially spanning a wide channel. A separation of scales has been proposed in which a distinction has been made between turbine- and array-scale phenomena. Provided that the array is composed of a sufficient number of turbines, this conceptual distinction allows the two scales to be analysed quasi-independently and allows a distinction to be made between the three-dimensional flow around a device and the predominantly two-dimensional flow around the array. This has been used to analyse the contributions individual turbines make to the power available to the turbines as well as the aggregate response of the flow to the turbines.

The conclusions of this thesis are summarised in three parts: the scale separated analytic models, summarising Chapters 2 and 3; the depth averaging process and the role of turbulence modelling in depth averaged simulations, summarising Chapters 4 to 6, and finally those relating to turbine operation, summarising Chapters 7 and 8. The chapter concludes with suggestions for future work.

9.1 Conclusions

9.1.1 Scale Separation

An analytic model of an array partially spanning a wide channel is developed through a separation of scales between the array-scale and turbine-scale flows. Three-dimensional mixing downstream of the turbine is assumed to occur much more quickly than the largely two-dimensional mixing downstream of the array due to the relative scale of the device diameter and array width. The two problems are coupled wherein the flow through the array provides the upstream boundary to the turbine-scale problem. The turbine-scale model is solved to determine the available turbine power and the downstream internal boundary to the array-scale problem, completing the coupling. Energy extraction at the device-scale results in only a static head discontinuity across the actuator disc, whereas array-scale energy extraction results in both a static head and velocity discontinuity, requiring iterative solution techniques to solve the model.

The power available to an array may be increased above that achieved by homogeneously deploying the turbines across the channel cross-section by reducing the inter-turbine spacing, thus increasing the local blockage ratio, to exploit the confinement of the flow passage around each turbine, thereby increasing the available array power. Available power also increases with Froude number, although to a lesser extent than increased blockage ratio.

Two special cases of the partial array model were considered; the infinitely wide channel, and the volume-flux constrained channel. An optimal local blockage ratio of $B_L \approx 0.40$ and increasing with Froude number exists for a turbine array in an infinitely wide channel. The volume-flux constrained channel is a special case of the open channel model in the limit that the change in cross-sectional area of the channel tends to zero, and allows the volume-flux constrained partial array model of Nishino and Willden (2012b) to be recovered.

9.1.2 Depth-averaged Simulations and Turbulence Modelling

Two-dimensional turbulence behaves differently to better understood three-dimensional turbulence in a number of ways, one key feature being a dual cascade in which energy is concentrated in large, coherent eddies and enstrophy cascades down to the Kolmogorov micro scales where it is dissipated. A simple eddy model was proposed to close the depth-averaged Reynolds stress term of the shallow water equations, and it was shown that, to a first approximation, the depth-averaged Reynolds stresses are dominated by the velocity fluctuations corresponding to the largest eddies in the domain. Assuming that turbulence production, advection and dissipation are largely in equilibrium in the flow, a simple constant relationship with the mean flow speed and characteristic scaling of the eddies at the injection wave number was proposed. A parameteric study was conducted for the turbulence model, which showed that the thrust and power of the array was largely unaffected by the magnitude of the turbulence intensity parameter, but that it did affect how quickly the wake was dissipated.

A further challenge of depth-averaged simulations is the accurate representation of three-dimensional arrays in a two dimensional model. The importance of the bypass flow for the array power has been established theoretically and experimentally, but this cannot be easily represented within a two-dimensional model. One difficulty is the depth-averaged representation of the turbine-, array- and global blockage ratios that is consistent with the three-dimensional problem. A depth-averaged analytic correction was proposed based on the scale separation principles presented in Chapter 3, to provide a sub-grid scale model defined in terms of the turbine thrust coefficient, based on the local basin efficiency of the turbines, allowing the correction to be applied as a simple post-processing step of a simulation. Agreement between the corrected array simulations and partial array analytic models was shown to increase as the number of turbines in the array increased and the local blockage ratio decreased.

9.1.3 Turbine Operation Characteristics

Blade element momentum theory, which has been successfully used for wind turbines, has been adapted to account for one of the key differences between tidal and wind turbines, where a pressure gradient develops upstream and downstream of a tidal turbine as a result of the constraint on the volume flux of the flow. The semi-analytic volume-flux constrained BEM model has been shown to agree well with three-dimensional numerical simulations.

The periodic variation in the strength of the tides and economic considerations concerning the selection of tidal turbine generators for the available tidal resource means that tidal turbines may depart from the cubic relationship assumed in actuator disc theory for some period of the tidal cycle. A number of strategies may be adopted to limit the turbine power to some maximum level, but experience in the wind turbine industry suggests that feathering the turbine blades may be particularly efficient. The volume-flux constrained BEM model was used, given a simple power control strategy, to determine performance characteristics of a tidal turbine during power capping. Rated power is achieved at lower flow speeds for more highly blocked turbines, as a higher thrust may be applied to the flow. Arrays were simulated in a tidal channel between two large basin forced by the M2 and M2 + S2 tidal constituents. The reduction in thrust that is achieved while the turbines operate at rated power means that the reduction in volume flux through the channel is less than that of an array without power capping. Thrust reduces more quickly as the flow speed increases than when it decreases due to a positive feedback that is established by the reducing resistance to the flow and the reducing level of thrust that must be applied to the flow as the flow speed increases, as opposed to the negative feedback that occurs as the flow speed decreases.

9.2 Future Work

9.2.1 Analytic Models

Actuator disc theory assumes that the flow passage around the disc is symmetric and that the wake expands uniformly in all directions. However devices in low local blockages typically have a lateral inter-turbine spacing greater than the depth of the flow, and in high local blockages the lateral inter-turbine spacing is typically considerably smaller than the vertical distance above and below the device. The relative contributions of these dimensions to the confinement of the flow is believed to affect turbine performance and may be of importance in predicting the power of arrays in which the lateral and vertical spacing are significantly different.

9.2.2 Depth-averaged Modelling

The differences between three- and two-dimensional turbulence mean that three-dimensional turbulence models have fairly limited applicability to two-dimensional simulations. One key challenge in tidal turbine modelling is that a significant proportion of the turbulence is generated at sub-grid length scales and needs to be modelled. A depth-averaged turbulence model which considers the production, advection, and dissipation of turbulence should be developed for tidal turbine modelling to account for the sub-grid scale turbulence generation. Presently there is a limited number of studies with which to parameterise such a model, and experimental and high resolution numerical work will be required to provide the necessary data.

9.2.3 Volume-flux Constrained BEM

A number of empirical and semi-empirical corrections are applied to blade element momentum theory for wind turbines to account for the tip and hub losses that are observed to occur along the span of the blades. These models have not been es-

tablished for tidal turbines, and may require a different formulation, particularly for flow near the tips where the influence of the domain boundaries may be particularly important. Further work is also required to establish how the swirl induction factor a' varies in the wake of the rotor in a volume flux constrained flow, as this would change elemental thrust and torque of the blade elements.

9.2.4 Power Capping

The dynamic balance that exists in tidal channels between the driving tidal amplitude, the channel bed friction and flow dynamics, and the thrust applied by the turbines has been studied analytically by Garrett and Cummins (2005) and Vennell (2010), for example. The variation in the available power and fraction of the time spent at rated power may change as a result of an altered dynamical balance in the channel, and would be important in determining the optimal rated power of the channel. The effect of the number of turbines and varying blockage ratios should also be explored in more detail, as these would also alter the power extracted from the flow.

9.3 Contributions

Open Channel Partial Array Model

The open channel partial array model is the first general formulation of a turbine array partially spanning a wide channel with a deformable free surface at both the turbine and array scales. This results in differences between the turbine- and array-scale model equations. Device-scale energy extraction results in only a static head discontinuity across the actuator disc, whereas array-scale energy extraction causes a static head and a velocity discontinuity to develop across the array, making the system more challenging to solve than the volume-flux constrained partial array model. The formulation in this thesis provides the first unified presentation of the more general

open channel equations and the volume-flux constrained partial array model and the limit of an infinitely wide channel.

Depth-averaged Modelling

Analysis of the role of two-dimensional turbulence in depth-averaged simulations of tidal turbine arrays is presented, and a simple turbulence model developed that combines two-dimensional turbulence theory with the concept of turbulent eddies. This is combined with an analytic correction for depth-averaged simulations to ensure that the local-, array-, and global blockage ratios of the array, as well as the thrust and power, are consistent between two- and three-dimensions to ensure the accurate depth-averaged simulation of turbine arrays.

Volume-flux Constrained BEM Theory

This thesis presents the volume-flux constrained BEM theory which allows traditional BEM theory for turbines in an infinitely large flow field to be directly applied to turbine in a volume-flux constrained flow field, such as tidal turbines. The theory provides a simple means by which performance characteristics of a turbine may be determined under different operating conditions and thereby allow a more accurate representation of a turbine than an actuator disc.

Power Capping

Volume-flux constrained BEM theory is utilised to determine the performance of the turbine under a power capping regime, given the turbine geometry and hydrodynamic properties. This allows the effect of turbine power capping with realistic turbine data on array performance to be assessed in a tidal channel. Arrays are simulated in channels with constant inflow velocity in addition to channels driven by tidal constituents to assess the impact on the array power and the flow in the channel.

References

Adcock, T. A. A., Draper, S., Houlsby, G. T., Borthwick, A. G. L., and Serhadglıoğlu, S. The available power from tidal stream turbines in the Pentland Firth. *Proc R Soc A*, 469(2157), 2013.

Adcock, T. A. A., Draper, S., Houlsby, G. T., Borthwick, A. G. L., and Serhadglıoğlu, S. Tidal stream power in the Pentland Firth - long term variability, multiple constituents and capacity factor. *Proc IMechE A: J Power and Energy*, 228(8): 854–861, 2014.

Ahmadian, R., Falconer, R., and Bockelmann-Evans, B. Far-field modelling of the hydro-environmental impact of tidal stream turbines. *Renewable Energy*, 38(107-116), 2012.

Albukrek, C. M., Urban, K., Rempfer, D., and Lumley, J. L. Divergence-free wavelet analysis of turbulent flows. *J Sci Computing*, 17:49–66, 2002.

Anderson, J. D. *A History of Aerodynamics*. Cambridge: Cambridge University Press, 1997.

Atwater, J. F. and Lawrence, G. A. Power potential of a split tidal channel. *Renewable Energy*, 35:329–332, 2010.

Bai, G., Li, J., Fan, P., and Li, G. Numerical investigations of the effects of different arrays on power extractions of horizontal axis tidal current turbines. *Renewable Energy*, 53:180–186, 2013.

Bai, L., Spencer, R. R. G., and Dudziak, G. Investigation of the influence of array arrangement and spacing on tidal energy converter (TEC) performance using a 3-dimensional CFD model. In *Proc* 8^{th} *European Wave and Tidal Energy Conf*, Uppsala, Sweden, 2009.

Baker, C. Tidal Power. *Energy Policy*, 19(8):792–797, 1991.

Batchelor, G. K. *An Introduction to Fluid Dynamics*. Cambridge: Cambridge University Press, 1967.

Batchelor, G. K. Computation of the energy spectrum in homogeneous two-dimensional turbulence. *Phys Fluids*, 12:II–262–II–270, 1969.

Belloni, C. S. K. and Willden, R. H. J. Flow field and performance analysis of bidirectional and open-centre ducted tidal turbines. In *Proc* 9^{th} *European Wave and Tidal Energy Conf*, Southampton, UK, 2011.

Beri, H. and Yao, Y. Double multiple streamtube model and numerical analysis of vertical axis wind turbine. *Energy and Power Eng*, 3(3):262–270, 2011.

Betz, A. Das Maximum der theoretisch moglichen Ausnutzung des Windes durch Windmotoren. *Zeit ges Turbinenwesen*, 26:307–309, 1920.

Black & Veatch. Phase II UK tidal stream energy resource assessment. Technical report, London: Black & Veatch Corporation, July 2005.

Bradshaw, P. The understanding and prediction of turbulent flow. *Aero J*, pages 403–418, 1972.

Brent, R. *Algorithms for minimization without derivatives*. Englewood Cliffs, NJ: Prentice Hall, 1973.

Burrows, R., Walkington, I. A., Yates, N. C., Hedges, T. S., Wolf, J., and Holt, J. The tidal range energy potential of the West Coast of the United Kingdom. *App Ocean Res*, 31:229–238, 2009.

Burton, T., Sharpe, D., Jenkins, N., and Bossanyi, E. *Wind Energy Handbook*. West Sussex: John Wiley & Sons, Ltd., 2001.

Callaghan, J. and Boud, R. *Future Marine Energy*. London: Carbon Trust, 2006.

Cebeci, T. *Turbulence Models and Their Application*. Long Beach: Horizons Publishing, 2004.

Celik, I. B. *Introductory Turbulence Modelling*. Morgantown: West Virginia University, 1999.

Charlier, R. H. and Finkl, C. W. *Ocean Energy - Tide and Tidal Power*. Berlin: Springer-Verlag, 2009.

Chertkov, M., Connaughton, C., Kolokolev, I., and Lebedev, V. Dynamics of energy condensation in two-dimensional turbulence. *Phys Rev Letters*, 99(8):084501, 2007.

Churchfield, M. J., Li, Y., and Moriarty, P. J. A large-eddy simulation study of wake propagation and power production in an array of tidal-current turbines. *Proc R Soc A*, 371(1985), 2013.

Cummins, P. F. The extractable power from a split tidal channel: An equivalent circuit analysis. *Renewable Energy*, pages 395–401, 2013.

Davidson, P. A. *Turbulence: An introduction for scientists and engineers*. Oxford: Oxford University Press, 2004.

Defant, A. *Physical Oceanography, Vol. 11*. New York: Pergamon Press, 1961.

Deparis, V., Legros, H., and Souchay, J. Tides in astronomy and astrophysics. chapter Investigations of Tides from the Antiquity to Laplace, pages 31–82. Berlin: Springer-Verlag, 2013.

Divett, T., Vennell, R., and Stevens, C. Optimisation of multiple turbine arrays in a channel with tidally reversing flow by numerical model with adaptive mesh. In *Proc* 9^{th} *European Wave and Tidal Energy Conf*, Southampton, UK, 2011.

Dorfman, J. R. and Cohen, E. G. D. Velocity correlation functions in two and three dimensions. *Phys Rev Letters*, 25:1257–1260, 1970.

Draper, S. *Tidal Stream Energy Extraction in Coastal Basins*. DPhil thesis, University of Oxford, 2011.

Draper, S., Houlsby, G. T., Oldfield, M. L. G., and Borthwick, A. G. L. Modelling tidal energy extraction in a depth-averaged coastal domain. *IET Renewable Power Generation*, 4:545–554, 2010.

Draper, S., Adcock, T. A. A., Borthwick, A. G. L., and Houlsby, G. T. An electrical analogy for the Pentland Firth tidal stream power resource. *Proc R Soc A*, 470 (2161), 2014.

DTI. Stingray tidal stream energy device - phase 3. Technical report, The Engineering Business Ltd., 2005.

Durbin, P. A. and Medic, G. *Fluid Dynamics with a Computational Perspective*. Cambridge: Cambridge University Press, 2007.

Ecke, R. The turbulence problem, an experimentalist's perspective. *Los Alamos Science*, 29:124–141, 2005.

Elghali, S. E. B., Balme, R., Saux, K. L., Benbouzid, M. E.-H., Charpentier, J. F., and Hauville, F. A simulation model for the evaluation of the electrical power potential harness by a marine current turbine. *IEEE J Ocean Eng*, 32(4):786–797, 2007.

Euler, L. Principes généraux du mouvement des fluides. *Mém Académie Sciences Berlin*, 11:274–315, 1757.

European Commission. Energy 2020: A Strategy for Competitive, Sustainable and Secure Energy COM(2010) 639 final, 2010.

Farazmand, M. M., Kevlahan, N. K.-R., and Protas, B. Controlling the dual cascade of two-dimensional turbulence. *J Fluid Mech*, 668:202–222, 2011.

Farge, M., Kevlahan, N. K. R., Perrier, V., and Schneider, K. Turbulence analysis, modelling and computation using wavelets. In van den Berg, J. C., editor, *Wavelets in Physics*. Cambridge: Cambridge University Press, 1999.

Fischer, H. B. *Mixing in inland and coastal waters*. New York: Academic Press, 1979.

Fjørtoft, R. On the changes in spectral distribution of kinetic energy for two-dimensional non-divergent flow. *Tellus*, 5:225–230, 1953.

Fraenkel, P. L. Marine current turbines: Pioneering the development of marine kinetic energy converters. *Proc IMechE A: J Power and Energy*, 221(1):159–169, 2007.

Fraenkel, P. Power from marine currents. *Proc IMechE A: J Power and Energy*, 216 (1):1–14, 2002.

Froude, R. On the part played in propulsion by differences of fluid pressure. *Trans Inst Naval Architects*, 30:390–405, 1889.

Funke, S. W., Farrell, P. E., and Piggott, M. D. Tidal turbine array optimisation using the adjoint approach. *Renewable Energy*, 63:658–673, 2014.

Garrett, C. and Cummins, P. Generating tidal power from currents. *J Waterway, Port, Coastal and Ocean Eng*, 130:114–118, 2004.

Garrett, C. and Cummins, P. The power potential of tidal currents in channels. *Proc R Soc A*, 461:2563–2572, 2005.

Garrett, C. and Cummins, P. The efficiency of a turbine in a tidal channel. *J Fluid Mech*, 588:243–251, 2007.

Garrett, C. and Cummins, P. Limits to tidal current power. *Renewable Energy*, 33 (11):2485–2490, 2008.

Garrett, C. and Greenberg, D. Predicting changes in the tidal regime: The open boundary problem. *J Phys Oceanography*, 7:171–181, 1977.

Geoscience Australia. *Australian Energy Resource Assessment*. Canberra: Geoscience Australia, 2010.

Glauert, H. Airplane propellers. In Durand, W. F., editor, *Aerodynamic Theory*. Berlin: Springer-Verlag, 1935.

Glauert, H. *The Elements of Aerofoil and Airscrew Theory*. Cambridge: Cambridge University Press, 1947.

Grubb, M. The integration of renewable electricity sources. *Energy Policy*, 19(7):670 – 688, 1991.

Hau, E. and von Renouard, H. *Wind turbines*. Berlin: Springer-Verlag, 2006.

Hench, J. L. and Luettich, R. A. Transient tidal circulation and momentum balances at a shallow inlet. *J Phys Oceanography*, 33:913–932, 2003.

Hervouet, J.-M. *Hydrodynamics of free surface flows*. Chichester: John Wiley & Sons, 2007.

Hinterberger, C., Fröhlich, J., and Rodi, W. Three-dimensional and depth-averaged large-eddy simulations of some shallow water flows. *J Hyd Eng*, 133, 2007.

Houlsby, G. T., Draper, S., and Oldfield, M. L. G. Application of linear momentum actuator disc theory to open channel flow. Technical Report OUEL 2296/08, Dept. of Engineering Science, University of Oxford, 2008.

Iwayama, T., Shepherd, T. G., and Watanabe, T. An 'ideal' form of decaying two-dimensional turbulence. *J Fluid Mech*, 456:183–198, 2002.

Jirka, G. H. Large scale flow structures and mixing processes in shallow flows. *J Hyd Res*, 39:567–573, 2001.

Kolmogorov, A. N. Dissipation of energy in locally isotropic turbulence. *Proc USSR Sciences*, 32:16–18, 1941a.

Kolmogorov, A. N. The local structure of turbulence in incompressible viscous fluid for very large Reynolds numbers. *Proc USSR Sciences*, 30:301–305, 1941b.

Komar, P. D. *Beach processes and sedimentation*. New Jersey, USA: Prentice-Hall, 1976.

Kraichnan, R. H. Inertial-range transfer in two- and three-dimensional turbulence. *J Fluid Mech*, 47(3):525–535, 1971.

Kraichnan, R. H. Eddy viscosity in two and three dimensions. *J Atmos Sci*, 33: 1521–1536, 1976.

Kraichnan, R. H. and Montgomery, D. Two-dimensional turbulence. *Rep Prog Physics*, 43:547–619, 1980.

Lanchester, F. A contribution to the theory of propulsion and the screw propeller. *Trans Inst Naval Architects*, 57:98–116, 1915.

Laplace, P. S. Théorie des attractions des sphéroïdes et de la figure de la terre. *Mém Académie Sciences Paris*, pages 341–419, 1782.

Leishman, J. G. *Principles of Helicopter Aerodynamics*. Cambridge, UK: Cambridge Aerospace Series, Cambridge University Press, 2006.

Lighthill, J. *Waves in Fluids*. Cambridge, UK: Cambridge University Press, 1978.

Lund, H. and Mathiesen, B. Energy system analysis of 100% renewable energy systems–The case of Denmark in years 2030 and 2050. *Energy*, 34(5):524 – 531, 2009. 4$^{\text{th}}$ Dubrovnik Conf Sust Dev Energy, Water & Environment.

MacKay, D. *Sustainable energy — Without the hot air*. Cambridge: UIT Cambridge, 2008.

Madsen, P. A., Rugbjerg, M., and Warren, I. R. Subgrid modelling in depth integrated flows. In *Proc* 21st *Int Conf Coastal Eng*, pages 505–511, New York, USA, 1988.

Masters, I., Chapman, J. C., Willis, M. R., and Orme, J. A. C. A robust blade element momentum theory model for tidal stream turbines including tip and hub loss corrections. *J Marine Eng and Tech*, 10(1):25–35, 2011.

McAdam, R. A., Houlsby, G. T., Oldfield, M. L. G., and McCulloch, M. D. Experimental Testing of the Transverse Horiztonal Axis Water Turbine. In *Proc* 8^{th} *European Wave and Tidal Energy Conf*, pages 360–365, Uppsala, Sweden, 2009.

McCombes, T., Johnstone, C., and Grant, A. Unsteady 3D wake modelling for marine current turbines. In *Proc* 8^{th} *European Wave and Tidal Energy Conf*, pages 548–557, Uppsala, Sweden, 2009.

Mellor, G. L. and Yamada, T. Development of a turbulence closure model for geophysical fluid problems. *Rev Geo Space Phys*, 20(4):851–875, 1982.

Miles, J. W. Resonant response of harbours: an equivalent-circuit analysis. *J Fluid Mech*, 46(2):241–265, 1971.

Muchala, S. and Willden, R. H. J. Impact of Tidal Turbine support structures on realisable turbine farm power, 2014. Personal communication.

Nadaoka, K. and Yagi, H. Shallow-water turbulence modelling and horizontal large-eddy computation of river flow. *J Hyd Eng*, 124(5):493–500, 1998.

Navier, C. L. M. H. Mémoire sur les lois du mouvement des fluides. *Mém l'Académie Sciences France*, 6:389–440, 1823.

Nieuwstadt, F. T. M. Direct and large-eddy simulation of free convection. In *Proc* 9^{th} *Int Heat Transfer Conf*, pages 37–47, 1990.

Nishino, T. and Willden, R. H. J. Effects of 3-D channel blockage and turbulent wake mixing on the limit of power extraction by tidal turbines. *Int J Heat and Fluid Flow*, 37:123–135, 2012a.

Nishino, T. and Willden, R. H. J. The efficiency of an array of tidal turbines partially blocking a wide channel. *J Fluid Mech*, 708:596–606, 2012b.

Nishino, T. and Willden, R. H. J. Two-scale dynamics of flow past a partial cross-stream array of tidal turbines. *J Fluid Mech*, 730:220–244, 2013.

Oetzel, K. G. and Vallis, G. K. Strain, vortices, and the enstrophy inertial range in two-dimesional turbulence. *Phys Fluids*, 9(10):2991–3004, 1997.

Paraschivoiu, I. Double-multiple stream tube model for studying vertical-axis wind turbines. *J Propulsion and Power*, 4(4):370–377, 1988.

Plew, D. R. and Stevens, C. L. Numerical modelling of the effect of tidal turbines on currents in tidal channels - Tory Channel, New Zealand. *Renewable Energy*, 57: 269–282, 2013.

Plumb, R. A. and Marshall, J. *Atmosphere, Ocean, and Climate Dynamics*. New York: Academic Press, 2007.

Poisson, S. D. Mémoire sur les équations générales de l'équilibre et du mouvement des corps solides élastiques et des fluides. *J École Polytechnique*, 13:1–174, 1831.

Popinet, S. Gerris: A tree-based solver for the incompressible Euler equations in complex geometries. *J Comp Phys*, 190(2):512–600, 2003.

Prandtl, L. Bereicht über Untersuchungen zur ausgebildeten Turbulenz. *Zeit Angewandte Mathematik und Mechanik*, 5:136–139, 1925.

Prandtl, L. Über die Rolle der Zähigkeit im Mechanismus der augebildete Turbulenz. *Nach Gesellschaft Wis Göttingen, Math-phys Klasse*, pages 6–18, 1945.

Prandtl, L. and Tietjens, O. G. *Fundamentals of Hydro- and Aeromechanics (translated)*. New York: Dover Publications, 1934.

Pugh, D. T. *Tides, surges, and mean sea level*. Chichester: John Wiley & Sons, 1987.

Rainey, R. C. T. The optimum position for a tidal barrage in the Severn estuary. *J Fluid Mech*, 636:497–507, 2009.

Rankine, W. On the mechanical properties of propellers. *Trans Inst Naval Architects*, 6:13–30, 1865.

Reynolds, O. On the dynamical theory of incompressible viscous fluids and the determination of the criterion. *Phil Trans R Soc London*, 186:123–164, 1895.

Rodi, W. *Turbulence models and their applications - A state of the art review*. Delft: International Association for Hydraulic Research, 1980.

Ryrie, S. C. An optimal control model of tidal power generation. *App Math Modelling*, 19:123–126, 1995.

Saint-Venant, A. J. C. B. Note á joindre au mémoire sur la dynamique des fluides. *Compt Ren Séances Académie Sciences, Paris*, 17:1240–1243, 1843.

Schluntz, J. *Tidal Turbine Array Modelling*. DPhil thesis, University of Oxford, 2014.

Schmitt, F. G. About Boussinesq's turbulent viscosity hypothesis: historical remarks and a direct evaluation of its validity. *Compt Ren Méc*, 335:617–627, 2007.

Sinclair Knight Merz. Renewable energy assessment. Technical report, Wellington: Energy Efficiency and Conservation Authority, 2006.

Smagorinsky, J. General circulation experiments with the primitive equations I. The basic experiment. *Monthly Weather Review*, 91:99–164, 1963.

Sreenivasan, K. R. and Antonia, R. A. The phenomenology of small-scale turbulence. *Ann Rev Fluid Mech*, 29:435–472, 1997.

Stokes, G. G. On the theories of the internal friction of fluids in motion, and of the equilibrium and motion of elastic solids. *Trans Cambridge Phil Soc*, 8:287–319, 1845.

Strickland, J. H. The Darrieus turbine: A performance prediction model using multiple streamtubes. Technical Report SAND75-041, Albuquerque: Sandia National Laboratory, 1975.

Tabeling, P. Two-dimensional turbulence. *Phys Rep*, 362:1–62, 2002.

Tennekes, H. and Lumley, J. L. *A First Course in Turbulence*. Cambridge: The MIT Press, 1972.

Turnock, S. R., Phillips, A. B., Banks, J., and Nicholls-Lee, R. Modelling tidal current turbine wakes using a coupled RANS-BEM approach as a tool for analysing power capture of arrays of turbines. *Ocean Eng*, 469:1300–1307, 2011.

Vennell, R. Tuning turbines in a tidal channel. *J Fluid Mech*, 663:253–267, 2010.

Vennell, R. Tuning tidal turbines in-concert to maximise farm efficiency. *J Fluid Mech*, 671:587–604, 2011.

Walkington, I. and Burrows, R. Modelling tidal stream power potential. *App Ocean Res*, 31:239–245, 2009.

Whelan, J. I., Thomson, M., Graham, J. M. R., and Peiró, J. Modelling of free-surface proximity and wave induced velocities around a horizontal axis tidal stream turbine. In *Proc* 7^{th} *European Wave and Tidal Energy Conf*, Porto, Portugal, 2007.

Whelan, J. I., Graham, J. M. R., and Peiró, J. A free-surface and blockage correction for tidal turbines. *J Fluid Mech*, 624:281–291, 2009.

White, F. M. *Fluid Mechanics*. London: McGraw Hill, 1994.

Wilson, R. E. and Lissaman, P. B. S. Applied aerodynamics of wind power machines. Technical report, Oregon State University, 1974.

Yates, N., Walkington, I., Burrows, R., and Wolf, J. The energy gains realisable through pumping for tidal range energy schemes. *Renewable Energy*, 58:79–84, 2013.

Zhai, Z., Zhang, Z., Zhang, W., and Chen, Q. Evaluation of various turbulence models in predicting airflow and turbulence in closed environments by CFD: Part 1: Summary of prevalent turbulence models. *HVAC&R Res*, 13(6), 2007.

Zu, T., Gan, J., and Erofeeva, S. Y. Numerical study of the tide and tidal dynamics in the South China Sea. *Deep-Sea Res: I*, 55:137–154, 2007.